Finite Element Simulation of a Poroelastic Model of the CSF System in the Human Brain during an Infusion Test

Almut Eisenträger

St John's College
University of Oxford

A thesis submitted for the degree of
Doctor of Philosophy in Numerical Analysis

Trinity Term 2012

Finite Element Simulation of a Poroelastic Model of the CSF System in the Human Brain during an Infusion Test

Almut Eisenträger

St John's College, University of Oxford

A thesis submitted for the degree of
Doctor of Philosophy in Numerical Analysis

Trinity Term 2012

Abstract

Cerebrospinal fluid (CSF) fills a system of cavities at the centre of the brain, known as ventricles, and the subarachnoid space surrounding the brain and the spinal cord. In addition, CSF is in free communication with the interstitial fluid of the brain tissue. Disturbances in CSF dynamics can lead to diseases that cause severe brain damage or even death. So-called infusion tests are frequently performed in the diagnosis of such diseases. In this type of test, changes in average CSF pressure are related to changes in CSF volume through infusion of known volumes of additional fluid.

Traditionally, infusion tests are analysed with single compartment models, which treat all CSF as part of one compartment and balance fluid inflow, outflow and storage through a single ordinary differential equation. Poroelastic models of the brain, on the other hand, have been used to simulate spatial changes with disease, particularly of the ventricle size, on larger time scales of days, weeks or months. Wirth and Sobey (2008) developed a two-fluid poroelastic model of the brain in which CSF pressure pulsations are linked to arterial blood pressure pulsations. In this thesis, this model is developed further and simulation results are compared to clinical data.

At first, the functional form of the compliance, which governs the storage of CSF in single compartment models, is examined by comparison of two different compliance models with clinical data. The derivations of a single-fluid and a two-fluid poroelastic model of the brain in spherical symmetry are laid out in detail and some of the parameters are related to the compliance functions considered earlier. The finite element implementation of the two-fluid model is described and finally simulation results of the average CSF pressure response and the pressure pulsations are compared to clinical data.

Acknowledgements

First of all, I must express my sincere gratitude to my supervisor, Ian Sobey. His constant encouragement, guidance and support helped me face the various challenges I encountered in my research.

I thank Marek Czosnyka for access to clinical data and discussions about the clinical background of my work. The Numerical Analysis group provided a great, supportive working environment with many opportunities to discuss and learn about mathematics, academia and, indeed, the world. Special thanks go to Jen Pestana and Ivo Panayotov for proof-reading this thesis.

I gratefully acknowledge financial support from the Engineering and Physical Sciences Research Council (EPSRC) as well as the Department of Computer Science, formerly Computing Laboratory, University of Oxford.

I would also like to thank the IT team of the Mathematical Institute. The numerous simulations that provide the results of my thesis were only possible because the departmental IT system kept working perfectly. Any issue or question I ever had was dealt with in no time.

Last, but not least, I thank my parents for their continuing support and encouragement, my friends, who have made my time in Oxford unforgettable, and Martijn for his love, understanding and comfort through stressful times.

The rational soul functions through the actions of its first instrument, psychic pneuma.

Galen according to J. Rocca, Galen on the brain (2003)

Contents

List of Figures

List of Tables

Notation

Conversion of clinical units to SI units

Pressure	$1\,\mathrm{mmHg} \approx 133.3\,\mathrm{Pa} = 133.3\,\mathrm{N/m^2}$
Volume	$1\,\mathrm{ml} = 10^{-6}\,\mathrm{m^3}$
Flow rate	$1\,\mathrm{ml/min} \approx 1.67 \cdot 10^{-8}\,\mathrm{m^3/s}$

List of variables

$\mathcal{A}, \boldsymbol{A}^{\mathrm{ode}}, \boldsymbol{A}^{\mathrm{bc}}, \boldsymbol{A}$	Descriptions of steady state, spherically symmetric, poroelastic model equations (weak form of ODE, discretisation of ODE, discretised boundary conditions, full discretised system)
$a_1, \ldots, a_4$	Integration constants
α, a	Biot–Willis parameter, measuring the saturation of a porous solid with fluid (in dimensional and nondimensionalised descriptions)
$\alpha_{\mathrm{a}}, \alpha_{\mathrm{v}}$	Biot–Willis parameters for arterial and venous blood
b	Nondimensionalised CSF storage function, related to γ
b_{a}	Nondimensionalised arterial blood storage function, related to γ_{a}
$\mathcal{B}, \boldsymbol{B}^{\mathrm{pde}}, \boldsymbol{B}^{\mathrm{bc}}, \boldsymbol{B}$	Descriptions of right hand side of time-dependent, spherically symmetric, poroelastic model equations (weak form of PDE, spatial discretisation of PDE, spatially discretised boundary conditions, full spatially discretised system)
C	CSF compliance
$c_1, \ldots, c_6$	Nondimensional constants in the poroelastic boundary conditions

d	§2: Number of free parameters in a single-compartment model
d	§3ff.: Diameter of modelled aqueduct of Sylvius connecting the ventricle and the subarachnoid space
$\mathcal{DA}, \boldsymbol{DA}^{\text{ode}}, \boldsymbol{A}^{\text{bc}}, \boldsymbol{DA}$	Linearisation of steady state, spherically symmetric, poroelastic model equations (weak form of ODE, discretisation of ODE, discretised boundary conditions, full discretised system)
E	Elasticity , parameter in compliance models
$\tilde{e}$	Constant parameter in pressure-dependent elasticity model
$\boldsymbol{\mathcal{E}}$	Linear strain tensor of solid matrix
$\epsilon, \epsilon_0, \varepsilon, \varepsilon^h, \varepsilon_i$	Volume dilation/volumetric strain of porous matrix (dimensional, scaling, nondimensionalised, piecewise linear approximation, nodal values)
$\tilde{\varepsilon}$	Perturbation to nondimensionalised volume dilation
η	Viscosity of CSF
F	Least squares objective function measuring the distance between measured and modelled CSF pressure response in single compartment model
$\boldsymbol{F}$	Deformation gradient
γ	CSF/fluid storage coefficient in porous material
$\gamma_{\text{a}}, \gamma_{\text{v}}$	Arterial blood and venous blood storage coefficients in brain tissue
h_i	Spatial step size in finite element discretisation of spherically symmetric poroelastic model
$\boldsymbol{I}$	Identity matrix/tensor
$\mathcal{I}_j, \mathcal{I}_j^{\text{l}}, \mathcal{I}_j^{\text{r}}$	Shorthand notation for repeating integrals in finite element description of spherically symmetric, poroelastic model
κ, κ_0, k	Permeability of solid matrix (dimensional, scaling, nondimensionalised)
L	§2: Adapted objective function measuring the difference between measured and modelled CSF pressure response in single compartment model
L	§3ff.: Length of modelled aqueduct of Sylvius, connecting the ventricle with the subarachnoid space
$\mathcal{L}, \boldsymbol{L}^{\text{pde}}, \boldsymbol{L}^{\text{bc}}, \boldsymbol{L}$	Descriptions of left hand side with time-derivatives of time-dependent, spherically symmetric, poroelastic model equations (weak form of PDE, spatial discretisation of PDE, spatially discretised boundary conditions, full spatially discretised system)
λ	First Lamé parameter

M_0, M	Permeability model parameter (dimensional, nondimensionalised)
μ	Second Lamé parameter
n	Power law index in generalised compliance model
N	Number of spatial elements in finite element discretisation of spherically symmetric, poroelastic model
ν	Poisson's ratio
ω	Damping parameter for partial Newton steps
P, P_0, p	CSF/fluid pore pressure (dimensional, scaling, nondimensionalised)
$P_\mathrm{a}, p_\mathrm{a}, P_\mathrm{v}, p_\mathrm{v}$	Arterial and venous blood pressures (dimensional, nondimensionalised)
p_c	Nondimensional, spatially independent, time-dependent CSF pressure contribution
P_b	Baseline CSF pressure before an infusion
P_plat	Plateau CSF pressure during a constant rate infusion test
P_r	Reference pressure in compliance models
P_ss	Venous blood pressure in the superior sagittal sinus
$P_\mathrm{left}, p_\mathrm{left}$	Left boundary pressures in planar poroelastic model problem (dimensional, nondimensionalised)
$P_\mathrm{right}, p_\mathrm{right}$	Right boundary pressures in planar poroelastic model problem (dimensional, nondimensionalised)
$P_\mathrm{in}, p_\mathrm{in}, P_\mathrm{out}, p_\mathrm{out}$	Inner and outer boundary values for CSF pressure in spherically symmetric, poroelastic model (dimensional, nondimensionalised)
P_sf	Reference pressure at which solid in poroelastic model is stress-free
φ	Test function in weak formulation of poroelastic model
φ_i	Piecewise linear basis function in finite element discretisation of spherically symmetric, poroelastic model
$\boldsymbol{Q}, Q, q$	Darcy/discharge velocity (vector, main component, nondimensionalised)
Q_0	Scaling for flow rates
$Q_\mathrm{in}, Q_\mathrm{out}$	CSF inflow and outflow rates
Q_inf	Fluid infusion rate of an infusion test
$Q_\mathrm{prod}, q_\mathrm{prod}$	CSF production rate (dimensional, nondimensionalised)
$Q_\mathrm{infv}, q_\mathrm{infv}$	Fluid infusion rate of an infusion test into the ventricle (dimensional, nondimensionalised)
$Q_\mathrm{infs}, q_\mathrm{infs}$	Fluid infusion rate of an infusion test into the subarachnoid space (dimensional, nondimensionalised)
$Q_\mathrm{aqu}, q_\mathrm{aqu}$	Outwards CSF flow rate through the aqueduct of Sylvius (dimensional, nondimensionalised)

$Q_{\text{por}}, q_{\text{por}}$	Outwards CSF flow rate through the porous tissue, integrated over the whole area at a specific radius (dimensional, nondimensionalised)
R, R_{out}, r	Radius (dimensional, outer=scaling, nondimensionalised)
R_{in}, ρ	Ventricle radius (dimensional, nondimensionalised)
r_i	Radial nodes in finite element description of spherically symmetric, poroelastic model
S_3, S_9	Cubic and 9^{th} degree stretch functions for the spatial discretisation of the poroelastic model
$\boldsymbol{\sigma}, \boldsymbol{\sigma}_{\text{s}}, \boldsymbol{\sigma}_{\text{f}}$	Stress tensor (total, solid matrix, pore fluid)
T, T_0, t	Time (dimensional, scaling, nondimensionalised)
T_1, T_2, T_3, T_4	Times of an infusion test: start of measurements, start of infusion, end of infusion, end of measurements
$\mathcal{T}$	Set of measurement time points used for parameter estimation
$\mathcal{R}$	Resistance to CSF outflow through the arachnoid villi
$\boldsymbol{U}, U, u, u_i, \boldsymbol{Du}$	Displacement of solid matrix (vector, main component, nondimensionalised, nodal values, derivatives w.r.t to nodal values of volume dilation)
V	Total CSF volume
V_{vent}	Ventricle volume
V_{par}	Total brain parenchyma volume
$V_0, V_{\text{f}}, V_{\text{f},0}$	Infinitesimal volume element, current fluid volume within element, initial fluid volume within element
w	Weight used in conversion of algebraic boundary conditions to differential equations
x	§2: Vector of scaled parameters for a single-compartment model of an infusion test
X, X_0, x	§3: Spatial direction in planar model (dimensional, scaling, nondimensionalised)
Y	Young's modulus
ζ	CSF/fluid volume increase within porous tissue
$\zeta_{\text{a}}, \zeta_{\text{v}}$	Arterial and venous blood volume increases within porous tissue

Chapter 1

Introduction

Contents

1.1 The human cerebrospinal fluid system

1.1.1 Normal physiology

Cerebrospinal fluid (CSF) is a clear, water-like liquid that fills a system of cavities at the centre of the brain, known as ventricles, as well as the subarachnoid space surrounding the brain and the spinal cord. The two lateral ventricles, one in each hemisphere, make up almost all the ventricular volume. They are connected to the smaller third ventricle, which in turn connects via the aqueduct of Sylvius to the fourth ventricle (Figure 1.1). Estimates for the total CSF volume in humans in the literature range between 150 ml and 200 ml. Most of this volume is distributed throughout the cranial and spinal subarachnoid space and only a fraction, on

average 25 ml, is contained within the ventricles (Fishman, 1992; Bradbury, 1993; Nolte, 2009).

CSF is in communication with the interstitial fluid of the brain tissue, which surrounds the neurons and glial cells and accounts for about 15–20% of the total brain volume. With an average brain volume of 1360 ml, the interstitial fluid volume is thus on the order of 200 ml. CSF-filled paravascular spaces follow arteries and veins into the brain tissue. Water and small molecules freely diffuse between these paravascular spaces and the interstitial fluid, as well as across the membranes separating the ventricles and subarachnoid spaces from the tissue. As a consequence, the composition and pressure of CSF and interstitial fluid are very similar under normal conditions (Fishman, 1992; Bradbury, 1993; Nolte, 2009; Iliff et al., 2012).

The majority of CSF is produced from arterial blood by the choroid plexuses lining the ventricle walls. The differences in salt concentration between CSF and blood plasma, particularly if the latter is disturbed, imply that this production is an active secretion process rather than an ultrafiltration. The rate of production is on average 500 ml per day and is considered to be independent of arterial blood pressure and CSF pressure within normal ranges (Fishman, 1992; Bradbury, 1993; Nolte, 2009). Thus, the total CSF volume is renewed two to three times every day. From the lateral ventricles, most CSF flows successively through the third and fourth ventricle and finally into the cranial and spinal subarachnoid space (Figure 1.2). Since the membranes between brain tissue and interstitial space are very permeable to water, a small part of CSF must follow the pressure gradient and flow through the porous brain tissue instead. From the subarachnoid space, CSF is absorbed through the arachnoid villi into venous blood, particularly into

the superior sagittal sinus. The absorption is driven by the pressure difference between CSF and venous blood, but the arachnoid villi act as one-way valves, that is, should this pressure difference become negative, then no fluid exchange occurs. CSF movements are not steady, but oscillatory due to changes in arterial and venous blood pressure, and hence CSF pressure, with the cardiac cycle (Fishman, 1992; Bradbury, 1993; Nolte, 2009).

The main function of CSF is mechanical stabilisation of the brain by reducing forces on the tissue through buoyancy. Besides, CSF serves as a space reservoir inside the rigid skull. For example, when arterial blood is pumped into the brain with each heartbeat, the additional volume is accommodated by other fluids leaving the brain, this being partly venous blood and partly CSF flowing out through the arachnoid villi as well as into the spinal subarachnoid space. Lastly, since CSF freely communicates with the interstitial fluid of the brain tissue, it is likely involved in the regulation of the extracellular environment of neurons through the transport of hormones, nutrients and waste products (Fishman, 1992; Bradbury, 1993; Nolte, 2009; Iliff et al., 2012).

1.1.2 Hydrocephalus

Disturbances of the CSF circulation can cause brain diseases such as hydrocephalus, normal pressure hydrocephalus (NPH) or idiopathic intracranial hypertension (IIH), also known as benign intracranial hypertension or pseudotumor cerebri. Hydrocephalus is characterised by the accumulation of CSF in enlarged ventricles, often accompanied by oedemas in the surrounding brain tissue, together with an increased intracranial pressure (ICP), that is, CSF pressure. In most cases, hydro-

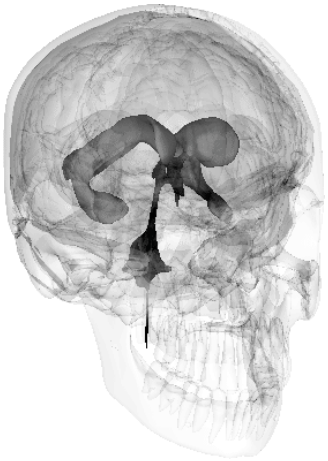

Figure 1.1: Ventricular system in the healthy human brain. The lateral ventricles (grey) connect to the third ventricle, which in turn is connected via the aqueduct of Sylvius to the fourth ventricle (all black).
Image derived from Life Science Databases (LSDB) (2009) and licensed under the Creative Commons Attribution-Share Alike 2.1 Japan license (`http://creativecommons.org/licenses/by-sa/2.1/jp/deed.en`).

The diagram originally presented here cannot be made freely available via ORA because of copyright. The diagram was derived from Figure 5–10 in J. Nolte. *The Human Brain: An Introduction to its Functional Anatomy*. Mosby, 6th edition, 2009.

Figure 1.2: Normal CSF flow path. CSF is mainly produced by the choroid plexuses in the ventricles from arterial blood. It flows from the lateral ventricles into the third ventricle, through the aqueduct of Sylvius and fourth ventricle into the subarachnoid space surrounding the brain and the spinal cord. From there it is absorbed into venous blood, particularly into the superior sagittal sinus via the arachnoid villi.
Derived from an image published in J. Nolte. *The Human Brain: An Introduction to its Functional Anatomy*. Mosby, 6th edition, 2009.

cephalus originates from a blockage of the CSF flow paths from the production site in the ventricles to the absorption site in the subarachnoid space but, theoretically, it can also be caused by an overproduction of CSF or reduced absorption into venous blood (Fishman, 1992; Nolte, 2009).

Symptoms of hydrocephalus include headache, nausea, vomiting, drowsiness, problems with vision and either of the Hakim Triad consisting of walking disturbances, dementia and urinary incontinence, which are also characteristic for NPH (NHS Choices, 2011b; Meier and Bartels, 2002). If untreated, hydrocephalus can lead to severe brain damage and eventually be fatal. Most cases of obstructive hydrocephalus can be treated by removal of the obstruction or by insertion of a shunt, which diverts the additional CSF out of the skull (Nolte, 2009), but shunt revision is often necessary and shunt failure is a common and life threatening complication that can occur any time (Hydrocephalus Association).

The other two diseases are still poorly understood. In NPH, the ventricles are enlarged without an apparent increase in CSF pressure or a measurable pressure gradient between the ventricles and the subarachnoid space. Recently, changes in the elastic parameters of the brain tissue and in water transport through the parenchyma with age have been proposed as potential causes. This corresponds well with the increased prevalence of NPH in the elderly (Levine, 1999; Streitberger et al., 2011; Tully and Ventikos, 2011; Wilkie et al., 2012b). The opposite symptom is IIH, increased CSF pressure with normal or even reduced ventricle size. Levine (2000) proposed increased volume of the subarachnoid space together with reduced CSF absorption as an explanation. Shunts lead to improvements of symptoms in about half of NPH patients (Meier and Bartels, 2002), whereas IIH can often be managed without surgery (Soler et al., 1998).

Congenital hydrocephalus is quite common, with reported incidence rates ranging between 1 in 2 000 and 1 in 500 births (MacMahon et al., 1953; CureResearch, 2003; NHS Choices, 2011a; National Institute of Neurological Disorders and Stroke, 2011). Normal pressure hydrocephalus is rarer. According to NHS Choices (2011a), under 1000 cases were recorded in England in 2009–2010. Given the population data from the 2011 census (Office for National Statistics, 2012), this yields an incidence rate of under 1 in 53 000 in the whole population. Taking into account that NPH usually affects the elderly, we can estimate an incidence rate of about 1 in 8700 by considering only people of 65 years or older. Incidence rates for other types of hydrocephalus, such as those due to head injury or tumour growth, are less readily available.

For a detailed introduction to different diseases relating to the CSF system, the reader is referred to Fishman (1992).

1.1.3 Infusion tests

Besides imaging techniques showing the size and form of the ventricles, so-called infusion tests are frequently performed in clinical practice to assess the CSF dynamics of a patient. For these tests, the CSF system is temporarily disturbed by infusion or removal of fluid in the CSF space and the pressure response measured, typically over a period of 10–30 minutes. Usually this is carried out via a lumbar puncture (Figure 1.3), but in some cases, intracranial infusion and pressure measurements are necessary, for example if the spinal subarachnoid space does not communicate with cranial CSF.

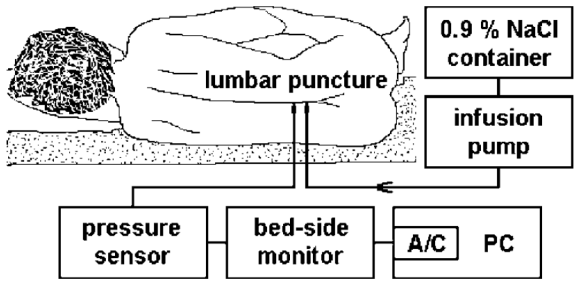

Figure 1.3: ICP monitoring system used during infusion test.
Image reproduced, with permission, from H. Juniewicz, M. Kasprowicz, M. Czosnyka, Z. Czosnyka, S. Gizewski, M. Dzik and J. D. Pickard. Analysis of intracranial pressure during and after the infusion test in patients with communicating hydrocephalus. *Physiological Measurement*, 26:1039–1048, 2005, IOP Publishing Ltd. doi: 10.1088/0967-3334/26/6/013.

The three main forms of infusion tests are a bolus injection, a constant rate infusion test and a constant pressure infusion test (Sundström et al., 2010). In the first type of test, a certain amount of fluid is rapidly injected into the CSF space to raise the pressure and the model parameters are inferred from the following return to baseline pressure (Marmarou et al., 1975). For a constant infusion test, artificial CSF is injected at a constant rate, ideally until a new steady pressure level is reached after about 10–20 minutes (Juniewicz et al., 2005). In a constant pressure infusion test, the infusion rate is automatically adapted and recorded to hold the CSF pressure successively at several constant pressure levels (Eklund et al., 2007). The oscillating pressure infusion test is a new alternative without widespread use yet (Andersson et al., 2010).

Each of these tests is usually analysed by fitting a single compartment model to the mean pressure response of that test (compare with 1.2.2 and chapter 2). In particular, the resistance to outflow can be estimated reliably and is often used in the diagnosis of CSF related diseases and the choice of treatment (Boon et al., 1997; Meier and Bartels, 2002; Czosnyka and Pickard, 2004; Eklund et al., 2007).

1.2 Mathematical models of CSF flow and hydrocephalus

1.2.1 Historical overview

More than two centuries ago, the coupling between volumes of CSF and blood in the brain, due to incompressibility and their enclosure in the rigid skull, was noticed by medical researchers (Monro, 1783). An increase of volume in one of the compartments has to be accompanied by a decrease of the volume in the other. Forty years later, Kellie (1824) refined this model by differentiating further between venous and arterial blood. The relationship that the sum of arterial blood, venous blood and CSF inside the skull is constant is now known as the Monro-Kellie doctrine.

Following animal studies and analyses of CSF dynamics in humans during the 50's, 60's and 70's the first mathematical models of the CSF pressure and volume dynamics were developed. These were typically lumped parameter models for one CSF compartment or several CSF and blood compartments with electrical circuit analogues (Agarwal et al., 1969; Guinane, 1972). Marmarou et al. (1975) proposed a single compartment model based on the exponential pressure-volume curve observed in experiments. With only minor adaptations, this model is now widely accepted and is the basis for diagnosis and clinical management of hydrocephalus (compare with 1.2.2).

Hakim et al. (1976) were the first to use the approach of biomechanical modelling on CSF dynamics and hydrocephalus. Although they only used the equations for

modelling an elastic solid, their description of the brain as an "open cell sponge made of viscoelastic material" was the starting point for poroelastic modelling of the brain. Nagashima et al. (1987) picked up this idea and developed a biphasic model for the onset of hydrocephalus using Biot's consolidation theory (Biot, 1941), also known as the theory of poroelasticity, which had originally been developed for the description of fluid-saturated soils.

An alternative biomechanical approach, namely viscoelastic modelling of the brain, started roughly at the same time. In this type of model the brain tissue is viewed as a single phase viscoelastic solid (Spertell, 1980). CSF flow through the tissue is thus neglected and the focus is fully on the transmission of pressure and the tissue displacements.

More recently, intracranial pressure oscillations due to the cardiac cycle have attracted the attention of researchers in biomechanical modelling of the brain. In viscoelastic models, the pressure oscillations usually enter the description via the boundary conditions (Sivaloganathan et al., 2005b; Wilkie et al., 2010), whereas generalised poroelastic descriptions allow for additional blood compartments within the tissue (Wirth and Sobey, 2009; Tully and Ventikos, 2011). The viscoelastic and poroelastic models will be considered further in 1.2.3 and 1.2.4, respectively.

1.2.2 Compartment models

Compartment models of CSF dynamics are lumped parameter models with similarities to electric circuits (Agarwal et al., 1969; Guinane, 1972). Storage of fluid in a compartment is governed by a compliance, which relates changes in volume within a compartment to changes in the pressure. The flow between compart-

ments is described via resistances. Balancing the flow rates with the rate of volume change in all compartments leads to a system of coupled ordinary differential equations for the pressure in each compartment.

The simplest type of compartment model is a single compartment model, representing only volume and pressure in a single CSF compartment. The model parameters are identified from a single test measurement of ICP during an infusion test. The inflow rate is the sum of the CSF production rate, assumed constant (Fishman, 1992; Nolte, 2009), and a known infusion rate. The outflow rate is assumed to be proportional to the pressure difference between CSF and venous blood in the superior sagittal sinus, with a constant resistance to outflow, following Davson et al. (1970).

This setup, described in detail in 2.2.1, yields a family of phenomenological models for CSF dynamics which differ only by the choice of compliance function (Sivaloganathan et al., 1998). Early authors believed the compliance to be constant (Guinane, 1972). Marmarou et al. (1975) proposed a compliance inversely proportional to the CSF pressure, after observations of an exponential pressure-volume curve in cats. This model is widely accepted, with the minor adaptation of measuring the pressure with respect to a reference pressure (Sklar and Elashvili, 1977; Czosnyka et al., 2004; Juniewicz et al., 2005), but the value and biological importance of this reference pressure are not yet known.

Recently, the basic assumptions of the Marmarou model have been questioned again. The constant resistance to CSF outflow could be confirmed for normal pressure ranges (Andersson et al., 2008), but the inverse pressure proportionality of the compliance is only true for higher pressures and the baseline pressure

of a patient may not be within this range (Qvarlander et al., 2010). Wirth and Sobey (2008) developed a generalisation of the Marmarou compliance model by considering changes in blood volume associated with partial collapse of bridging veins. In chapter 2, we will examine and compare their model to that used by Juniewicz et al. (2005).

Despite the simplicity of the single compartment model and its limitations, this model and its parameters, particularly the resistance to outflow, are used in many clinical settings for the diagnosis and management of CSF related diseases, see for example Boon et al. (1997); Meier and Bartels (2002); Juniewicz et al. (2005); Eklund et al. (2007); Weerakkody et al. (2011); Czosnyka et al. (2011). Furthermore, new infusion test protocols have been developed, such as the constant pressure infusion test (Eklund et al., 2007) and the oscillating pressure infusion test (Andersson et al., 2010), as well as new methods for analysis of the measurements (Andersson et al., 2007; Manchester et al., 2008). When comparing results from different clinical studies, these differences in protocol need to be taken into account, since parameter estimations can differ between them (Sundström et al., 2010).

Other compartment models that have been developed for CSF dynamics are typically a variation on a single compartment model or a multi-compartment model. These have not reached as widespread use as the single compartment models discussed above. Examples of the former include the approach by Egnor et al. (2001, 2002), who, inspired by elastic models of hydrocephalus, derived an oscillatory single compartment model of the CSF-blood interaction and proposed disturbances of the CSF pulsations to be the cause of communicating hydrocephalus, as well as the model by Cieślicki (2007), who included arterial blood pressure oscillations via an oscillating CSF production rate and allowed the superior sagittal

sinus pressure to change with breathing. Recent multi-compartment models are often derived from biomechanical considerations (Cirovic et al., 2003; Linninger et al., 2005, 2009b). For example, Cirovic et al. (2003) developed a model with five compartments, one for CSF, one for arterial blood and three for different parts of the venous bed. He concluded that the CSF compliance was mainly due to the collapsibility of the venous bed. This laid the foundation for the compliance model by Wirth and Sobey (2008) mentioned above.

1.2.3 Single phase biomechanical brain models

Single phase biomechanical models of the brain usually treat the parenchyma as a continuous solid made of a viscoelastic material. These models are used to examine the size of the ventricles and the distribution of pressure across the parenchyma for a given ventricular pressure. Many of the viscoelastic models use simplified geometries to allow for closed form solutions, such as the spherical model by Spertell (1980) or the cylindrical geometry introduced by Sivaloganathan et al. (2005a,b), but finite element simulations have also been used to simulate more realistic geometries of the brain (Miller, 1999; Dutta-Roy et al., 2008).

If the focus is on long time scales of days or weeks, such as during the development of hydrocephalus or NPH, strain rate effects can be neglected and the model simplifies to that of a purely elastic solid (Hakim et al., 1976; Dutta-Roy et al., 2008). For smaller time scales, such as when considering effects related to the cardiac cycle or head impact simulations, the viscoelastic effects need to be included. However, there is no consensus yet on which constitutive model best describes the viscoelastic response of the brain tissue and authors have generally moved from

linear models (Spertell, 1980) to more complex non-linear constitutive equations. For example, the model by Sivaloganathan et al. (2005a,b) using a "standard solid" was extended to a fractional Zener model for the tissue, which was used to investigate the differences between infant and adult hydrocephalus, due to differences in material parameters and boundary conditions, and the role of pressure pulsations on the development of hydrocephalus (Wilkie et al., 2010, 2011, 2012a,b). They concluded that the effects due to pressure pulsations are too small to produce tissue damage and thus are not likely to be a causal factor for hydrocephalus.

It is important to note that most of the models mentioned above use the representation of the strain in linear, small deformation theory. This means that geometrical non-linearities are neglected, compare with 3.2.2, and the Lagrangian (reference) and Eulerian (current) representations are not distinguished. When such models are used for situations that produce large deformations, their solutions should be considered with great caution. While they may still give some qualitative insight, their accuracy is likely considerably diminished. Examples of models that do take the geometric non-linearities into account are Miller (1999) and Dutta-Roy et al. (2008). Details of general large deformation, non-linear viscoelasticity theory can be found in Drapaca et al. (2007).

Another challenge for any biomechanical modelling of the brain is the choice of appropriate material parameters. Bilston (2002) demonstrates how the "garden hose effect" makes tissue appear stiffer when its blood vessels are perfused with pressurised blood and hence shows the difficulty of inferring in vivo material parameters from in vitro experiments. In addition, Cheng et al. (2008) reviewed the various methodologies used for experimental measurements of viscoelastic tissue

parameters, which need to be taken into consideration when comparing results from the literature. Magnetic resonance elastography (MRE) is a fairly recent and promising method of non-invasive measurements of elastic and viscoelastic tissue parameters in vivo (Klatt et al., 2007; Green et al., 2008; Sánchez et al., 2010) and has already been used to assess changes in these parameters with age or disease (Sack et al., 2009; Streitberger et al., 2011; Freimann et al., 2012). For example, the softer brain tissue observed in NPH patients may explain why simulations with default parameters in the past have failed to reproduce NPH with a transparenchymal pressure gradient below 1 mmHg that is observed clinically (Dutta-Roy et al., 2008). In particular, this technique offers the possibility to measure spatial variations of viscoelastic parameters and thus is very promising for biomechanical modelling of living tissue.

1.2.4 Multi phase biomechanical brain models

Following the description of the brain as an "open cell sponge made of viscoelastic material" (Hakim et al., 1976), Nagashima et al. (1987) were the first to apply Biot's consolidation theory (Biot, 1941) to the development of hydrocephalus. They used the finite element method to simulate the enlargement of the ventricles in a two-dimensional slice of the brain for a given transparenchymal pressure gradient. While some authors dismiss a biphasic approach (Miller, 1998; Dutta-Roy et al., 2008), there is experimental evidence that the porous effects are important for slow volumetric responses such as those appearing during hydrocephalus (Franceschini et al., 2006).

Similar to the single phase approach, many models use simplified geometries to investigate qualitative effects of different aspects of the constitutive equations. For

example, Kaczmarek et al. (1997) considered analytic solutions in cylindrical geometry for a given flow rate across the parenchyma rather than pressure boundary conditions and Sivaloganathan et al. (2005c) examined the size of effects from a deformation-dependent permeability. Recently, Wilkie et al. (2012a) concluded with a similar model that the shear stresses induced in the tissue by oscillatory flow through the parenchyma with the cardiac cycle are too small to cause tissue damage.

The other often used geometry is that of a thick spherical shell. Levine (1999, 2000) proposed an efficient absorption of CSF from the parenchyma as explanation for normal pressure hydrocephalus (NPH) and examined the influence of the Biot-Willis parameter as well as different boundary conditions at the skull on the development of the opposite symptom, idiopathic intracranial hypertension (IIH). Sobey and Wirth (2006) showed quantitatively that the permeability would need to be increased by two orders of magnitude for parenchymal absorption to induce NPH and computations by Shahim et al. (2012), who iterate Levine's model to include the non-linearity in the flow boundary condition due to the increased ventricle radius, confirm that the permeability to flow through the brain tissue is the main factor determining the size of the transparenchymal pressure gradient in NPH.

Smillie et al. (2005) on the other hand, considered the intermediate stages of obstructive hydrocephalus with only partial obstruction of the aqueduct of Sylvius with CSF volume conservation boundary conditions and Tully and Ventikos (2009) extended their ideas by coupling the spherical poroelastic model to a three dimensional simulation of CSF flow through the aqueduct of Sylvius with a local obstruction. In this case, the ventricular dilation is overestimated by assuming an

aqueduct constriction along the full length, as is necessary for the Poiseuille term in the boundary conditions used by Smillie et al. (2005).

Numerical simulations on more detailed geometries were considered for example by Taylor and Miller (2004), who reassessed the value of Young's modulus from viscoelastic models, Wirth and Sobey (2006), who compared qualitative effects of deformation-dependent permeability in axisymmetric ventricle configurations and more realistic geometries, and Li et al. (2011), who considered the influence of gravity on brain oedema for different head positions.

The warning about small strain theory used for large deformations on page 41 similarly applies for most poroelastic models of the brain. Few models explicitly state that large deformation theory should be used (Taylor and Miller, 2004; García and Smith, 2009). Furthermore, poroelastic models suffer from the same uncertainty about material parameters as viscoelastic models, maybe even more so as additional parameters are needed to describe the interaction between the solid and the fluid phase. Advances in measurement techniques may help overcome these limitations with time. Diffusion tensor imaging (DTI) can be used to infer anisotropic permeabilities (Shahim et al., 2010) and similar methods to magnetic resonance elastography (MRE) have been employed in magnetic resonance poroelastography (MRPE) to measure poroelastic parameters non-invasively (Perriñez et al., 2010).

While Hakim et al. (1976) considered the pores of the sponge-like brain to represent both the blood vessels and the extracellular fluid in the tissue, poroelastic models of the brain have traditionally been used to model either CSF or blood flow (Drysdale et al., 2010) separately. In the last few years, as interest in the oscillations of CSF pressure has increased, models have been developed that include both fluid

networks. Linninger et al. (2009a) include special boundary conditions at several locations in the choroid plexus and in the brain that mimic arterial blood volume changes obtained from blood flow measurements into the head. Their model couples a poroelastic model of the parenchyma, pulsating due to the blood volume changes, with a fluid solid interaction model of the CSF in the ventricles and the subarachnoid space. Their model agrees well with CSF flow measurements from MRI. Wirth and Sobey (2009), on the other hand, developed a multi-fluid poroelastic model of the brain with separate CSF, arterial blood and venous blood compartments, in which the fluid pressures and volumes interact through the tissue. With some simplifying assumptions, this leads to a poroelastic model of CSF flow with a spatially constant term from the arterial blood pressure, driving pressure oscillations throughout the parenchyma. Assuming a spatially constant CSF pressure and integrating the poroelastic equations over the parenchyma, we could relate this model to a single compartment model with an additional term describing the arterial blood pressure oscillations (Sobey et al., 2010, 2012). An alternative approach of multi-fluid poroelastic modelling of the brain, using multiple-network poroelastic theory (MPET), was proposed by Tully et al. (2010). In this model, the different fluid compartments interact through fluid exchange. The standard poroelastic model and the extension by Wirth and Sobey (2009) will be further described in chapter 3 and the two approaches for multi-fluid poroelastic models are compared in 3.5.5.

So far, poroelastic models of the brain in vivo ignore viscous effects inherent in the solid skeleton, but compression tests of brain tissue in vitro point towards the need for such a poroviscoelastic description (Kyriacou et al., 2002; Franceschini et al., 2006; Cheng and Bilston, 2007). Thus, we still have not reached "a suitable

non-linear constitutive equation (i. e. a relation between stress and strain) for the brain, in order to account for the large deformations typical of hydrocephalus" as well as "an appropriate set of boundary conditions" that Tenti et al. (2000) called for.

1.3 Scope

When modelling CSF dynamics, several time scales are of importance. The longest time scale of days, weeks or even months of the development of hydrocephalus is usually considered with steady-state or quasi-steady-state models using an elastic or poroelastic description of the parenchyma.

The shortest time scale is that of the cardiac cycle. Traditionally, viscoelastic models have been employed to simulate tissue displacements on this time scale. Generalisations of poroelastic models for several fluid compartments have only recently been developed to describe the interaction of CSF and blood pressure oscillations within the tissue.

A third, intermediate time scale has been largely neglected by the biomechanical modelling community despite its significance in clinical practice. This is the time scale of minutes up to about one hour for the duration of an infusion test. These tests are instead modelled and analysed by compartment models, which have no spatial variation, cannot predict ventricle displacements or stress in the parenchyma, and are often purely phenomenological, that is, they offer no mechanical or biological explanation for the observations.

In this thesis, we will simulate CSF dynamics during the constant rate infusion test

with the multi-fluid poroelastic model proposed by Wirth and Sobey (2009). The results are compared to clinical data sets, comprising of the infusion rate, times of the infusion, arterial blood pressure and CSF pressure obtained via a lumbar puncture or intracranial pressure measurements.

At first, in chapter 2, we will analyse these clinical data sets with single compartment models, as is common in clinical practice. We will consider the problem of estimating parameter values from the mean pressure response neglecting oscillations at heart rate and in particular focus on comparing the phenomenological compliance model used by Juniewicz et al. (2005) with the model derived by Wirth and Sobey (2008) from collapsibility of veins.

In chapter 3, the details of the single fluid and multi-fluid poroelastic models will be set out. The models contains non-linearities due to strain dependence in the permeability as well as pressure dependence in the CSF storage coefficient. Integrating the multi-fluid poroelastic model over the parenchyma volume allows us to relate the CSF storage coefficient in the poroelastic model to the compliance function in the single compartment model. This provides a way of estimating some of the parameters of the poroelastic model from parameter fits on the single compartment model as well as giving a possibility of better modelling of the compliance once the CSF storage in the poroelastic model is understood better. In addition, the single compartment model is extended by an oscillatory term describing the CSF pressure oscillations due to arterial blood pressure oscillations.

Chapter 4 contains the description of the finite element simulation of the multi-fluid poroelastic model. Due to the spherical symmetry, only one spatial dimension needs to be considered. Particular attention is given to solving the fluid volume

conservation boundary conditions accurately. Boundary conditions without time derivatives lead to algebraic equations in the spatially discretised system. These are framed in a differential framework in such a way that errors in the algebraic equation decay in time. Numerical tests complete the chapter.

The finite element simulation is applied to clinical data in chapter 5. We consider details of the solution in time and space and specifically check where the additional fluid is stored during the infusion test. Finally, we will use the parameters estimated in chapter 2, to attempt to fit the simulation results to some of the clinical data sets. Our conclusions are set out in chapter 6 and potential future directions for research are highlighted.

Chapter 2

Parameter estimations for single compartment models

The material in this chapter has been published in the multi-authored paper

> A. Eisenträger, I. Sobey and M. Czosnyka. Parameter estimations for the cerebrospinal fluid infusion test. *Mathematical Medicine and Biology Advance Access published February, 16, 2012*. doi: 10.1093/imammb/dqs001

for which A.E. was the primary author and visual and textual material from that paper has been used extensively.

Contents

2.1 Motivation

Before simulating the infusion test with poroelastic models, we consider a more common approach to mathematical modelling of this problem, namely with single compartment models. This will lead to a better understanding of the use of the infusion test and its parameters by clinicians and allows us later to relate and compare the different types of models (see 3.5.4).

In single compartment models of CSF dynamics, the relation between increases in total craniospinal CSF volume V and increases in the intracranial pressure (ICP) P are governed by a pressure dependent compliance. Most models for the compliance are purely phenomenological, that is, they describe the functional dependence of the compliance on the CSF pressure, but offer no mechanical or biological explanation for this dependence (Sivaloganathan et al., 1998). The most commonly used version is based on the exponential pressure-volume curve first observed by Marmarou et al. (1975). However, there is some evidence from clinical measurements that the elasticity, a constant in this type of compliance model, may in fact vary with pressure (Juniewicz et al., 2005).

More recently, Wirth and Sobey (2008) developed a model of the compliance from biomechanical considerations, following ideas in Cirovic et al. (2003). The observation that the CSF compliance is largely determined by the compliance of the venous bed, and can thus be modelled by the partial collapse of elastic tubes, leads to an inverse pressure power law over the clinically significant pressure range. This allows the elasticity to vary with ICP and the models used by Juniewicz et al. (2005) and Marmarou et al. (1975), for which the elasticity is constant, are special cases of this theory.

In this chapter, we examine how the model by Wirth and Sobey (2008) compares to that used by Juniewicz et al. (2005) with respect to simulating the constant rate infusion test and obtaining parameter estimations from measurements. For this purpose, we analyse the influence of each of the parameters on the models and consider the problem of estimating parameters from pressure data. Below, we will use the phraseology 'standard model' when using the compliance model in Juniewicz et al. (2005) and 'generalised model' when the compliance is that from Wirth and Sobey (2008).

A least squares minimisation is used to determine parameter values from synthetic pressure data and clinical data sets of constant rate infusion tests for both the standard model and the generalised model. The standard model, which uses a closed-form solution to a governing differential equation, results in prediction of resistance, baseline ICP and elasticity (and through these the normal CSF production rate). The generalised model, which requires numerical solution of a governing differential equation within a least squares process, needs estimation of these same parameters and an additional parameter, a power law index; details are given below.

The layout of this chapter is that in section 2.2 we summarise details of the governing differential equation for ICP variation with time and models for cerebral compliance. In section 2.3 we consider solutions of the governing differential equations and study how prediction of mean ICP is affected by changes in the various governing parameters. In section 2.4 we outline the methodology for estimating optimal values of parameters from data and in section 2.5 we consider estimating parameters from synthetic data (that is, known parameter values are used to generate data which is then subject to parameter estimation using least

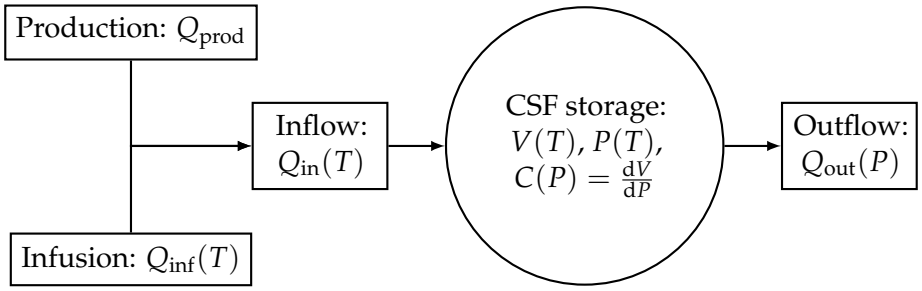

Figure 2.1: Schematic of single compartment model for CSF dynamics.

squares optimisation) before applying the optimisation method to clinical data in section 2.6. Our observations are discussed in section 2.7.

2.2 Theoretical models

2.2.1 Model derivation

We use a single compartment model, based on the description in Juniewicz et al. (2005). This is a lumped parameter model that treats all the CSF in and around the brain and spinal cord as being in one compartment without spatial variations and links its volume, $V(T)$, to the CSF pressure, $P(T)$, via a pressure dependent compliance, $C(P) = \frac{dV}{dP}$. Oscillations on the time scale of the heart rate are neglected and all quantities represent an average over a cardiac cycle. A schematic of the model can be found in Figure 2.1.

Since CSF is water like and incompressible, conservation of CSF mass is equivalent to the conservation of CSF volume, V, so that

$$\frac{dV}{dT} = Q_{\text{in}} - Q_{\text{out}} \,, \tag{2.1}$$

where the inflow rate is given as

$$Q_{\text{in}} = \begin{cases} Q_{\text{prod}} \,, & \text{before and after the infusion,} \\ Q_{\text{prod}} + Q_{\text{inf}} \,, & \text{during the infusion,} \end{cases} \tag{2.2}$$

and the outflow rate as

$$Q_{\text{out}} = \frac{P - P_{\text{ss}}}{\mathcal{R}} \,, \tag{2.3}$$

with a constant CSF production rate Q_{prod}, constant infusion rate Q_{inf}, intracranial CSF pressure (ICP) P, venous blood pressure P_{ss} in the superior sagittal sinus and constant resistance $\mathcal{R}$ to CSF outflow through the arachnoid villi (Fishman, 1992; Nolte, 2009). Other absorption sites have been proposed, such as absorption throughout the parenchyma and via the nasal lymphatic system (Levine, 1999; Johnston et al., 2004). However it is unclear how much CSF escapes through these routes. The linear relationship between intracranial pressure and the overall outflow of CSF has been confirmed over normal pressure ranges for the duration of an infusion test (Davson et al., 1970; Andersson et al., 2008). The values for P_{ss} and $\mathcal{R}$ can thus be considered as averages of their respective values at the different absorption sites.

CSF volume change is linked to ICP via a pressure dependent compliance

$$C(P) = \frac{\mathrm{d}V}{\mathrm{d}P} \,, \tag{2.4}$$

so that the fluid balance (2.1) yields

$$C(P)\frac{\mathrm{d}P}{\mathrm{d}T} = Q_{\text{in}} - \frac{P - P_{\text{ss}}}{\mathcal{R}} \,. \tag{2.5}$$

As noted by Sivaloganathan et al. (1998), this represents a family of models, where each model is defined by the choice of the compliance $C(P)$.

In the time before the infusion begins, oscillations at heart rate being neglected, a steady state with a baseline pressure P_b is assumed, giving

$$0 = Q_\mathrm{prod} - \frac{P_\mathrm{b} - P_\mathrm{ss}}{\mathcal{R}} \,, \tag{2.6}$$

which allows the unknown production rate Q_prod and pressure P_ss in the sagittal sinus to be eliminated by introducing P_b into the equation to obtain

$$C(P)\frac{\mathrm{d}P}{\mathrm{d}T} = Q - \frac{P - P_\mathrm{b}}{\mathcal{R}} \,, \tag{2.7}$$

with initial condition $P(T_1) = P_\mathrm{b}$ and

$$Q = \begin{cases} 0 \,, & \text{for } T_1 \leq T \leq T_2 \,, \\ Q_\mathrm{inf} \,, & \text{for } T_2 < T \leq T_3 \,, \\ 0 \,, & \text{for } T_3 < T \leq T_4 \,, \end{cases} \tag{2.8}$$

where T_1 is the beginning of the test (on occasion, data is not usable until some time $T_1 > 0$), T_2 the start of the infusion, T_3 the end of the infusion and T_4 the end of the test.

2.2.2 Standard compliance model

The standard model for the compliance used in Juniewicz et al. (2005) is

$$C(P) = \frac{1}{E(P - P_\mathrm{r})} \,, \tag{2.9}$$

with an elasticity coefficient E and a reference pressure P_r. The role of the latter has not been fully understood and as noted above, different values have been suggested for P_r, including zero (Marmarou et al., 1978) and the venous outflow pressure (Czosnyka et al., 2004). Wirth and Sobey (2008) suggested an alternate

value based on mechanical properties of the bridging veins and blood viscosity. Inserting (2.9) into the ordinary differential equation (2.7), it can be reformulated as

$$\frac{\mathrm{d}P}{\mathrm{d}T} = \begin{cases} -\frac{E}{\mathcal{R}}\left(P(T)-P_\mathrm{r}\right)\left(P(T)-P_\mathrm{b}\right)\,, & \text{for } T_1 \le T \le T_2\,, \\ -\frac{E}{\mathcal{R}}\left(P(T)-P_\mathrm{r}\right)\left(P(T)-(P_\mathrm{b}+\mathcal{R}Q_\mathrm{inf})\right)\,, & \text{for } T_2 < T \le T_3\,, \\ -\frac{E}{\mathcal{R}}\left(P(T)-P_\mathrm{r}\right)\left(P(T)-P_\mathrm{b}\right)\,, & \text{for } T_3 < T \le T_4\,, \end{cases} \tag{2.10}$$

which, with the initial condition $P(T_1) = P_\mathrm{b}$, yields the solution

$$P(T) = \begin{cases} P_\mathrm{b}\,, & \text{for } T_1 \le T \le T_2\,, \\ P_\mathrm{r} + \frac{(P_\mathrm{b}-P_\mathrm{r})(\mathcal{R}Q_\mathrm{inf}+P_\mathrm{b}-P_\mathrm{r})}{(P_\mathrm{b}-P_\mathrm{r})+\mathcal{R}Q_\mathrm{inf}\exp\left(-\frac{E}{\mathcal{R}}(\mathcal{R}Q_\mathrm{inf}+P_\mathrm{b}-P_\mathrm{r})(T-T_2)\right)}\,, & \text{for } T_2 < T \le T_3\,, \\ P_\mathrm{r} + \frac{(P_\mathrm{b}-P_\mathrm{r})}{1+D\exp\left(-\frac{E}{\mathcal{R}}(P_\mathrm{b}-P_\mathrm{r})(T-T_3)\right)}\,, & \text{for } T_3 < T \le T_4\,. \end{cases} \tag{2.11}$$

The parameter

$$D = \frac{P_\mathrm{b}-P_\mathrm{r}}{P(T_3)-P_\mathrm{r}} - 1 \tag{2.12}$$

establishes continuity of ICP at time T_3, the end of the infusion.

Although not always commented on, once the resistance and ICP are known, it is straightforward to calculate the increase in CSF fluid volume during the test, and particularly the maximum increase in CSF volume, expected at the end of the infusion, by

$$\begin{aligned} \Delta V(T) &= \int_{T_1}^{T} \left(Q_\mathrm{in}(s) - Q_\mathrm{out}(s)\right)\mathrm{d}s = \int_{T_1}^{T}\left(Q_\mathrm{prod} + Q(s) - \frac{P(s)-P_\mathrm{ss}}{\mathcal{R}}\right)\mathrm{d}s \\ &= \int_{T_1}^{T}\left(Q(s) - \frac{P(s)-P_\mathrm{b}}{\mathcal{R}}\right)\mathrm{d}s\,. \end{aligned} \tag{2.13}$$

2.2.3 Generalised compliance model

Wirth and Sobey (2008) propose a generalisation of the compliance (2.9) with a pressure dependent elasticity

$$E(P) = \tilde{e}\,(P - P_\mathrm{r})^{n-1}\ , \tag{2.14}$$

so that

$$C(P) = \frac{1}{E(P)(P - P_\mathrm{r})} = \frac{1}{\tilde{e}(P - P_\mathrm{r})^n}\ , \tag{2.15}$$

with an unknown power n. Note that the dimension of $\tilde{e}$ depends on the power n

$$[\tilde{e}] = \frac{\mathrm{mmHg}^{(1-n)}}{\mathrm{m}^3}\ . \tag{2.16}$$

This model yields a non-linear ordinary differential equation for ICP, P,

$$\frac{\mathrm{d}P}{\mathrm{d}T} = \begin{cases} -\frac{\tilde{e}}{\mathcal{R}}\,(P(T) - P_\mathrm{r})^n\,(P(T) - P_\mathrm{b})\ , & \text{for } T_1 \le T \le T_2\ , \\ -\frac{\tilde{e}}{\mathcal{R}}\,(P(T) - P_\mathrm{r})^n\,(P(T) - (P_\mathrm{b} + \mathcal{R}Q_\mathrm{inf}))\ , & \text{for } T_2 < T \le T_3\ , \\ -\frac{\tilde{e}}{\mathcal{R}}\,(P(T) - P_\mathrm{r})^n\,(P(T) - P_\mathrm{b})\ , & \text{for } T_3 < T \le T_4\ . \end{cases} \tag{2.17}$$

Closed-form solutions can be found for specific values of n, such as for $n = 1$ (standard model), given by (2.11), and for the linear case $n = 0$, which encodes a constant compliance, where

$$P(T) = \begin{cases} P_\mathrm{b}\ , & \text{for } T_1 \le T \le T_2\ , \\ P_\mathrm{b} + \mathcal{R}Q_\mathrm{inf} - \mathcal{R}Q_\mathrm{inf}\exp\left(-\frac{\tilde{e}}{\mathcal{R}}\,(T - T_2)\right)\ , & \text{for } T_2 < T \le T_3\ , \\ P_\mathrm{b} + (P(T_3) - P_\mathrm{b})\exp\left(-\frac{\tilde{e}}{\mathcal{R}}\,(T - T_3)\right)\ , & \text{for } T_3 < T \le T_4\ . \end{cases} \tag{2.18}$$

However, for $n \neq 1$, other than for some fractional values, only implicit integral solutions to (2.17) can be found. Hence, for values of $n \neq 1$, the ODE is solved numerically.

Wirth and Sobey (2008) also predicted that the reference pressure for the compliance should be

$$P_{\mathrm{r}} = P_{\mathrm{ss}} + \Delta P - K \,, \tag{2.19}$$

where ΔP is the pressure drop across the bridging veins and K is a measure of the bending stiffness of the bridging veins. Following their discussion, the latter two terms are of similar size, so that the reference pressure P_{r} may be a rough approximation of the pressure in the sagittal sinus P_{ss}. Hence, the production rate can be approximated, using this substitution in (2.6), as

$$Q_{\mathrm{prod}} = \frac{P_{\mathrm{b}} - P_{\mathrm{r}}}{\mathcal{R}} \,. \tag{2.20}$$

2.3 Parameter variations

To obtain some intuition of the influences on ICP evolution of the different parameters, we consider variations of the parameters around an average set of parameter values given in Table 2.1. The times are typical values from the data sets, the other values are chosen similar to the averages given in Juniewicz et al. (2005, Table 2). First we consider changes in $E, \mathcal{R}, P_{\mathrm{r}}$ and P_{b} in the standard model (2.11) and then consider changes in n and $\tilde{e}$ in the generalised model (2.17). For the standard model, that is $n = 1$, the analytic solution (2.11) is used, otherwise the model ICP is calculated by numerically integrating (2.17) with MATLAB's `ode45`, a Runge–Kutta formula described in Dormand and Prince (1980). The results of these calculations are plotted in Figures 2.2–2.8, showing the intracranial pressure, inflow and outflow rate and the increase in fluid volume, and discussed in detail below.

Table 2.1: Standard parameter values (for standard model $n = 1$).

Start time of data	T_1	=	0	min
Start time of infusion	T_2	=	5	min
End time of infusion	T_3	=	20	min
End time of data	T_4	=	25	min
Infusion rate	Q_{inf}	=	1.5	$^{\text{ml}}/_{\text{min}}$
Elasticity	E	=	0.2	$^{1}/_{\text{ml}}$
Resistance	$\mathcal{R}$	=	15	$^{\text{mmHg min}}/_{\text{ml}}$
Reference pressure	P_{r}	=	5	mmHg
Baseline pressure	P_{b}	=	10	mmHg

In each of the plots, a thick solid line represents the values obtained from the standard parameters and the values corresponding to the variations are plotted in various other line styles. Panel (a) shows the variations in CSF pressure (ICP) P. Both the inflow rates (grey) and the corresponding outflow rates (black) are given in panel (b) and the increase in CSF volume, integrated numerically from (2.13), is plotted in panel (c).

Changes of the elasticity E have a linear effect on the slope of the pressure curve, thus scaling the curve horizontally. The plateau pressure is reached earlier for larger values of E and later, or not at all during the given infusion time, for smaller values and similarly the baseline pressure is reached earlier or later after the infusion was stopped (Figure 2.2a). The form of the outflow rate closely follows the form of the pressure curve (Figure 2.2b), since the plateau pressure coincides with the outflow rate balancing the inflow rate. The increase in fluid volume is higher for smaller values of E and smaller for larger values (Figure 2.2c).

The actual form of the pressure curve between the baseline pressure and the plateau pressure can be changed by varying the reference pressure P_{r} (Figure 2.3a). Lower values of this parameter correspond to a steepening of the pressure curve

early after the change in inflow rate and a flattening thereafter. The outflow rate again follows the changes of the pressure curve, with a superimposed vertical shift of both, inflow and outflow rate, due to the change in CSF production rate (Figure 2.3b). These changes result in a higher increase in CSF volume for higher reference pressure and vice versa (Figure 2.3c). Adding the same value to both, the reference pressure P_r and the baseline pressure P_b, only shifts the pressure curve up or down without any effect on its shape or on the flow and volume curves. A change in the baseline pressure can be regarded as such a shift of both pressures together with a change of the reference pressure.

The resistance $\mathcal{R}$ is the only parameter that has an effect on the difference between the plateau and the baseline pressures (Figure 2.4a), which is obvious from the volume balance in the new steady state $P_{plat} - P_b = \mathcal{R}Q_{inf}$. For pressure values close to the baseline pressure P_b, the effect of the resistance on the pressure derivative in (2.7) diminishes, thus the slope of the pressure curve is similar at the beginning of the infusion. This results in the plateau pressure being reached earlier for smaller resistances, corresponding to smaller plateau pressures. In these cases, the outflow and inflow rates balance earlier (Figure 2.4b) and the increase in CSF volume is smaller (Figure 2.4c). Since variations in the reference pressure or the resistance also change the CSF production rate, we next consider variations of both parameters together, with the production rate kept constant. In this case, the pressure curve between the baseline pressure and the plateau pressure is simply scaled to fit this range (Figure 2.5a), while there are no changes in the flow rates or fluid volume increase at all (Figure 2.5b, c). Hence the effects of variations in resistance can be viewed as a combination of this scaling together with a change in the reference pressure.

Considering the generalised model (2.17), variations of the power n with constant $\tilde{e}$ (Figure 2.6) have similar effects as changes in the elasticity in the standard model (Figure 2.2). This can be expected because the main influence of n in this setting is on the size of the elasticity $E(P) = \tilde{e}\,(P - P_{\mathrm{b}})^{n-1}$. Only when keeping the value of $E(P)$ constant at a specific pressure, for example for the baseline pressure, can we examine the influence of the power itself (Figure 2.7). It is no surprise that the pressure curves look similar at the beginning of the infusion, since there, the pressure is still close to the baseline pressure and hence the elasticity varies only slightly. Overall, increasing the power n leads to a steepening of the pressure curve and the outflow rate and thus to a smaller increase in CSF volume.

The example in Figure 2.8 makes the non-linear nature of the relationship between the parameters and the pressure curve even clearer. Two sets of different parameter values yield extremely similar values for the pressure curves, only a small shift in the flow curves and almost indistinguishable volume curves. These values were only chosen by hand. Using one set as a starting guess for a least squares fit to the ICP curve of the other set, would probably lead to even closer results. This non-linearity makes the inverse problem of determining parameter values which include the power law index from observed ICP during an infusion test difficult.

2.4 Methodology for parameter estimation

2.4.1 Clinical data

The entirely anonymous clinical data used in this study originates from eleven constant rate infusion tests carried out at Addenbrooke's Hospital, Cambridge,

UK. Each data set consists of the times when the infusion started and stopped, the constant infusion rate, CSF pressure, taken either from the ventricles or from the spinal column, and arterial blood pressure, usually measured via a finger cuff. The infusion lasted around 15 minutes and both pressures are measured at a rate of 30 data points per second for the whole duration of the test, that is approximately ten minutes before until five minutes after the infusion, thus yielding about 54000 data points.

For most data sets, the beginning of the test T_1 coincides with the beginning of the measurements $t = 0$, but in some cases, there are jumps or drifts in the pressure before the infusion. This part of the data is not considered as these effects are most likely due to movements of the patient or a readjustment of the pressure sensor. Similar situations can occur after the infusion, for example a patient might sit up to relieve side effects such as headache and nausea. This kind of information is not available with the data sets, so the reliability of ICP measurement after the infusion is not known and that data is not used here. Hence, only the period between T_1 and T_3 is taken into account for parameter estimation and $\mathcal{T}$ is defined as the set containing measurement times in this acceptable range.

2.4.2 Preprocessing

Some straightforward preprocessing of the data will yield starting points for a least squares fit. To smooth out oscillations at heart rate, $P_{\mathrm{w}}(T)$ is defined as the mean of the measured CSF pressure P_{measured} over a one minute window starting at time T and ${P_{\mathrm{w}}}^{+}$ and ${P_{\mathrm{w}}}^{-}$ as the maximum and minimum value of $P_{\mathrm{w}}(T)$, respectively. With this, coarse guesses for the parameters, denoted with

superscript g for "guess", can be defined as

$$P_{\mathrm{b}}{}^{\mathrm{g}} = P_{\mathrm{w}}{}^{-} \,, \qquad P_{\mathrm{r}}{}^{\mathrm{g}} = \max\left\{P_{\mathrm{b}}{}^{\mathrm{g}} - 4\,\mathrm{mmHg}\,, 1\,\mathrm{mmHg}\right\}, \tag{2.21}$$

$$\mathcal{R}^{\mathrm{g}} = \frac{P_{\mathrm{w}}{}^{+} - P_{\mathrm{b}}{}^{\mathrm{g}}}{Q_{\mathrm{inf}}}\,, \qquad E^{\mathrm{g}} = 0.25\frac{1}{\mathrm{ml}}\,. \tag{2.22}$$

The guess for the baseline pressure is taken as the minimal mean of the pressure, the reference pressure is assumed to lie 4 mmHg below that, as the average values from Juniewicz et al. (2005), $P_{\mathrm{b}} = 10.7$ and $P_{\mathrm{r}} = 6.6$, indicate. In order to avoid problems later with the scaling in (2.24) below, the value for $P_{\mathrm{r}}{}^{\mathrm{g}}$ should be bounded away from 0. Hence, it is always set to at least 1 mmHg. The assumption that the maximum of the average pressure is the new plateau pressure, that is a new steady state pressure for the increased inflow rate, yields the starting guess for $\mathcal{R}$. The value for E is again taken as a value typical for patients with hydrocephalus, similar to the mean value of $0.24\,\mathrm{ml}^{-1}$ for 20 infusion tests from Juniewicz et al. (2005).

For the generalised model, we define furthermore

$$\tilde{e}^{\mathrm{g}} = E^{\mathrm{g}}\left(P_{\mathrm{b}}{}^{\mathrm{g}} - P_{\mathrm{r}}{}^{\mathrm{g}}\right)^{(1-n^{\mathrm{g}})} \tag{2.23}$$

depending on the guess n^{g} for the power n. With all these guesses, we can define the normalised parameters

$$x_1 = \frac{P_{\mathrm{b}}}{P_{\mathrm{b}}{}^{\mathrm{g}}}\,, \quad x_2 = \frac{\tilde{e}}{\mathcal{R}}\frac{\mathcal{R}^{\mathrm{g}}}{\tilde{e}^{\mathrm{g}}}, \quad x_3 = \frac{P_{\mathrm{r}}}{P_{\mathrm{r}}{}^{\mathrm{g}}}\,, \quad x_4 = \frac{\mathcal{R}Q_{\mathrm{inf}} + P_{\mathrm{b}}}{\mathcal{R}^{\mathrm{g}}Q_{\mathrm{inf}} + P_{\mathrm{b}}{}^{\mathrm{g}}}\,, \quad x_5 = n\,. \tag{2.24}$$

2.4.3 Parameter estimation

We consider three different methods for the estimation of the parameter values: for the standard model, that is $n = 1$, for the generalised model with a different

fixed value of $n = 0.7$ as suggested by Wirth and Sobey (2008) and lastly with n being one of the parameters to be estimated. Table 2.2 lists the differences between these three methods. In each case, the least squares objective function is defined as

$$F : \mathbb{R}^d \mapsto \mathbb{R} : \quad x \mapsto \sum_{t \in \mathcal{T}} \left(P_{\text{model}}[x](T) - P_{\text{measured}}(T) \right)^2 , \tag{2.25}$$

where d is the number of parameters to be estimated, that is either 4 or 5.

The values of F can span several orders of magnitude for moderate changes in the parameters. Hence, we use the logarithm of F scaled by the number of data points. Furthermore, the numerical solution of the model pressure becomes complex for certain areas in the parameter space, thus, leading to a complex value for the objective function F. Obviously, complex pressures are not physical, so we want the optimisation algorithm to avoid these areas. Contour plots (not shown) over planes in the parameter space show that often the absolute value of F in these areas decreases as x moves further away from the physically sensible domain. Hence, we penalise the complex part of F, so that the final objective function for each of the methods is chosen as

$$L : \mathbb{R}^d \mapsto \mathbb{R} : \quad x \mapsto \log \left(\frac{|\Re(F(x)) + 1000 i \Im(F(x))|}{|\mathcal{T}|} \right) . \tag{2.26}$$

Other problematic areas in the parameter space contain regions where the ODE solver failed to compute a solution for the whole time interval and regions with several close steep peaks, possibly with local minima in between. These regions, however, are bound well away from the global minimum. The area around the global minimum looks sufficiently smooth on contour plots. Repeating the minimisation with different random starting points, we expect to find the global minimum despite the complicated regions. The starting value $x^0 \in \mathbb{R}^d$ is chosen as a pseudo-random vector from $[0, 2]^d$ with uniform distribution (MATLAB: `rand`

Table 2.2: Comparison of the parameter estimation methods (A) standard model, (B) generalised model with fixed n and (C) generalised model with variable n: dimension d of parameter space in which the optimum is searched, power in the compliance model n with the initial guess n^{g} and the method of computing the model pressure $P_{\mathrm{model}}[x]$.

Method	d	n	n^{g}	Computation of model pressure $P_{\mathrm{model}}[x]$
A	4	1.0	1.0	Analytic solution (2.11) of standard model
B	4	0.7	0.7	Numerical solution of generalised model (2.17) with `ode45` in MATLAB
C	5	variable	1.0	Numerical solution of generalised model (2.17) with `ode45` in MATLAB

seeded with `rng('shuffle')`). The minimisation algorithm used is `fminsearch` in MATLAB, a Nelder–Mead simplex algorithm (Lagarias et al., 1998), with tolerances 10^{-6} both for x and the objective function value.

2.4.4 Postprocessing

Having estimated the parameters for each of the fitting methods, an approximation of the production rate Q_{prod} can be computed from (2.20) and the maximal increase in fluid volume ΔV during the test can be estimated by numerically integrating the difference between the production and absorption of CSF (2.13).

2.5 Tests with artificial data

To test the models and implementation, four artificial data sets are created using known parameters, parameter estimations carried out on these data sets and the results compared to the original known parameters. Two data sets are prepared for each model using $n = 1$ and $n = 0.7$, one set consisting of the pressure

curve described by the models in section 2.2 and another set where, for each data point, the pressure at each time T was chosen randomly from the interval $[0.9P(T), 1.1 \cdot P(T)]$ around the model value with uniform distribution, to simulate noise in the data from oscillations at heart rate. For the differences between the data sets see Table 2.3 and Figure 2.9 for the pressure plots. Their common parameter values are

$$\tilde{e} = 0.5 \frac{\text{mmHg}^{(1-n)}}{\text{ml}} , \qquad \mathcal{R} = 10^{\text{mmHg min/ml}} , \tag{2.27}$$

$$P_\text{b} = 10\text{mmHg} , \qquad P_\text{r} = 5\text{mmHg} . \tag{2.28}$$

For each of the four artificial data sets, the parameters are estimated with the three methods from subsection 2.4.3 and compared to the values in (2.27) and Table 2.3 that were used to create the data set. Each estimation was repeated in batches with new random initial guesses, until at least 5 minimisations terminated successfully. The parameter values of the best fit in each case, from 5 to 9 estimations, are stated in Table 2.4, along with the resulting objective function value L.

In all cases, both the baseline pressure P_b and the resistance to outflow $\mathcal{R}$ are estimated well, with relative errors below 0.1%. This is expected, since these values are directly related to the baseline pressure, that is the average pressure before the infusion, and the difference between the plateau and baseline pressures, respectively. Furthermore, good results are achieved when fixing the value of n to the appropriate value used to create that data set, that is using method A, $n = 1$, for data sets AD1 and AD2 and method B, $n = 0.7$ for data sets AD3 and AD4. Choosing the wrong fixed value for n (method B for AD1 and AD2, method A for AD3 and AD4) leads to large errors in $\tilde{e}$ and P_r as well. These three parameters together determine the pressure dependency of the compliance $C(P)$ and hence

Table 2.3: Differences between artificial data sets.

Set	n	rand
AD1 standard model	1	no
AD2 standard model with variance	1	yes
AD3 generalised model	0.7	no
AD4 generalised model with variance	0.7	yes

are closely linked. This observation is strengthened when comparing method C with the other two methods. Figure 2.10 shows for set AD4 that over the pressure range reached during the infusion test, the resulting compliance function is almost the same for all three estimation methods. Hence, we cannot reliably distinguish between the compliance functions and estimate all five parameters including n. Especially with noisy data (AD2, AD4), the objective function appears to be very shallow around the minimum (plots not shown). For clinical practice this would imply that the value of the compliance $C(P)$ over an appropriate pressure range is probably more informative than the values of $\tilde{e}$ or E, n and P_r on their own. In the following section on application to clinical data, we discontinue using method C and consider only the two power index values, $n = 1$ (method A) and $n = 0.7$ (method B).

2.6 Application to clinical data

We initially considered anonymous clinical data from eleven infusion tests carried out at Addenbrooke's Hospital, Cambridge, UK. Four of these tests, in our notation sets 01, 05, 09, 10, were aborted prematurely because the intracranial pressure rose to dangerously high levels. In these cases the plateau pressure was not reached and we find that the data sets do not contain sufficient information to reliably

Table 2.4: Relative error norms for artificial data tests in the parameter values and the objective function value L. Relative errors less than 0.1% are given in scientific notation.

Set	M	$\frac{n-n^{\text{fit}}}{n}$	$\frac{\tilde{e}-\tilde{e}^{\text{fit}}}{\tilde{e}}$	$\frac{\mathcal{R}-\mathcal{R}^{\text{fit}}}{\mathcal{R}}$	$\frac{P_{\text{r}}-P_{\text{r}}^{\text{fit}}}{P_{\text{r}}}$	$\frac{P_{\text{b}}-P_{\text{b}}^{\text{fit}}}{P_{\text{b}}}$	L
AD1	A	–	$6{\cdot}10^{-4}$	$5{\cdot}10^{-6}$	0.2%	$1{\cdot}10^{-5}$	-16.499356
AD1	B	30%	158%	$2{\cdot}10^{-4}$	56%	$6{\cdot}10^{-4}$	-7.816947
AD1	C	2%	7%	$3{\cdot}10^{-6}$	4%	$2{\cdot}10^{-5}$	-13.022012
AD2	A	–	2%	0.1%	2%	$4{\cdot}10^{-4}$	0.374048
AD2	B	30%	155%	0.1%	54%	$2{\cdot}10^{-4}$	0.374408
AD2	C	5%	17%	0.1%	13%	$5{\cdot}10^{-4}$	0.374039
AD3	A	43%	65%	0.1%	85%	$5{\cdot}10^{-4}$	-8.893937
AD3	B	–	$4{\cdot}10^{-4}$	$2{\cdot}10^{-6}$	0.1%	$1{\cdot}10^{-5}$	-17.110569
AD3	C	0.3%	0.8%	$1{\cdot}10^{-5}$	0.8%	$7{\cdot}10^{-6}$	-17.661566
AD4	A	43%	65%	0.1%	83%	$3{\cdot}10^{-4}$	0.242239
AD4	B	–	0.3%	$2{\cdot}10^{-5}$	0.7%	$0.7{\cdot}10^{-4}$	0.242259
AD4	C	21%	40%	$8{\cdot}10^{-4}$	41%	$5{\cdot}10^{-4}$	0.242220

estimate the parameters and have been omitted below. In practice, these infusion tests can be repeated with a lower infusion rate or supplemented with overnight ICP monitoring. The input data for the remaining sets 00, 02, 03, 04, 06, 07, 08 is given in Table 2.5. The infusion rate for all of these tests was $1.5\,{}^{\text{ml}}/_{\text{min}}$.

The results of the least squares fits for these infusion tests with methods A and B are given in Table 2.6 and the corresponding plots can be found in Figures 2.11–2.12. For data set 00, the measured versus modelled pressure for both methods (Figure 2.11a), inflow and outflow rates (Figure 2.11b) as well as the increase in fluid volume (Figure 2.11c) during the test are shown. For the other data sets, we only show the pressure plots (Figure 2.12). In each of these plots, the similarity between the solutions from the two parameter estimation methods is apparent. Only the inflow and outflow rates are shifted vertically due to a different estimate of the production rate (Figure 2.11b). Any other differences are hardly visible. Accordingly, the objective function values L in Table 2.6 are very similar between

the two methods for any given data set, often agreeing to three digits despite the different values for n.

As with the artificial data sets, both the baseline pressure P_b and the resistance to CSF outflow $\mathcal{R}$ can be estimated consistently with either method. Similarly, the compliance is estimated consistently by both methods. In Table 2.6, we have given the average value over the pressure range achieved during the infusion test

$$C_\mathrm{avg} = \frac{1}{P_\mathrm{plat} - P_\mathrm{b}} \int_{P_\mathrm{b}}^{P_\mathrm{plat}} C(P)\mathrm{d}P = \frac{1}{P_\mathrm{plat} - P_\mathrm{b}} \int_{P_\mathrm{b}}^{P_\mathrm{plat}} \frac{1}{\tilde{e} \cdot (p - P_\mathrm{r})^n}\mathrm{d}P \,. \tag{2.29}$$

This value depends on the plateau pressure

$$P_\mathrm{plat} = P_\mathrm{b} + \mathcal{R}Q_\mathrm{inf} \tag{2.30}$$

and thus on the infusion rate used in this test. So, this averaged value would not be useful for assessment of a patient's health on its own, but rather the full compliance curve, as for example given in Figure 2.10 for artificial data set AD4, should be considered. Nevertheless, this averaged value is a good indicator of how well the two estimation methods agree in estimating the compliance over the given pressure range of the infusion test data set considered. And indeed for each data set, the average compliances from methods A and B are very close. In order to encode the similar compliance functions with different values of n, the values for the elasticity parameter $\tilde{e}$ and the reference pressure P_r also have to differ.

Similarly to the compliance, we can also compute an average value for the elasticity

$$E_\mathrm{avg} = \frac{1}{P_\mathrm{plat} - P_\mathrm{b}} \int_{P_\mathrm{b}}^{P_\mathrm{plat}} E(P)\mathrm{d}P = \frac{1}{P_\mathrm{plat} - P_\mathrm{b}} \int_{P_\mathrm{b}}^{P_\mathrm{plat}} \tilde{e} \cdot (p - P_\mathrm{r})^{n-1}\mathrm{d}P \,. \tag{2.31}$$

For method A, the elasticity is constant and equal to the elasticity parameter $\tilde{e}$. For method B, this average value again is specific to the infusion test since it depends on the infusion rate. For some sets, the estimates of the production rate Q_prod differ

Table 2.5: Input data for infusion test data sets: T_1 Start of test, T_2 start of infusion, T_3 end of infusion, T_4 end of test, arterial blood pressure (ABP). Infusion rate was $Q_{\text{inf}} = 1.5\,\text{ml/min}$ for each test.

Set	00	02	03	04	06	07	08
T_1 [min]	0.0	0.0	9.0	0.0	12.0	0.0	0.0
T_2 [min]	5.5	5.4	15.3	8.3	14.8	12.7	13.0
T_3 [min]	19.9	34.4	34.8	24.8	39.8	26.7	27.0
T_4 [min]	24.0	36.3	38.7	31.8	47.1	27.0	31.7
ABP [mmHg]	86	68	52	67	93	125	68

a lot from the average value of about $0.35\,\text{ml/min}$ given in the literature (Fishman, 1992; Nolte, 2009). However, the physiological and pathophysiological variation of this value is not available in the literature. Since the estimated production rate depends on the sagittal sinus pressure P_{ss}, assumed to be approximately equal to the reference pressure P_{r} and the latter is not reliably estimated, it is not surprising that the estimates for the production rate (2.20) are also inconsistent between the two methods. In the equation for the increase in fluid content ΔV (2.13), the production rate cancels, so that we obtain consistent values from methods A and B again. This value could for example be used to check simulations of the infusion test with biomechanical models, such as Hakim and Hakim (1984); Kaczmarek et al. (1997); Sivaloganathan et al. (1998); Sobey et al. (2010); Wilkie et al. (2011).

2.7 Conclusions

We have estimated parameters of two single compartment models to fit the models to clinical data of the constant rate infusion test. First of all, we need to note that the quality of any parameter estimates depends on how well the model describes different features of the data and the quality of the data measurements.

Table 2.6: Results of parameter estimations: objective function value L, elasticity power n, elasticity constant $\tilde{e}$ in $\mathrm{mmHg}^{(1-n)}/\mathrm{ml}$, reference pressure P_r and baseline pressure P_b in mmHg, resistance to CSF outflow $\mathcal{R}$ in $\mathrm{mmHg\,min/ml}$, average compliance C_avg in $\mathrm{ml/mmHg}$, average elasticity E_avg in ml^{-1}, CSF production rate Q_prod in $\mathrm{ml/min}$, additional volume ΔV in ml at the end of the infusion.

Set	M	L	n	$\tilde{e}$	P_r	P_b	$\mathcal{R}$	C_avg	E_avg	Q_prod	ΔV
00	A	2.70149	1.0	0.24	2.13	9.97	15.43	0.24	0.24	0.51	5.65
00	B	2.70316	0.7	0.68	5.85	9.96	15.52	0.24	0.31	0.27	5.73
02	A	-0.27893	1.0	0.16	5.70	6.17	4.23	2.57	0.16	0.11	17.02
02	B	-0.28547	0.7	0.25	6.14	6.21	4.26	2.65	0.19	0.02	17.48
03	A	3.13269	1.0	0.36	4.69	7.75	10.18	0.31	0.36	0.30	4.96
03	B	3.13258	0.7	0.87	6.78	7.77	10.17	0.32	0.48	0.10	5.00
04	A	1.78375	1.0	0.53	10.72	11.47	5.15	0.56	0.53	0.14	4.62
04	B	1.78529	0.7	0.96	11.63	11.48	5.15	0.57	0.69	0.02	4.62
06	A	2.29899	1.0	0.12	2.78	7.56	12.44	0.70	0.12	0.38	13.24
06	B	2.30042	0.7	0.30	5.44	7.58	12.54	0.71	0.15	0.17	13.46
07	A	2.16668	1.0	0.48	7.86	8.43	10.97	0.43	0.48	0.05	7.12
07	B	2.17461	0.7	0.88	8.39	8.43	11.15	0.43	0.52	$4{\cdot}10^{-3}$	7.36
08	A	2.90932	1.0	0.08	-12.93	8.05	11.76	0.44	0.08	1.78	7.52
08	B	2.90960	0.7	0.24	-7.78	8.04	11.87	0.45	0.09	1.33	7.62

In our case, this has two main implications. Infusion tests that had to be aborted before reaching a steady plateau pressure did not contain sufficient information for a reliable parameter estimation. Secondly, since the model only describes the average pressure response to the infusion, short term effects such as oscillations with the cardiac cycle as well as temporal waves on time scales of a few minutes were not represented and thus are equivalent to noise.

For a successful infusion test, which clearly reached a plateau pressure, both the baseline pressure and the plateau pressure are recovered reliably and, hence, so is the resistance to CSF absorption, which is widely used in clinical practice for diagnosis and treatment decisions. With respect to the two compliance models, we conclude that both fit the data similarly well. This is due to the fact that they both essentially encode the same functional form of the compliance versus pressure over the pressure range observed during the infusion test. This means that the parameters describing this functional form are strongly interdependent and neither value is likely to be of clinical significance separately. In particular, it is not possible to estimate all five parameters of the generalised compliance model by Wirth and Sobey (2008) from the average pressure response of a constant infusion test. Hence, instead of considering the values of the parameters, we propose looking at the compliance–pressure curve directly, while keeping in mind that the estimation is only valid over the limited pressure range of the infusion test.

In addition, the fact that both models encode the same functional form of the compliance and fit the clinical data well demonstrates that the biomechanical considerations by Wirth and Sobey (2008) offer a good explanation for this functional form, which has been observed and repeatedly confirmed over the last

three decades. Thus, further research into the collapsibility of the brain's bridging veins and measurements of their mechanical parameters may provide a better understanding of the compliance reserve in humans, both in health and disease, and provide better knowledge of the limitations of single compartment models for different pressure ranges.

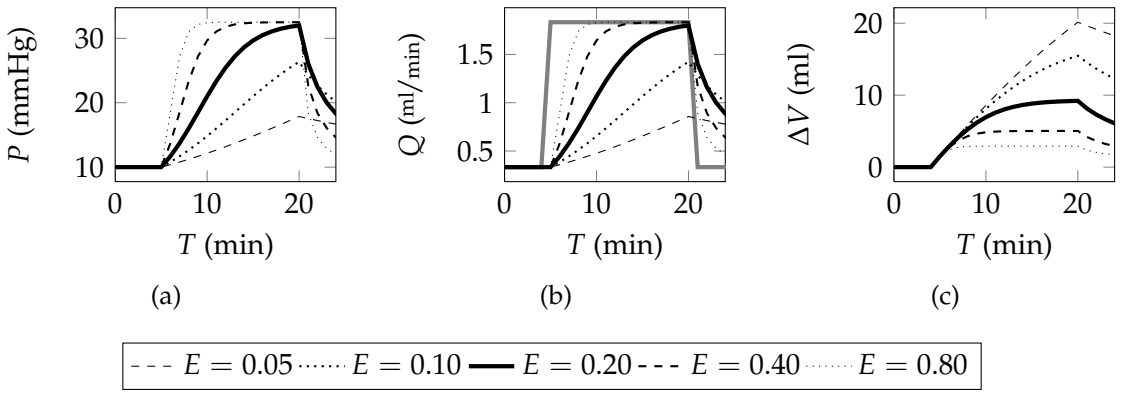

Figure 2.2: Variation of elasticity E in ml^{-1} in standard model: (a) intracranial pressure, (b) inflow (grey, concurrent) and outflow (black), (c) increase in CSF volume.

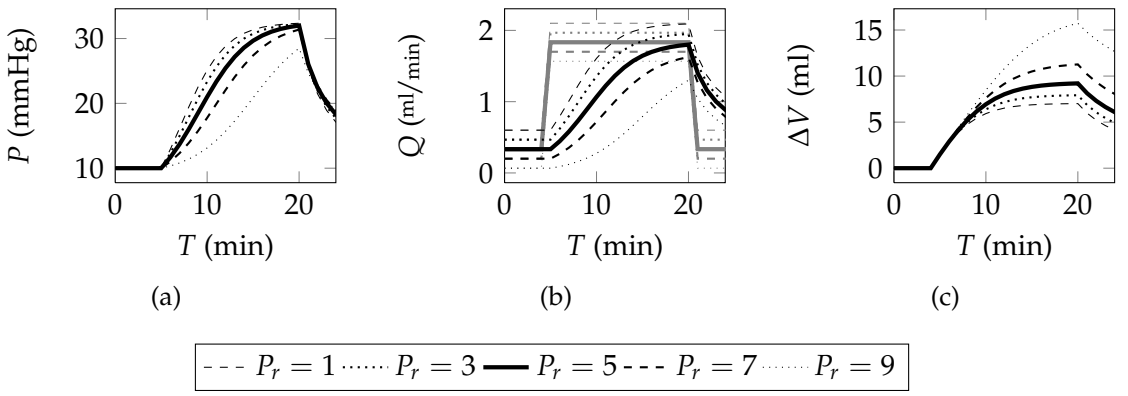

Figure 2.3: Variation of reference pressure P_r in mmHg in standard model: (a) intracranial pressure, (b) inflow (grey) and outflow (black), (c) increase in CSF volume.

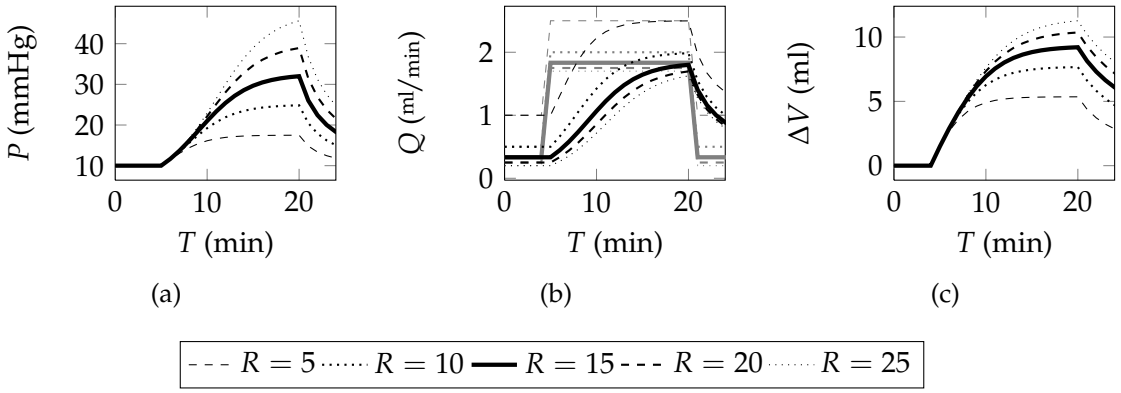

Figure 2.4: Variation of resistance to outflow $\mathcal{R}$ in standard model: (a) intracranial pressure, (b) inflow (grey) and outflow (black), (c) increase in CSF volume.

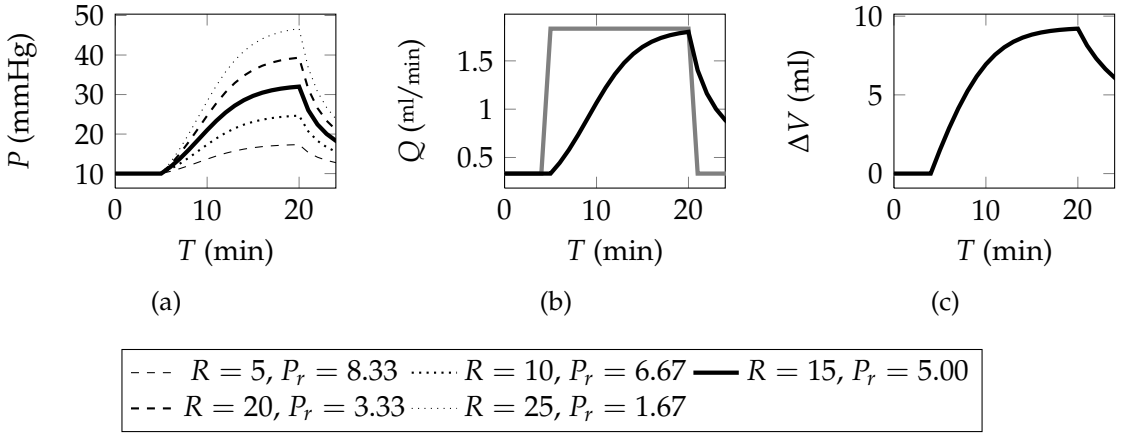

Figure 2.5: Variation of resistance to outflow $\mathcal{R}$ and reference pressure P_r in standard model with production rate Q_prod fixed: (a) intracranial pressure, (b) inflow (grey) and outflow (black), (c) increase in CSF volume. Lines in (b) and (c) are concurrent.

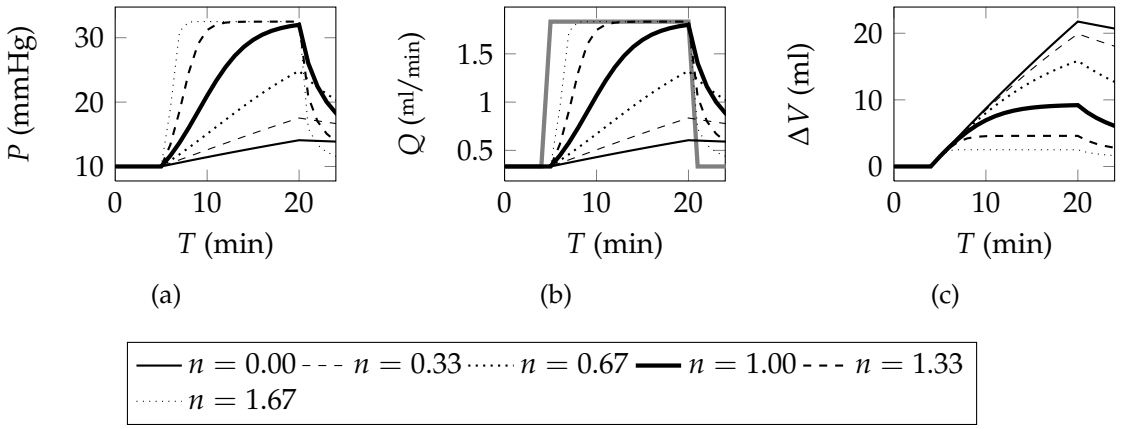

Figure 2.6: Variation of compliance power n in generalised model: (a) intracranial pressure, (b) inflow (grey) and outflow (black), (c) increase in CSF volume.

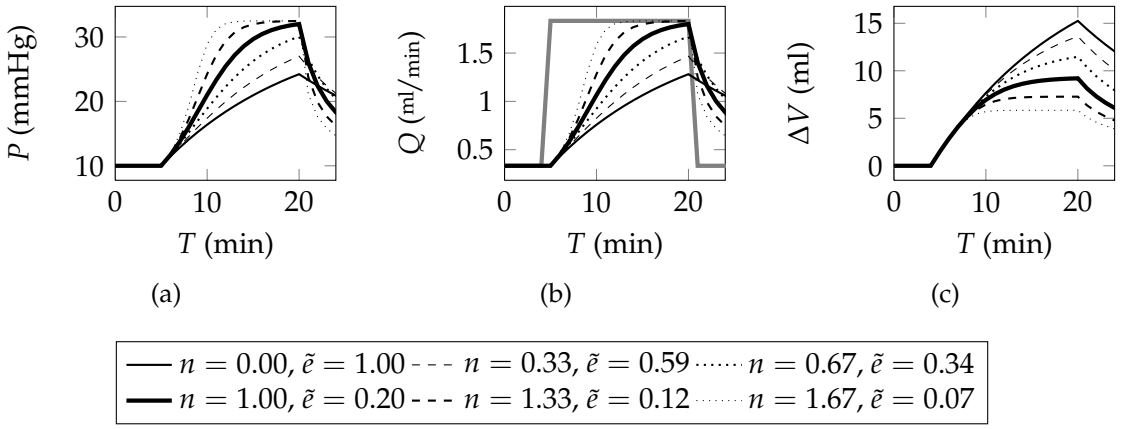

Figure 2.7: Variation of compliance power n and elasticity parameter $\tilde{e}$ in generalised model with elasticity at base pressure $E(P_b)$ fixed: (a) intracranial pressure, (b) inflow (grey) and outflow (black), (c) increase in CSF volume.

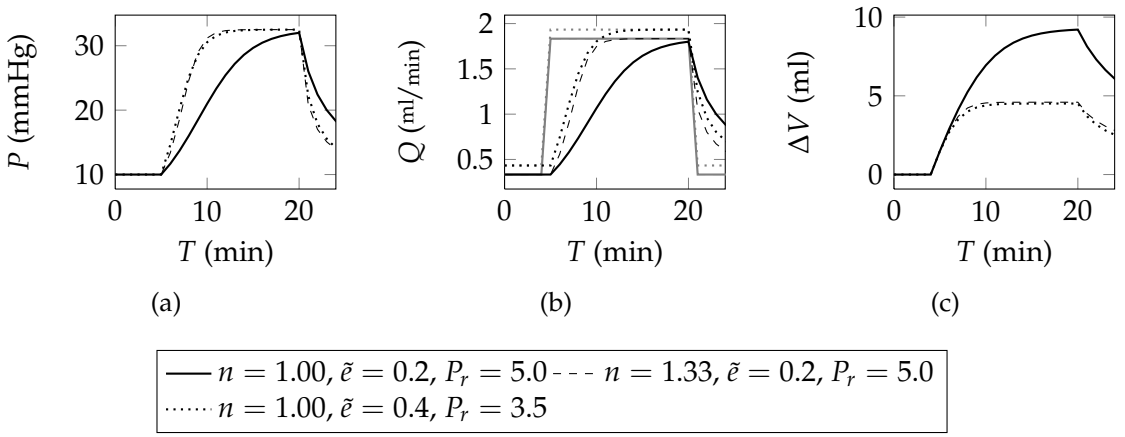

Figure 2.8: Variation of compliance power n, elasticity parameter $\tilde{e}$ and reference pressure P_{r} in generalised model: (a) intracranial pressure, (b) inflow (grey) and outflow (black), (c) increase in CSF volume.

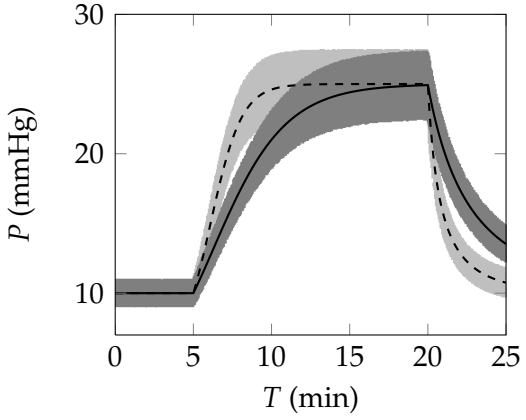

Figure 2.9: Pressure for artificial data sets: (- -) AD1, (shaded light grey) AD2, (—) AD3, (shaded dark grey) AD4.

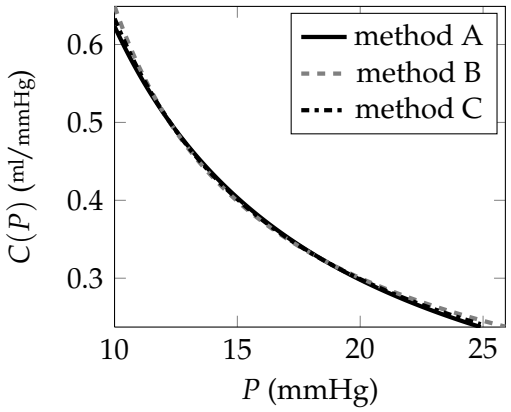

Figure 2.10: Estimated compliance functions over the observed pressure range for set AD4, estimated with the three different parameter estimation methods.

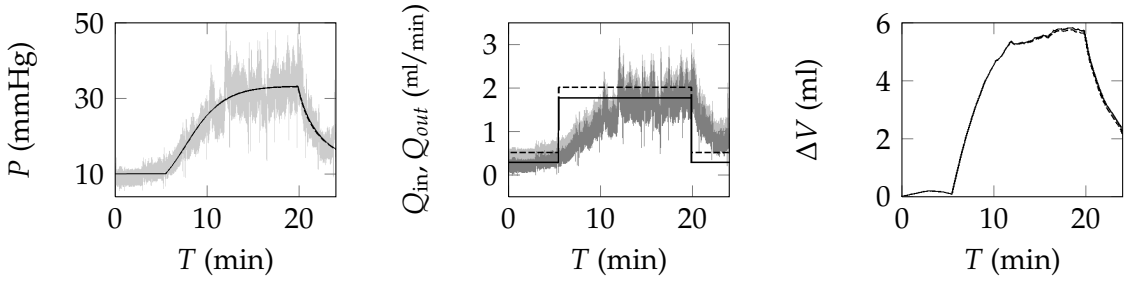

Figure 2.11: Parameter fits for data set 00: (a) intracranial pressure: measured (light grey), from fit with method A (- -), from fit with method B (—); (b) inflow for method A (- -), inflow for method B (—), outflow for method A (light grey), outflow for method B (dark grey); (c) increase in CSF volume: method A (- -), method B (—).

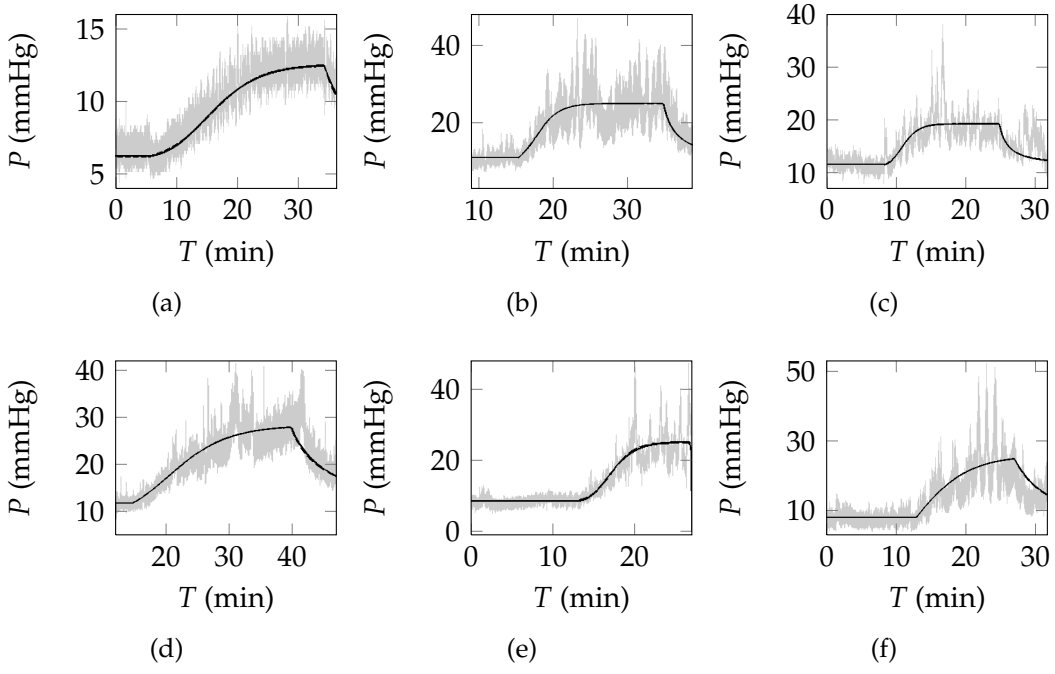

Figure 2.12: Intracranial pressure from parameter fits for data sets (a) 02, (b) 03, (c) 04, (d) 06, (e) 07, (f) 08: measured (light grey), method A (- -), method B (—).

Chapter 3

Poroelastic modelling

Contents

3.1 Motivation for poroelastic brain modelling

Two alternative descriptions of poroelastic models were developed, Biot's consolidation theory for soil mechanics (Biot, 1941) and Bowen's derivation from the theory of mixtures (Bowen, 1980, 1982). The former is the basis for the theory of poroelasticity used today to describe porous, elastic materials in different applications, including soil mechanics and biological tissues (Coussy, 2004; Wang, 2000). As noted in 1.2.4 several authors have applied this theory to derive various models of the interaction between brain tissue and cerebrospinal fluid to further the understanding of CSF related diseases such as hydrocephalus.

The models described in this chapter are mostly based on a series of papers treating the brain as a thick, spherical shell of a porous elastic material with one concentric spherical ventricle (Smillie et al., 2005; Sobey and Wirth, 2006; Wirth and Sobey, 2009). In the last of these papers, Wirth and Sobey (2009) generalised the poroelastic equations by introducing additional disconnected blood compartments in the parenchyma, which interact with the CSF only indirectly through the tissue. The aqueduct of Sylvius connecting the ventricle and the subarachnoid space surrounding the brain is modelled by a straight cylindrical tube, but has no effect on the spherical symmetry. Instead of a given CSF pressure at either end, the fluid volume balances in the ventricle and the subarachnoid space are used as boundary conditions.

In this chapter, we lay out the derivations of a single-fluid poroelastic model of the brain in spherical symmetry and how this can be generalised to a two-fluid poroelastic model using arterial blood pressure as input to simulate CSF pressure oscillations following the cardiac cycle. This latter model is the one we discretise in a finite element framework and use to simulate constant rate infusion tests in the following chapters.

The single-fluid poroelastic governing equations under the assumption of small deformations are derived in section 3.2. They are based on the linear theory in Biot (1941), but we allow for non-linearities due to a deformation dependent permeability and pressure dependence in the CSF storage coefficient. As we have shown in Wirth et al. (2012), deformation dependence in the permeability can limit the flow rate through a poroelastic material. Since we will use volume conservation boundary conditions, this means that our model equations may lead to ill-posed problems. To identify the circumstances under which this may cause

problems for the numerical solutions, we examine this effect in detail on a planar steady-state model problem in section 3.3.

The equations for the spherically symmetric single-fluid poroelastic model of the brain, including boundary conditions and non-dimensionalisation, are set out in section 3.4. In section 3.5, we develop the two-fluid model, which we will use to simulate constant rate infusion tests in the following chapters, from a three-fluid poroelastic model with separate compartments for CSF, arterial blood and venous blood. In addition, we relate the two-fluid model to the single-compartment models from chapter 2 and compare our multi-fluid poroelastic approach with an alternative description by Tully and Ventikos (2011).

Finally, in section 3.6, we justify our use of the small deformation theory and point out the challenges in large deformation models of the brain.

3.2 Poroelastic governing equations

3.2.1 The theory of poroelasticity

The equations derived in this section model an elastic solid with interconnected, fluid filled pores. The continuum hypothesis postulates that the poroelastic material can be modelled as a superimposition of a solid and a fluid material. This means that an intermediate length scale is considered: larger than the pore scale, so that each volume element contains both, solid and fluid, but smaller than the macro scale, so that a differential description is sensible. For an in-depth analysis of the subject the reader is referred to Coussy (2004) and for a large collection of solved problems in geophysics to Wang (2000).

The governing equations derived in the remainder of this section are closely related to the linear theory described by Biot (1941). However, we allow for certain non-linearities due to a strain dependent permeability as proposed by Sobey and Wirth (2006) and pressure dependence in the specific compliance (Wirth and Sobey, 2009). The following assumptions will be made throughout this section:

(1) The material is homogeneous and isotropic.
(2) Deformations are small and reversible.
(3) The stress-strain relation of the solid matrix is linear (Hooke's law).
(4) The fluid is Newtonian and incompressible and flow through the solid matrix is governed by Darcy's law.
(5) The conditions are isothermal, body forces zero and inertial terms negligible.

3.2.2 Kinematics

The independent variables describing the poroelastic material are chosen as the displacement of the solid matrix, $\boldsymbol{u}$, and the fluid pore pressure, P. For small strain linear theory to hold, the derivatives of the solid displacements have to be small

$$\|\nabla \boldsymbol{u}\| \ll 1 \,. \tag{3.1}$$

In this case, also the distinction between the Lagrangian and Eulerian framework is not necessary. Given the deformation gradient

$$\boldsymbol{F} := \boldsymbol{I} + \nabla \boldsymbol{u} \tag{3.2}$$

under this assumption, the Green–Lagrange strain tensor, $\boldsymbol{\Lambda}$, reduces to the linear strain tensor, $\boldsymbol{\mathcal{E}}$,

$$\begin{aligned}\boldsymbol{\Lambda} &:= \frac{1}{2}\left(\boldsymbol{F}^T \cdot \boldsymbol{F} - \boldsymbol{I}\right) = \frac{1}{2}\left(\nabla \boldsymbol{u}^T + \nabla \boldsymbol{u} + \nabla \boldsymbol{u}^T \cdot \nabla \boldsymbol{u}\right) \\ &\approx \frac{1}{2}\left(\nabla \boldsymbol{u}^T + \nabla \boldsymbol{u}\right) =: \boldsymbol{\mathcal{E}} \,.\end{aligned} \tag{3.3}$$

Similarly, the Jacobian, J, of the deformation gradient, which measures volume changes, can be linearised

$$J := \det(\boldsymbol{F}) \approx 1 + \nabla \cdot \boldsymbol{u} = 1 + \operatorname{tr}(\boldsymbol{\mathcal{E}}) =: 1 + \epsilon \,, \tag{3.4}$$

with the linearised volume dilation or volumetric strain, ϵ, which measures the local change in volume.

3.2.3 Fluid volume balance

We assume Darcy flow through the porous medium so that the flux, Darcy velocity, or discharge velocity, $\boldsymbol{Q}$, is proportional to the pressure gradient

$$\boldsymbol{Q} = -\frac{\kappa(\epsilon)}{\eta} \nabla P \,, \tag{3.5}$$

with fluid viscosity η and a strain-dependent permeability κ. In geophysics, the permeability is usually assumed to remain constant (Biot, 1941; Coussy, 2004; Wang, 2000). Applying this theory to soft tissues opened the possibility for pores to partially or fully close. We want to investigate the influence this has on simulations of cerebrospinal fluid flow through the brain. Hence, we consider the exponential permeability model proposed by Lai and Mow (1980)

$$\kappa(\epsilon) = \kappa_0 \exp(M_0 \epsilon) \tag{3.6}$$

with a model parameter $M_0 \geq 0$, such that compressing the material decreases the permeability. The special case $M_0 = 0$ reduces the problem to constant permeability. Further permeability models in combination with different linear and non-linear stress-strain relations were analysed by Wirth et al. (2012).

Furthermore, we assume the following relation between the increase in relative fluid content, ζ, per volume element V_0, the volume dilation, ϵ, and the fluid pressure, P,

$$\zeta := \frac{V_\mathrm{f} - V_{\mathrm{f},0}}{V_0} = \alpha\epsilon + \gamma(P)P \; . \tag{3.7}$$

The Biot–Willis parameter, α, usually with a value between zero and one, measures the ratio of fluid volume change to total volume change when the pressure is held constant. Wirth and Sobey (2006) argue that the stiffness of blood vessels means the value of α should lie above the value 0.83, indicated by the volume ratio of cerebrospinal fluid and blood in the brain, and later estimate the value from the compliance in compartment models to be around 0.9995 (Wirth and Sobey, 2009). Levine (2000) argues that, due to active dilation of blood vessels to keep cranial blood flow constant, even an apparent value of $\alpha > 1$ is conceivable.

The specific compliance or storage coefficient, γ, describes how much additional fluid can be forced into the solid matrix by increasing the pressure while keeping the total volume constant. Traditionally, γ is considered a constant (Biot, 1941; Coussy, 2004; Wang, 2000). In soft tissue, however, it is easy to imagine a pressure dependency of this parameter, modelling the collapsibility of veins in the tissue (Wirth and Sobey, 2008, 2009).

Since the water-like CSF is incompressible, the fluid mass balance is equivalent to the fluid volume balance. The change in fluid volume in a volume element is equal

to the difference of flow into and out of the element. In the limit, this becomes

$$\frac{\partial \zeta}{\partial T} = -\nabla \cdot \boldsymbol{Q} \,, \tag{3.8}$$

which yields

$$\alpha \frac{\partial \epsilon}{\partial T} + \frac{\partial}{\partial T}(\gamma(P)P) = \nabla \cdot \left(\frac{\kappa(\epsilon)}{\eta} \nabla P \right) \,. \tag{3.9}$$

3.2.4 Conservation of momentum

According to Terzaghi's principle of effective stress (Biot, 1941), the total stress of a poroelastic material can be decomposed into the elastic stress of the solid structure, $\boldsymbol{\sigma}_\mathrm{s}$, and the negative pore fluid pressure, P, weighted by the Biot–Willis parameter, α. Unlike in the development of hydrocephalus, the displacements during an infusion test stay small. Given this fact and in the absence of better knowledge of the brain tissue's stress-strain relation, we assume Hooke's law with Lamé parameters λ and μ, so that

$$\boldsymbol{\sigma} = \boldsymbol{\sigma}_\mathrm{s} - \alpha P \boldsymbol{I} = (\lambda \epsilon \boldsymbol{I} + 2\mu \boldsymbol{\mathcal{E}}) - \alpha P \boldsymbol{I} \,. \tag{3.10}$$

It is important to note again that stress as well as strain relate to the porous solid structure on an intermediate length scale larger than the pore diameter. Hence, the material parameters depend on its porosity and are distinct from those for the same material without pores, such as on the microscopic scale.

Furthermore, we need to take into account that the brain grows in an environment with positive pressure. Hence, all pressures have to be measured with respect to a reference pressure, P_sf, at which the solid matrix is stress-free. Wirth and Sobey (2006) argue that its value should be somewhere between venous blood

pressure and intracranial CSF pressure. They chose a value of approximately $P_{\text{sf}} = 6\,\text{mmHg}$, about 1 mmHg higher than venous blood pressure.

The densities of CSF and brain tissue are very similar, thus body forces can be neglected. For physiological values of parameters, inertial terms turn out to be negligible as well (Wirth and Sobey, 2009), so that the conservation of momentum requires the total stress to be divergence-free

$$\nabla \cdot \boldsymbol{\sigma} = 0\,, \tag{3.11}$$

thus,

$$0 = \nabla \cdot \left(\lambda \epsilon \boldsymbol{I} + 2\mu \boldsymbol{\mathcal{E}} - \alpha P \boldsymbol{I}\right)\,. \tag{3.12}$$

3.3 Steady state planar model problem

3.3.1 Motivation and description of the planar model problem

In the poroelastic model of the brain, we will apply CSF volume conservation inside the ventricles and in the subarachnoid space. This leads to boundary conditions specifying the flow rate rather than the pressure. Before considering that problem, we want to investigate the influence of the strain-dependent permeability on the flow rate and the consequences this has on existence and uniqueness of solutions for poroelastic problems with flow boundary conditions. Thus, we are able to identify the potential difficulties this might cause in the numerical solutions.

To avoid complicated calculations in spherical geometry hiding the essential features of the poroelastic governing equations, this analysis is carried out on

Figure 3.1: Planar poroelastic model problem with boundary conditions.

a model problem in simplified planar geometry. We consider a layer of infinite transverse extent of isotropic porous elastic material of thickness X_0, filled with an incompressible Newtonian fluid. The solid is fixed at one end, free at the other end and constant pressures are prescribed at either end (Figure 3.1). The steady-state equations for this model problem can be solved analytically for constant or exponentially strain-dependent pressure and used to calculate the maximum flow rate attainable in either case.

In Wirth et al. (2012), we carried out a similar analysis for zero pressure at the fixed end in a large deformation framework and compared different combinations of hyperelastic models and permeability models. Since the small deformation theory is deemed sufficient for simulations of the infusion test, compare with section 3.6, here we consider the small deformation case in detail, allowing both boundary pressures to vary.

3.3.2 Planar steady state poroelastic model equations

Due to the geometry, the displacements in Y- and Z-direction as well as partial derivatives with respect to those are zero. Thus, we obtain for the displacements,

strain and volume dilation from (3.3)–(3.4)

$$\boldsymbol{U} = (U,\,0,\,0)^{\mathrm{T}}\,, \qquad \nabla\boldsymbol{U} = \mathrm{diag}\left(\frac{\partial U}{\partial X},\,0,\,0\right) = \boldsymbol{\mathcal{E}}\,, \qquad \epsilon = \frac{\partial U}{\partial X}\,. \tag{3.13}$$

Similarly, the flux (3.5), proportional to the pressure gradient, has only one component

$$\nabla P = \left(\frac{\partial P}{\partial X},\,0,\,0\right)^{\mathrm{T}}\,, \qquad \boldsymbol{Q} = \left(-\frac{\kappa(\epsilon)}{\eta}\frac{\partial P}{\partial X},\,0,\,0\right)^{\mathrm{T}}\,, \tag{3.14}$$

so that the steady state fluid balance (3.9) yields

$$0 = \nabla\cdot\left(\frac{\kappa(\epsilon)}{\eta}\nabla P\right) = \frac{\partial}{\partial X}\left(\frac{\kappa(\epsilon)}{\eta}\frac{\partial P}{\partial X}\right)\,. \tag{3.15}$$

The total stress (3.10) is

$$\begin{aligned}\boldsymbol{\sigma} &= (\lambda\epsilon\boldsymbol{I} + 2\mu\boldsymbol{\mathcal{E}}) - \alpha P\boldsymbol{I} = \mathrm{diag}\left(\lambda\epsilon + 2\mu\frac{\partial U}{\partial X} - \alpha P,\,\lambda\epsilon - \alpha P,\,\lambda\epsilon - \alpha P\right)\\ &= \mathrm{diag}((\lambda+2\mu)\epsilon - \alpha P,\,\lambda\epsilon - \alpha P,\,\lambda\epsilon - \alpha P)\,,\end{aligned} \tag{3.16}$$

hence, only the X-component of the stress balance (3.12) is non-zero and needs to be considered

$$\begin{pmatrix}0\\0\\0\end{pmatrix} = \nabla\cdot\boldsymbol{\sigma} = \begin{pmatrix}\frac{\partial}{\partial X}((\lambda+2\mu)\epsilon - \alpha P)\\ \frac{\partial}{\partial Y}(\lambda\epsilon - \alpha P)\\ \frac{\partial}{\partial Z}(\lambda\epsilon - \alpha P)\end{pmatrix} = \left((\lambda+2\mu)\frac{\partial\epsilon}{\partial X} - \alpha\frac{\partial P}{\partial X}\right)\begin{pmatrix}1\\0\\0\end{pmatrix}\,. \tag{3.17}$$

These equations can be rewritten as a system of ordinary first and second order differential equations

$$\epsilon = \frac{\mathrm{d}U}{\mathrm{d}X}\,, \qquad 0 = (\lambda+2\mu)\frac{\mathrm{d}\epsilon}{\mathrm{d}X} - \alpha\frac{\mathrm{d}P}{\mathrm{d}X}\,, \qquad 0 = \frac{\mathrm{d}}{\mathrm{d}X}\left(\frac{\kappa(\epsilon)}{\eta}\frac{\mathrm{d}P}{\mathrm{d}X}\right)\,, \tag{3.18}$$

which is closed by four boundary conditions. At the fixed end, the displacements

are zero,

$$U(X_0) = 0\,, \tag{3.19}$$

at the free end, the normal stress in the poroelastic material needs to balance the fluid pressure

$$-P(0) = (\lambda + 2\mu)\epsilon(0) - \alpha P(0)\,, \tag{3.20}$$

and at either end, a pressure is prescribed

$$P(0) = P_{\text{left}}\,, \qquad P(X_0) = P_{\text{right}}\,. \tag{3.21}$$

To non-dimensionalise (3.18), let

$$x = \frac{X}{X_0} \in [0,1]\,, \qquad \varepsilon(x) = \frac{\epsilon(X)}{\epsilon_0}\,, \qquad u(x) = \frac{U(X)}{\epsilon_0 X_0}\,, \tag{3.22}$$

$$P_0 = \frac{(\lambda + 2\mu)}{\alpha}\epsilon_0\,, \qquad p(x) = \frac{P(X)}{P_0}\,, \qquad k(\varepsilon) = \frac{\kappa(\epsilon)}{\kappa_0}\,, \tag{3.23}$$

$$p_{\text{left}} = \frac{P_{\text{left}}}{P_0}\,, \qquad p_{\text{right}} = \frac{P_{\text{right}}}{P_0}\,, \qquad M = M_0\epsilon_0\,, \tag{3.24}$$

for a suitable constant ϵ_0, which yields

$$\varepsilon = \frac{\mathrm{d}u}{\mathrm{d}x}\,, \tag{3.25}$$

$$\frac{\mathrm{d}p}{\mathrm{d}x} = \frac{\mathrm{d}\varepsilon}{\mathrm{d}x}\,, \tag{3.26}$$

$$0 = \frac{\mathrm{d}}{\mathrm{d}x}\left(k(\varepsilon)\frac{\mathrm{d}p}{\mathrm{d}x}\right)\,, \tag{3.27}$$

with the dimensionless permeability

$$k(\varepsilon) = \exp(M\varepsilon)\,. \tag{3.28}$$

Inserting (3.26) into (3.27) yields the decoupled equation

$$0 = \frac{\mathrm{d}}{\mathrm{d}x}\left(k(\varepsilon)\frac{\mathrm{d}\varepsilon}{\mathrm{d}x}\right)\,. \tag{3.29}$$

The boundary conditions become

$$u(1) = 0\,, \quad \varepsilon(0) + \frac{1-\alpha}{\alpha} p(0) = 0\,, \quad p(0) = p_{\text{left}}\,, \quad p(1) = p_{\text{right}}\,. \tag{3.30}$$

From a solution for the pressure and the strain, the non-dimensional flux can be computed by

$$q = -k(\varepsilon)\frac{\mathrm{d}p}{\mathrm{d}x} = -\exp(M\varepsilon)\frac{\mathrm{d}p}{\mathrm{d}x}\,. \tag{3.31}$$

The dimensional flux is then

$$Q = \frac{\kappa_0 P_0}{\eta X_0} q\,(1,\,0,\,0)^{\mathrm{T}}\,. \tag{3.32}$$

3.3.3 Analytic solution and maximal flow rate

Constant permeability

With constant permeability $k(\varepsilon) \equiv 1$, that is $M_0 = M = 0$, the equation (3.29) becomes linear and the system (3.25)–(3.27) can easily be integrated

$$\varepsilon(x) = a_1 x + a_2\,, \qquad p(x) = a_1 x + a_3\,, \qquad u(x) = \frac{a_1}{2}x^2 + a_2 x + a_4\,. \tag{3.33}$$

Inserting these solutions into the boundary conditions (3.30) yields a linear system of equations for the integration constants, which can be solved sequentially

$$a_3 = p_{\text{left}}\,, \quad a_1 = p_{\text{right}} - p_{\text{left}}\,, \quad a_2 = -\frac{1-\alpha}{\alpha} a_3\,, \quad a_4 = -\frac{a_1}{2} - a_2\,. \tag{3.34}$$

From the solutions and the integration parameters, an expression for the flux (3.31) can be obtained

$$q = -\frac{\mathrm{d}p}{\mathrm{d}x} = -a_1 = p_{\text{left}} - p_{\text{right}}\,. \tag{3.35}$$

It depends linearly on the pressure difference and hence is not limited. For any value of the flux and any value of the pressure at one end, the pressure at the other end can easily be computed along with the solutions for the pressure, volume dilation and displacements.

Exponential permeability

For exponential permeability, that is with $M_0 > 0$, the uncoupled differential equation for the volume dilation (3.29) yields

$$0 = \frac{\mathrm{d}}{\mathrm{d}x}\left(\exp(M\varepsilon)\frac{\mathrm{d}\varepsilon}{\mathrm{d}x}\right) = \exp(M\varepsilon)\left(M\left(\frac{\mathrm{d}\varepsilon}{\mathrm{d}x}\right)^2 + \frac{\mathrm{d}^2\varepsilon}{\mathrm{d}x^2}\right) , \tag{3.36}$$

so that ε needs to fulfil

$$0 = M\left(\frac{\mathrm{d}\varepsilon}{\mathrm{d}x}\right)^2 + \frac{\mathrm{d}^2\varepsilon}{\mathrm{d}x^2} = M\left(\frac{\mathrm{d}\varepsilon}{\mathrm{d}x}\right)^2 + \frac{\mathrm{d}}{\mathrm{d}x}\left(\frac{\mathrm{d}\varepsilon}{\mathrm{d}x}\right) . \tag{3.37}$$

This leads to solutions of the form

$$\varepsilon(x) = \frac{1}{M}\ln\left(a_1 x + 1\right) + a_2 , \tag{3.38}$$

$$p(x) = \frac{1}{M}\ln\left(a_1 x + 1\right) + a_3 , \tag{3.39}$$

$$u(x) = \frac{(a_1 x + 1)}{a_1 M}(\ln(a_1 x + 1) - 1) + a_2 x + a_4 , \tag{3.40}$$

with

$$\frac{\mathrm{d}\varepsilon}{\mathrm{d}x} = \frac{\mathrm{d}p}{\mathrm{d}x} = \frac{a_1}{M}\frac{1}{a_1 x + 1} \tag{3.41}$$

and the requirement that $a_1 > -1$ for the solutions to be continuous on $[0, 1]$.

Again, the boundary conditions (3.30) can be solved sequentially for the integration constants

$$a_3 = p_{\text{left}} \,, \qquad a_1 = \exp(M(p_{\text{right}} - p_{\text{left}})) - 1 \,, \tag{3.42}$$

$$a_2 = -\frac{1-\alpha}{\alpha} a_3 \,, \qquad a_4 = \frac{a_1 + 1}{a_1 M} \left(1 - \ln|a_1 + 1|\right) - a_2 \,, \tag{3.43}$$

but this time the system depends non-linearly on the pressure values. With these values, the flux (3.31) can be expressed as a function of the integration constants and hence of the left and right pressures via

$$\begin{aligned} q &= -\exp\left(\ln(a_1 x + 1) + M a_2\right) \frac{a_1}{M(a_1 x + 1)} = -\frac{a_1}{M} \exp(M a_2) \\ &= \frac{1}{M}\left[1 - \exp(M(p_{\text{right}} - p_{\text{left}}))\right] \cdot \exp\left(-M \frac{1-\alpha}{\alpha} p_{\text{left}}\right) . \end{aligned} \tag{3.44}$$

In the special case $\alpha = 1$, the exponential on the right is equal to one and the flux depends only on the pressure difference between the left and right boundary. If the pressure is higher at the right, fixed end, the flux is negative, that is going from the right to the left, and unbounded in absolute value. In the other direction, with the higher pressure at the free end, the dimensionless flux, q, is bounded by its asymptotic limit $\frac{1}{M}$ for growing pressure difference.

A similar behaviour occurs when considering a fixed left pressure, p_{left}, with the flux being limited from above by

$$q_{\text{max, right}} = \frac{1}{M} \exp\left(-M \frac{1-\alpha}{\alpha} p_{\text{left}}\right) \tag{3.45}$$

and converging asymptotically to this limit as the right pressure, p_{right}, tends to $-\infty$. All pressures are measured with respect to a reference pressure, P_{sf}, at which the solid matrix is stress free, so negative values are feasible (compare 3.2.4).

Table 3.1: Comparison of flow rates from solutions to the steady state, planar, poroelastic model problem with different sets of pressure boundary conditions: pressures, P_{left}, P_{right}, at the left and right boundary, respectively, in mmHg; type of permeability model; minimal permeability, $\min(\kappa)$ in m^2; flow rate through a cube with 10 cm side length, $Q \cdot X_0^2$, in $^{\text{ml}}/_{\text{min}}$; and line styles for the plots in Figure 3.2.

P_{left}	P_{right}	permeability	$\min(\kappa)$	$Q \cdot X_0^2$	line style
1.0	0.0	constant	$14.0 \cdot 10^{-13}$	1.3	- - - - - - - -
1.0	0.0	exponential	$7.7 \cdot 10^{-13}$	0.9	———
3.0	2.0	constant	$14.0 \cdot 10^{-13}$	1.3	- - - - - - - -
3.0	2.0	exponential	$6.8 \cdot 10^{-13}$	0.8	———
4.0	2.0	constant	$14.0 \cdot 10^{-13}$	2.5	- - - - - - - -
4.0	2.0	exponential	$3.7 \cdot 10^{-13}$	1.2	———

If, on the other hand, the right pressure is fixed and the left pressure varied, then the flux does not behave monotonically. Its derivative with respect to p_{left} is

$$\begin{aligned}\frac{\mathrm{d}q}{\mathrm{d}p_{\text{left}}} &= \exp(Mp_{\text{right}} - Mp_{\text{left}}) \cdot \exp\left(-M\frac{1-\alpha}{\alpha}p_{\text{left}}\right) \\ &\quad + \frac{1-\alpha}{\alpha}\left[\exp(Mp_{\text{right}} - Mp_{\text{left}}) - 1\right] \cdot \exp\left(-M\frac{1-\alpha}{\alpha}p_{\text{left}}\right) \\ &= \underbrace{\frac{1}{\alpha}\exp\left(-M\frac{1-\alpha}{\alpha}p_{\text{left}}\right)}_{>0} \cdot \left[\exp(Mp_{\text{right}} - Mp_{\text{left}}) - (1-\alpha)\right]\end{aligned} \tag{3.46}$$

and switches signs from positive to negative as

$$p_{\text{left}} = p_{\text{right}} - \frac{1}{M}\ln(1-\alpha)\,. \tag{3.47}$$

For this left pressure, the flux is maximal with a value of

$$q_{\text{max, left}} = \frac{\alpha}{M}(1-\alpha)^{\frac{1-\alpha}{\alpha}}\exp\left(-M\frac{1-\alpha}{\alpha}p_{\text{right}}\right)\,. \tag{3.48}$$

Wirth (2005); Sobey and Wirth (2006) obtain the same limit, up to different non-dimensionalisation constants and for zero pressure at the right boundary, when considering the inverse problem of computing the necessary left pressure to achieve a given flux. They argue that out of the two solutions for fluxes between

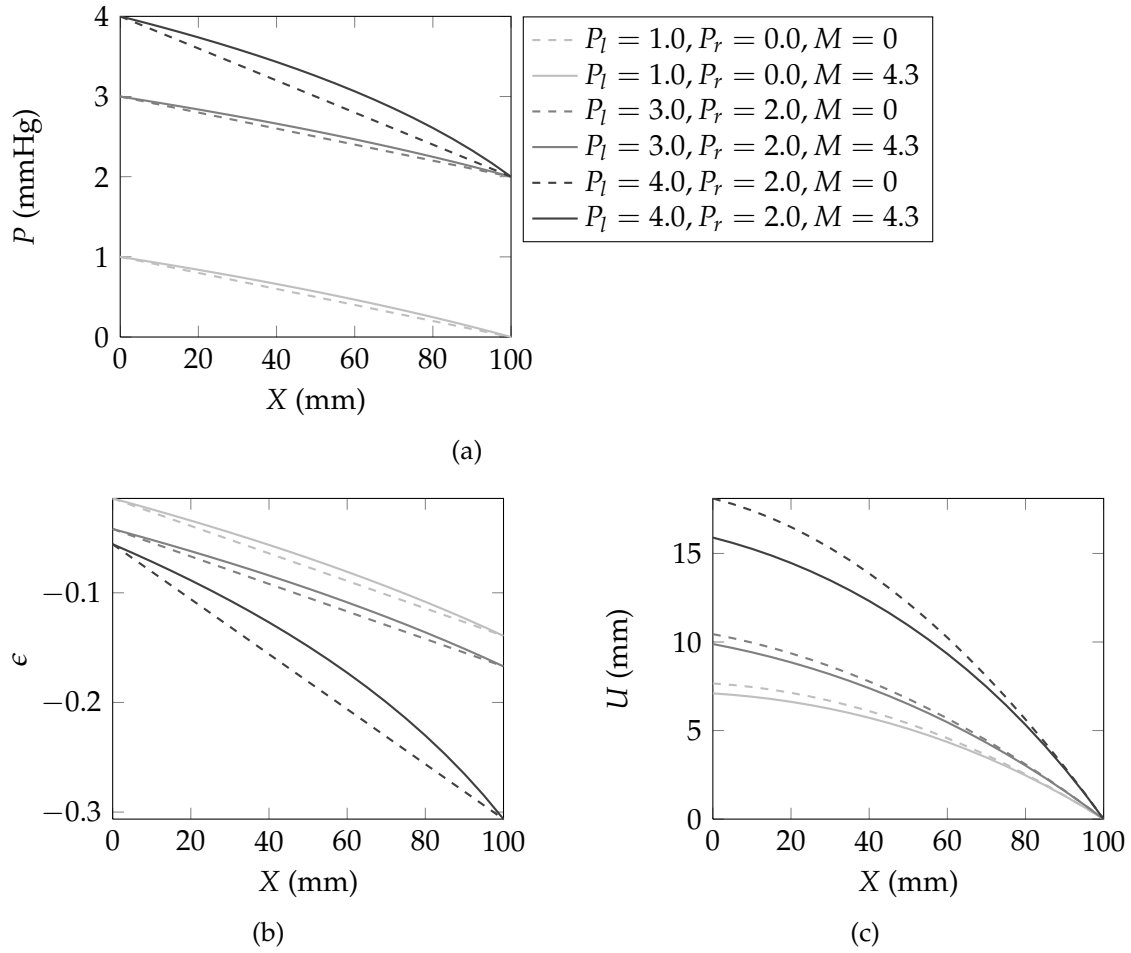

Figure 3.2: Analytic solutions to the steady state, planar, poroelastic model problem for different sets of pressure boundary conditions (see Table 3.1) with constant (dashed) or exponentially strain-dependent (continuous) permeability: (a) pressure, (b) volume dilation, (c) displacements.

zero and this maximal value, the one with the lower pressure is stable and the one with the higher pressure unstable.

Some examples have been computed for different sets of boundary pressures and constant or exponentially strain-dependent permeability. Table 3.1 lists those conditions along with the minimal permeability in the compressed material and the flow rate through a cube of side length X_0. This flow rate was obtained by multiplying the flux with with a representative area of X_0^2. Figure 3.2 shows the

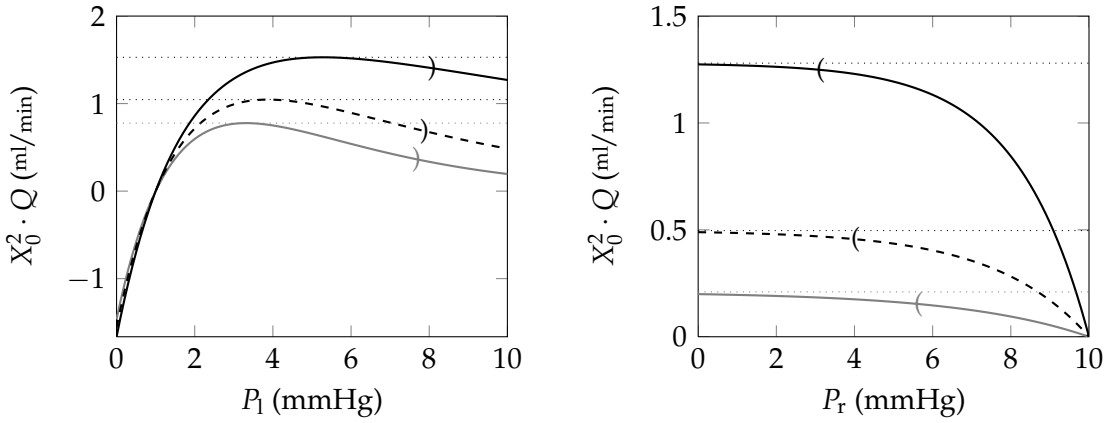

Figure 3.3: Flow rate through a cube of side length X_0 versus pressure with their respective maximal values for different values of the Biot–Willis parameter α: (a) flow rate versus left boundary pressure for right boundary pressure $P_\mathrm{right} = 1\,\mathrm{mmHg}$; (b) flow rate versus right boundary pressure for left boundary pressure $P_\mathrm{left} = 10\,\mathrm{mmHg}$: $\alpha = 0.5$ (grey), $\alpha = 0.7$ (dashed), $\alpha = 0.9$ (black). The brackets indicate the pressures, at which the model becomes unphysical due to material inversion as $\epsilon = -1$.

pressure, volume dilation and displacement distributions through the material for these examples. The flow rate versus left or right boundary pressure with their respective maximal values for different values of the Biot–Willis parameter α is shown in Figure 3.3. There, we also indicate, when the model becomes unphysical as the volume dilation reaches -1. Again, the flow rate through a cube of side length X_0 is considered. Furthermore, it is indicated where the model would fully break down due to material inversion.

The above computations show that a poroelastic problem with flow boundary conditions may not be well-posed. Neither existence nor uniqueness of solutions is guaranteed if the material is compressed. This needs to be kept in mind when considering time-dependent problems or different geometries where analytic solutions are harder to compute or may not even exist. In addition, solutions to

the material equations can be unphysical if they imply model inversion, or violate the small deformation assumption.

3.4 Single-fluid poroelastic model of the brain

3.4.1 Motivation for the spherically symmetric brain model

We follow Levine (2000); Smillie et al. (2005); Sobey and Wirth (2006); Wirth and Sobey (2009) in modelling the brain as a thick, hollow, spherical shell made of isotropic, poroelastic material and filled with an incompressible, Newtonian fluid. The solid matrix is made up of cells and cytoskeleta, encompassing the interstitial fluid network, which readily communicates with cerebrospinal fluid surrounding the parenchyma. Blood is considered as a component of the solid matrix. This introduces compressibility despite each material phase being intrinsically incompressible, because it can rapidly leave the cranium (Levine, 2000). Oscillations at heart rate time scales are neglected and all quantities are averaged over a cardiac cycle.

This spherical symmetry is the simplest fully three-dimensional geometry that can be used to model the brain. Yet, due to symmetry, only one spatial direction, namely the radial direction, needs to be considered, leaving us with comparatively simple partial differential equations. A lot of computational work is saved for simulations, since only one spatial dimension needs to be discretised (compare with chapter 4). In addition, this geometry allows to quickly examine the qualitative influence of adaptations of the governing equations to the system as a whole.

The spine is responsible for a large part of the total compliance of the craniospinal system, for about one-third according to Matsumoto et al. (1986), while Löfgren and Zwetnow (1973) even ascribe the majority of the volume change to the spinal compartment. Nevertheless, the mechanism with which the spine accommodates additional CSF is similar to that in the brain parenchyma, by displacement of venous blood (Czosnyka et al., 2004). Hence, not including a spinal compartment in the model is only expected to change the interpretation of the compliance, as the value used here has to account for both, spinal and cranial compliances. As most former authors, we will thus ignore the spine in our model, but note that coupling the spherically symmetric model of the brain with spinal models, such as the one-dimensional tube-law models by Cirovic (2009); Cirovic and Kim (2010, 2012), is an interesting direction for future research.

Another simplification is that flow through the aqueduct of Sylvius is modelled as steady Poiseuille flow, dependent only on the pressure difference between the ventricle and the subarachnoid space. Tully and Ventikos (2009) coupled a fully three-dimensional computational fluid dynamics (CFD) model of the aqueduct to a similar spherically symmetric poroelastic model of the brain. They showed that the displacements for a partially obstructed aqueduct are significantly smaller than for a uniform constriction. However, the shape of the displacement curve over time does not change, hence an intermediate aqueduct diameter would probably yield a very similar solution.

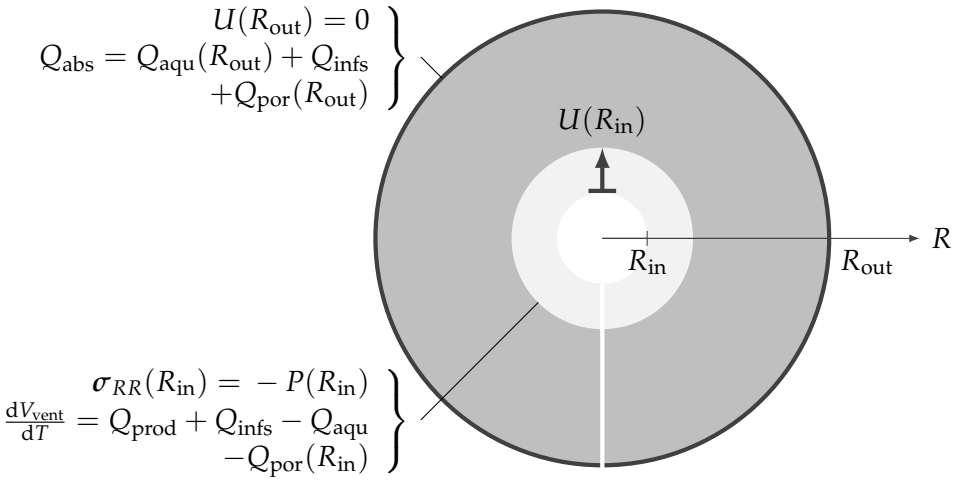

Figure 3.4: Spherically symmetric poroelastic model with boundary conditions.

3.4.2 Spherically symmetric geometry

We model the brain parenchyma as a spherical shell with outer radius R_{out} containing a single concentric ventricle of radius R_{in} (Figure 3.4). For details on tensor computations in spherical coordinates, the reader is referred to the literature, for example Coussy (2004, Appendix A.3) or Batchelor (1967, Appendix 2). In these coordinates, we obtain

$$\nabla \boldsymbol{u} = \begin{pmatrix} \frac{\partial U}{\partial R} & \frac{1}{R}\left(\frac{\partial U}{\partial \theta} - U_\theta\right) & \frac{1}{R}\left(\sin\theta\,\frac{\partial U}{\partial \varphi} - U_\varphi\right) \\ \frac{\partial U_\theta}{\partial R} & \frac{1}{R}\left(\frac{\partial U_\theta}{\partial \theta} + U\right) & \frac{1}{R}\left(\frac{1}{\sin\theta}\,\frac{\partial U_\theta}{\partial \varphi} - \cot\theta\, U_\varphi\right) \\ \frac{\partial U_\varphi}{\partial R} & \frac{1}{R}\,\frac{\partial U_\varphi}{\partial \theta} & \frac{1}{R}\left(\frac{1}{\sin\theta}\,\frac{\partial U_\varphi}{\partial \varphi} - \cot\theta\, U_\theta + U\right) \end{pmatrix} . \tag{3.49}$$

Due to spherical symmetry, displacements in θ- and φ-direction, as well as derivatives along these directions are zero

$$\boldsymbol{u} = U e_R + 0 e_\theta + 0 e_\varphi\,, \qquad \frac{\partial(\cdot)}{\partial \theta} = 0\,, \qquad \frac{\partial(\cdot)}{\partial \varphi} = 0\,, \tag{3.50}$$

so that $\nabla \boldsymbol{U}$ and the deformation gradient (3.2) are diagonal

$$\nabla \boldsymbol{U} = \operatorname{diag}\left(\frac{\partial U}{\partial R}, \frac{U}{R}, \frac{U}{R}\right) , \qquad \boldsymbol{F} = \operatorname{diag}\left(1 + \frac{\partial U}{\partial R}, 1 + \frac{U}{R}, 1 + \frac{U}{R}\right) . \tag{3.51}$$

Hence, the same holds for the linear strain tensor (3.3)

$$\boldsymbol{\mathcal{E}} = \frac{1}{2}\left(\nabla \boldsymbol{U} + \nabla \boldsymbol{U}^T\right) = \operatorname{diag}\left(\frac{\partial U}{\partial R}, \frac{U}{R}, \frac{U}{R}\right) \tag{3.52}$$

and the volume dilation (3.4), the trace of the strain tensor, is

$$\epsilon = \operatorname{tr}(\boldsymbol{\mathcal{E}}) = \frac{\partial U}{\partial R} + 2\frac{U}{R} . \tag{3.53}$$

This can be integrated to obtain an expression for the displacements from the volume dilation

$$U(R, T) = \frac{1}{R^2}\left(\int_{R_\star}^{R} s^2 \epsilon(s, T) \mathrm{d}s + U_\star R_\star^2\right) \tag{3.54}$$

with suitable constants $U_\star, R_\star$ to satisfy a boundary condition.

Since the pressure gradient and thus the flux (3.5) only have radial components

$$\boldsymbol{Q} = -\frac{\kappa(\epsilon)}{\eta}\nabla P = -\frac{\kappa(\epsilon)}{\eta}\left(\frac{\partial P}{\partial R} e_R + 0 e_\theta + 0 e_\varphi\right) , \tag{3.55}$$

the following spherical version of the fluid volume balance (3.8) is obtained

$$\frac{\partial \zeta}{\partial T} = -\nabla \cdot \boldsymbol{Q} = \frac{1}{R^2}\frac{\partial}{\partial R}\left(R^2 \frac{\kappa(\epsilon)}{\eta}\frac{\partial P}{\partial R}\right) . \tag{3.56}$$

The stress tensor (3.10) becomes diagonal as well

$$\boldsymbol{\sigma} = \operatorname{diag}\begin{pmatrix} \lambda\epsilon + 2\mu\frac{\partial U}{\partial R} - \alpha P \\ \lambda\epsilon + 2\mu\frac{U}{R} - \alpha P \\ \lambda\epsilon + 2\mu\frac{U}{R} - \alpha P \end{pmatrix} = \operatorname{diag}\begin{pmatrix} (\lambda + 2\mu)\frac{\partial U}{\partial R} + 2\lambda\frac{U}{R} - \alpha P \\ \lambda\frac{\partial U}{\partial R} + 2(\lambda + \mu)\frac{U}{R} - \alpha P \\ \lambda\frac{\partial U}{\partial R} + 2(\lambda + \mu)\frac{U}{R} - \alpha P \end{pmatrix} . \tag{3.57}$$

Again due to spherical symmetry, the terms in $\nabla \cdot \sigma$ simplify to

$$\nabla \cdot \sigma = \left(\frac{\partial \sigma_{RR}}{\partial R} + \frac{1}{R} \left(2\sigma_{RR} - \sigma_{\theta\theta} - \sigma_{\varphi\varphi} \right) \right) e_R + 0e_\theta + 0e_\varphi \tag{3.58}$$

with

$$\frac{\partial \sigma_{RR}}{\partial R} = (\lambda + 2\mu) \frac{\partial^2 U}{\partial R^2} + \frac{2\lambda}{R} \frac{\partial U}{\partial R} - 2\lambda \frac{U}{R^2} - \alpha \frac{\partial P}{\partial R} , \tag{3.59}$$

$$\frac{1}{R} \left(2\sigma_{RR} - \sigma_{\theta\theta} - \sigma_{\varphi\varphi} \right) = \frac{4\mu}{R} \left(\frac{\partial U}{\partial R} - \frac{U}{R} \right) . \tag{3.60}$$

Thus, the equation for the conservation of momentum obtained is

$$0 = (\nabla \cdot \sigma)_R = (\lambda + 2\mu) \left(\frac{\partial^2 U}{\partial R^2} + \frac{2}{R} \frac{\partial U}{\partial R} - \frac{2U}{R^2} \right) - \alpha \frac{\partial P}{\partial R} . \tag{3.61}$$

Using (3.7) and (3.53) in (3.56) and (3.61), respectively, yields the final set of equations for the volume dilation and the pressure

$$0 = (\lambda + 2\mu) \frac{\partial \epsilon}{\partial R} - \alpha \frac{\partial P}{\partial R} , \tag{3.62}$$

$$\alpha \frac{\partial \epsilon}{\partial T} + \frac{\partial}{\partial T} (\gamma(P) P) = \frac{1}{R^2} \frac{\partial}{\partial R} \left(R^2 \frac{\kappa(\epsilon)}{\eta} \frac{\partial P}{\partial R} \right) , \tag{3.63}$$

coupled with equation (3.54) for the displacements.

3.4.3 Boundary conditions

We want to use physiologically meaningful boundary conditions, particularly fluid volume conservation rather than given pressures, as set out first in Smillie et al. (2005). An alternative version with pressure boundary conditions will be used as well to validate the numerical scheme in section 4.6.

The outside of the brain is attached to the skull, rigid in adults, via arachnoid and dura mater. We neglect the small thickness of the subarachnoid space as justified

by Levine (2000, Appendix A6). Thus, the displacements at the outer radius are assumed to be zero

$$U(R_{\text{out}}, T) = 0 \, . \tag{3.64}$$

Inserting this into the equation for the displacements (3.54), we obtain the following expression

$$U(R, T) = -\frac{1}{R^2} \int_R^{R_{\text{out}}} s^2 \epsilon(s, T) \mathrm{d}s \, , \tag{3.65}$$

which will be inserted into the other boundary conditions to obtain integral-boundary conditions with respect to the strain.

The normal stress in the tissue at the ventricle wall ($R = R_{\text{in}}$) has to balance the pressure inside the ventricle

$$-P = \sigma_{RR} = \lambda\epsilon + 2\mu \left(\epsilon - 2\frac{U}{R} \right) - \alpha P = (\lambda + 2\mu)\epsilon - 4\mu \frac{U}{R} - \alpha P \, , \tag{3.66}$$

so that

$$(\lambda + 2\mu)\epsilon - 4\mu \frac{U}{R} + (1 - \alpha)P = 0 \, . \tag{3.67}$$

We want to ensure CSF volume conservation both inside the ventricle and at the skull. Assuming the volume of the subarachnoid space to be constant and given zero displacement of the brain tissue, all fluid that is flowing into the subarachnoid space through the aqueduct of Sylvius, Q_{aqu}, seeping out of the tissue, $Q_{\text{por}}(R_{\text{out}})$, or injected into the subarachnoid or the spine, $Q_{\text{infs}}(T)$, has to be absorbed into

venous blood via the arachnoid villi, Q_{abs}. Hence, at the outer boundary $R = R_{\text{out}}$,

$$\begin{aligned}\underbrace{\frac{P - P_{\text{sag}}(T)}{\mathcal{R}}}_{Q_{\text{abs}}} = &+ \underbrace{\frac{\pi d^4}{128\eta L}\left[P(R_{\text{in}}, T) - P(R_{\text{out}}, T)\right]}_{Q_{\text{aqu}}} \\ &\underbrace{-4\pi R_{\text{out}}^2 \frac{\kappa(\epsilon)}{\eta}\frac{\partial P}{\partial R}}_{Q_{\text{por}}(R_{\text{out}})} + Q_{\text{infs}}(T)\ .\end{aligned} \tag{3.68}$$

The absorption, Q_{abs}, of CSF is modelled proportional to the pressure difference between intracranial pressure and sagittal sinus pressure, as in chapter 2. The total amount of CSF flowing from the porous tissue into the subarachnoid space, $Q_{\text{por}}(R_{\text{out}})$, equals the integral of the radial Darcy velocity of the fluid integrated over the outer area of the brain. For simplicity, the flow through the aqueduct of Sylvius, Q_{aqu}, is modelled as Poiseuille flow.

For the fluid volume balance inside the ventricle, we consider the change of its volume given by the displacements of the ventricle wall

$$\begin{aligned}\frac{\mathrm{d}V_{\text{vent}}}{\mathrm{d}T} &= \frac{\mathrm{d}}{\mathrm{d}T}\left(\left[\frac{4}{3}\pi(R_{\text{in}} + U(R_{\text{in}}, T))^3\right]\right) \\ &= 4\pi(R_{\text{in}} + U(R_{\text{in}}, T))^2 \left.\frac{\partial U}{\partial T}\right|_{R_{\text{in}}} \approx 4\pi R_{\text{in}}^2 \left.\frac{\partial U}{\partial T}\right|_{R_{\text{in}}},\end{aligned} \tag{3.69}$$

where the last term is a linearised approximation, valid for small deformations. The change in ventricle volume needs to accommodate the difference between inflow via CSF production, Q_{prod}, and a possible intraventricular infusion, $Q_{\text{infv}}(T)$, with the outflow through the aqueduct, Q_{aqu}, and into the porous tissue, $Q_{\text{por}}(R_{\text{in}})$.

Thus, the volume balance at $R = R_{\text{in}}$ is

$$4\pi R_{\text{in}}^2 \frac{\partial U}{\partial T} = Q_{\text{prod}} + Q_{\text{infv}}(T) - \underbrace{\left(-4\pi R_{\text{in}}^2 \frac{\kappa(\epsilon)}{\eta} \frac{\partial P}{\partial R}\right)}_{Q_{\text{por}}(R_{\text{in}})} - \underbrace{\frac{\pi d^4}{128\eta L} \left[P(R_{\text{in}}, T) - P(R_{\text{out}}, T)\right]}_{Q_{\text{aqu}}} . \tag{3.70}$$

In addition, a shunt, draining CSF from the ventricle either into the subarachnoid space or to another place in the body, could easily be added to the description.

Alternatively to the flow boundary conditions (3.68) and (3.70), the pressures inside the ventricle (at $R = R_{\text{in}}$) and in the subarachnoid space (at $R = R_{\text{out}}$) can be specified directly

$$P(R_{\text{in}}, T) = P_{\text{in}}(T) , \qquad P(R_{\text{out}}, T) = P_{\text{out}}(T) . \tag{3.71}$$

3.4.4 Non-dimensionalisation

To non-dimensionalise the system, define the dimensionless variables and parameters

$$\rho = \frac{R_{\text{in}}}{R_{\text{out}}} , \quad r = \frac{R}{R_{\text{out}}} , \quad t = \frac{T}{T_0} , \quad \varepsilon(r,t) = \frac{\epsilon(R,T)}{\epsilon_0} , \quad u(r,t) = \frac{U(R,T)}{\epsilon_0 R_{\text{out}}} , \tag{3.72}$$

with suitable constants T_0, ϵ_0. Thus, for any function w

$$\frac{\partial w}{\partial R} = \frac{1}{R_{\text{out}}} \frac{\partial w}{\partial r} , \qquad \frac{\partial w}{\partial T} = \frac{1}{T} \frac{\partial w}{\partial t} . \tag{3.73}$$

This yields the same differential equation for the dimensionless volume dilation and displacements as for their dimensional counterparts (3.53)

$$\varepsilon = \frac{\partial u}{\partial r} + 2\frac{u}{r} , \tag{3.74}$$

so that, as in (3.65),

$$u(r,t) = \frac{1}{r^2}\int_r^1 z^2 \varepsilon(z,t)\mathrm{d}z \,. \tag{3.75}$$

For the pressure, we first integrate (3.62) with respect to R and obtain

$$P(R,T) = \frac{\lambda+2\mu}{\alpha}\epsilon(R,T) + P_\mathrm{c}(T) \,, \tag{3.76}$$

with a spatially constant pressure $P_\mathrm{c}(T)$. Defining

$$P_0 = \frac{\lambda+2\mu}{\alpha}\epsilon_0 \,, \qquad p(r,t) = \frac{P(R,T)}{P_0} \,, \qquad p_\mathrm{c}(r,t) = \frac{P_\mathrm{c}(R,T)}{P_0} \,, \tag{3.77}$$

we obtain

$$p(r,t) = \varepsilon(r,t) + p_\mathrm{c}(t) \,, \qquad\qquad \frac{\partial p}{\partial r} = \frac{\partial \varepsilon}{\partial r} \,. \tag{3.78}$$

Inserting this into equation (3.63) for the fluid volume balance yields

$$a\frac{\partial \varepsilon}{\partial t} + b(p)\frac{\partial p}{\partial t} = a\frac{\partial \varepsilon}{\partial t} + b(p)\left(\frac{\partial \varepsilon}{\partial t} + \frac{\mathrm{d}p_\mathrm{c}}{\mathrm{d}t}\right) = \frac{1}{r^2}\frac{\partial}{\partial r}\left(r^2 k(\varepsilon)\frac{\partial \varepsilon}{\partial r}\right) \,, \tag{3.79}$$

with dimensionless permeability from (3.6)

$$k(\varepsilon) = \frac{\kappa(\epsilon)}{\kappa_0} = \exp(M\varepsilon) \,, \qquad \text{with} \qquad M = M_0\epsilon_0 \,, \tag{3.80}$$

and

$$a = \frac{\alpha^2\eta R_\mathrm{out}^2}{(\lambda+2\mu)\kappa_0 T_0} \,, \qquad b(p) = \frac{\eta R_\mathrm{out}^2}{\kappa_0 T_0}\left(\gamma(P_0 p) + P_0 p \left.\frac{\mathrm{d}\gamma}{\mathrm{d}P}\right|_{P_0 p}\right) \,. \tag{3.81}$$

Given a differentiable specific compliance $\gamma(P)$, we can easily compute the dimensionless $b(p)$. Similarly, we can integrate this equation and obtain the specific compliance from $b(p)$

$$\gamma(P) = \frac{1}{P}\left(\frac{\kappa_0 T_0 P_0}{\eta R_\mathrm{out}^2}\int b(p)\mathrm{d}p + C_\gamma\right) \tag{3.82}$$

up to an integration constant C_γ.

Non-dimensionalising the boundary conditions (3.67), (3.68) and (3.70), we get

$$0 = \varepsilon(\rho,t) - c_1 u(\rho,t) + (1-\alpha)p_c(t)\ , \tag{3.83}$$

$$\left.\frac{\partial u}{\partial t}\right|_{(\rho,t)} = c_2 k(\varepsilon)\left.\frac{\partial \varepsilon}{\partial r}\right|_{(\rho,t)} - c_3\left(\varepsilon(\rho,t) - \varepsilon(1,t)\right) + \frac{1}{\rho^2}\left(q_{\text{prod}} + q_{\text{infv}}(t)\right)\ , \tag{3.84}$$

$$\begin{aligned} 0 = {} & c_4 k(\varepsilon)\left.\frac{\partial \varepsilon}{\partial r}\right|_{(1,t)} - c_5\varepsilon(\rho,t) + (1+c_5)\,\varepsilon(1,t) \\ & + p_c(t) - p_{\text{sag}}(t) - c_6 q_{\text{infs}}(t)\ , \end{aligned} \tag{3.85}$$

or alternatively from the pressure boundary conditions (3.71),

$$p(\rho,t) = p_{\text{in}}(t)\ , \qquad p(1,t) = p_{\text{out}}(t)\ . \tag{3.86}$$

with the constants

$$c_1 = \frac{4\alpha\mu}{(\lambda+2\mu)\rho}\ , \qquad c_2 = \frac{(\lambda+2\mu)\kappa_0 T_0}{\alpha\eta R_{\text{out}}^2}\ , \qquad c_3 = \frac{(\lambda+2\mu)d^4 T_0}{512\alpha\eta L R_{\text{in}}^2 R_{\text{out}}}\ , \tag{3.87}$$

$$c_4 = 4\pi\frac{\kappa_0}{\eta}\mathcal{R}R_{\text{out}}\ , \qquad c_5 = \frac{\pi d^4\mathcal{R}}{128\eta L}\ , \qquad c_6 = \frac{\alpha\mathcal{R}Q_0}{(\lambda+2\mu)\epsilon_0}\ , \tag{3.88}$$

$$Q_0 = \frac{4\pi\epsilon_0 R_{\text{out}}^3}{T_0}\ , \tag{3.89}$$

and the dimensionless fluxes

$$q_{\text{prod}} = \frac{Q_{\text{prod}}}{Q_0}\ , \qquad q_{\text{infv}} = \frac{Q_{\text{infv}}}{Q_0}\ , \qquad q_{\text{infs}} = \frac{Q_{\text{infs}}}{Q_0}\ . \tag{3.90}$$

3.4.5 Steady state case

The steady state case is considered here to gain insight into the behaviour of solutions and will be used to produce initial conditions for the time-dependent problem which satisfy the boundary conditions. In addition, steady state solutions can be used to model changes over long time-scales, such as for the development

of obstructive hydrocephalus (Smillie et al., 2005). For $\frac{\partial}{\partial t}(\cdot) = 0$, equation (3.79) becomes

$$0 = \frac{\mathrm{d}}{\mathrm{d}r}\left(r^2 k(\varepsilon)\frac{\mathrm{d}\varepsilon}{\mathrm{d}r}\right) . \tag{3.91}$$

Constant permeability

For $M = 0$, that is with constant permeability $k(\varepsilon) \equiv 1$, solutions are of the form

$$\varepsilon(r) = \frac{a_1}{r} + a_2 . \tag{3.92}$$

This implies for the pressure (3.78) and displacements (3.75)

$$p(r) = \frac{a_1}{r} + (a_2 + p_\mathrm{c}) , \qquad u(r) = \frac{a_1}{2}\left(1 - \frac{1}{r^2}\right) + \frac{a_2}{3}\left(r - \frac{1}{r^2}\right) . \tag{3.93}$$

The dependency of the functions on the integration parameters is linear. For constant permeability, all boundary conditions are linear as well, thus the integration parameters can be found by solving a small linear system of equations for either set of boundary conditions. This means, that for constant permeability, the problem is well posed.

Combining the stress boundary condition (3.83) with pressure boundary conditions (3.86), the integration parameters can be computed as

$$\begin{aligned} a_1 &= \frac{\rho}{1-\rho}\left(p_\mathrm{in} - p_\mathrm{out}\right) , \quad a_2 = \frac{c_1 \frac{a_1}{2}\left(1 - \frac{1}{\rho^2}\right) - \frac{a_1}{\rho} + (1-\alpha)\left(a_1 - p_\mathrm{out}\right)}{\alpha - \frac{c_1}{3}\left(\rho - \frac{1}{\rho^2}\right)} , \\ p_\mathrm{c} &= p_\mathrm{out} - a_1 - a_2 . \end{aligned} \tag{3.94}$$

For example, the derivative of the pressure or strain, defined by the first integration constant a_1 is determined only by the pressure difference and an extra factor describing the geometry of the problem.

For stress and flow boundary conditions (3.83)–(3.85), a_1 is determined by the total flow rate from the ventricle to the subarachnoid space via the volume balance (3.84)

$$a_1 = \frac{q_{\text{prod}} + q_{\text{infv}}}{c_2 + c_3\rho(1-\rho)} \,. \tag{3.95}$$

For the other two integration constants, we define an intermediate constant

$$a_3 = p_{\text{sag}} + c_6 q_{\text{infs}} + a_1 \cdot \left(c_4 + c_5 \cdot \left(\frac{1}{\rho} - 1 \right) - 1 \right) \,, \tag{3.96}$$

which yields

$$a_2 = \frac{\frac{c_1 a_1}{2}\left(1 - \frac{1}{\rho^2}\right) - \frac{a_1}{\rho} - (1-\alpha)a_3}{\alpha - \frac{c_1}{3}\left(\rho - \frac{1}{\rho^2}\right)} \,, \qquad p_{\text{c}} = a_3 - a_2 \,. \tag{3.97}$$

Example solutions of this problem for different pressure boundary conditions are shown in Figure 3.5.

Exponential permeability

For exponential permeability with $M > 0$, the steady state equation (3.91) is equivalent to

$$\begin{aligned} 0 = \frac{\mathrm{d}}{\mathrm{d}r}\left(r^2 k(\varepsilon) \frac{\mathrm{d}\varepsilon}{\mathrm{d}r} \right) &= 2rk(\varepsilon)\frac{\mathrm{d}\varepsilon}{\mathrm{d}r} + r^2 \frac{\mathrm{d}k}{\mathrm{d}\varepsilon}\left(\frac{\mathrm{d}\varepsilon}{\mathrm{d}r}\right)^2 + r^2 k(\varepsilon)\frac{\mathrm{d}^2\varepsilon}{\mathrm{d}r^2} \\ &= \underbrace{r\exp(M\varepsilon)}_{>0} \cdot \left[2\frac{\mathrm{d}\varepsilon}{\mathrm{d}r} + Mr\left(\frac{\mathrm{d}\varepsilon}{\mathrm{d}r}\right)^2 + r\frac{\mathrm{d}^2\varepsilon}{\mathrm{d}r^2} \right] . \end{aligned} \tag{3.98}$$

Both the radius and the exponential term are strictly positive, thus the volume dilation $\varepsilon(r)$ has to satisfy

$$2\frac{\mathrm{d}\varepsilon}{\mathrm{d}r} + Mr\left(\frac{\mathrm{d}\varepsilon}{\mathrm{d}r}\right)^2 + r\frac{\mathrm{d}^2\varepsilon}{\mathrm{d}r^2} = 0 \,. \tag{3.99}$$

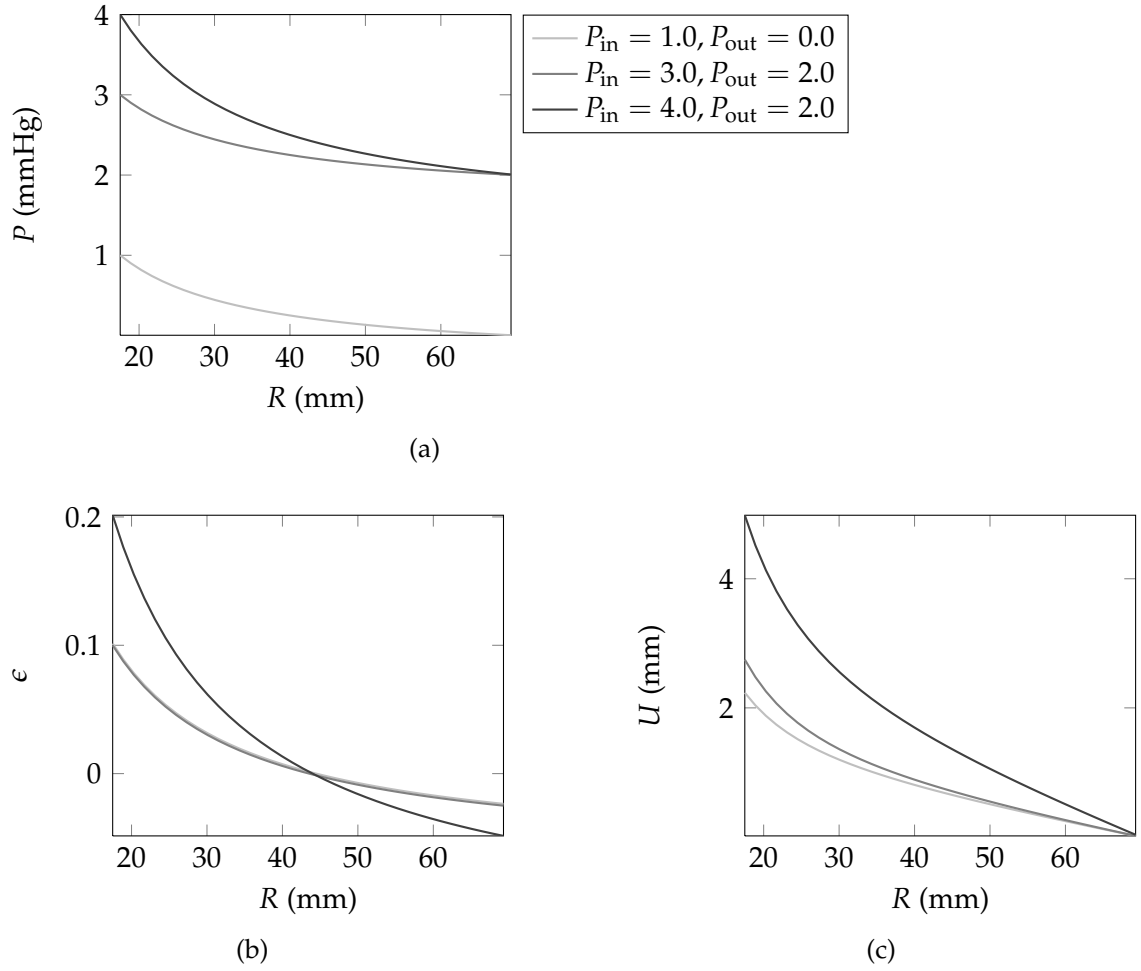

Figure 3.5: Analytic solutions to the steady state, spherically symmetric, poroelastic model problem for different sets of pressure boundary conditions with constant permeability: (a) pressure, (b) volume dilation, (c) displacements.

In this case, solutions have the general form

$$\varepsilon(r) = \frac{1}{M} \ln \left| \frac{a_1}{r} + a_2 \right| \ , \tag{3.100}$$

where continuity requires that a_2 cannot lie between $-a_1$ and $-\frac{a_1}{\rho}$. This leads to pressures (3.78) and displacements (3.75) of the form

$$p(r) = \frac{1}{M} \ln \left| \frac{a_1}{r} + a_2 \right| + p_c \ , \tag{3.101}$$

$$\begin{aligned} u(r) = \frac{1}{6Ma_2^3 r^2} \Big[& a_1 a_2^2 r^2 - 2a_1^2 a_2 r - 2a_1^3 \ln \left| \frac{a_1}{r} \right| \\ & + 2 \left(r^3 a_2^3 + a_1^3 \right) \ln \left| \frac{a_1}{r} + a_2 \right| + a_3 \Big] \ , \end{aligned} \tag{3.102}$$

with

$$a_3 = 2a_1^2 a_2 - a_1 a_2^2 + 2a_1^3 \ln |a_1| - 2(a_2^3 + a_1^3) \ln |a_1 + a_2| \ . \tag{3.103}$$

In this case, the integration constants clearly have non-linear influence on the solutions. Existence or uniqueness of solutions are not guaranteed, but for small M, that is when the permeability changes only very slightly from its default value with the volume dilation, the solution is expected to be close to the solution of the above problem with constant permeability, thus in particular, we expect a solution to exist and be well behaved with respect to the boundary conditions.

3.5 Multi-fluid poroelastic model of the brain

3.5.1 Motivation for multi-fluid poroelastic modelling of the brain

Poroelastic models of the brain were first developed to describe the onset and development of hydrocephalus, a process that lasts days, weeks or even months. Single-fluid poroelastic models, neglecting oscillations at heart rate, were completely sufficient for that purpose. When considering the infusion test, which lasts only minutes, those oscillations are clearly visible, become more important and should be included in the analysis.

Wirth and Sobey (2009, Appendix A) derived the equations for a multi-fluid poroelastic model of the brain as a generalisation to Biot (1941), with several disconnected fluid networks inside the same porous elastic matrix, interacting only indirectly via the solid. Those fluid networks describe CSF, arterial and venous blood. Later, Tully and Ventikos (2011) proposed a slightly different model of the brain, employing Multiple-Network Poroelastic Theory (MPET), which models fluid in several communicating networks of different porosities and permeabilities. The two models are compared in 3.5.5. Since we are not concerned with the details of blood flow and volume throughout the parenchyma and want to keep the number of additional material parameters low, we will assume no fluid transfer between the blood and CSF networks and follow the description in Wirth and Sobey (2009).

3.5.2 Three-fluid poroelastic governing equations

The assumptions for the multi-fluid poroelastic model derived in Wirth and Sobey (2009) are very similar to those for the poroelastic model described in section 3.2: homogeneity and isotropy; reversible, small deformations; a linear stress-strain relation; Darcy flow of the CSF phase through the solid matrix; and zero body forces. Pressure oscillations at heart rate will be explicitly included via the arterial blood pressure. Nevertheless, Wirth and Sobey (2009) claim, following scale analysis, that for physiological parameter values inertial terms are negligible even at this time scale. Note that their analysis included only the velocity of the solid phase, but the CSF velocity relative to the solid is very low and hardly influenced by arterial pressure oscillations. We therefore neglect inertial terms in the multi-fluid poroelastic model as well. Since in this model all fluid compartments of the brain are included, incompressibility not only of the fluids, but also of the solid phase can be assumed.

Following a similar argument to Biot (1941), Wirth and Sobey (2009) assume the existence of an energy potential to obtain symmetry in the equations and arrive at the following governing equations for a multi-fluid poroelastic model with three fluids: CSF (no subscript), arterial blood (subscript a) and venous and capillary blood (subscript v)

$$\boldsymbol{\sigma} = \boldsymbol{\sigma}_{\mathrm{s}} - \alpha P \boldsymbol{I} - \alpha_{\mathrm{a}} P_{\mathrm{a}} \boldsymbol{I} - \alpha_{\mathrm{v}} P_{\mathrm{v}} \boldsymbol{I} \,, \tag{3.104}$$

$$\zeta = \alpha \epsilon + \gamma P - \gamma_{\mathrm{a}} P_{\mathrm{a}} - \gamma_{\mathrm{v}} P_{\mathrm{v}} \,, \tag{3.105}$$

$$\zeta_{\mathrm{a}} = \alpha_{\mathrm{a}} \epsilon - \gamma_{\mathrm{a}} P + \gamma_{\mathrm{aa}} P_{\mathrm{a}} - \gamma_{\mathrm{av}} P_{\mathrm{v}} \,, \tag{3.106}$$

$$\zeta_{\mathrm{v}} = \alpha_{\mathrm{v}} \epsilon - \gamma_{\mathrm{v}} P - \gamma_{\mathrm{av}} P_{\mathrm{a}} + \gamma_{\mathrm{vv}} P_{\mathrm{v}} \,, \tag{3.107}$$

where the solid stress is given by Hooke's law, as in (3.10)

$$\boldsymbol{\sigma}_{\mathrm{s}} = (\lambda\epsilon\boldsymbol{I} + 2\mu\boldsymbol{\mathcal{E}}) \, . \tag{3.108}$$

As for a traditional single-fluid poroelastic material, the pressures are measured with respect to a reference pressure, at which the solid is stress-free (compare with 3.2.4).

Blood vessels are often described via so-called tube laws, relating their cross-sectional area with the transmural pressure, that is the pressure difference between the fluid inside and outside of the vessel (Cirovic et al., 2003). The cross-sectional area can be easily translated into the increase in arterial or venous blood content, $\zeta_{\mathrm{a}}, \zeta_{\mathrm{v}}$, so that for constant volume dilation, equations (3.106) and (3.107) should be of the form

$$\zeta_{\mathrm{a}} = \tilde{\gamma}_{\mathrm{a}} \cdot (P_{\mathrm{a}} - P) \, , \qquad \zeta_{\mathrm{v}} = \tilde{\gamma}_{\mathrm{v}} \cdot (P_{\mathrm{v}} - P) \, , \tag{3.109}$$

where the storage compliances $\tilde{\gamma}_{\mathrm{a}}, \tilde{\gamma}_{\mathrm{v}}$ could in general be pressure-dependent. This implies

$$\tilde{\gamma}_{\mathrm{a}} = \gamma_{\mathrm{aa}} = \gamma_{\mathrm{a}} \, , \qquad \tilde{\gamma}_{\mathrm{v}} = \gamma_{\mathrm{vv}} = \gamma_{\mathrm{v}} \, , \qquad \gamma_{\mathrm{av}} = 0 \, . \tag{3.110}$$

Arteries are normally distended so that their volume change is governed by the tensile stiffness of the artery wall. Thus, the tube law for arteries is usually expressed linearly (Cirovic et al., 2003) and the specific compliance for arterial blood, γ_{a}, is small. We neglect cerebral autoregulation, the active control of cerebral blood flow within a certain pressure range by actively constricting or dilating arterial walls within seconds of a pressure change (Aaslid et al., 1989), since it is not sufficiently quantified. Veins on the other hand, can be in distended or partially collapsed state. They undergo much larger volume changes with

changes in transmural pressure governed by a non-linear tube law (Wirth and Sobey, 2008). This implies a pressure dependent specific venous blood compliance larger than that for arterial blood

$$\gamma_{\mathrm{v}}(P_{\mathrm{v}} - P) > \gamma_{\mathrm{a}} \,. \tag{3.111}$$

Incompressibility of all phases implies that the total volume change in a volume element of the material is equal to the sum of the fluid volume changes within that element. Therefore, summing equations (3.105)–(3.107) yields

$$\epsilon = \zeta + \zeta_{\mathrm{a}} + \zeta_{\mathrm{v}} = (\alpha_{\mathrm{a}} + \alpha + \alpha_{\mathrm{v}}) \cdot \epsilon + (\gamma - \gamma_{\mathrm{a}} - \gamma_{\mathrm{v}}) \cdot P \,, \tag{3.112}$$

so that

$$\alpha + \alpha_{\mathrm{a}} + \alpha_{\mathrm{v}} = 1 \,, \qquad\qquad \gamma = \gamma_{\mathrm{a}} + \gamma_{\mathrm{v}} \,. \tag{3.113}$$

This means in particular that the specific CSF compliance is pressure dependent.

The specific compliances $\gamma, \gamma_{\mathrm{a}}, \gamma_{\mathrm{v}}$ can be related to their respective Biot–Willis parameters $\alpha, \alpha_{\mathrm{a}}, \alpha_{\mathrm{v}}$, Skempton's coefficients $\beta, \beta_{\mathrm{a}}, \beta_{\mathrm{v}}$, and the bulk modulus $K = \lambda + \frac{2\mu}{3}$ via

$$\gamma = \frac{1 - \alpha\beta}{\beta K}\alpha \,, \qquad \gamma_{\mathrm{a}} = \frac{1 - \alpha_{\mathrm{a}}\beta_{\mathrm{a}}}{\beta_{\mathrm{a}} K}\alpha_{\mathrm{a}} \,, \qquad \gamma_{\mathrm{v}} = \frac{1 - \alpha_{\mathrm{v}}\beta_{\mathrm{v}}}{\beta_{\mathrm{v}} K}\alpha_{\mathrm{v}} \,. \tag{3.114}$$

Comparing the specific CSF compliance at normal pressure, γ, multiplied by the parenchyma volume to the total cranial compliance, approximating β by 1, and keeping in mind that α is expected to lie above the value 0.83 (Wirth and Sobey, 2006), Wirth and Sobey (2009) obtain an estimate of $\alpha \approx 0.9995$. Similarly, comparing the specific arterial blood compliance with the tube law given in Cirovic et al. (2003), for $\beta_{\mathrm{a}} \approx 1$, the arterial blood Biot–Willis parameter, α_{a}, can be estimated to be of the order of magnitude of 10^{-5}, so that we obtain $\alpha_{\mathrm{a}} < \alpha_{\mathrm{v}} \ll \alpha$.

3.5.3 Simplification to the two-fluid model

Following Wirth and Sobey (2009), we simplify the three-fluid model to a two-fluid model, described in Sobey et al. (2010, 2012), considering only the influence of arterial blood pressure oscillations on CSF pressure and flow. Pressure waves travel at a speed of the order of $10\,\mathrm{m/s}$ through the large cerebral arteries (Giller and Aaslid, 1994). For time scales down to the heart rate, we can therefore safely assume that arterial blood pressure is spatially constant. In addition, we assume the venous blood pressure to be roughly constant. In 3.2.4, we argued that the reference pressure is close to venous blood pressure and in 3.5.2, we derived that the venous blood Biot–Willis parameter α_v is small. Thus, the term $\alpha_\mathrm{v} P_\mathrm{v} \boldsymbol{I}$ in (3.104) can be neglected and we obtain

$$\boldsymbol{\sigma} = \boldsymbol{\sigma}_\mathrm{s} - \alpha P \boldsymbol{I} - \alpha_\mathrm{a} P_\mathrm{a} \boldsymbol{I} \,. \tag{3.115}$$

Since ζ in (3.105) describes the increase in CSF with respect to a reference state, constant venous blood pressure can be eliminated by resetting the reference value for ζ

$$\zeta = \alpha \epsilon + \gamma P - \gamma_\mathrm{a} P_\mathrm{a} \,. \tag{3.116}$$

Inserting this into the equations for conservation of momentum (3.11) and of fluid volume (3.8) yields

$$0 = \nabla \cdot (\lambda \epsilon \boldsymbol{I} + 2\mu \boldsymbol{\mathcal{E}} - \alpha P \boldsymbol{I}) - \underbrace{\nabla \cdot (\alpha_\mathrm{a} P_\mathrm{a} \boldsymbol{I})}_{=0} \,, \tag{3.117}$$

$$\alpha \frac{\partial \epsilon}{\partial T} + \frac{\partial}{\partial T}(\gamma(P) P) = \nabla \cdot \left(\frac{\kappa(\epsilon)}{\eta} \nabla P \right) + \gamma_\mathrm{a} \frac{\partial P_\mathrm{a}}{\partial T} \,. \tag{3.118}$$

The only difference to the single-fluid poroelastic model (3.12), (3.9) is the source term in the CSF volume balance describing the influence of arterial blood pressure oscillations.

In spherical symmetry, these equations are

$$0 = (\lambda + 2\mu)\frac{\partial \epsilon}{\partial R} - \alpha \frac{\partial P}{\partial R} \,, \tag{3.119}$$

$$\alpha \frac{\partial \epsilon}{\partial T} + \frac{\partial}{\partial T}(\gamma(P)P) = \frac{1}{R^2}\frac{\partial}{\partial R}\left(R^2 \frac{\kappa(\epsilon)}{\eta}\frac{\partial P}{\partial R}\right) + \gamma_\mathrm{a}\frac{\partial P_\mathrm{a}}{\partial T} \,. \tag{3.120}$$

An extra term for the arterial blood pressure also needs to be included in the stress boundary condition

$$0 = (\lambda + 2\mu)\epsilon - 4\mu\frac{U}{R} + (1-\alpha)P - \alpha_\mathrm{a} P_\mathrm{a} \,. \tag{3.121}$$

The flow boundary conditions (3.68)–(3.70) or pressure boundary conditions (3.71) can be reused without change.

Defining the dimensionless arterial blood pressure and the respective specific storage

$$p_\mathrm{a}(t) = \frac{P_\mathrm{a}(T)}{P_0} \,, \qquad\qquad b_\mathrm{a} = \frac{\eta R_\mathrm{out}^2}{\kappa_0 T_0}\gamma_\mathrm{a} \,, \tag{3.122}$$

we can non-dimensionalise these equations in the same way as the single-fluid model in 3.4.4. The full problem for $\varepsilon(r,t)$ and $p_\mathrm{c}(t)$ is repeated here for convenience

$$a\frac{\partial \varepsilon}{\partial t} + b(p)\left(\frac{\partial \varepsilon}{\partial t} + \frac{\mathrm{d}p_\mathrm{c}}{\mathrm{d}t}\right) = \frac{1}{r^2}\frac{\partial}{\partial r}\left(r^2 \exp(M\varepsilon)\frac{\partial \varepsilon}{\partial r}\right) + b_\mathrm{a}\frac{\mathrm{d}p_\mathrm{a}}{\mathrm{d}t} \,, \tag{3.123}$$

with boundary conditions

$$0 = \varepsilon(\rho,t) - c_1 u(\rho,t) + (1-\alpha)p_\mathrm{c}(t) - \alpha_\mathrm{a} p_\mathrm{a}(t) \,, \tag{3.124}$$

$$\left.\frac{\partial u}{\partial t}\right|_{(\rho,t)} = c_2 k(\varepsilon)\left.\frac{\partial \varepsilon}{\partial r}\right|_{(\rho,t)} - c_3\left(\varepsilon(\rho,t) - \varepsilon(1,t)\right) + \frac{1}{\rho^2}\left(q_\mathrm{prod} + q_\mathrm{infv}(t)\right) \,, \tag{3.125}$$

$$\begin{aligned} 0 = {} & c_4 k(\varepsilon)\left.\frac{\partial \varepsilon}{\partial r}\right|_{(1,t)} - c_5\varepsilon(\rho,t) + (1+c_5)\,\varepsilon(1,t) \\ & + p_\mathrm{c}(t) - p_\mathrm{sag}(t) - c_6 q_\mathrm{infs}(t) \,, \end{aligned} \tag{3.126}$$

or pressure boundary conditions alternative to the latter two

$$p(\rho, t) = p_{\text{in}}(t) \,, \qquad p(1, t) = p_{\text{out}}(t) \,, \tag{3.127}$$

and expressions for the dimensionless displacements and CSF pressure

$$u(r, t) = \frac{1}{r^2} \int_r^1 z^2 \varepsilon(z, t) \mathrm{d}z \,, \qquad \varepsilon = \frac{\partial u}{\partial r} + 2\frac{u}{r} \,, \tag{3.128}$$

$$p(r, t) = \varepsilon(r, t) + p_{\text{c}}(t) \,, \qquad \frac{\partial p}{\partial r} = \frac{\partial \varepsilon}{\partial r} \,. \tag{3.129}$$

3.5.4 Space average two-fluid model

The spherically symmetric single-fluid poroelastic model has been related to single-compartment models described in chapter 2 by Sobey and Wirth (2006); Wirth and Sobey (2009). The same derivation can be executed with the two-fluid poroelastic model, similar to our description in Sobey et al. (2012).

We start by integrating the local CSF volume balance (3.120) over the parenchyma volume

$$V_{\text{par}} = \int_{R_{\text{in}}}^{R_{\text{out}}} 4\pi R^2 \mathrm{d}R \tag{3.130}$$

to obtain

$$\begin{aligned} &\int_{R_{\text{in}}}^{R_{\text{out}}} 4\pi R^2 \alpha \frac{\partial \epsilon}{\partial T} \mathrm{d}R + \int_{R_{\text{in}}}^{R_{\text{out}}} 4\pi R^2 \frac{\partial}{\partial T}(\gamma(P)P) \mathrm{d}R \\ &\qquad = \int_{R_{\text{in}}}^{R_{\text{out}}} 4\pi \frac{\partial}{\partial R}\left(R^2 \frac{\kappa(\epsilon)}{\eta} \frac{\partial P}{\partial R} \right) \mathrm{d}R + \int_{R_{\text{in}}}^{R_{\text{out}}} 4\pi R^2 \gamma_{\text{a}} \frac{\partial P_{\text{a}}}{\partial T} \mathrm{d}R \,. \end{aligned} \tag{3.131}$$

For the first term on the left hand side, interchanging integration and differentiation, using the fact, following from (3.53), that

$$\frac{\partial}{\partial R}\left(R^2 U \right) = R^2 \epsilon \,, \tag{3.132}$$

and remembering that the displacement is zero at the outer boundary, we obtain

$$\begin{aligned}\int_{R_{\text{in}}}^{R_{\text{out}}} 4\pi R^2 \alpha \frac{\partial \epsilon}{\partial T} \mathrm{d}R &= \frac{\mathrm{d}}{\mathrm{d}T}\left(\int_{R_{\text{in}}}^{R_{\text{out}}} 4\pi \alpha R^2 \epsilon \mathrm{d}R\right) \\ &= \alpha \frac{\mathrm{d}}{\mathrm{d}T}\left(4\pi \int_{R_{\text{in}}}^{R_{\text{out}}} \frac{\partial\left(R^2 U\right)}{\partial R} \mathrm{d}R\right) = -\alpha \frac{\mathrm{d}V_{\text{vent}}}{\mathrm{d}T} \,.\end{aligned} \tag{3.133}$$

For the second term on the left hand side, we again interchange integration and differentiation. In addition, we assume the pressure to be almost spatially constant and define the average CSF pressure, P_{avg}, over the parenchyma. Indeed, the pressure drop between the ventricles and the subarachnoid space is negligible compared to the average pressure as long as the aqueduct is sufficiently open. Thus, we obtain

$$\begin{aligned}\int_{R_{\text{in}}}^{R_{\text{out}}} 4\pi R^2 \frac{\partial}{\partial T}(\gamma(P)P) \mathrm{d}R &= \frac{\mathrm{d}}{\mathrm{d}T}\left(\int_{R_{\text{in}}}^{R_{\text{out}}} 4\pi R^2 \gamma(P) P \mathrm{d}R\right) \\ &\approx \frac{\mathrm{d}}{\mathrm{d}T}\left(\int_{R_{\text{in}}}^{R_{\text{out}}} 4\pi R^2 \gamma(P_{\text{avg}}) P_{\text{avg}} \mathrm{d}R\right) = V_{\text{par}} \frac{\mathrm{d}}{\mathrm{d}T}\left(\gamma(P_{\text{avg}}) P_{\text{avg}}\right) \\ &= V_{\text{par}}\left(P_{\text{avg}} \left.\frac{\mathrm{d}\gamma}{\mathrm{d}P}\right|_{P_{\text{avg}}} + \gamma(P_{\text{avg}})\right) \frac{\mathrm{d}P_{\text{avg}}}{\mathrm{d}T} \,.\end{aligned} \tag{3.134}$$

The first term on the right hand side of (3.131) can be integrated directly and yields

$$\begin{aligned}\int_{R_{\text{in}}}^{R_{\text{out}}} 4\pi \frac{\partial}{\partial R}\left(R^2 \frac{\kappa(\epsilon)}{\eta} \frac{\partial P}{\partial R}\right) \mathrm{d}R &= 4\pi \left[R^2 \frac{\kappa(\epsilon)}{\eta} \frac{\partial P}{\partial R}\right]_{R_{\text{in}}}^{R_{\text{out}}} \\ &= 4\pi R_{\text{out}}^2 \left.\frac{\kappa(\epsilon)}{\eta} \frac{\partial P}{\partial R}\right|_{R_{\text{out}}} - 4\pi R_{\text{in}}^2 \left.\frac{\kappa(\epsilon)}{\eta} \frac{\partial P}{\partial R}\right|_{R_{\text{in}}} .\end{aligned} \tag{3.135}$$

Combining this with the flow boundary conditions (3.68) and (3.70), we obtain

$$\begin{aligned}&\int_{R_{\text{in}}}^{R_{\text{out}}} 4\pi \frac{\partial}{\partial R}\left(R^2 \frac{\kappa(\epsilon)}{\eta} \frac{\partial P}{\partial R}\right) \mathrm{d}R = \\ &\qquad \text{‘} = Q_{\text{prod}} + Q_{\text{inf}}(T) - \frac{P - P_{\text{sag}}(t)}{\mathcal{R}} - \frac{\mathrm{d}V_{\text{vent}}}{\mathrm{d}T} \,.\end{aligned} \tag{3.136}$$

The final term, relating to arterial blood pressure oscillations, can again just be integrated

$$\int_{R_{\text{in}}}^{R_{\text{out}}} 4\pi R^2 \gamma_{\text{a}} \frac{\partial P_{\text{a}}}{\partial T} \mathrm{d}R = V_{\text{par}} \gamma_{\text{a}} \frac{\mathrm{d}P_{\text{a}}}{\mathrm{d}T} \,. \tag{3.137}$$

Now, we can insert all of these terms into (3.131), assuming the average pressure throughout the parenchyma

$$\begin{aligned}(1-\alpha)\frac{\mathrm{d}V_{\mathrm{vent}}}{\mathrm{d}T} + V_{\mathrm{par}}\left(P_{\mathrm{avg}}\left.\frac{\mathrm{d}\gamma}{\mathrm{d}P}\right|_{P_{\mathrm{avg}}} + \gamma(P_{\mathrm{avg}})\right)\frac{\mathrm{d}P_{\mathrm{avg}}}{\mathrm{d}T} \\ = Q_{\mathrm{prod}} + Q_{\mathrm{inf}}(T) - \frac{P_{\mathrm{avg}} - P_{\mathrm{sag}}(T)}{\mathcal{R}} + V_{\mathrm{par}}\gamma_{\mathrm{a}}\frac{\mathrm{d}P_{\mathrm{a}}}{\mathrm{d}T}\ .\end{aligned} \tag{3.138}$$

For $\alpha = 1$, the term from the change in ventricle volume is cancelled. For α close to 1 it is likely small and the equation becomes

$$\begin{aligned}V_{\mathrm{par}}\left(P_{\mathrm{avg}}\left.\frac{\mathrm{d}\gamma}{\mathrm{d}P}\right|_{P_{\mathrm{avg}}} + \gamma(P_{\mathrm{avg}})\right)\frac{\mathrm{d}P_{\mathrm{avg}}}{\mathrm{d}T} \\ = Q_{\mathrm{prod}} + Q_{\mathrm{inf}}(T) - \frac{P_{\mathrm{avg}} - P_{\mathrm{sag}}(T)}{\mathcal{R}} + V_{\mathrm{par}}\gamma_{\mathrm{a}}\frac{\mathrm{d}P_{\mathrm{a}}}{\mathrm{d}T}\ ,\end{aligned} \tag{3.139}$$

which is very similar to the single compartment model (2.7) in chapter 2.

First of all, the storage coefficient γ as a function of pressure can be related to the compliance function via

$$P\frac{\mathrm{d}\gamma}{\mathrm{d}P} + \gamma(P) = \frac{1}{V_{\mathrm{par}}}C(P)\ . \tag{3.140}$$

Remember that in this chapter, all pressures were measured with respect to the pressure, P_{sf}, at which the solid is stress-free, so we need to account for that when translating the compliance function. In particular, we will also measure the reference pressure, P_{r}, appearing in the compliance function with respect to the stress-free pressure. Since the specific compliance, γ, is mostly made up of the compliance of veins, we are essentially going backwards in the derivation of Wirth and Sobey (2008) for the generalised inverse power law for the compliance from collapsing veins. For the compliance function with general n, they proposed, we obtain

$$\gamma(P) = \frac{1}{P}\left(\frac{(P - P_{\mathrm{r}})^{1-n}}{(1-n)\tilde{e}V_{\mathrm{par}}} + a_1\right)\ , \tag{3.141}$$

with an undetermined integration constant, a_1, and for the special case $n = 1$,

$$\gamma(P) = \frac{1}{P}\left(\frac{\ln|P - P_\mathrm{r}|}{EV_\mathrm{par}} + a_1\right) . \tag{3.142}$$

Note however, that we actually do not need to know $\gamma(P)$ to solve the problem. Comparing the above differential equation (3.140) with the equation for the non-dimensional storage coefficient (3.81), we find that we can directly use the compliance in

$$b(p) = \frac{\eta R_\mathrm{out}^2}{\kappa_0 T_0 V_\mathrm{par}} C(P_0 p) . \tag{3.143}$$

This relation between the two models may help with the choice of parameter values for simulations of the spatially varying model.

The difference between the CSF volume balance (3.139) and the version (2.7) in chapter 2 is the last term. It relates CSF pressure oscillations, which were ignored in the single-compartment model, directly to arterial blood pressure oscillations, at the expense of only one extra parameter. Due to the different time scales, solving this ODE numerically will be computationally more expensive than the single-fluid version, but still much cheaper than the full spatially varying model. If the displacements or stresses are not required, this model may improve estimates of the cerebral compliance due to the extra information provided by the CSF and arterial blood pressure amplitudes. For the case of the standard compliance model 2.9, even an approximate closed form solution is given by Cieślicki (2007), who included the arterial blood pressure oscillations via an oscillating production rate and added a further term describing changes in the superior sagittal sinus pressure due to breathing.

3.5.5 Comparison with Tully and Ventikos (2011)

Tully and Ventikos (2011) adapted multiple-network poroelastic theory (MPET) models, described for example in detail by Berryman and Wang (1995) and mentioned by Coussy (2004) in the case of the double-porosity network, to provide a slightly different multi-fluid poroelastic model of the brain. Their model allows fluid transport between the different compartments, which they call fluid networks, but does not have pressure coupling between the fluids as the model by Wirth and Sobey (2009). Both models can be seen as different special cases of a more general multi-fluid poroelastic model, where the increase of fluid content in each network is linked to the other networks by both these effects:

$$\zeta_i = \alpha_i \epsilon + \gamma_{ii} P_i - \sum_{j \neq i} \gamma_{ij} P_j \,, \tag{3.144}$$

$$\frac{\partial \zeta_i}{\partial T} = \nabla \cdot \left(\frac{\kappa}{\eta} \nabla P_i \right) + \sum_{j \neq i} \dot{s}_{j \to i} \,. \tag{3.145}$$

In Wirth and Sobey (2009), the fluid transfer between networks is zero, that is all $\dot{s}_{j \to i} = 0$, whereas in Tully and Ventikos (2011), the non-diagonal specific compliances are neglected, $\gamma_{ij} = 0$, for $j \neq i$.

Any type of flow rates $\dot{s}_{j \to i}$ could be inserted in equation (3.145), such as passive diffusion across a membrane or even active biological transport processes, as soon as qualitative models for those become available. Similarly, the specific compliances γ_{ij} in (3.144) could in theory be pressure and time dependent. One of the simplest examples of a full model would be given if all specific compliances are constant and the flow rates between networks depend linearly on the pressure difference, $\dot{s}_{j \to i} = k_{ij}(P_j - P_i)$, as considered by Tully and Ventikos (2011). In that

case, the general model for the fluid volume balance in network i would be

$$\alpha_i \frac{\partial \epsilon}{\partial T} + \gamma_{ii} \frac{\partial P_i}{\partial T} - \sum_{j \neq i} \gamma_{ij} \frac{\partial P_j}{\partial T} = \nabla \cdot \left(\frac{\kappa}{\eta} \nabla P_i \right) + \sum_{j \neq i} k_{ij} (P_j - P_i) \ . \tag{3.146}$$

3.6 Note on large deformations

The linearised equations (3.3)–(3.4) used in this chapter are only valid for small deformations. In particular, the model could attain a volume dilation below $\epsilon = -1$ at finite stress, which implies negative element volume and is unphysical. Hence, the bounds for the flow rate in the planar model in section 3.3, (3.45) and (3.48), are only theoretical bounds and the model may break down earlier already.

In Wirth et al. (2012), we carried out an analysis on a similar planar poroelastic problem to that in section 3.3, relating the energy functions of several linear and non-linear hyperelastic models in combination with different permeability models to the flux under large deformations. Depending on this combination, the flux can be either unlimited, have a limiting value for increasing pressure difference, or be choked, that is reach zero, already at a finite pressure difference. As opposed to section 3.3, that analysis is limited to the case of zero pressure at the fixed end.

For the infusion test, the small deformation assumption is expected to be satisfied and the current formulation to be sufficient. If simulation results arise that do predict large deformations those should be viewed very cautiously. Given the simplified geometry, all our simulation results are only qualitative in any case.

Few non-linear poroelastic models of the brain exist. Taylor and Miller (2004) use a linear stress-strain relationship within a large deformation poroelastic framework

for their model of the development of hydrocephalus. First attempts to include non-linear stress-strain relations, have also been made. García and Smith (2009) model drug delivery through a small sphere of brain parenchyma by coupling an advective-diffuse mass transport equation to the poroelastic flow. The solid is modelled with a hyperelastic isotropic energy function of the form

$$W = \sum_{k=1}^{N} \frac{\mu_k}{\alpha_k} \left(\lambda_r^{\alpha_k} + 2\lambda_\theta^{\alpha_k} - 3 - \alpha_k \ln(J) \right) + \frac{\mu'}{2}(J-1)^2$$

for the radial and circumferential stretch ratios λ_r and λ_θ, respectively. The material parameters μ_k, α_k and μ' can be adjusted to the required shape of the stress-strain curve. A comparison of two choices of material parameters with analytic small strain solutions clearly shows the divergence of the two models at higher loads.

The biggest obstruction to a reliable, fully non-linear, poroelastic description of the brain is still the fact that the constitutive equations of the brain are unknown due to the lack of exact in-vivo measurements of displacements, permeabilities and pressures in the brain under different conditions. To make matters worse, the material parameters likely differ between patients, spatially, with age, or even at short time-scales due to biological effects such as cerebral autoregulation. Advances in non-invasive in vivo measurements of viscoelastic and poroelastic tissue parameters may help overcome these limitations in the future (Klatt et al., 2007; Green et al., 2008; Sánchez et al., 2010; Perriñez et al., 2010; Shahim et al., 2010).

Chapter 4

Finite element simulations of poroelastic infusion test models

Contents

4.1 Introduction

We want to simulate the spherically symmetric, two-fluid poroelastic model of CSF flow through the brain parenchyma described in section 3.5 during the infusion test. For this purpose we need to solve equation (3.123) for $t \in [0, t_{\max}]$ and $r \in [\rho, 1]$, together with flow type boundary conditions (3.124)–(3.126) or pressure type boundary conditions (3.124), (3.127).

The finite element method is a standard method for the solution of partial differential equations. Literature for (linear) steady state problems is readily available (Süli and Mayers, 2006; Braess, 2007; Elman et al., 2008). For time dependent problems, the method of lines approach (Brenan et al., 1989; Hesthaven and Warburton, 2008) is often used, that is, only the spatial variables are discretised, resulting in a system of ordinary differential equations (ODEs). Together with discretised boundary conditions, this often leads to a system of differential algebraic equations (DAEs) with a singular mass matrix, as will be the case here. We also consider how to formulate these algebraic boundary conditions as differential equations in such a way that errors in these algebraic equations decay in time.

In section 4.2, we set out the weak form of the steady state and time dependent problems. The space domain discretisation with respect to the radius is derived in section 4.3. The treatment of the boundary conditions is described in section 4.4 and some details of the solution of the discretised problems are given in section 4.5. Finally, we present numerical tests to validate the discretisation in section 4.6.

4.2 Weak formulation

4.2.1 Steady state case

The steady state version of the final, non-dimensionalised, multi-fluid poroelastic differential equation (3.123) is the same as that for the single-fluid model (3.91). Following the analysis in 3.4.5, solutions exist for the case of constant permeability. Since the production rates we consider are small, so are the volume dilations. Thus, even for the exponential permeability function, we will stay close to the constant

permeability case and thus expect solutions to exist. As the system is second order in space, existence of classical solutions implies the existence of weak solutions in the Sobolev space $H^1([\rho,1])$.

To obtain the weak form of (3.91), we multiply the equation with a test function $\varphi \in H_0^1([\rho,1]) = \{\varphi \in H^1([\rho,1]) \mid \varphi(\rho) = \varphi(1) = 0\}$ and integrate over the radius. Using the divergence theorem, we obtain

$$0 = \int_\rho^1 \frac{\mathrm{d}}{\mathrm{d}r}\left(r^2 \exp(M\varepsilon)\frac{\mathrm{d}\varepsilon}{\mathrm{d}r}\right)\varphi \mathrm{d}r = -\int_\rho^1 r^2 \exp(M\varepsilon)\frac{\mathrm{d}\varepsilon}{\mathrm{d}r}\frac{\mathrm{d}\varphi}{\mathrm{d}r}\mathrm{d}r =: \mathcal{A}(\varepsilon;\varphi)\ , \quad (4.1)$$

defining the non-linear operator $\mathcal{A} : H^1([\rho,1]) \times H_0^1([\rho,1]) \mapsto \mathbb{R}$.

We will later solve this equation using a Newton type iteration. So we need to compute the linearisation $\mathcal{DA}$ of $\mathcal{A}$. Let $\tilde{\varepsilon}$ have small norm $\|\tilde{\varepsilon}\|_{H^1} = \mathcal{O}(\delta)$ and consider

$$\begin{aligned}
\mathcal{A}(\varepsilon+\tilde{\varepsilon};\varphi) =& -\int_\rho^1 r^2 \exp(M(\varepsilon+\tilde{\varepsilon}))\frac{\mathrm{d}(\varepsilon+\tilde{\varepsilon})}{\mathrm{d}r}\frac{\mathrm{d}\varphi}{\mathrm{d}r}\mathrm{d}r \\
=& -\int_\rho^1 r^2 \exp(M\varepsilon)\left(1+M\tilde{\varepsilon}+\mathcal{O}(\delta^2)\right)\left(\frac{\mathrm{d}\varepsilon}{\mathrm{d}r}\frac{\mathrm{d}\varphi}{\mathrm{d}r}+\frac{\mathrm{d}\tilde{\varepsilon}}{\mathrm{d}r}\frac{\mathrm{d}\varphi}{\mathrm{d}r}\right)\mathrm{d}r \\
=& -\int_\rho^1 r^2 \exp(M\varepsilon)M\tilde{\varepsilon}\frac{\mathrm{d}\varepsilon}{\mathrm{d}r}\frac{\mathrm{d}\varphi}{\mathrm{d}r}\mathrm{d}r - \int_\rho^1 r^2 \exp(M\varepsilon)\frac{\mathrm{d}\tilde{\varepsilon}}{\mathrm{d}r}\frac{\mathrm{d}\varphi}{\mathrm{d}r}\mathrm{d}r \\
&+ \mathcal{A}(\varepsilon;\varphi) + \mathcal{O}(\delta^2)\ .
\end{aligned} \quad (4.2)$$

Thus, we define

$$\mathcal{DA}(\varepsilon;\tilde{\varepsilon},\varphi) := -\int_\rho^1 r^2 \exp(M\varepsilon)M\tilde{\varepsilon}\frac{\mathrm{d}\varepsilon}{\mathrm{d}r}\frac{\mathrm{d}\varphi}{\mathrm{d}r}\mathrm{d}r - \int_\rho^1 r^2 \exp(M\varepsilon)\frac{\mathrm{d}\tilde{\varepsilon}}{\mathrm{d}r}\frac{\mathrm{d}\varphi}{\mathrm{d}r}\mathrm{d}r\ . \quad (4.3)$$

4.2.2 Time dependent case

For the time dependent problem, we will employ the method of lines (Brenan et al., 1989), where only space is discretised and which leads to a system of ODEs. For

ease of notation, from now on, we will use $\dot{w}$ as notation for all time derivatives, both for partial $\left(\frac{\partial w}{\partial t}\right)$ and ordinary ones $\left(\frac{\mathrm{d}w}{\mathrm{d}t}\right)$. A proof of existence of solutions is beyond the scope of this thesis because several special cases may need to be considered. For example, numerical experiments have shown that the solution can explode if the pressure-dependent storage coefficient, $b(p)$, diverges. In the models considered here this happens if the CSF pressure approaches the reference pressure, p_r, see 3.5.4.

We multiply the time dependent PDE (3.123) by r^2 and by a test function $\varphi \in H_0^1([\rho, 1])$ as above and integrate over the radius

$$\begin{aligned} &\int_\rho^1 r^2 \left(a\dot{\varepsilon} + b(\varepsilon + p_\mathrm{c})\left(\dot{\varepsilon} + \dot{p}_\mathrm{c}\right)\right)\varphi \mathrm{d}r \\ &= \int_\rho^1 \frac{\partial}{\partial r}\left(r^2 \exp(M\varepsilon)\frac{\partial \varepsilon}{\partial r}\right)\varphi + r^2 b_\mathrm{a}\dot{p}_\mathrm{a}\varphi \mathrm{d}r \,. \end{aligned} \tag{4.4}$$

The left hand side can be split into the contributions of $\dot{\varepsilon}$ and $\dot{p}_\mathrm{c}$

$$\begin{aligned} &\int_\rho^1 r^2 \left(a\dot{\varepsilon} + b(\varepsilon + p_\mathrm{c})\left(\dot{\varepsilon} + \dot{p}_\mathrm{c}\right)\right)\varphi \mathrm{d}r \\ &\quad = \int_\rho^1 r^2 \left(a + b(\varepsilon + p_\mathrm{c})\right)\dot{\varepsilon}\varphi \mathrm{d}r + \dot{p}_\mathrm{c}\int_\rho^1 r^2 b(\varepsilon + p_\mathrm{c})\varphi \mathrm{d}r \\ &\quad =: \mathcal{L}(\varepsilon, p_\mathrm{c}; \dot{\varepsilon}, \dot{p}_\mathrm{c}, \varphi) \,. \end{aligned} \tag{4.5}$$

The divergence theorem is again employed for the first term of the right hand side and we obtain

$$\begin{aligned} &\int_\rho^1 \frac{\partial}{\partial r}\left(r^2 \exp(M\varepsilon)\frac{\partial \varepsilon}{\partial r}\right)\varphi + r^2 b_\mathrm{a}\dot{p}_\mathrm{a}\varphi \mathrm{d}r \\ &\quad = -\int_\rho^1 r^2 \exp(M\varepsilon)\frac{\partial \varepsilon}{\partial r}\frac{\partial \varphi}{\partial r}\mathrm{d}r + b_\mathrm{a}\dot{p}_\mathrm{a}\int_\rho^1 r^2\varphi \mathrm{d}r \\ &\quad =: \mathcal{B}(\varepsilon; \dot{p}_\mathrm{a}, \varphi) \,. \end{aligned} \tag{4.6}$$

In the implementation, we will take advantage of the fact that the contributions of ε and $\dot{p}_\mathrm{a}$ are additive and that $\mathcal{B}(\varepsilon; 0, \varphi) = \mathcal{A}(\varepsilon; \varphi)$. The overall equation is

$$\mathcal{L}(\varepsilon, p_\mathrm{c}; \dot{\varepsilon}, \dot{p}_\mathrm{c}, \varphi) = \mathcal{B}(\varepsilon; \dot{p}_\mathrm{a}, \varphi) \,. \tag{4.7}$$

The CSF compliance has only been measured for the whole brain, usually even including the compliance of the spine. Changes of blood flow in some parts of the brain are likely to influence blood flow in other parts as well. In addition, with an open aqueduct of Sylvius, we expect only a small spatial gradient in the pressure and hence in the compliance $b(\varepsilon + p_c)$. So, similar to 3.5.4, we model the compliance to be spatially constant and defined by the spatially averaged pressure, $p_{avg} = \varepsilon_{avg} + p_c$,

$$b(\varepsilon + p_c) \approx b(\varepsilon_{avg} + p_c) =: b_{avg} \, . \tag{4.8}$$

Combining (3.81) and (3.140), we obtain the specific compliance from the compliance function C of single compartment models

$$b_{avg} = \frac{\eta R_{out}^2}{\kappa_0 T_0 V_{par}} C(P_0 \cdot (\varepsilon_{avg} + p_c) + P_{sf}) \, . \tag{4.9}$$

Thus, the differential operator (4.5) can be simplified by taking the specific storage out of the integral

$$\mathcal{L}(\varepsilon, p_c; \dot{\varepsilon}, \dot{p}_c, \varphi) = \left(a + b_{avg}\right) \int_\rho^1 r^2 \dot{\varepsilon} \varphi \mathrm{d}r + \dot{p}_c b_{avg} \int_\rho^1 r^2 \varphi \mathrm{d}r \, . \tag{4.10}$$

4.3 Spatial discretisation

4.3.1 Nodes and basis functions

With a permeability as small as in brain tissue, we expect steep gradients in the boundary regions. Thus, the nodes need to be concentrated close to the boundaries. For this purpose, we define a cubic stretch, S_3, of the unit interval and by applying

this twice, a ninth-order stretch, S_9,

$$S_3(x) := (3-2x)x^2 \,, \qquad S_9(x) := (S_3 \circ S_3)(x) = S_3(S_3(x)) \,. \tag{4.11}$$

Defining a uniform distribution of the unit interval $x_i := \frac{i}{N}$ with N elements and $N+1$ nodes, this can be transformed to a cubically stretched, non-uniform mesh on the interval $[\rho, 1]$ via

$$r_i := \rho + (1-\rho)S_3(x_i) = \rho + (1-\rho)S_3\left(\frac{i}{N}\right) \,, \tag{4.12}$$

or a 9^{th}-order stretched mesh via

$$r_i := \rho + (1-\rho)S_9(x_i) = \rho + (1-\rho)S_9\left(\frac{i}{N}\right) \,, \tag{4.13}$$

so that in each case $\rho = r_0 < r_1 < \cdots < r_{N-1} < r_N = 1$ (Figure 4.1a). Given the nodes, we can define the step sizes $h_i := r_i - r_{i-1}$.

On this mesh, piecewise linear basis functions are defined as

$$\varphi_k(r) := \begin{cases} \frac{1}{h_k}(r - r_{k-1}) \,, & \text{for } r_{k-1} \le r \le r_k \,, \\ \frac{1}{h_{k+1}}(r_{k+1} - r) \,, & \text{for } r_k < r \le r_{k+1} \,, \\ 0 \,, & \text{otherwise,} \end{cases} \tag{4.14}$$

for $k = 0, \ldots, N$ (Figure 4.1b). Their weak derivatives are piecewise constant

$$\frac{\mathrm{d}\varphi_k}{\mathrm{d}r}(r) = \begin{cases} \frac{1}{h_k} \,, & \text{for } r_{k-1} \le r \le r_k \,, \\ -\frac{1}{h_{k+1}} \,, & \text{for } r_k < r \le r_{k+1} \,, \\ 0 \,, & \text{otherwise.} \end{cases} \tag{4.15}$$

These basis functions span finite-dimensional subspaces of $H^1([\rho, 1])$ and $H^1_0([\rho, 1])$

$$V^h := \operatorname{span}\{\varphi_k \,|\, k = 0, \ldots, N\} \subset H^1([\rho, 1]) \,, \tag{4.16}$$

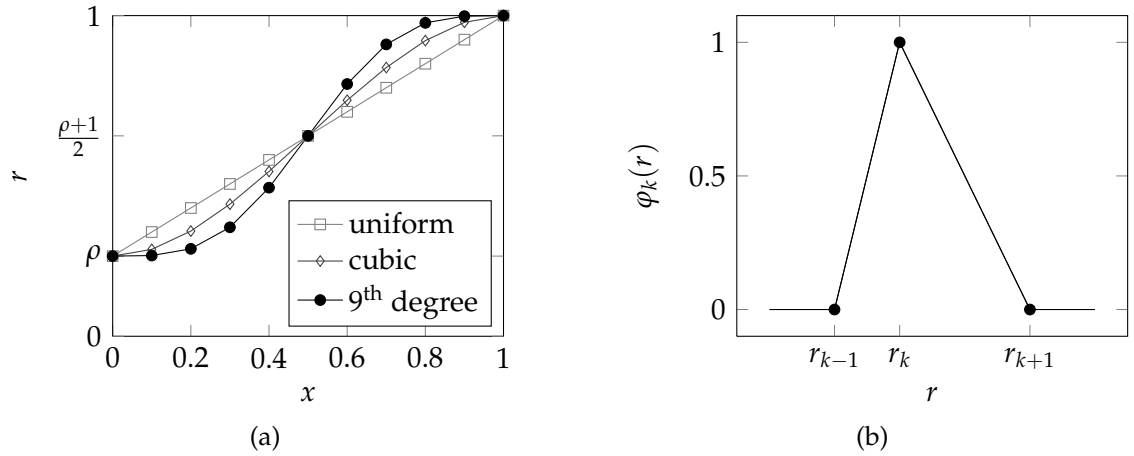

Figure 4.1: Spatial discretisation: (a) uniform, cubic and ninth degree distribution of nodes in the unit interval for $N = 10$. (b) piecewise linear basis function φ_k.

$$V_0^h := \operatorname{span}\{\varphi_k \,|\, k = 1, \ldots, N-1\} = V^h \cap H_0^1([\rho, 1]) \,, \tag{4.17}$$

containing the piecewise linear functions on the mesh. Thus, we can approximate the strain ε as

$$\varepsilon(r) \approx \varepsilon^h(r) := \sum_{k=0}^{N} \varepsilon_k \varphi_k(r) \tag{4.18}$$

with constants ε_k in steady state, or

$$\varepsilon(r,t) \approx \varepsilon^h(r,t) := \sum_{k=0}^{N} \varepsilon_k(t) \varphi_k(r) \tag{4.19}$$

with functions $\varepsilon_k(t)$ in the time dependent problem.

4.3.2 Computing the displacements from piecewise linear volume dilation

For piecewise linear volume dilation ε^h, the displacements can be computed analytically by integrating (3.74) element wise. Given an interval $[r_-, r_+] \subset (0, 1]$

and a linear polynomial ε^h such that $\varepsilon^h(r_-) = \varepsilon_-$ and $\varepsilon^h(r_+) = \varepsilon_+$, we can write

$$\varepsilon^h(r) = a_1 r + a_2 \qquad \text{with} \qquad a_1 = \frac{\varepsilon_+ - \varepsilon_-}{r_+ - r_-}\,, \qquad a_2 = \frac{r_+\varepsilon_- - r_-\varepsilon_+}{r_+ - r_-}\,. \tag{4.20}$$

According to (3.54) the displacements solving the ODE

$$\frac{\partial u}{\partial r} + 2\frac{u}{r} = \varepsilon^h\,, \qquad\qquad u(r_+) = u_+\,, \tag{4.21}$$

satisfy

$$u(r) = \frac{1}{r^2}\left(\int_{r_+}^{r} \varepsilon^h(s)s^2 \mathrm{d}s + u_+ r_+^2\right) = u_+\frac{r_+^2}{r^2} + \frac{a_1}{4}\frac{r^4 - r_+^4}{r^2} + \frac{a_2}{3}\frac{r^3 - r_+^3}{r^2}\,. \tag{4.22}$$

At the left boundary, this yields

$$u_- = u_+\frac{r_+^2}{r_-^2} - \frac{(\varepsilon_+ - \varepsilon_-)\left(r_+^4 - r_-^4\right)}{4r_-^2\,(r_+ - r_-)} - \frac{(r_+\varepsilon_- - r_-\varepsilon_+)\left(r_+^3 - r_-^3\right)}{3r_-^2\,(r_+ - r_-)}\,. \tag{4.23}$$

Applying this on every interval for piecewise linear strain ε^h with $\varepsilon^h(r_k) = \varepsilon_k$ and using the boundary condition (3.64), that is $u(1) = 0$, we obtain a recursion formula for all $u_k = u(r_k), k = 0, \ldots, N$.

$$u_N = 0\,, \tag{4.24}$$

$$u_{k-1} = u_k\frac{r_k^2}{r_{k-1}^2} - \frac{(\varepsilon_k - \varepsilon_{k-1})\left(r_k^4 - r_{k-1}^4\right)}{4r_{k-1}^2(r_k - r_{k-1})} - \frac{(r_k\varepsilon_{k-1} - r_{k-1}\varepsilon_k)\left(r_k^3 - r_{k-1}^3\right)}{3r_{k-1}^2(r_k - r_{k-1})}\,. \tag{4.25}$$

In particular, this means that each u_j depends linearly on the values of ε_k and we can define the matrix containing these coefficients

$$\boldsymbol{Du}_{jk} = \frac{\partial u_j}{\partial \varepsilon_k}\,, \qquad\qquad (u_0\ \cdots\ u_N)^{\mathrm{T}} = \boldsymbol{Du}\,(\varepsilon_0\ \cdots\ \varepsilon_N)^{\mathrm{T}}\,. \tag{4.26}$$

Similarly, the time derivatives become

$$(\dot{u}_0\ \cdots\ \dot{u}_N)^{\mathrm{T}} = \boldsymbol{Du}\cdot(\dot{\varepsilon}_0\ \cdots\ \dot{\varepsilon}_N)^{\mathrm{T}} \tag{4.27}$$

and the spatial derivative can easily be obtained from (3.74)

$$\left.\frac{\partial u}{\partial r}\right|_{r=r_k} = \varepsilon_k - 2\frac{u_k}{r_k} \,. \tag{4.28}$$

4.3.3 Matrix system for steady state

In steady state, the Galerkin finite element solution $\varepsilon^h \in V^h$ is required to satisfy

$$\mathcal{A}(\varepsilon^h; \varphi) = 0 \qquad \forall \varphi \in V_0^h \,. \tag{4.29}$$

Since V_0^h is spanned by $\varphi_k, k = 1, \ldots, N-1$ and $\mathcal{A}$ is linear in φ, this is equivalent to

$$\mathcal{A}(\varepsilon^h; \varphi_j) = 0 \qquad \forall j = 1, \ldots, N-1 \,. \tag{4.30}$$

This is a system of $N-1$ non-linear equations for the coefficients $\varepsilon_k, k = 0, \ldots, N$ of ε^h in (4.18). We will solve these equations via a Newton type iteration. Thus for a given ε^h, we need to compute the correction step $\tilde{\varepsilon}^h := \sum_{k=0}^N \tilde{\varepsilon}_k \varphi_k$ satisfying the linear equations

$$\mathcal{DA}(\varepsilon^h; \tilde{\varepsilon}^h, \varphi) = -\mathcal{A}(\varepsilon^h; \varphi) \qquad \forall \varphi \in V_0^h \tag{4.31}$$

or

$$\mathcal{DA}(\varepsilon^h; \tilde{\varepsilon}^h, \varphi_j) = -\mathcal{A}(\varepsilon^h; \varphi_j) \qquad \forall j = 1, \ldots, N-1 \,. \tag{4.32}$$

Since the basis functions φ_k have local support, all integrals in $\mathcal{A}$ and $\mathcal{DA}$ in (4.30) and (4.32) are greatly simplified, so that

$$\mathcal{A}(\varepsilon^h, \varphi_j) = -\int_{r_{j-1}}^{r_j} r^2 \exp(M\varepsilon^h) \frac{\mathrm{d}\varepsilon^h}{\mathrm{d}r} \frac{\mathrm{d}\varphi_j}{\mathrm{d}r} \mathrm{d}r - \int_{r_j}^{r_{j+1}} r^2 \exp(M\varepsilon^h) \frac{\mathrm{d}\varepsilon^h}{\mathrm{d}r} \frac{\mathrm{d}\varphi_j}{\mathrm{d}r} \mathrm{d}r \,. \tag{4.33}$$

Within each element, ε^h is linear, so that its derivative is given by the values at

the two neighbouring nodes. The derivatives of the basis functions were given in (4.15). Defining the following shorthand notation

$$\begin{aligned} \mathcal{I}_j &:= \int_{r_{j-1}}^{r_j} r^2 \exp(M\varepsilon^h)\mathrm{d}r \,, \\ \mathcal{I}_j^{\mathrm{l}} &:= \int_{r_{j-1}}^{r_j} r^2 \exp(M\varepsilon^h)\varphi_{j-1}\mathrm{d}r \,, \qquad \mathcal{I}_j^{\mathrm{r}} := \int_{r_{j-1}}^{r_j} r^2 \exp(M\varepsilon^h)\varphi_j\mathrm{d}r \,, \end{aligned} \tag{4.34}$$

this becomes

$$\mathcal{A}(\varepsilon^h;\varphi_j) = -\frac{\varepsilon_j - \varepsilon_{j-1}}{h_j^2}\mathcal{I}_j + \frac{\varepsilon_{j+1}-\varepsilon_j}{h_{j+1}^2}\mathcal{I}_{j+1} \,, \tag{4.35}$$

Similarly, we derive

$$\begin{aligned} \mathcal{DA}(\varepsilon^h;\tilde{\varepsilon}^h,\varphi_j) = &-M\frac{\varepsilon_j-\varepsilon_{j-1}}{h_j^2}\left(\mathcal{I}_j^{\mathrm{l}}\tilde{\varepsilon}_{j-1} + \mathcal{I}_j^{\mathrm{r}}\tilde{\varepsilon}_j\right) \\ &+M\frac{\varepsilon_{j+1}-\varepsilon_j}{h_{j+1}^2}\left(\mathcal{I}_{j+1}^{\mathrm{l}}\tilde{\varepsilon}_j + \mathcal{I}_{j+1}^{\mathrm{r}}\tilde{\varepsilon}_{j+1}\right) \\ &-\frac{\tilde{\varepsilon}_j-\tilde{\varepsilon}_{j-1}}{h_j^2}\mathcal{I}_j + \frac{\tilde{\varepsilon}_{j+1}-\tilde{\varepsilon}_j}{h_{j+1}^2}\mathcal{I}_{j+1} \,. \end{aligned} \tag{4.36}$$

With these details, (4.32) can be reformulated as an under-determined matrix-vector equation

$$\boldsymbol{DA}^{\mathrm{ode}}(\boldsymbol{x})\tilde{\boldsymbol{x}} = \boldsymbol{A}^{\mathrm{ode}}(\boldsymbol{x}) \,, \tag{4.37}$$

with

$$\boldsymbol{x}_k = \begin{cases} \varepsilon_k \,, & \text{for } k = 0,\ldots,N \,, \\ p_{\mathrm{c}} \,, & \text{for } k = N+1 \,, \end{cases} \qquad \tilde{\boldsymbol{x}}_k = \begin{cases} \tilde{\varepsilon}_k \,, & \text{for } k = 0,\ldots,N \,, \\ \tilde{p}_{\mathrm{c}} \,, & \text{for } k = N+1 \,, \end{cases} \tag{4.38}$$

$$\boldsymbol{A}_j^{\mathrm{ode}}(\boldsymbol{x}) = \mathcal{A}(\varepsilon^h;\varphi_j) \,, \tag{4.39}$$

and $\boldsymbol{DA}_{jk}^{\mathrm{ode}}(\boldsymbol{x})$ being the total coefficient of $\tilde{\varepsilon}_k$ in (4.36) for $k = 0,\ldots,N$ and zero for $k = N+1$. As expected for piecewise linear finite elements, the matrix $\boldsymbol{DA}^{\mathrm{ode}}$ is highly sparse with only three non-zero elements per row (Figure 4.2a, p. 136).

The boundary conditions, considered in 4.4.1, will add three more rows, making the matrix square.

4.3.4 Matrix system for time-stepping

Similarly to the steady state, in the time dependent problem, we are looking for the Galerkin finite element solution $\varepsilon^h(r,t)$ as a linear combination of the basis functions (4.19), together with $p_c \in \mathbb{R}$ satisfying the appropriate differential equation (4.7) for all test functions

$$\mathcal{L}(\varepsilon^h, p_c; \dot{\varepsilon}^h, \dot{p}_c, \varphi) = \mathcal{B}(\varepsilon^h; \dot{p}_a, \varphi) \qquad \forall \varphi \in V_0^h \,, \tag{4.40}$$

which again due to linearity in the last argument of $\mathcal{L}$ and $\mathcal{B}$ is equivalent to

$$\mathcal{L}(\varepsilon^h, p_c; \dot{\varepsilon}^h, \dot{p}_c, \varphi_j) = \mathcal{B}(\varepsilon^h; \dot{p}_a, \varphi_j) \qquad \forall j = 1, \dots, N-1 \,. \tag{4.41}$$

Defining the inner product

$$\langle f, g \rangle := \int_\rho^1 r^2 f(r) g(r) \mathrm{d}r \,, \tag{4.42}$$

noticing that

$$\dot{\varepsilon}^h(r,t) = \frac{\partial}{\partial t}\left(\sum_{k=0}^{N} \varepsilon_k(t)\varphi_k(r)\right) = \sum_{k=0}^{N} \dot{\varepsilon}_k(t)\varphi_k(r) \tag{4.43}$$

and remembering the local support of φ_k, this can be written compactly as

$$\begin{aligned} \mathcal{L}(\varepsilon^h, p_c; \dot{\varepsilon}^h, \dot{p}_c, \varphi_j) &= \left(a + b^h_{\mathrm{avg}}\right) \sum_{k=0}^{N} \langle \varphi_k, \varphi_j \rangle \, \dot{\varepsilon}_k(t) + b^h_{\mathrm{avg}} \langle 1, \varphi_j \rangle \, \dot{p}_c(t) \\ &= \left(a + b^h_{\mathrm{avg}}\right) \sum_{k=j-1}^{j+1} \langle \varphi_k, \varphi_j \rangle \, \dot{\varepsilon}_k(t) + b^h_{\mathrm{avg}} \langle 1, \varphi_j \rangle \, \dot{p}_c(t) \,, \end{aligned} \tag{4.44}$$

while on the other hand

$$\mathcal{B}(\varepsilon^h; \dot{p}_\mathrm{a}, \varphi_j) = \boldsymbol{A}_j^{\mathrm{ode}}(\boldsymbol{x}(t)) + b_\mathrm{a} \left\langle 1, \varphi_j \right\rangle \dot{p}_\mathrm{a} =: \boldsymbol{B}_j^{\mathrm{pde}}(\boldsymbol{x}(t), \dot{p}_\mathrm{a}(t)) \,. \tag{4.45}$$

We can define the matrix $\boldsymbol{L}^{\mathrm{pde}}(\boldsymbol{x}(t))$ via

$$\boldsymbol{L}_{jk}^{\mathrm{pde}}(\boldsymbol{x}(t)) = \begin{cases} \left(a + b_{\mathrm{avg}}^h(t)\right) \left\langle \varphi_k, \varphi_j \right\rangle \,, & \text{for } k = j-1, j, j+1,\ j = 1, \ldots, N-1 \,, \\ b_{\mathrm{avg}}^h(t) \left\langle 1, \varphi_j \right\rangle \,, & \text{for } k = N+1 \,, \\ 0 \,, & \text{otherwise,} \end{cases} \tag{4.46}$$

and the time dependent vector

$$\boldsymbol{x}_k(t) = \begin{cases} \varepsilon_k(t) \,, & \text{for } k = 0, \ldots, N \,, \\ p_\mathrm{c}(t) \,, & \text{for } k = N+1 \,. \end{cases} \tag{4.47}$$

Thus (4.41) can be written as a matrix vector ODE

$$\boldsymbol{L}^{\mathrm{pde}}(\boldsymbol{x}(t))\ \dot{\boldsymbol{x}}(t) = \boldsymbol{B}^{\mathrm{pde}}(\boldsymbol{x}(t), \dot{p}_\mathrm{a}(t)) \,. \tag{4.48}$$

The sparsity pattern of $\boldsymbol{L}^{\mathrm{pde}}$ (Figure 4.3a, p. 140) is similar to that of $\boldsymbol{DA}^{\mathrm{ode}}$ (Figure 4.2a, p. 136), describing the correction step in the steady state problem, but there are extra non-zero elements in the last column for the time derivative of p_c. The boundary conditions closing this system are considered in 4.4.2.

4.4 Boundary conditions

4.4.1 Steady state boundary conditions

We consider two sets of boundary conditions. Both cases include stress continuity at the ventricle wall, (3.83), which yields for the steady state finite element approximation ε^h

$$\begin{aligned} 0 &= \varepsilon_0 - c_1 u_0 + (1-\alpha) p_c = \varepsilon_0 - c_1 \boldsymbol{D}\boldsymbol{u}_{0,0:N} \left(\varepsilon_0 \ \cdots \ \varepsilon_N\right)^T + (1-\alpha) p_c \\ &= \left(1 - c_1 \boldsymbol{D}\boldsymbol{u}_{00},\, -c_1 \boldsymbol{D}\boldsymbol{u}_{01},\, \cdots,\, -c_1 \boldsymbol{D}\boldsymbol{u}_{0N},\, (1-\alpha)\right)\boldsymbol{x} =: \boldsymbol{A}_1^{\mathrm{bc}}(\boldsymbol{x}) \,. \end{aligned} \tag{4.49}$$

The two flow boundary conditions, (3.84)–(3.85), yield

$$0 = c_2 \exp(M\varepsilon_0) \frac{\varepsilon_1 - \varepsilon_0}{h_1} - c_3 \left(\varepsilon_0 - \varepsilon_N\right) + \frac{1}{\rho^2} \left(q_{\mathrm{prod}} + q_{\mathrm{infv}}\right) =: \boldsymbol{A}_2^{\mathrm{bc}}(\boldsymbol{x}) \,, \tag{4.50}$$

$$\begin{aligned} 0 &= c_4 \exp(M\varepsilon_N) \frac{\varepsilon_N - \varepsilon_{N-1}}{h_N} - c_5 \varepsilon_0 + (1 + c_5)\, \varepsilon_N + p_c - p_{\mathrm{sag}} - c_6 q_{\mathrm{infs}} \\ &=: \boldsymbol{A}_3^{\mathrm{bc}}(\boldsymbol{x}) \,, \end{aligned} \tag{4.51}$$

whereas the alternative pressure boundary conditions, (3.86), lead to

$$0 = \varepsilon_0 + p_c - p_{\mathrm{in}} =: \boldsymbol{A}_4^{\mathrm{bc}}(\boldsymbol{x}) \,, \qquad 0 = \varepsilon_N + p_c - p_{\mathrm{out}} =: \boldsymbol{A}_5^{\mathrm{bc}}(\boldsymbol{x}) \,. \tag{4.52}$$

Taking partial derivatives with respect to $\boldsymbol{x}_k$, yields $\boldsymbol{D}\boldsymbol{A}^{\mathrm{bc}}$, such that for small $\|\tilde{\boldsymbol{x}}\| = \mathcal{O}(\delta)$

$$\boldsymbol{A}^{\mathrm{bc}}(\boldsymbol{x} + \tilde{\boldsymbol{x}}) = \boldsymbol{A}^{\mathrm{bc}}(\boldsymbol{x}) + \boldsymbol{D}\boldsymbol{A}^{\mathrm{bc}}(\boldsymbol{x})\tilde{\boldsymbol{x}} + \mathcal{O}(\delta^2) \,, \qquad \boldsymbol{D}\boldsymbol{A}^{\mathrm{bc}}_{jk}(\boldsymbol{x}) = \frac{\partial \boldsymbol{A}^{\mathrm{bc}}_j}{\partial \boldsymbol{x}_k} \,. \tag{4.53}$$

For flow boundary conditions define

$$\boldsymbol{A} := \begin{pmatrix} \boldsymbol{A}^{\mathrm{ode}} \\ \boldsymbol{A}^{\mathrm{bc}}_{(1:3)} \end{pmatrix} \qquad \text{and} \qquad \boldsymbol{D}\boldsymbol{A} := \begin{pmatrix} \boldsymbol{D}\boldsymbol{A}^{\mathrm{ode}} \\ \boldsymbol{D}\boldsymbol{A}^{\mathrm{bc}}_{(1:3),(0:N+1)} \end{pmatrix} \tag{4.54}$$

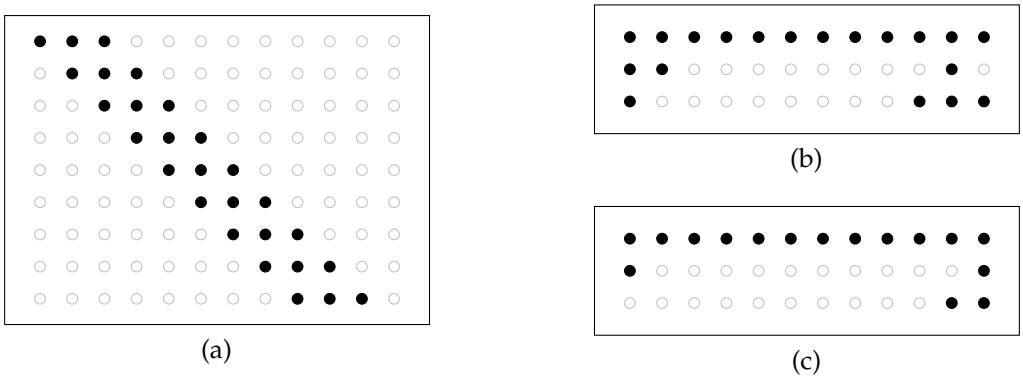

Figure 4.2: Sparsity patterns of the matrix representations of the steady state problem: zero elements (grey circles), non-zero elements (black dots): (a) $\boldsymbol{DA}^{\text{ode}}$ for the finite element representation of the ODE, (b) $\boldsymbol{DA}^{\text{bc}}_{(1:3),(0:N+1)}$ for ventricle wall stress and flow boundary conditions, (c) $\boldsymbol{DA}^{\text{bc}}_{(1,4,5),(0:N+1)}$ for ventricle wall stress and pressure boundary conditions.

and in the case of pressure boundary conditions

$$\boldsymbol{A} := \begin{pmatrix} \boldsymbol{A}^{\text{ode}} \\ \boldsymbol{A}^{\text{bc}}_{(1,4,5)} \end{pmatrix} \qquad \text{and} \qquad \boldsymbol{DA} := \begin{pmatrix} \boldsymbol{DA}^{\text{ode}} \\ \boldsymbol{DA}^{\text{bc}}_{(1,4,5),(0:N+1)} \end{pmatrix} . \tag{4.55}$$

Thus, the full system of equations for the Newton step $\tilde{\boldsymbol{x}}$ is

$$\boldsymbol{DA}(\boldsymbol{x})\tilde{\boldsymbol{x}} = -\boldsymbol{A}(\boldsymbol{x}) . \tag{4.56}$$

The respective spy plots of these matrix blocks are given in Figure 4.2.

4.4.2 Time dependent boundary conditions: transforming DAEs into ODEs

For the time dependent model of the brain during the infusion test, the boundary conditions are crucial. In 3.5.4, we have shown, how the overall pressure response

can be derived from the boundary conditions and an averaged parenchyma response. Four of the five potential boundary conditions, (3.83)–(3.86), of the time dependent problem do not contain time derivatives. Thus in the spatially discretised problem, they will lead to algebraic rather than differential equations with respect to time. This fact makes the finite element system with boundary conditions a system of differential algebraic equations (DAEs) of the form

$$\begin{pmatrix} \boldsymbol{M}(\boldsymbol{x}(t)) \\ 0 \end{pmatrix} \dot{\boldsymbol{x}} = \begin{pmatrix} \boldsymbol{f}(\boldsymbol{x}(t), t) \\ \boldsymbol{g}(\boldsymbol{x}(t), t) \end{pmatrix} . \tag{4.57}$$

It is not straightforward to find consistent initial conditions for DAEs, so most numerical solvers of DAEs attempt to find such initial conditions close to some input vector, before commencing time-stepping (Brenan et al., 1989; Shampine et al., 1999). To have a larger choice of time-stepping methods, the algebraic equations can be formulated as differential equations. We attempt to do this in a way such that any errors in satisfying these algebraic equations decay in time.

To explain how the algebraic equations are set in a differential framework, consider the simplest algebraic condition in one variable

$$g(x(t), t) = x(t) - h(t) = 0 , \tag{4.58}$$

where $h(t)$ is a continuously differentiable function. Straightforward differentiation yields an ordinary differential system

$$\dot{x}(t) = \dot{h}(t) , \qquad x(0) = h(0) . \tag{4.59}$$

However, if we consider the same problem with inexact initial data

$$\dot{x}(t) = \dot{h}(t) , \qquad x(0) = h(0) + c , \tag{4.60}$$

then the solution $x(t) = h(t) + c$ will always be the value c away from the solution to the original algebraic equation (4.58). In addition, any errors from numerical integration can accumulate and further decrease the quality of the solution.

A linear combination of the algebraic and differential equations (4.58) and (4.60) leads to a new differential system of the form

$$\dot{x}(t) = \dot{h}(t) - w \cdot (x(t) - h(t)) \,, \qquad x(0) = h(0) + c \,. \tag{4.61}$$

The solution to this problem is

$$x(t) = h(t) + c\exp(-wt) \tag{4.62}$$

and, for $w > 0$, converges asymptotically to the solution of the algebraic equation (4.58) as $t \to \infty$. Any errors in the initial data or that are acquired during time-stepping disappear exponentially fast.

Generalising this approach to the system (4.57) yields

$$\begin{pmatrix} \boldsymbol{M}(\boldsymbol{x}(t)) \\ \frac{\partial \boldsymbol{g}}{\partial \boldsymbol{x}} \end{pmatrix} \dot{\boldsymbol{x}} = \begin{pmatrix} \boldsymbol{f}(\boldsymbol{x}(t), t) \\ -\frac{\partial \boldsymbol{g}}{\partial t} - w\boldsymbol{g}(\boldsymbol{x}(t), t) \end{pmatrix} \,, \tag{4.63}$$

which, to our knowledge, is a new approach for approximating the solution to differential-algebraic equations. The parameter w can be adapted with respect to the time scales of the system, to balance the speed at which errors decay with the need for smaller time steps.

It is important to note that this approach does not necessarily lead to a good approximation of the solution to the DAE system (4.57). This depends on how well the initial data solves the algebraic equations and the sensitivity of the system to the initial data. Since we use the steady-state solution as initial data, the

algebraic boundary conditions are already satisfied fairly accurately and we can easily check their accuracy for the remainder of the simulation. If the errors in the algebraic boundary conditions stay small, the system (4.63) is only a small perturbation of the DAE system (4.57). We will check how well the algebraic boundary conditions are satisfied in 4.6.4. In addition, for physiological parameter values and constant sources at the boundaries, the numerical solution does not appear to be very sensitive to the initial data and converges to a stable steady state solution if the arterial blood pressure is neglected or to a solution oscillating around the steady state for periodic arterial blood pressure.

With the above approach, the time dependent boundary conditions, (3.83)–(3.86), become

$$\boldsymbol{L}_1^{\mathrm{bc}}(\boldsymbol{x})\dot{\boldsymbol{x}} := \boldsymbol{D}\boldsymbol{A}_1^{\mathrm{bc}}\dot{\boldsymbol{x}} = -w\boldsymbol{A}_1^{\mathrm{bc}}(\boldsymbol{x}) =: \boldsymbol{B}_1^{\mathrm{bc}}(\boldsymbol{x}) \,, \tag{4.64}$$

$$\boldsymbol{L}_2^{\mathrm{bc}}(\boldsymbol{x})\dot{\boldsymbol{x}} := (\boldsymbol{D}\boldsymbol{u}_{0,(0:N)},\, 0)\dot{\boldsymbol{x}} = \dot{u}_0 = \boldsymbol{A}_2^{\mathrm{bc}}(\boldsymbol{x}) =: \boldsymbol{B}_2^{\mathrm{bc}}(\boldsymbol{x}) \,, \tag{4.65}$$

$$\boldsymbol{L}_3^{\mathrm{bc}}(\boldsymbol{x})\dot{\boldsymbol{x}} := \boldsymbol{D}\boldsymbol{A}_3^{\mathrm{bc}}(\boldsymbol{x})\dot{\boldsymbol{x}} = \dot{p}_{\mathrm{sag}} + c_6\dot{q}_{\mathrm{infs}} - w\boldsymbol{A}_3^{\mathrm{bc}}(\boldsymbol{x}) =: \boldsymbol{B}_3^{\mathrm{bc}}(\boldsymbol{x}) \,, \tag{4.66}$$

$$\boldsymbol{L}_4^{\mathrm{bc}}(\boldsymbol{x})\dot{\boldsymbol{x}} := \dot{\varepsilon}_0 + \dot{p}_{\mathrm{c}} = \dot{p}_{\mathrm{in}} + w(p_{\mathrm{in}} - \varepsilon_0 - p_{\mathrm{c}}) =: \boldsymbol{B}_4^{\mathrm{bc}}(\boldsymbol{x}) \,, \tag{4.67}$$

$$\boldsymbol{L}_5^{\mathrm{bc}}(\boldsymbol{x})\dot{\boldsymbol{x}} := \dot{\varepsilon}_N + \dot{p}_{\mathrm{c}} = \dot{p}_{\mathrm{out}} + w(p_{\mathrm{out}} - \varepsilon_N - p_{\mathrm{c}}) =: \boldsymbol{B}_5^{\mathrm{bc}}(\boldsymbol{x}) \,. \tag{4.68}$$

Similar to the steady state system, we choose from these equations depending on the choice of boundary conditions. Let

$$\boldsymbol{L} := \begin{pmatrix} \boldsymbol{L}^{\mathrm{pde}} \\ \boldsymbol{L}^{\mathrm{bc}}_{(1:3),(0:N+1)} \end{pmatrix} \qquad \text{and} \qquad \boldsymbol{B} := \begin{pmatrix} \boldsymbol{B}^{\mathrm{pde}} \\ \boldsymbol{B}^{\mathrm{bc}}_{(1:3)} \end{pmatrix} \,, \tag{4.69}$$

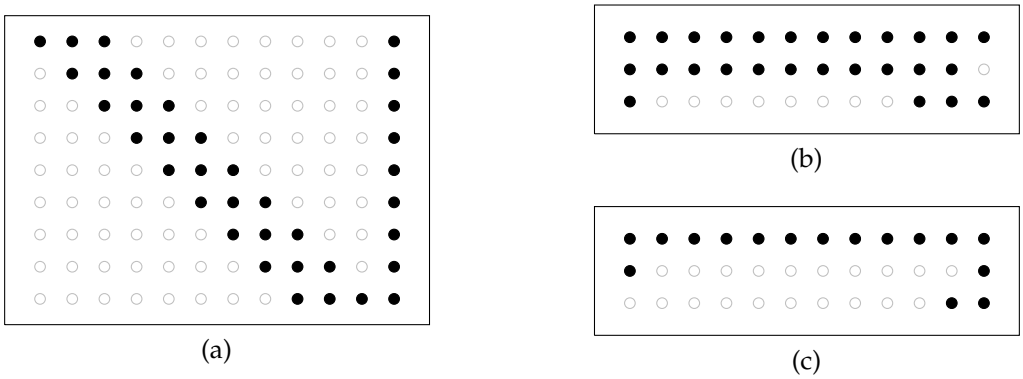

Figure 4.3: Sparsity patterns of the matrix representations of the time dependent problem: zero elements (grey circles), non-zero elements (black dots): (a) $\boldsymbol{L}^{\text{pde}}$ for the finite element representation of the PDE, (b) $\boldsymbol{L}^{\text{bc}}_{(1:3),(0:N+1)}$ for ventricle wall stress and flow boundary conditions, (c) $\boldsymbol{L}^{\text{bc}}_{(1,4,5),(0:N+1)}$ for ventricle wall stress and pressure boundary conditions.

for flow boundary conditions, and

$$\boldsymbol{L} := \begin{pmatrix} \boldsymbol{L}^{\text{pde}} \\ \boldsymbol{L}^{\text{bc}}_{(1,4,5),(0:N+1)} \end{pmatrix} \qquad \text{and} \qquad \boldsymbol{B} := \begin{pmatrix} \boldsymbol{B}^{\text{pde}} \\ \boldsymbol{B}^{\text{bc}}_{(1,4,5)} \end{pmatrix} , \tag{4.70}$$

for pressure boundary conditions. So, the full time dependent system is

$$\boldsymbol{L}(\boldsymbol{x})\dot{\boldsymbol{x}} = \boldsymbol{B}(\boldsymbol{x}, \dot{p}_a(t)) . \tag{4.71}$$

The respective sparsity patterns of the matrix blocks are given in Figure 4.3.

4.5 Solution techniques

4.5.1 Gauß–Legendre quadrature for integrals

To create the entries of the matrices $\boldsymbol{DA}^{\text{ode}}$ and $\boldsymbol{L}^{\text{pde}}$, we need to evaluate the integrals $\mathcal{I}_j, \mathcal{I}_j^{\text{l}}, \mathcal{I}_j^{\text{r}}$ in (4.34). Although analytic solutions are possible via partial

integration, the so obtained formulas are likely to be unstable for small spatial step size. This is because they contain differences of function values at neighbouring nodes, which become very similar for small step sizes. Instead, we approximate those integrals with Gauß–Legendre quadrature (Süli and Mayers, 2006; Press et al., 2007; Abramowitz and Stegun, 1965). Using n nodes, these formulas are exact for any polynomial of degree up to $2n-1$.

The integrands we consider are each a quadratic or cubic polynomial times an exponential function. This means that the exponential is effectively approximated by a polynomial of degree $2n-4$. Thus, we want to use at least $n=3$ nodes. Using 4 or 5 nodes had hardly any influence on the computation time compared to 3 nodes, so we can as well use the theoretically more expensive yet more accurate formula with 5 nodes.

The nodes in the interval $[-1,1]$ are the roots of the n-th degree Legendre polynomial P_n and the respective weights are given as

$$w_i = \frac{2}{(1-x_i^2)(P_n'(x_i))^2} \tag{4.72}$$

(Abramowitz and Stegun, 1965). For $n=5$, these are

$$x_1 = -x_5 = -\frac{1}{3}\sqrt{5+2\sqrt{\frac{10}{7}}}\,, \qquad w_1 = w_5 = \frac{1}{900}\left(322-13\sqrt{70}\right)\,, \tag{4.73}$$

$$x_2 = -x_4 = -\frac{1}{3}\sqrt{5-2\sqrt{\frac{10}{7}}}\,, \qquad w_2 = w_4 = \frac{1}{900}\left(322+13\sqrt{70}\right)\,, \tag{4.74}$$

$$x_3 = 0\,, \qquad w_3 = \frac{128}{225}\,. \tag{4.75}$$

The integration interval $[r_{j-1}, r_j]$ is mapped to the interval $[-1,1]$, the integrand

evaluated at the nodes x_k and summed according to the formula

$$\int_{-1}^{1} f(x)\mathrm{d}x \approx \sum_{k=1}^{n} w_k f(x_k) \,. \tag{4.76}$$

Numerical values of nodes and weights for other n can be found for example in Abramowitz and Stegun (1965) up to $n = 96$.

4.5.2 Steady state iteration with partial Newton steps

For the steady state problem, the full non-linear system of equations that we need to solve for $\boldsymbol{x} = (\varepsilon_0, \ldots, \varepsilon_N, p_\mathrm{c})^\mathrm{T}$ is given by the Galerkin equations (4.30) together with the boundary conditions (4.49)–(4.51) if we are interested in flow boundary conditions or (4.30), (4.49) and (4.52) if we want to solve the alternative pressure boundary conditions. In both cases, these form a non-linear system of $N + 2$ equations for the same number of unknowns.

Common methods for solving non-linear multidimensional equations are based on the Newton method, also known as Newton–Raphson method (Süli and Mayers, 2006; Press et al., 2007). In its original version, the function is approximated by its linearisation at the current point and the next iteration point is chosen as the root of that linearisation. In our case, this means that at iteration m, we need to solve the linear system (4.56) for $\tilde{\boldsymbol{x}}^{(m)}$ from a given $\boldsymbol{x}^{(m)}$ and update

$$\boldsymbol{x}^{(m+1)} = \boldsymbol{x}^{(m)} + \tilde{\boldsymbol{x}}^{(m)} \,. \tag{4.77}$$

The Newton method converges quadratically if the initial guess is close enough to a root, but may converge slowly or even diverge otherwise. Especially when iteration points are close to local extrema, so that the derivatives are almost zero, the computed correction could be far too large.

To avoid this overshoot, we instead take only a partial Newton step, that is, we update

$$\boldsymbol{x}^{(m+1)} = \boldsymbol{x}^{(m)} + \lambda^{(m)} \tilde{\boldsymbol{x}}^{(m)} \,, \tag{4.78}$$

with a damping parameter

$$\lambda^{(m)} = 1 - \omega^m \in (0, 1] \tag{4.79}$$

for $\omega \in [0, 1)$. In this way, the steps taken at the beginning of the iteration are more conservative, but later converge to the full Newton step as the current iteration point is approaching the region of quadratic convergence. We should thus recover almost quadratic convergence. Computing the step length according to (4.79) is a simplification of a damped Newton iteration, described for example by Press et al. (2007). In that algorithm, each step length $\lambda^{(m)}$ was chosen to ensure sufficient decrease in the 2-norm of the residue, thus relating the Newton iteration to a minimisation problem. The simple version used here converged for all tested cases, usually already with $\omega = 0.5$. Especially given the fact that the Newton iteration takes only negligible time compared to the time-stepping, a more complicated method was not considered necessary. An example of the convergence with and without damping is given in Figure 4.4.

4.5.3 Time stepping with a MATLAB ODE solver

The time dependent finite element problem, (4.71), is a system of ordinary differential equations. With arterial blood pressure oscillations, that is with $b_\mathrm{a} \neq 0$, this system is stiff. We leave the details of the time-stepping to a general purpose ODE solver. Out of the MATLAB ODE suite (Shampine and Reichelt, 1997), three

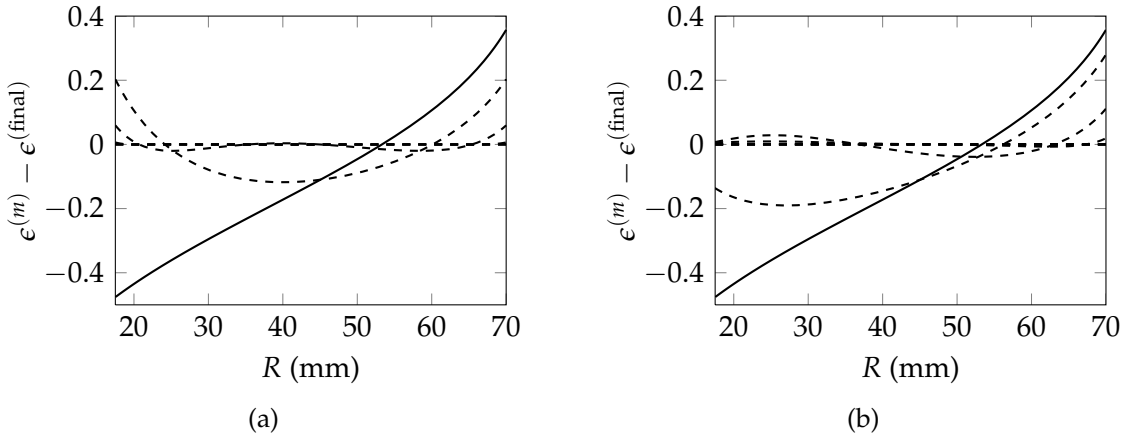

Figure 4.4: Newton convergence of volume dilation in steady state. Difference of inital guess and final Newton solution (continuous), differences of intermediate solutions and final Newton solution (dashed). (a) No damping, $\omega = 0$. The first step overshoots the solution at the inner (left) boundary, afterwards the iterative solution converges. (b) Damping with $\omega = 0.5$. The iterative solution converges almost monotonically. While this example violates the small deformation assumption, it is only used to illustrate the convergence behaviour of the iteration.

solvers can deal with stiff problems with a non-constant mass matrix. Those are ode15s, a backward differentiation formula (BDF1), ode23t, based on the trapezoidal rule (TRX2), and ode23tb, a combination of the trapezoidal rule and a backward differentiation formula (TR-BDF2). We will compare these three solvers in 4.6.5.

4.5.4 Preconditioning

To improve the conditioning of the systems, (4.56) and (4.71), which need to be solved in intermediate steps, we use some straightforward preconditioning strategies. For each Newton iteration in the steady state problem, we scale the equations so that each of them has about the same weight, that is, we compute the

sums of the absolute values in each row of $\boldsymbol{DA}$

$$s_i := \sum_{j=0:N+1} |\boldsymbol{DA}_{ij}| \tag{4.80}$$

and solve the preconditioned system

$$\operatorname{diag}\left(\frac{1}{s_0}, \ldots, \frac{1}{s_{N+1}}\right) \boldsymbol{DA}(\boldsymbol{x})\tilde{\boldsymbol{x}} = -\operatorname{diag}\left(\frac{1}{s_0}, \ldots, \frac{1}{s_{N+1}}\right) \boldsymbol{A}(\boldsymbol{x}) \tag{4.81}$$

instead of (4.56) for the full Newton step $\tilde{\boldsymbol{x}}$.

After having computed the steady state solution, hence the initial condition for the time dependent problem, we have already more information about the relative sizes of the pressure and volume dilation. Thus we can rescale the time dependent solution vector $\boldsymbol{x}$ via

$$\boldsymbol{X}_{jk} = \begin{cases} \max_j\{|\varepsilon_j(0)|\}\,, & \text{for } j = k = 0, \ldots, N\,, \\ |p_{\mathrm{c}}(0)|\,, & \text{for } j = k = N+1\,, \\ 0, & \text{otherwise,} \end{cases} \qquad \boldsymbol{x}^{\mathrm{rs}} = \boldsymbol{X}^{-1}\boldsymbol{x}\,, \tag{4.82}$$

to give the strain and pressure components equal weight. In this way, we also avoid components of the volume dilation dropping below the absolute tolerance which the Matlab ODE solvers considers as zero, even though they are still moderate in size compared to the maximum component in the volume dilation.

In addition, the mass matrix at time $t = 0$ should be a good preconditioner for the mass matrix at any later time, since it already contains all the information about the spatial discretisation. So we furthermore pre-multiply (4.71) by the inverse of the initial mass matrix and obtain the following ODE system for $\boldsymbol{x}^{\mathrm{rs}}(t)$

$$\left[\boldsymbol{L}^{-1}(\boldsymbol{x}(0))\boldsymbol{L}(\boldsymbol{X}\boldsymbol{x}^{\mathrm{rs}})\boldsymbol{X}\right]\, \dot{\boldsymbol{x}}^{\mathrm{rs}} = \boldsymbol{L}^{-1}(\boldsymbol{x}(0))\boldsymbol{B}(\boldsymbol{X}\boldsymbol{x}^{\mathrm{rs}}, \dot{p}_a(t))\,. \tag{4.83}$$

4.6 Numerical testing & validation

4.6.1 Spatial step sizes, measurements of accuracy and convergence rates

To ensure that the numerical solution is a reliable approximation to the solution, the numerics need to be validated. In particular, we consider the accuracy and spatial convergence rates of the solutions for different mesh sizes. First note how the spatial step sizes behave for the cubic and 9^{th} degree polynomial discretisations given by (4.12) and (4.13), see Figure 4.5. In both cases, the maximal spatial step size at the centre of the domain decreases approximately like N^{-1}. The difference between the two discretisations is in the minimal step size, next to the boundary. For the cubic discretisation, this decreases quadratically as the number of elements, N, grows, whereas for the 9^{th} degree polynomial discretisation, the minimal step size decreases as fourth order

$$h_{\max,\,S_3}, h_{\max,\,S_9} = \mathcal{O}(N^{-1})\,, \quad h_{\min,\,S_3} = \mathcal{O}(N^{-2})\,, \quad h_{\min,\,S_9} = \mathcal{O}(N^{-4})\,. \tag{4.84}$$

To compare these two discretisations, we determine the convergence rates of the numerical solutions for both with increasing number of elements.

In all cases, we consider relative errors in the infinity norm to an analytic solution if available and relative differences to the finest discretisation if there is no analytic solution

$$\text{RelErr}(f) := \frac{\|f_{\text{num}} - f_{\text{ana}}\|_\infty}{\|f_{\text{ana}}\|_\infty}\,, \qquad \text{RelDiff}(f) := \frac{\|f_{\text{coarse}} - f_{\text{finest}}\|_\infty}{\|f_{\text{finest}}\|_\infty}\,. \tag{4.85}$$

Where there is no analytic solution to compare with, the relative difference between

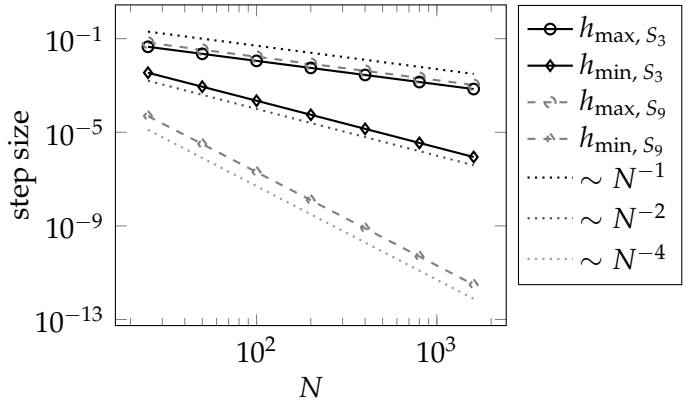

Figure 4.5: Minimal and maximal spatial step size versus number of elements N for the two spatial discretisations with cubic and 9$^{\text{th}}$ degree polynomials. The maximal step decreases for both approximately linear, $h_{\max,\, S_3}, h_{\max,\, S_9} = \mathcal{O}(N^{-1})$. The minimal step size decreases quadratic for the cubic discretisation, $h_{\min,\, S_3} = \mathcal{O}(N^{-2})$, and as fourth order for the 9$^{\text{th}}$ degree polynomial, $h_{\min,\, S_9} = \mathcal{O}(N^{-4})$.

the numerical solution on a mesh and that on the finest mesh is an indicator of the size of the relative error, provided the scheme converges.

In addition, we use the idea behind Richardson extrapolation to compute rates at which errors decrease with spatial refinement (Birkhoff and Rota, 1978). Consider an approximation $y(h)$ of some quantity y, for which the error depends on the step size h in the following form:

$$E_h = y(h) - y = ah^k + \text{higher order terms.} \tag{4.86}$$

Neglecting the higher order terms, it follows that for any positive constant c

$$\frac{y(ch) - y(h)}{y(c^2h) - y(ch)} = \frac{E_{ch} - E_h}{E_{c^2h} - E_{ch}} = \frac{(ch)^k - h^k}{(c^2h)^k - (ch)^k} = \frac{c^k - 1}{(c^k - 1)c^k} = \frac{1}{c^k}\,, \tag{4.87}$$

so that the rate k can be computed via

$$k = \frac{1}{\log c} \log\left(\frac{y(c^2h) - y(ch)}{y(ch) - y(h)}\right) \tag{4.88}$$

from numerical approximations with step sizes h, ch and c^2h. In our case, $h \sim \frac{1}{N}$ and we will use $c = 2$, that is doubling the number of elements for each refinement as well as $c = 4$.

When considering Richardson convergence rates computed from numerical simulations via (4.88), we need to keep in mind that the error was assumed to only depend on the spatial discretisation as in (4.86). If the computed rates at different step sizes disagree, then this shows that the assumption is violated and other factors influence the error. However, the computed rates can still be used as indicators of how well the numerical approximations converge and for which step sizes the error is likely dominated by the spatial discretisation.

4.6.2 Spatial convergence of steady state

To start, let us consider the steady state problem with pressure boundary conditions and constant permeability, (4.30), (4.49), (4.52). Comparing the numerical solution on $N = 25, \ldots, 1600$ elements to the analytic solution, (3.92)–(3.93), reveals approximately quadratic convergence in N for both the pressure and the volume dilation, independent of which discretisation was used (Figure 4.6). This rate was also confirmed via (4.88).

For exponential permeability or flow boundary conditions, we have no analytic solution to compare with. Instead, we compare the numerical solution on coarser meshes with $N = 25, \ldots, 800$ elements to that on the finest mesh with $N = 1600$ elements. For pressure boundary conditions (Figure 4.7a), we again observe quadratic convergence independent of the mesh, as confirmed by (4.88). For the problem with flow boundary conditions given by (4.30) and (4.49)–(4.51), we

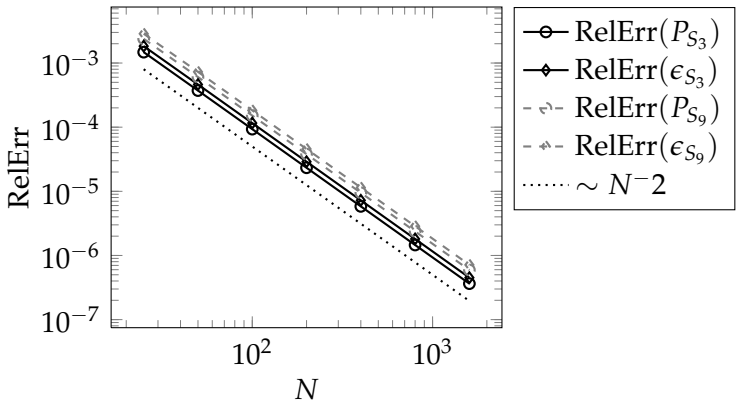

Figure 4.6: Convergence of steady state pressure (circles) and volume dilation (diamond) for pressure boundary conditions and constant permeability, comparing numerical solutions on $N = 25, \ldots, 1600$ elements to the analytic solution. The Newton iteration was stopped when a relative tolerance of 10^{-12} was reached. The dotted line indicates quadratic rate.

observe quadratic convergence on the cubic mesh and in the volume dilation on the 9^{th} degree polynomial (Figure 4.7b). The relative difference in pressure on the 9^{th} degree polynomial mesh initially decreases faster than quadratically, but increases as N is doubled from 400 to 800. This indicates on the one hand that the 9^{th} degree polynomial discretisation may be better than the cubic discretisation for a smaller number of elements, as the boundary region and hence the boundary conditions are resolved better than for the cubic discretisation. On the other hand, this shows, how the step size close to the boundary for fine 9^{th} degree polynomial discretisations becomes too small and rounding errors significantly decrease the accuracy of the numerical approximations.

For the solutions in Figures 4.6–4.7, the damped Newton iteration was stopped when each of the equations was solved to 10^{-12} accuracy and the infinity norm of the last Newton step was within 10^{-12} relative tolerance of the solution vector for both the pressure and the volume dilation. The slowest steady state computation

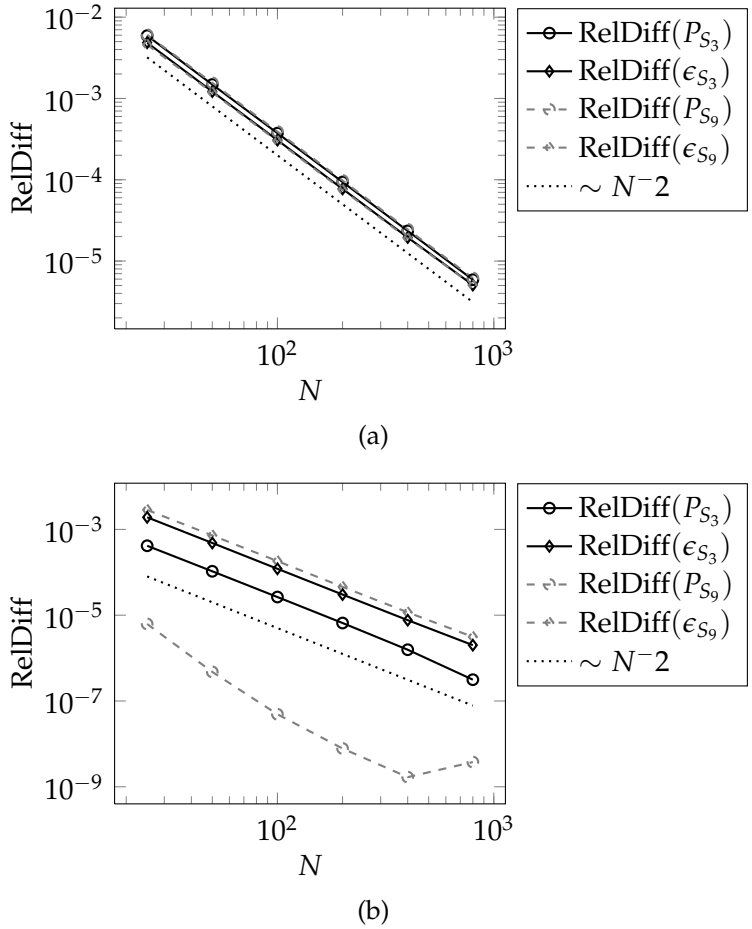

Figure 4.7: Convergence of steady state pressure (circles) and volume dilation (diamond) with exponential permeability, comparing solutions for $N = 25, \ldots, 800$ to the solution on $N = 1600$ elements. The Newton iteration was stopped when a relative tolerance of 10^{-12} was reached. The dotted lines indicate quadratic rates: (a) pressure boundary conditions, (b) flow boundary conditions.

on $N = 1600$ elements took just under 2 seconds for the Newton iteration and less than 4 seconds in total, including all data initialisation. For the smaller meshes up to $N = 800$ elements, each of the computations took less than 1 second.

The reason for the reduced accuracy on the finest 9^{th} degree mesh is the poor conditioning of the matrices used in the computation of the Newton step. In Figure 4.8, we show the condition number of this matrix versus the number of elements for the cubic and 9^{th} degree discretisation. For comparison, we have included the condition numbers before preconditioning as well. For the cubic discretisation with preconditioning, the condition number scales quadratically with N. Considering the 9^{th} degree discretisation instead or omitting the preconditioning each doubles the growth rate. At the finest discretisation with $N = 1600$ elements, the condition number for the 9^{th} degree discretisation is five orders of magnitude larger than that for the cubic discretisation. This clearly is enough to have a larger influence on the error than is expected from the discretisation given infinite precision.

Figure 4.9 shows the singular values for $N = 25$ for both discretisations with and without preconditioning as described in 4.5.4. For larger N, they are similarly distributed. The preconditioning mostly affects the large singular values, but hardly changes the smallest one. For coarse discretisations, the current preconditioning is sufficient. For finer discretisations better preconditioners would be necessary.

4.6.3 Spatial convergence of time dependent simulations

Before looking at the full time dependent problem with arterial blood pressure oscillations, we consider simulations where the arterial blood pressure source term

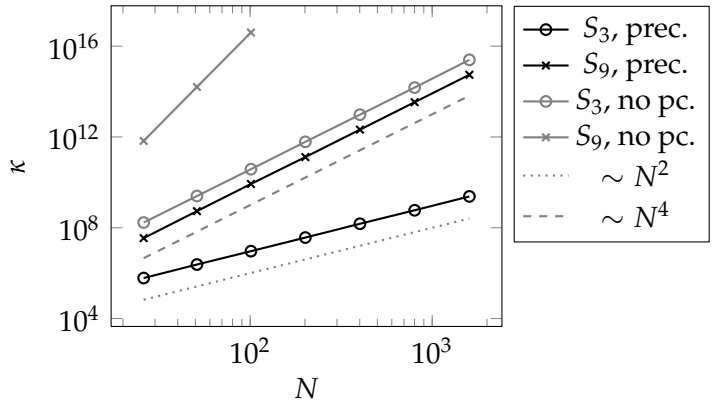

Figure 4.8: Conditioning of the full stiffness matrix of the Newton step, made up of $\boldsymbol{DA}^{\text{ode}}$ for the discretised ODE and $\boldsymbol{DA}^{\text{bc}}_{(1:3)}$ for the discretised flow boundary conditions. Comparing the condition numbers for the cubic (circles) and 9^{th} degree (crosses) discretisations with (black) and without (grey) preconditioning versus number of elements N. The dotted line indicates quadratic growth, the dashed line growth of order N^4.

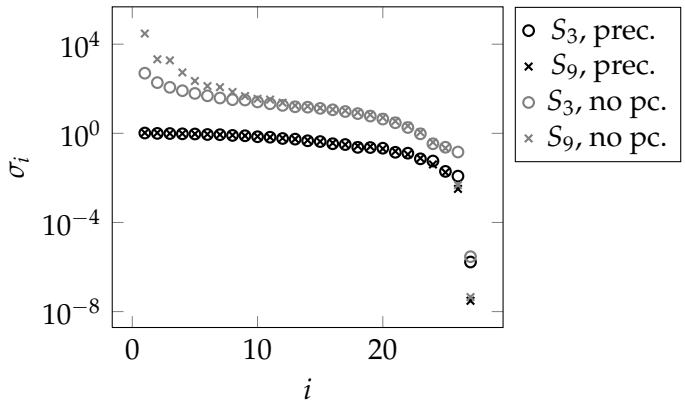

Figure 4.9: Singular values of the full stiffness matrix of the Newton step, made up of $\boldsymbol{DA}^{\text{ode}}$ for the discretised ODE and $\boldsymbol{DA}^{\text{bc}}_{(1:3)}$ for the discretised flow boundary conditions for $N = 25$ elements. Comparing the singular values for the cubic (circles) and 9^{th} degree (crosses) discretisations with (black) and without (grey) preconditioning.

has been set constant and equal to the average blood pressure over the whole test interval. In this way, the problem is less stiff and the simulations are a lot faster. We also expect the error to be related more strongly to the spatial error than to the time-stepping error, so that the influence of the discretisation is more visible. The flow boundary conditions include a constant infusion rate for part of the time interval with a short continuous transition of 1 second duration at the beginning and the end of the infusion. We compute this simulation for $N = 25, \ldots, 400$, doubling the number of elements for each refinement and using ode23tb for the time integration. The relative tolerance used for both the Newton iteration of the initial condition and the ODE solver was 10^{-6}. All simulations took between 10 minutes and 1.5 hours on similar desktop machines, except the one on 400 elements with the 9^{th} degree stretch. This simulation had repeated warnings about poorly conditioned matrices and took almost 13 hours.

The Richardson convergence rates for refinement with $N = 25, 50, 100$ elements, as well as the Richardson convergence rates with $N = 25, 100, 400$ are given in Table 4.1 and the relative difference between the coarse solutions and the finest one are plotted in Figure 4.10. For the cubic discretisation, we obtain an approximately linear Richardson convergence rate for $N = 25, 100, 400$, with a slightly better rate in the pressure initially ($N = 25, 50, 100$). A possible explanation for this change in behaviour is the fact that the error is the sum of the spatial error and the time-stepping error. For coarse discretisations, the spatial error dominates, whereas for finer spatial discretisations, the time stepping is the main source of errors. Since we do not explicitly control the size of the internal time steps, but let the ODE solver choose this to achieve a given tolerance, we cannot easily examine the influence of the time steps on the accuracy of the solution.

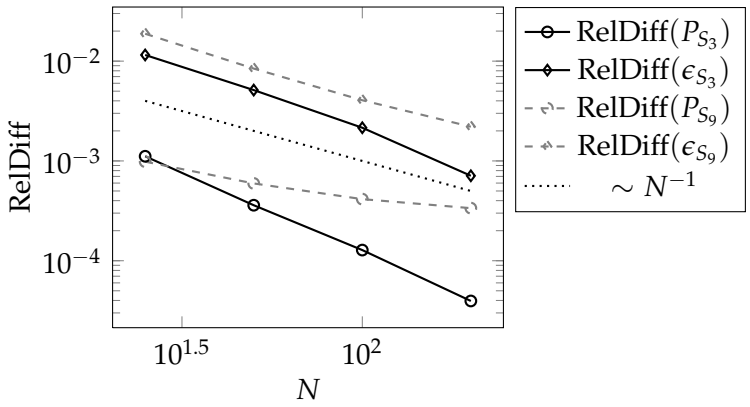

Figure 4.10: Spatial convergence of time-dependent pressure (circles) and volume dilation (diamonds) for the non-oscillating problem without arterial blood pressure. Comparing the numerical solutions on $N = 25, \ldots, 200$ elements to that on $N = 400$ elements. The dotted line indicates linear rate.

Table 4.1: Estimates of spatial convergence rates of time-dependent pressure and volume dilation computed via Richardson extrapolation

	cubic		9^{th} degree	
	ϵ	P	ϵ	P
initial rate ($N = 25, 50, 100$)	1.03	1.54	1.06	0.97
overall rate ($N = 25, 100, 400$)	1.00	1.08	0.45	0.32

Comparing the 9^{th} degree discretisation with the cubic one, we see poorer error rates over the whole refinement range ($N = 25, 100, 400$), after approximately linear rates initially ($N = 25, 50, 100$). Since these relative differences to the solution on the finest mesh are much larger than those for the cubic discretisation, it is unlikely that these are only due to the time stepping error. Instead, they are probably caused by accumulated rounding errors due the small spatial step sizes at the boundary. For example, one of the contributions to the right hand side (4.45) of the ODE system is given by (4.35), see page 132, via (4.39). For small h_j, the values of the volume dilation at neighbouring nodes are very similar and thus $\varepsilon_j - \varepsilon_{j-1}$ has limited accuracy in floating point arithmetic. In addition, this number

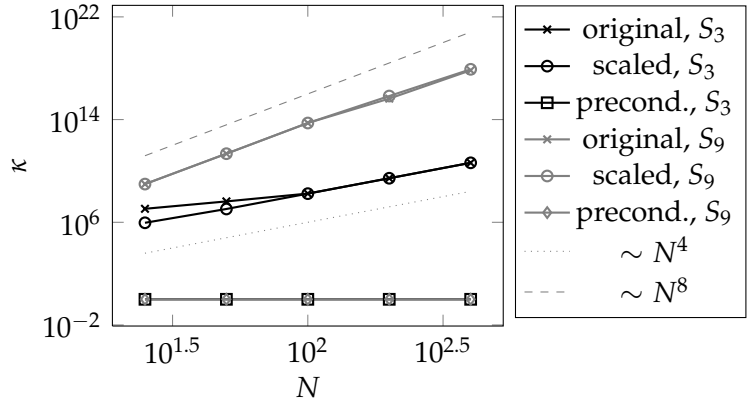

Figure 4.11: Condition number of mass matrix at $T = 3.33\,\mathrm{s}$, for cubic (black) and 9^{th} degree discretisations, in the original description, after scaling the volume dilation and pressure relative to their norms at initial time and after preconditioning with the inverse of the mass matrix at initial time. The dotted and dashed line indicate fourth order and eighth order growth, respectively.

is multiplied by a large number, $\frac{1}{h_j^2}$, so this error is amplified.

Furthermore, we have considered the condition number of the mass matrix, in particular to investigate the influence of the scaling and preconditioning described in 4.5.4. Figure 4.11 shows the condition number of the mass matrix at time $T = 3.33\,\mathrm{s}$ for cubic and 9^{th} degree discretisations in its original formulation, after rescaling the pressure and volume dilation, and after preconditioning. The values at later times, after 6, 12 and 18 minutes, were within a factor four of the respective values given in Figure 4.11. The rescaling only has an influence on the condition number for coarse cubic discretisations, otherwise its influence was probably too small to be visible. However, we can clearly see that preconditioning with the mass matrix at initial time is successful at reducing the condition number to order one.

From the condition numbers alone, one might think that the preconditioning is more important than the rescaling to increase accuracy, but comparing the results

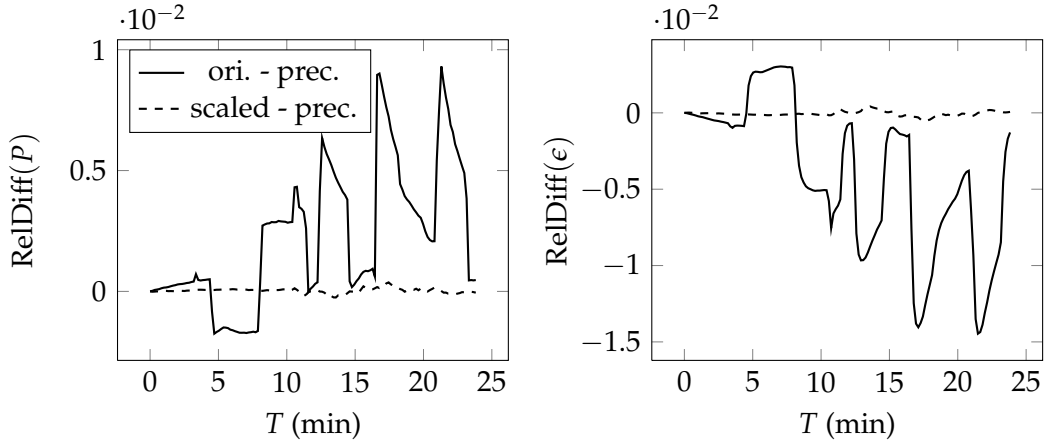

Figure 4.12: Influence of scaling volume dilation and pressure and preconditioning. Plotted are the relative differences in pressure and volume dilation at the skull, averaged over 10 s windows, between the preconditioned simulation and the scaled simulation (dashed) as well as between the preconditioned simulation and the simulation in the original formulation (continuous). For all three simulations, the cubic discretisation with $N = 50$ elements and the ODE solver ode15s were used.

of simulations indicates the opposite. In Figure 4.12, we compare the relative differences in pressure and volume dilation at the skull in the original formulation and the preconditioned formulation to those in the scaled and preconditioned formulations. These simulations were computed on a cubic mesh with $N = 50$ elements using ODE solver ode15s and included arterial blood pressure oscillations. The preconditioning after the rescaling only has a very small influence on the results, of order 10^{-4}, whereas the relative difference from scaling is of the order of 10^{-2}. Hence rescaling is clearly necessary. The given preconditioning probably has so little effect because the ODE solver is likely reusing information from previous time steps, thus effectively using a very similar preconditioning strategy. Since our explicit preconditioning does not have a significant influence on the computation time either, we see no harm in leaving this extra step in the computations nevertheless.

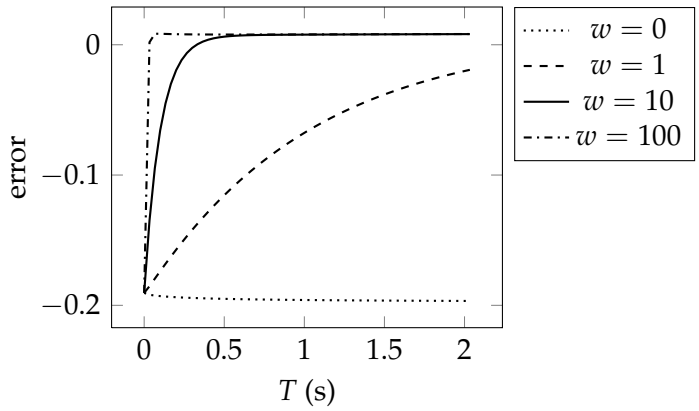

Figure 4.13: Error in satisfying the discretised, non-dimensional, algebraic, outer flow boundary condition (3.85) in the first two seconds of the simulation after perturbing the initial volume dilation for different weights w in the transformation of the DAE system to an ODE system.

4.6.4 Weights for conversion of algebraic to differential equations

In 4.4.2, we described a strategy to transform the system of DAEs (4.57) into a system of ODEs (4.63) by considering a linear combination of the algebraic equations and the differential equations obtained by differentiating these with respect to time. To test whether and how well this strategy works for our problem, we consider the time-dependent problem without arterial blood pressure oscillations, zero infusion and initial data that is perturbed from the steady state solution. For this perturbation, we multiplied the volume dilation by a factor 1.1.

Figure 4.13 shows the error in satisfying the non-dimensional outer flow boundary condition (3.85) in discretised form for the first two seconds of the simulation for varying weights w in this linear combination. In all cases, the error in satisfying the stress boundary condition across the ventricle wall (3.124) was several orders of magnitude smaller and is not shown.

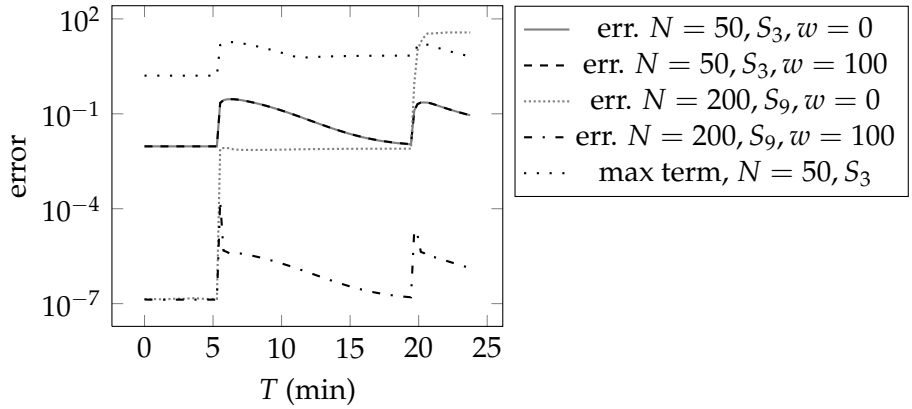

Figure 4.14: Error in satisfying the discretised, non-dimensional, algebraic, outer flow boundary condition (3.85) for a full simulation with different meshes and different weights w in the transformation of the DAE system to an ODE system. The loosely dotted line indicates the maximum absolute value of all terms in (3.85).

The value $w = 0$ corresponds to using the differentiated form of the algebraic equations. In this case, the error in satisfying the algebraic boundary condition stays constant. For all positive values of w, the error converges to the same value, but at different speeds, faster for larger w, as expected. This final value is also independent of how big the initial perturbation was.

How big the final error in satisfying the boundary condition is depends on the discretisation, particularly close to the boundary. In Figure 4.14, we show the influence of the weight for different meshes over a full simulation with infusion, but still without oscillations in arterial blood pressure. For these simulations, the steady state solution was used as initial condition without perturbation. For a 50 element cubic mesh, no difference is visible between $w = 0$ and $w = 100$. In both cases, the error grows quickly at the beginning and the end of the infusion, but slowly decays afterwards. This trajectory is following the changes of the volume dilation at the boundary. For a finer mesh with 200 elements and 9^{th} degree

polynomial stretch, the error before the infusion is much smaller and similarly indistinguishable between $w = 0$ and $w = 100$. Only as the infusion is started, the difference becomes apparent. For $w = 0$, errors in satisfying the boundary condition caused by rounding errors accumulate as the infusion is started and stopped, whereas for $w = 100$, these errors quickly decay towards the original level and then follow a trajectory similar to that on 50 elements.

Thus, our strategy of transforming the DAE system into an ODE system is successful at keeping the errors in the algebraic equations close to the level determined by the discretisation and the size of the solution. Its effects are most visible for very fine discretisations that suffer from rounding errors (compare 4.6.3).

4.6.5 Comparison of ODE solvers

The three solvers out of the MATLAB ODE suite (Shampine and Reichelt, 1997) that can deal with stiff problems with a non-constant mass matrix are ode15s, a backward differentiation formula (BDF1), ode23t, based on the trapezoidal rule (TRX2), and ode23tb, a combination of the trapezoidal rule and a backward differentiation formula (TR-BDF2). To compare their accuracy and stability on this problem, we simulated the same problem with each of these solvers on different spatial meshes. In this way, we can try to separate the influence of the spatial discretisation and the time-stepping on the error. The time dependent problem considered here has arterial blood pressure included as input as well as a constant infusion with short transition phases at the beginning and end. For each solver, the cubic discretisation was used and the relative tolerance was chosen as 10^{-6}.

Table 4.2: Comparison of Matlab ODE solvers. Wall clock times for simulations on two spatial meshes ($N = 50$, $N = 200$) and the maximal relative differences in pressure and volume dilation between the meshes for each solver.

	ode23t	ode15s	ode23tb
wall clock time for $N = 50$	8.4h	9.0h	16.5h
wall clock time for $N = 200$	21.1h	25.5h	40.0h
max. relative pressure diff.	$43.0 \cdot 10^{-4}$	$8.8 \cdot 10^{-4}$	$7.1 \cdot 10^{-4}$
max. rel. volume dilation diff.	$1.8 \cdot 10^{-2}$	$1.8 \cdot 10^{-2}$	$1.8 \cdot 10^{-2}$

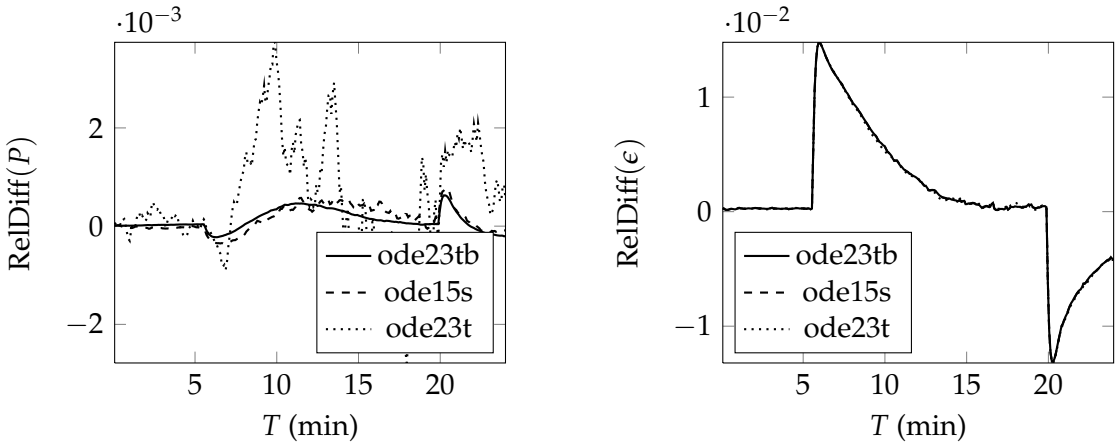

Figure 4.15: Comparison of the stability of different Matlab ODE solvers. For each solver, the difference in the numerical solutions on two spatial meshes ($N = 50$, $N = 200$) is considered over time. (a) Relative differences in average pressure over 10 second windows. (b) Relative differences in average volume dilation over 10 second windows.

In Table 4.2, the wall clock times for the simulations on two meshes ($N = 50$, $N = 200$) for each solver are given as well as the maximal relative difference in pressure and volume dilation between the simulations on the fine and coarse mesh. Figure 4.15 shows how much the solution changes for each solver if the mesh is refined from 50 to 200 elements and in Figure 4.16 the solutions with different solvers on the same spatial mesh are compared explicitly.

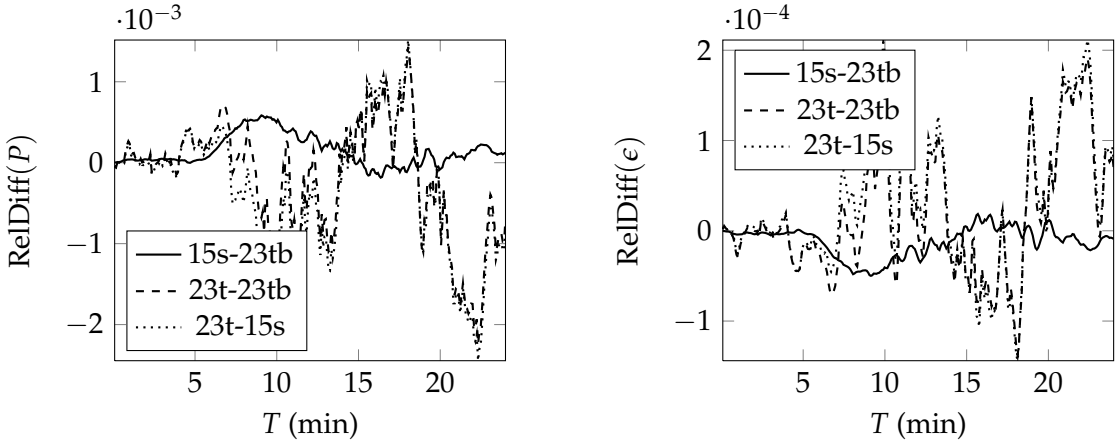

(a) (b)

Figure 4.16: Comparison of the stability of different Matlab ODE solvers. Considering the relative difference in pressure and volume dilation on a mesh with $N = 200$ elements between pairs of solvers. (a) Relative differences in average pressure over 10 second windows. (b) Relative differences in average volume dilation over 10 second windows.

With respect to the volume dilation, the difference due to the spatial discretisation is larger than the differences between the solvers, as can be seen from panels 4.15b and 4.16b. Instead, the different solvers can be assessed by considering the pressure. While ode23t is clearly the fastest solver, it is also the one with the largest error in pressure (Table 4.2, Figures 4.15a, 4.16a). The maximum relative difference in pressure between the two meshes is for ode23t about five times as large as for the other two solvers (Table 4.2). Similarly, the difference of the ode23t solution to the solutions with the other two solvers is larger than the differences between ode23tb and ode15s, for both the pressure and the volume dilation (Figure 4.16).

For ode23tb and ode15s, the change of going from 50 to 200 elements is very similar (Figure 4.15). The largest differences are small bumps after about 5 minutes and 20 minutes of the test, which are related to the infusion being switched on and off. For ode23tb, the transition to the finer mesh appears to be smoother than for

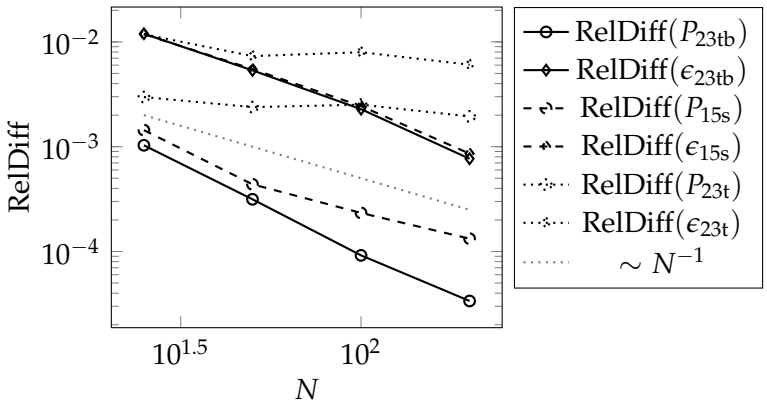

Figure 4.17: Comparison of spatial convergence for simulations with different Matlab ODE solvers. Maximum relative difference in pressure (circles) and volume dilation (diamonds) between the numerical solutions on $N = 25, \ldots, 200$ elements and that on $N = 400$ elements for each solver. The dotted line indicates linear rate.

ode15s, but overall the difference in accuracy between the two solvers seems to be very small. The relative differences between the pressure and volume dilations computed with ode23tb and ode15s on $N = 200$ elements are within 10^{-3}.

In addition to the comparisons so far, we have considered the spatial convergence for each solver. Figure 4.17 shows for each solver the relative differences in pressure and volume dilation between the solutions on $N = 25, \cdots, 200$ elements and the solution on $N = 400$ elements. In Table 4.3, the corresponding estimates for the spatial Richardson convergence rates computed with $N = 25, 50, 100$ and $N = 25, 100, 200$ are given. We can see that for ode23t, the time-stepping error dominates already for fairly coarse discretisations, whereas the solutions on both ode23tb and ode15s seem to improve with spatial refinement, at least initially close to linear rate $\mathcal{O}(N^{-1})$. This is similar to the rate observed for the non-stiff problem without arterial blood oscillations considered in 4.6.3.

Given that ode15s is much faster than ode23tb, taking only about 60% of the time, but is almost as accurate as ode23tb for coarse meshes, this is the best choice as

Table 4.3: Comparison of spatial convergence for simulations with different Matlab ODE solvers. Estimates of spatial Richardson convergence rates of pressure and volume dilation for $N = 25, 50, 100$ and $N = 25, 100, 200$.

	ode23t		ode15s		ode23tb	
	ϵ	P	ϵ	P	ϵ	P
Estimated rate on $N = 25, 50, 100$	0.95	0.25	1.04	1.45	1.03	1.60
Estimated rate on $N = 25, 100, 400$	1.07	0.13	1.01	1.05	1.00	1.13

default ODE solver for the simulations in chapter 5. If stability issues arise in some cases, then those simulations can be repeated with ode23tb.

4.6.6 Conclusions of numerical tests

Following the tests in this section, we can choose the default numerical settings to be used for simulations in the following chapter, where we will compare the simulations with clinical data. It is clear that very fine meshes suffer from instabilities due to rounding errors. At 50 elements, with a cubic mesh, the relative error in both the pressure and the volume dilation is of the order 10^{-2}. The pressure measurements we compare with are unlikely to be much more accurate (Blo, 1994). In addition, such a simple model as ours (spherical geometry, homogeneous, isotropic material, no biological processes) can only give qualitative predictions. Thus, keeping in mind the long computation times, a mesh with 50 elements seems sufficient for most of the simulations.

For the steady state Newton iteration we choose the damping parameter $\omega = 0.5$ and a relative tolerance of 10^{-6}. ODE solver ode15s will be used for the time dependent problem together with the same relative tolerance. The choice of weight in the DAE to ODE transformation did not make much difference for

the given mesh. To be on the safe side with arterial blood pressure oscillations included, we choose a higher value of $w = 10^4$.

All of these numerical parameters could be changed if a simulation appears to be inaccurate or a more detailed solution is required.

Chapter 5

Analysis of clinical data

Contents

5.1 Introduction

In this chapter, we use the finite element code of the two-fluid poroelastic model described in the previous chapters to simulate infusion tests and compare computed results with clinical data. The aim is to analyse whether the pressure data of an infusion test can provide more information about a patient's CSF dynamics than is currently obtained with analysis using single compartment models, particularly with respect to mechanical properties of the brain tissue, which could then be used for diagnosis or simulations of treatment outcomes. In addition, we are able to examine how the additional fluid injected during an infusion test is stored in the brain, which may help assess the invasiveness and specific effects of infusion tests.

The clinical data sets are the same ones we examined for compartment models in chapter 2. In that chapter, we concluded that it is not possible to distinguish between different types of phenomenological compliance functions, as long as they describe the same compliance–pressure curve over the observed pressure range. Thus for simplicity, we will by default use the standard compliance function for the storage compliance (2.9),

$$C(P) = \frac{1}{E(P - P_{\mathrm{r}})} \,, \tag{5.1}$$

in (3.143).

Infusions directly into the ventricles are possible and sometimes used, for example in cases of a malformation that disconnects the spinal subarachnoid space from the cranial CSF space, but in general, infusion tests via lumbar puncture are considered less invasive and hence are preferred (Behrens et al., 2012). Since we have no information on the infusion location for our clinical data sets, we will thus assume lumbar infusion in all cases. In the spherical multi-fluid poroelastic model without a spinal component, this translates to an infusion at the outer boundary. As long as the aqueduct is sufficiently open, CSF can freely flow between the outer boundary and the ventricle so that the difference to the solution with a ventricular infusion is minimal.

We will start with the details of one example simulation with a default set of parameter values in 5.2. An extensive parameter variation around these default values in 5.3 is then used to determine which parameters should be changed in order to try and fit simulations to clinical data. Section 5.4 contains the results of such fits obtained manually for a few data sets. Finally, in section 5.5, we examine the long term behaviour of the multi-fluid poroelastic model if the infusion were continued for several hours.

Table 5.1: Standard parameter values for parameter variations on the poroelastic model.

Unstressed ventricle radius	R_{in}	=	$18\,\text{mm}$
Outer brain radius	R_{out}	=	$70\,\text{mm}$
Aqueduct diameter	d	=	$4\,\text{mm}$
Elasticity	E	=	$0.24\,\text{ml}^{-1}$
Compliance reference pressure	P_{r}	=	$2.13\,\text{mmHg}$
Sagittal sinus pressure	P_{sag}	=	$2.13\,\text{mmHg}$
CSF production rates	Q_{prod}	=	$0.51\,\frac{\text{ml}}{\text{min}}$
Infusion rate	Q_{inf}	=	$1.5\,\frac{\text{ml}}{\text{min}}$
Resistance to CSF outflow	$\mathcal{R}$	=	$15.4\,\text{mmHg}\frac{\text{min}}{\text{ml}}$
Young's modulus	Y	=	$4.39\,\text{mmHg}$
Poisson's ratio	ν	=	0.35
Lamé parameters	λ	=	$\frac{Y\nu}{(1+\nu)(1-2\nu)} = 3.79\,\text{mmHg}$
	μ	=	$\frac{Y}{2(1+\nu)} = 1.63\,\text{mmHg}$
Biot–Willis parameter	α	=	1
Arterial blood B.–W. parameter	α_{a}	=	0
Arterial blood storage coefficient	γ_{a}	=	$6 \cdot 10^{-6}\,\text{mmHg}^{-1}$
Permeability constant	κ_0	=	$1.4 \cdot 10^{-14}\,\text{m}^2$
Permeability model constant	M_0	=	4.3
CSF viscosity	η	=	$7.5 \cdot 10^{-6}\,\text{mmHg}\,\text{s}$
Stress-free pressure	P_{sf}	=	$6\,\text{mmHg}$

5.2 Example simulation with default parameter values

At first, we consider the results of the multi-fluid poroelastic simulation for the set of default parameter values given in Table 5.1. For parameters that can be directly related to the compartment model fitted in chapter 2, that is E, P_{r}, P_{sag} and $\mathcal{R}$, we have used the values from the parameter fit for data set 00 (Table 2.6). This data set also provides the arterial blood pressure input (Figure 5.1) and infusion data. The material parameters of brain tissue for the poroelastic model, that is Y, ν and hence the Lamé parameters λ and μ, as well as κ_0, M_0 and η are mostly taken from

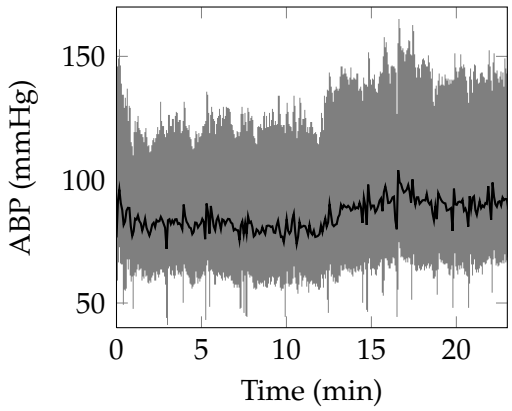

Figure 5.1: Arterial blood pressure input (grey) from data set 00 and mean over 5s window (black).

Wirth and Sobey (2006), who did an extensive literature search for these values. For simplicity, we set the Biot–Willis parameter, α, to one, as we did when relating the multi-fluid poroelastic model to the compartment model in 3.5.4. Thus follows that the arterial blood Biot–Willis parameter, α_{a}, needs to be zero.

The diameter, d, of the aqueduct of Sylvius is also taken from Wirth and Sobey (2006), but we believe that their values for the ventricle radius and outer brain radius are too large. With these values, the ventricle and parenchyma volumes are 113 ml and above 4000 ml, respectively, and hence both much larger than the average values of about 25 ml and 1360 ml provided in the medical literature (Fishman, 1992; Nolte, 2009). Instead, we use values for the radii that approximate these volumes. Finally, we took the values for the arterial blood storage coefficient, γ_{a}, and the stress-free reference pressure, P_{sf} from Wirth and Sobey (2009).

Figure 5.2 shows the simulated pressure response at the outer boundary, its average over 5 second time windows and the peak-to-peak amplitude estimated by the difference between the maximum and minimum value within this time window. The maximum spatial pressure difference is only about one tenth of the temporal

pressure amplitude and thus is not shown. At each time, it can be inferred from the spatial distribution of the volume dilation according to

$$\frac{\partial P}{\partial R} = \frac{(\lambda + 2\mu)}{\alpha} \frac{\partial \epsilon}{\partial R} \,. \tag{5.2}$$

The spatial and temporal distributions of the volume dilation, the increase in CSF content and the porous flow velocity are shown in Figures 5.3, 5.4 and 5.5, respectively. Notably, no strong oscillations at the cardiac time scale are visible in either of these plots. It is clear to see that, as the infusion starts, CSF flows into the outer layers of the tissue, which distend rapidly to accommodate the extra fluid, while the bulk of the tissue between these boundary layers is compressed. This compression allows the bulk of the tissue to be displaced outwards and hence increase the ventricle volume.

With continuing infusion, fluid is able to traverse deeper into the tissue. At the same time, the absorption rate increases as the pressure rises so that the increased inflow rate is partially balanced (Figure 5.2). This effect is best visible from the reduced flow into the tissue (Figure 5.5). The maxima of volume dilation, CSF content, flow velocity and displacements at the boundaries are reached roughly at 10 minutes after the beginning of the test and hence after about 4-5 minutes of infusion.

After around 20 minutes of the test, the infusion is stopped and the effects are reversed. Due to the high pressure, the absorption rate is now higher than the CSF production rate, so fluid rapidly leaves the brain. The outermost layers of the brain tissue compress as CSF leaves the tissue and the ventricles decrease in size, even below their steady state volume. At the end of the test after 24 minutes, the steady state has not at all been reached yet.

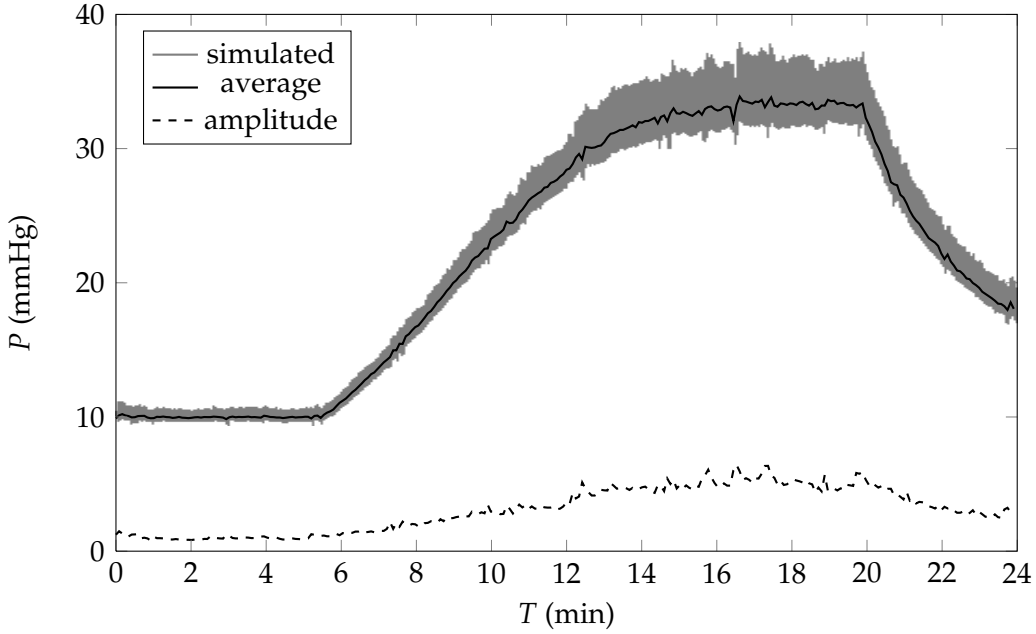

Figure 5.2: Simulated intracranial pressure during an infusion test for data set 00, with default parameter values from Table 5.1: CSF pressure at the outer boundary (grey), average pressure over 5 s windows (solid, black) and pressure peak-to-peak amplitude (dashed) estimated by the difference between maximum and minimum values in these time windows.

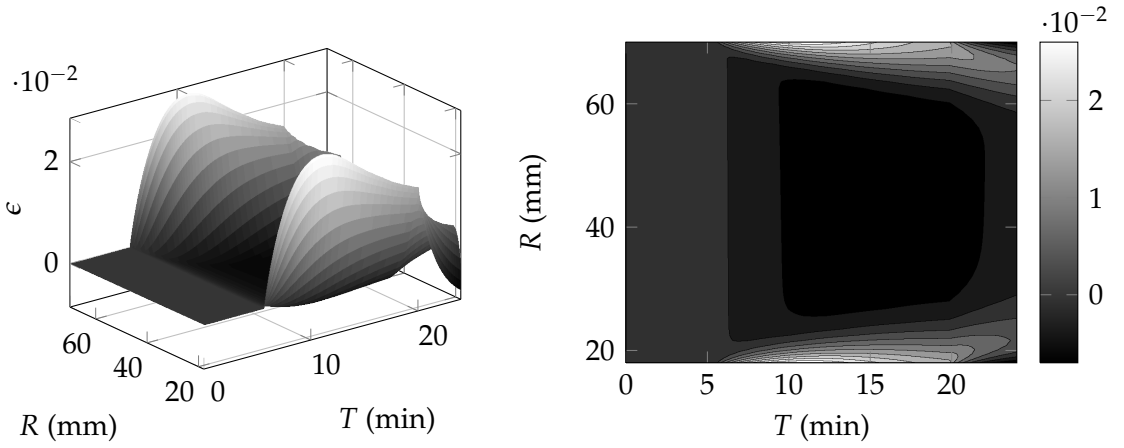

Figure 5.3: Simulated volume dilation, ϵ, across the parenchyma during an infusion test for data set 00, with default parameter values from Table 5.1: (a) 3D plot, (b) corresponding contour plot.

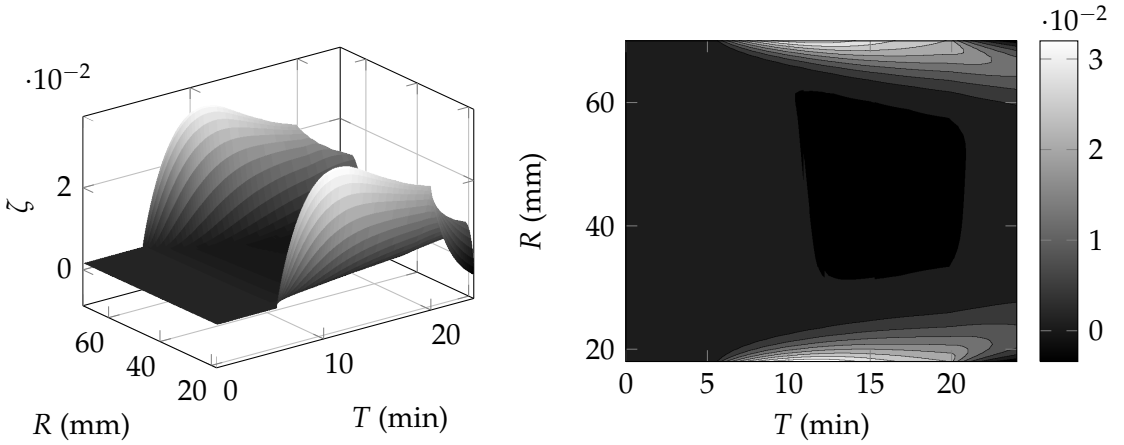

(a) (b)

Figure 5.4: Simulated increase in CSF volume content, ζ, across the parenchyma during an infusion test for data set 00, with default parameter values from Table 5.1: (a) 3D plot, (b) corresponding contour plot.

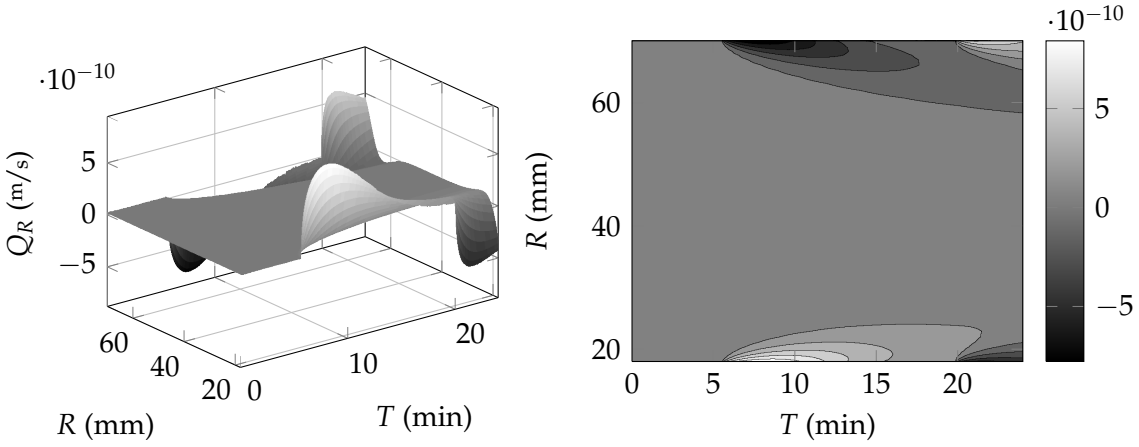

(a) (b)

Figure 5.5: Simulated outward radial porous flow rate, Q_R, in $^{\mathrm{m}}/_{\mathrm{s}}$ across the parenchyma during an infusion test for data set 00, with default parameter values from Table 5.1: (a) 3D plot, (b) corresponding contour plot.

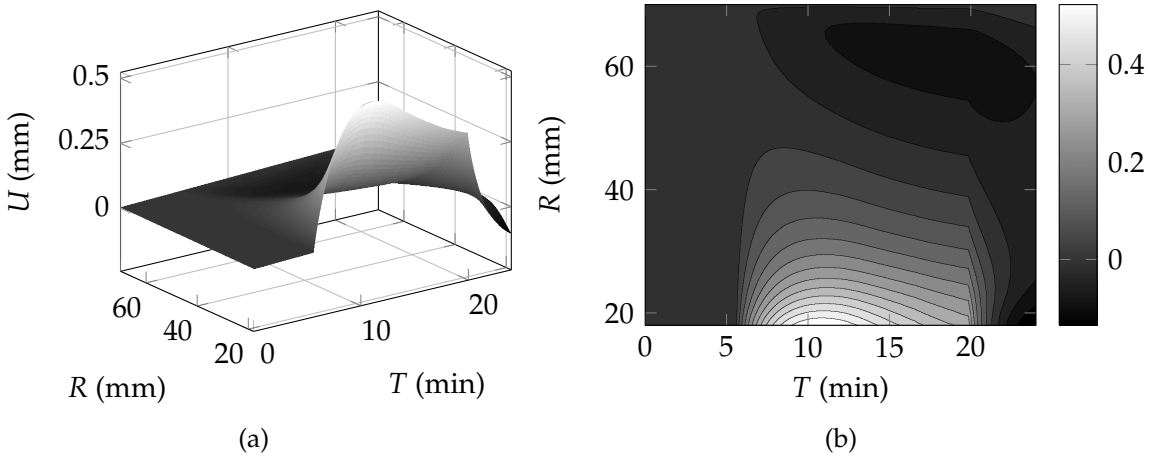

Figure 5.6: Simulated outward displacements, U, in mm across the parenchyma during an infusion test for data set 00, with default parameter values from Table 5.1: (a) 3D plot, (b) corresponding contour plot.

Finally, we consider the portions of additional fluid volume taken up by the ventricle and the brain tissue. Figure 5.7 shows the temporal changes in ventricle volume and CSF content in the parenchyma, as well as their sum. According to Fishman (1992), 15–20% of the brain volume is extracellular space, filled with extracellular fluid. As noted in section 1.1, CSF readily communicates with the extracellular fluid. Thus for our purposes, there is no need to distinguish between the two fluids. The values plotted in Figure 5.7 assume an initial CSF content of 15% in the tissue, thus are at the lower end.

As noted earlier, the ventricle radius and hence its volume rapidly increase during about the first 5 minutes of the infusion, then reach a maximum and decline. The parenchymal CSF volume continues to rise during the whole infusion, but the total volume appears to reach a maximum by the end of the infusion. At the end of the infusion, the behaviour is mirrored. The ventricle shrinks rather quickly below its initial size and the parenchymal CSF decreases at a slower rate. While our model does not contain the subarachnoid space, hence in particular no

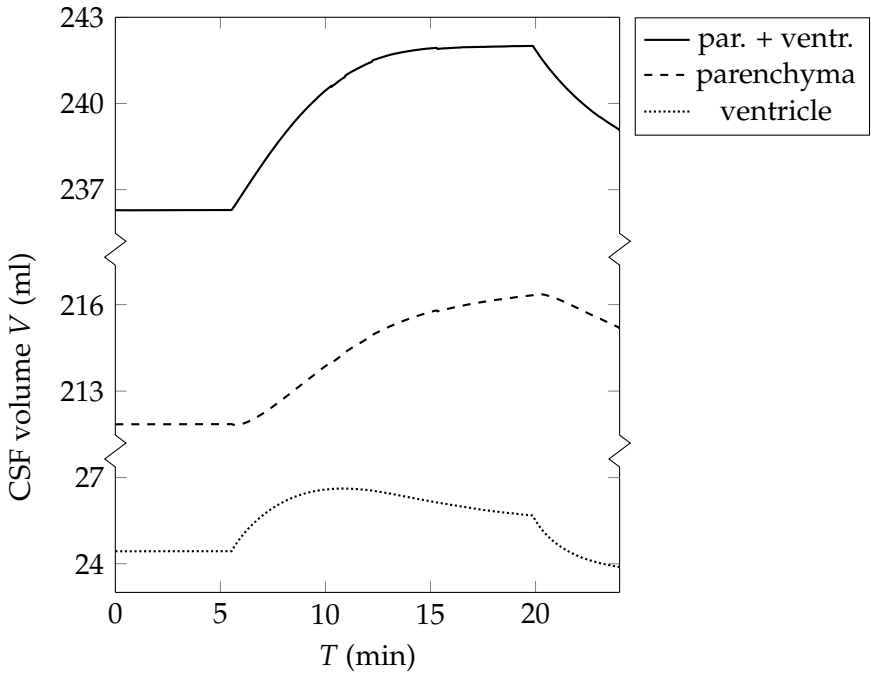

Figure 5.7: Simulated CSF volume portions in the ventricle and the parenchyma during an infusion test for data set 00, with default parameter values from Table 5.1. Note that the model does not include compartments for the subarachnoid space and, in particular, no spinal CSF compartment. Thus the sum of parenchymal and ventricular CSF volume constitutes the total CSF volume in this model.

spinal compartment, this would likely only change the total fluid volume stored in the ventricle and within the parenchyma, not their relative contributions to this storage.

5.3 Parameter variations around default values

Having considered the simulation with default parameter values in detail, we can now look at the changes produced by varying each of the parameters. In each of the following plots, the result with the default parameter values will be indicated

by a thick, solid line, whereas the simulations from other parameter values are shown with different line styles.

For each of the parameter variations, the figure layout is the following: panel (a) shows the pressure at the outer boundary averaged over 20s windows. In most cases, the pressure difference between the parenchyma and the subarachnoid space is much smaller than the mean pressure, so that no difference would be visible if taking the pressure at any other point. In addition, we consider infusion tests via lumbar puncture, that is the pressure measurements are taken in the spinal column. Thus, in our model without a spine, the pressure in the subarachnoid space most closely resembles those measurements. Panel (b) shows the pressure peak-to-peak amplitude, approximated by the difference between maximum and minimum pressure within the 20s windows. To be able to analyse the influence of the parameters on the strain, and hence on the tissue displacements we furthermore plot the 20s averages and corresponding amplitude approximation of the volume dilation at the skull in panels (c) and (d), respectively. The steep temporal gradients in mean volume dilation at the beginning and the end of the infusion ($T \sim 5\,\text{min}$, $T \sim 20\,\text{min}$) lead to overestimation of the amplitude for a limited time. These values were capped at twice the mean value of the volume dilation amplitude.

We start with varying those parameters that can be directly related to the parameters in the compartment model in 2.3. For these, we can check whether the changes in mean pressure match those obtained earlier. In addition, we can now consider influences of these parameters on the pressure amplitude as well as on the volume dilation.

Increasing the elasticity has the effect of decreasing the compliance and hence the CSF storage coefficient of the brain tissue. This means that a higher pressure

is necessary to accommodate a certain amount of additional fluid volume in the tissue. Thus at the start of the infusion, the pressure rises faster than for lower values of the elasticity (Figures 5.8a, 2.2a). As a consequence, the absorption rate also increases faster, so that the inflow rate is balanced earlier and less additional volume needs to be stored. Thus the volume dilation at the boundary stays smaller and even reduces as the additional fluid is distributed deeper into the tissue (Figure 5.8c). Similar effects happen on cardiac time scales due to the additional arterial blood volume. With an increased elasticity, the CSF pressure amplitude as well as the oscillations of the brain tissue are increased (Figures 5.8b, d).

Similar to the elasticity, the reference pressure has a direct influence on the specific compliance by shifting the compliance-pressure-curve along the pressure axis (compare Figure 2.10). Decreasing its value increases the pressure difference $(P - P_{\mathrm{r}})$ and thus decreases the compliance with the effects already described qualitatively (Figures 5.9, 2.3). In addition, this reduces the relative difference between the compliance value at plateau pressure level and baseline pressure level so that the ratio of pressure amplitude between these levels is reduced. When increasing the reference pressure, we need to take into account that the model breaks down as the difference between minimum CSF pressure and reference pressure approaches zero. Qvarlander et al. (2010) examined the relationship between mean pressure and its amplitude, and thus the compliance, down to small CSF pressures. They concluded that the Marmarou model, which is used here, holds for high pressures only and that there is a transition to constant compliance at lower pressures. A detailed analysis of the compliance curve over the full pressure range, such as might follow from Cirovic et al. (2003), within the poroelastic framework is beyond the scope of this thesis, so that we will have to ensure a sufficiently low reference pressure in the simulations.

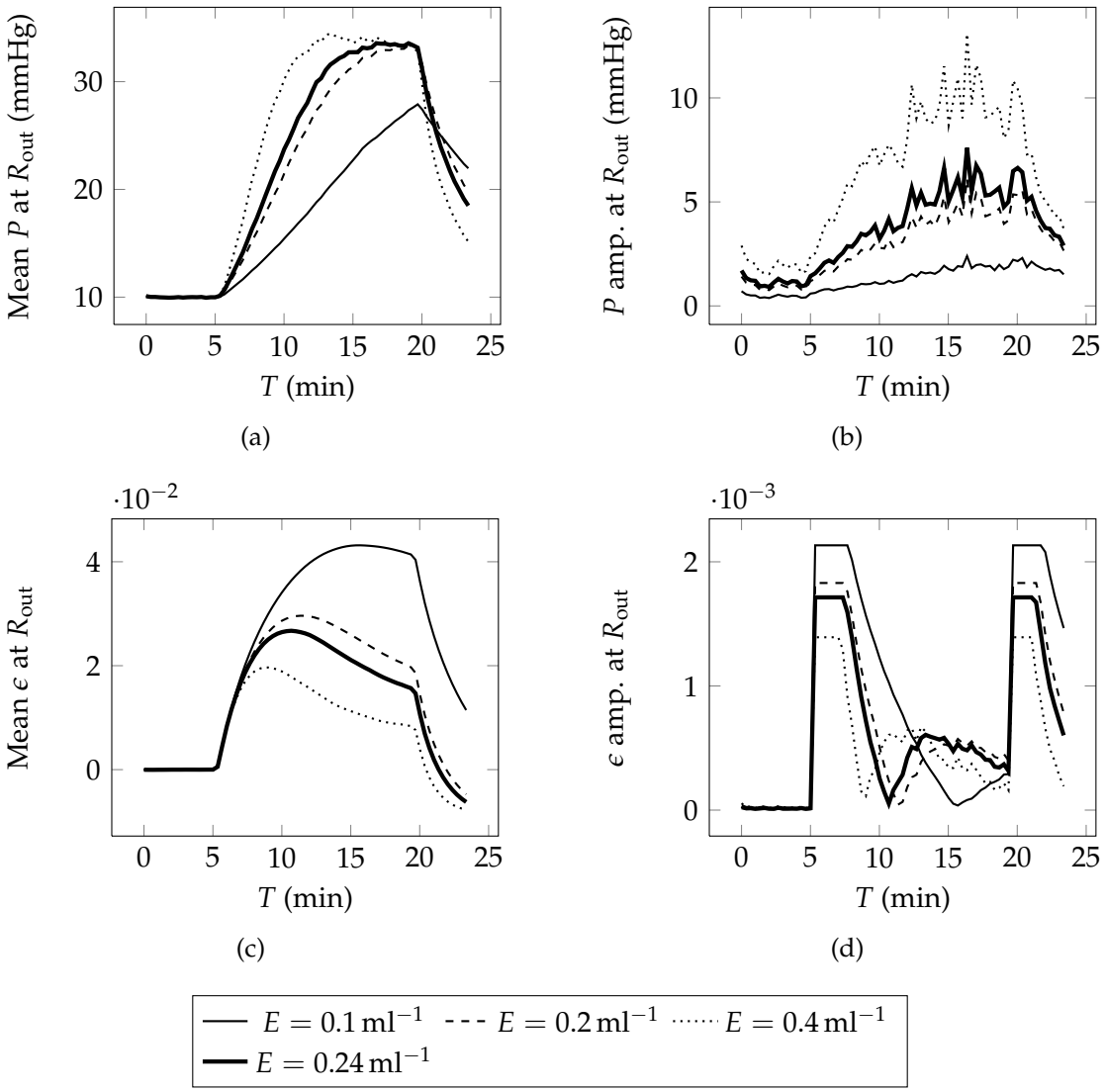

Figure 5.8: Variation of the elasticity, E: (a) mean pressure at the skull, averaged over 20s window; (b) pulse pressure at the skull, difference of maximum and minimum value over 20s windows; (c) mean volume dilation at the skull, averaged over 20s windows; (d) pulse volume dilation, difference of maximum and minimum value over 20s windows. Spikes beyond twice the average in amplitude were capped.

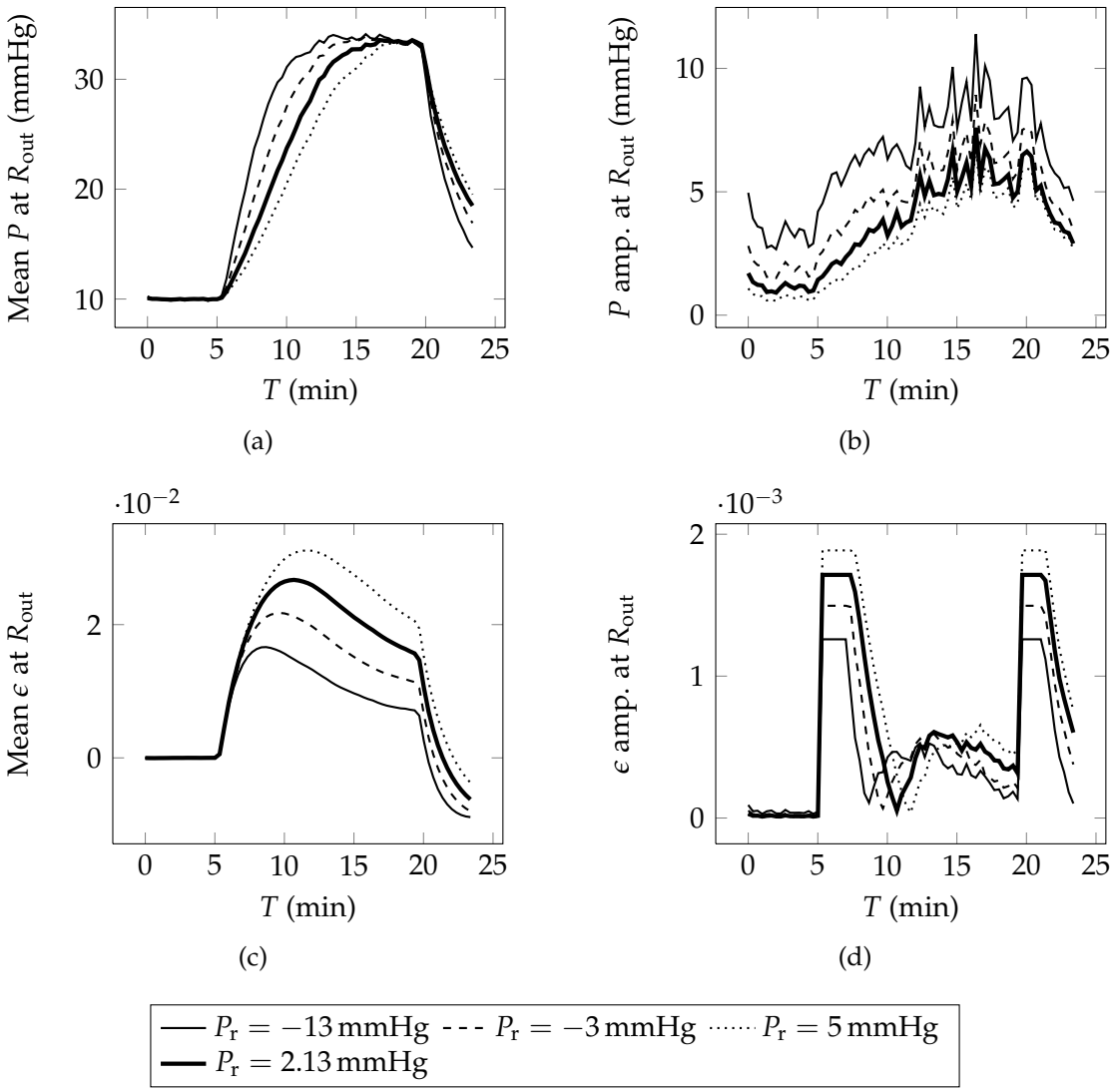

Figure 5.9: Variation of compliance reference pressure, P_{r}: (a) mean pressure at the skull, averaged over 20s window; (b) pulse pressure at the skull, difference of maximum and minimum value over 20s windows; (c) mean volume dilation at the skull, averaged over 20s windows; (d) pulse volume dilation, difference of maximum and minimum value over 20s windows. Spikes beyond twice the average in amplitude were capped.

Note that in chapter 2, the reference pressure and the sagittal sinus pressure were assumed to be equal and, together with the baseline pressure before the infusion, determined the CSF production rate. In the poroelastic model, the reference pressure, the sagittal sinus pressure and the CSF production rate are independent parameters and the average pressure before the infusion is instead a result of the simulation. Increasing the sagittal sinus pressure means that a higher mean pressure is necessary to absorb the produced CSF volume before the infusion, thus first of all shifting the mean pressure up. With increased mean pressure, the specific compliance increases, with all the known effects of steepening of the rise of mean pressure at the beginning of the infusion, increased pressure amplitude and a smaller volume dilation (Figure 5.10). Increasing the CSF production rate has basically the same effect (Figure 5.11).

As was already explained in 2.3, the resistance to outflow $\mathcal{R}$ is the main parameter determining how much the pressure needs to rise for the absorption rate to balance a given infusion rate. As opposed to the variation in chapter 2, here we keep the production rate fixed, so that the baseline pressure before the infusion needs to rise as well if the outflow resistance is increased (Figures 5.12a, 2.4a). As before, an increased pressure causes decreased compliance and thus increased pressure amplitude (Figure 5.12b). The volume dilation does not appear to change, so almost all of the fluid volume increase is accommodated via displacement of blood due to the increased CSF pressure. (Figure 5.12c, d, compare Figure 2.4).

In the next step, we consider those parameters without equivalence in the compartment model. Most of these have little to no effect on the mean CSF and its amplitude, but do change the volume dilation and hence the displacement of the brain tissue. When changing the parenchyma geometry, by either changing the

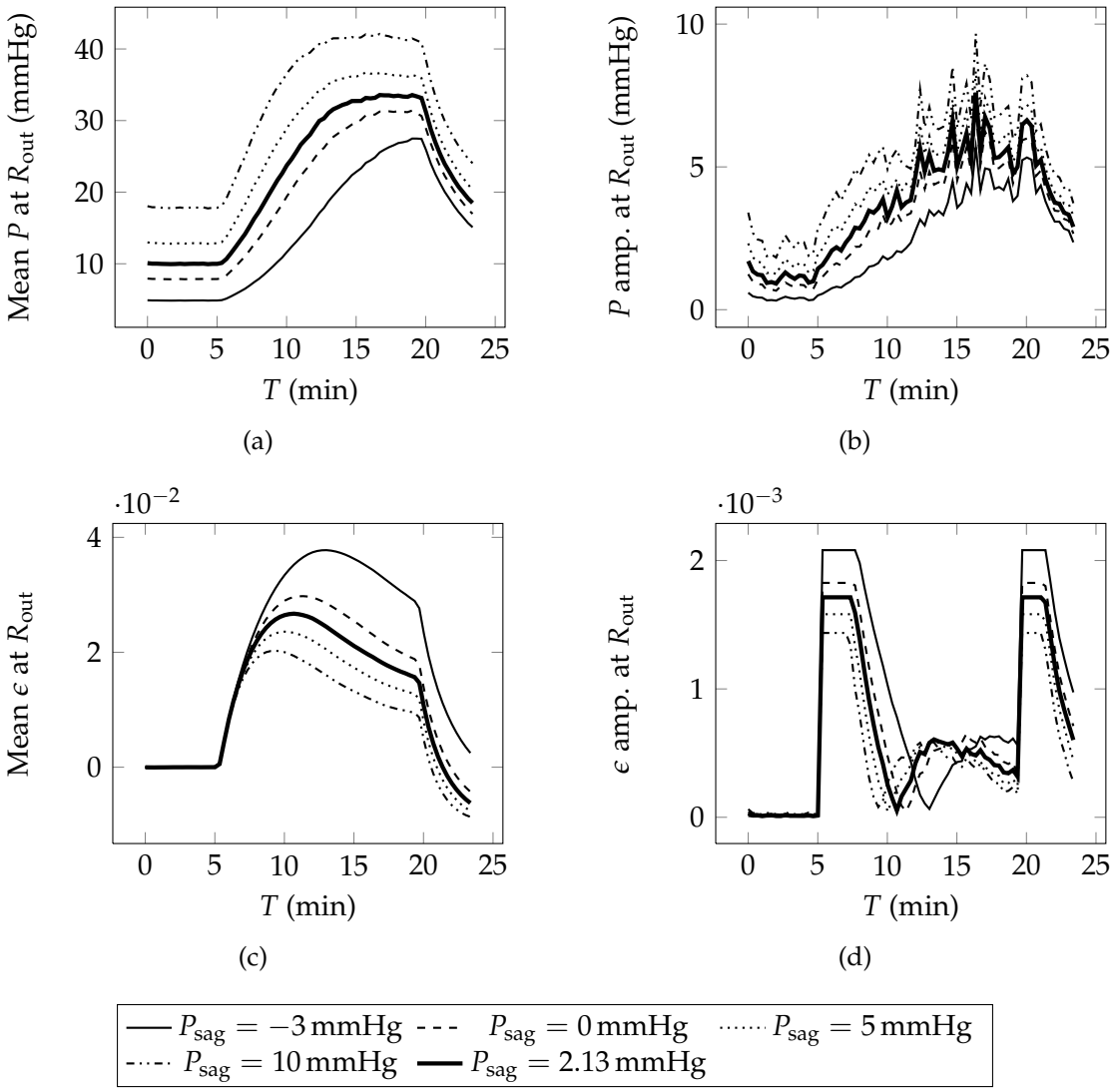

Figure 5.10: Variation of sagittal sinus (venous) pressure, P_{sag}, in mmHg: (a) mean pressure at the skull, averaged over 20s window; (b) pulse pressure at the skull, difference of maximum and minimum value over 20s windows; (c) mean volume dilation at the skull, averaged over 20s windows; (d) pulse volume dilation, difference of maximum and minimum value over 20s windows. Spikes beyond twice the average in amplitude were capped.

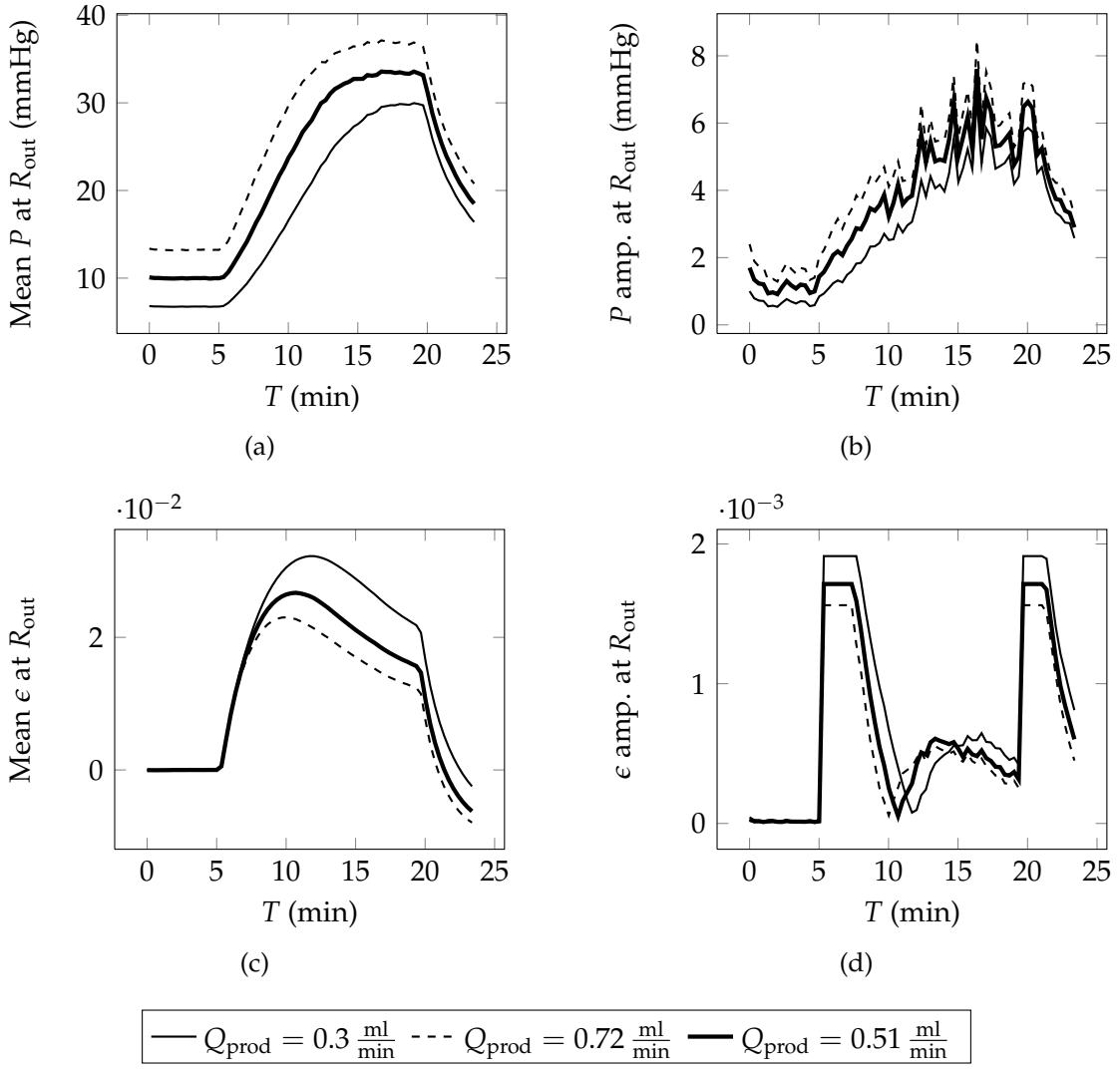

Figure 5.11: Variation of the CSF production rate, Q_{prod}: (a) mean pressure at the skull, averaged over 20s window; (b) pulse pressure at the skull, difference of maximum and minimum value over 20s windows; (c) mean volume dilation at the skull, averaged over 20s windows; (d) pulse volume dilation, difference of maximum and minimum value over 20s windows. Spikes beyond twice the average in amplitude were capped.

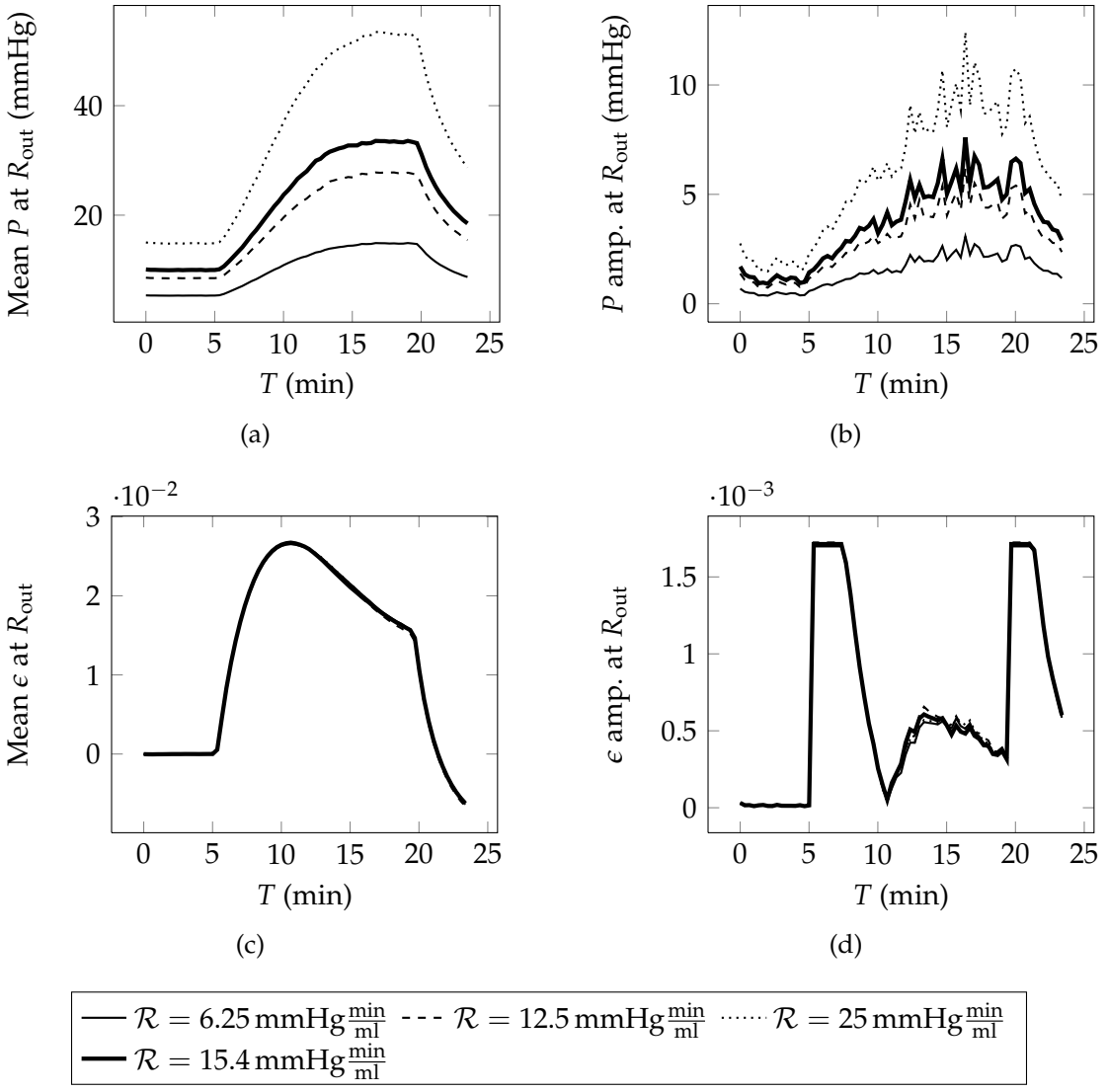

Figure 5.12: Variation of outflow resistance, $\mathcal{R}$: (a) mean pressure at the skull, averaged over 20s window; (b) pulse pressure at the skull, difference of maximum and minimum value over 20s windows; (c) mean volume dilation at the skull, averaged over 20s windows; (d) pulse volume dilation, difference of maximum and minimum value over 20s windows. Spikes beyond twice the average in amplitude were capped.

unstressed ventricle radius (Figure 5.13) or the outer brain radius while keeping the ventricle radius to scale (Figure 5.14), we need to keep in mind that we computed the specific CSF storage coefficient by scaling the total CSF compliance with the parenchyma volume (3.143). Thus it is not surprising that there is hardly any influence on the mean pressure. We have not added such scaling for the arterial blood storage coefficient, γ_a, so that the relative sizes of γ and γ_a are changing when changing the parenchyma volume. This explains the increased pressure amplitude for increased outer radius (Figure 5.14b). When changing only the ventricle radius, the decrease in parenchyma volume with increased radius is much smaller hence the decrease in pressure amplitude for increased ventricle radius is much less pronounced (Figure 5.13b). In both cases, increasing either or both radii increases the surface area of the brain tissue and therefore the tissue volume that CSF can permeate into in a short time. Hence, the same amount of CSF volume can be taken up through a smaller increase of tissue volume dilation close to the boundary. This explains the decreased mean volume dilation at the outer boundary with increased radii, as well as the corresponding decrease in volume dilation amplitude (Figure 5.13c, d, 5.14c, d).

Figure 5.15 indicates that a blockage of the aqueduct of Sylvius cannot be diagnosed via a lumbar infusion test and that imaging techniques or ventricular CSF pressure measurements are necessary. The ventricular CSF pressure must clearly be greatly increased to force all produced CSF through the tissue and compress the parenchyma as far as indicated by the volume dilation at the outer boundary. Nevertheless, according to the boundary conditions, the pressure in the cranial subarachnoid space, and hence in the spine, is fully determined by the CSF absorption through the arachnoid villi. In a real hydrocephalic brain, this absorption is

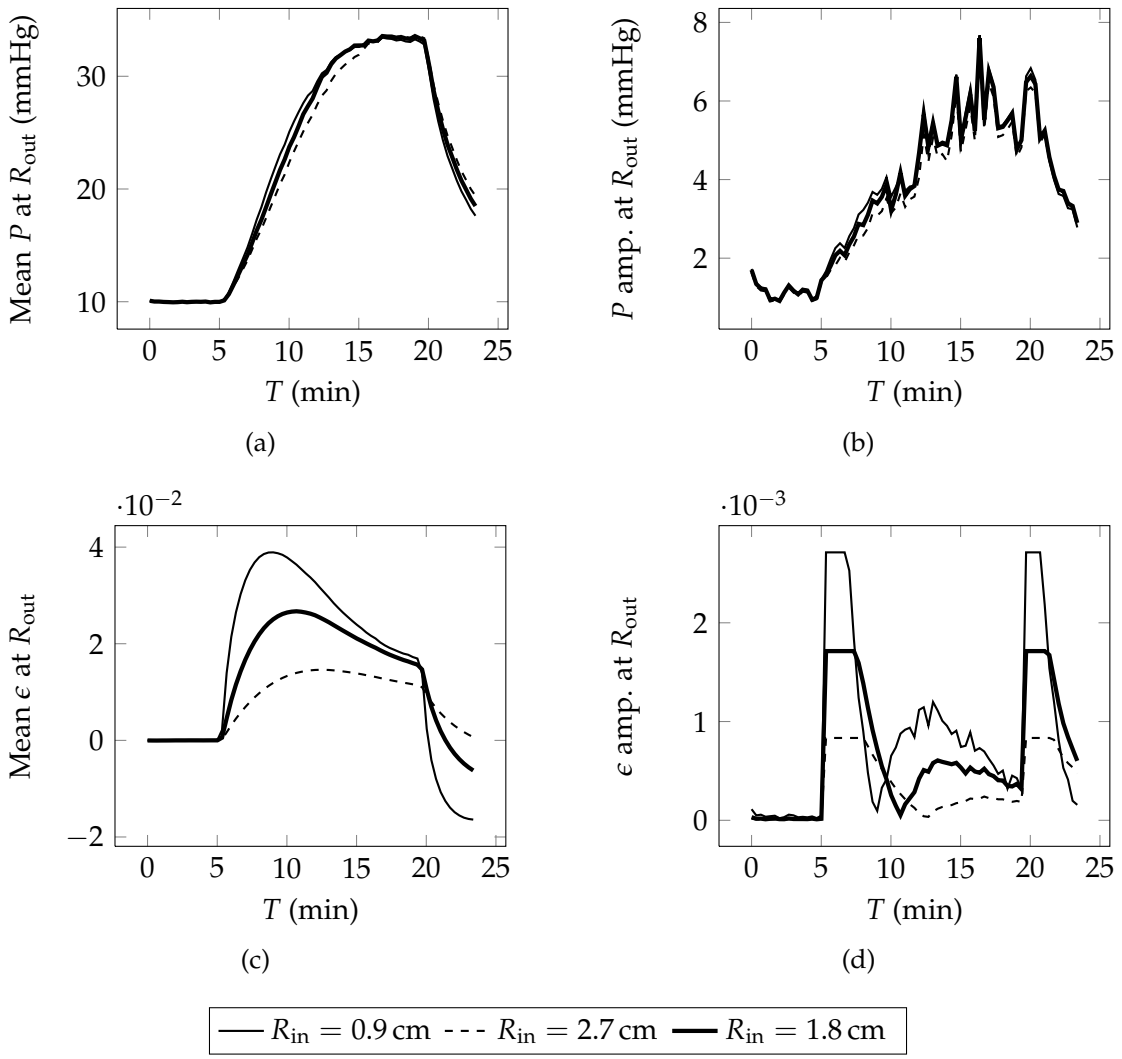

Figure 5.13: Variation of unstressed ventricle radius R_{in}: (a) mean pressure at the skull, averaged over 20s window; (b) pulse pressure at the skull, difference of maximum and minimum value over 20s windows; (c) mean volume dilation at the skull, averaged over 20s windows; (d) pulse volume dilation, difference of maximum and minimum value over 20s windows. Spikes beyond twice the average in amplitude were capped.

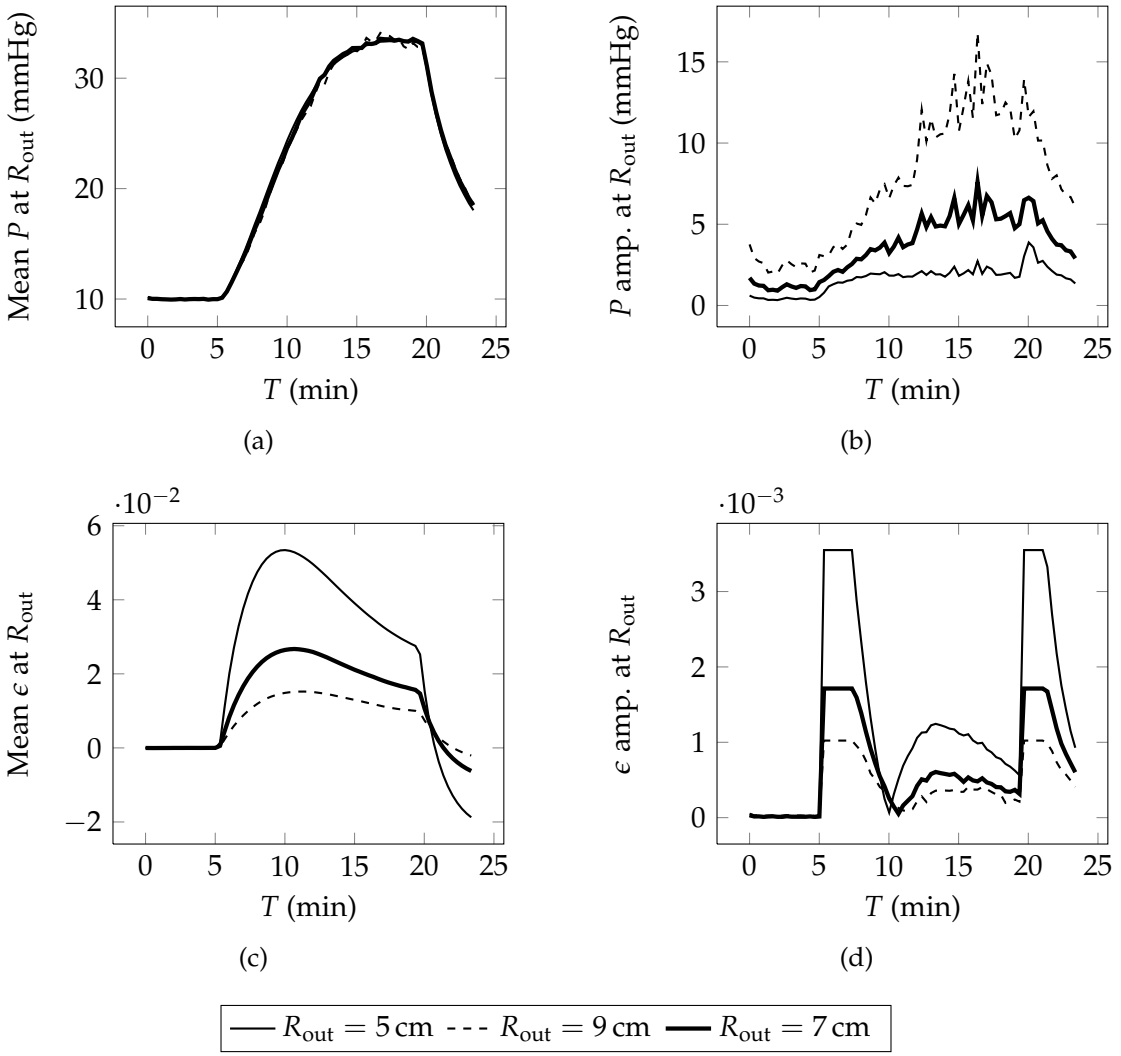

Figure 5.14: Variation of outer brain radius R_{out}, with appropriately scaled ventricle radius R_{in}: (a) mean pressure at the skull, averaged over 20s window; (b) pulse pressure at the skull, difference of maximum and minimum value over 20s windows; (c) mean volume dilation at the skull, averaged over 20s windows; (d) pulse volume dilation, difference of maximum and minimum value over 20s windows. Spikes beyond twice the average in amplitude were capped.

likely impeded as the brain tissue is pushed against the skull closing the subarachnoid space. We will not consider the case of a blocked aqueduct any further. The development of non-communicating hydrocephalus on longer time scales with poroelastic models has been researched at length (see 1.2.4). In addition, volume dilations of $\epsilon \approx -0.5$, as seen here for strongly blocked aqueducts, render the small strain assumption of our model invalid.

The two elastic parameters, Young's modulus and Poisson's ratio, have no visible influence on the pressure, but both decrease the volume dilation in mean value and amplitude, when their value is increased, that is when the tissue is assumed to be stiffer or less compressible (Figures 5.16, 5.17). Since we have no displacement or strain data to compare with, we will just leave these parameters at their default value when trying to fit the simulations to clinical data. Taking into account the uncertainty around these values (Wirth and Sobey, 2006; Cheng et al., 2008; Streitberger et al., 2011) means that our simulation of volume dilation and displacements is only qualitative.

Changing the permeability to CSF flow through brain tissue over several orders of magnitude only has a small effect on the pressure compared to the effect on the volume dilation (Figure 5.18). If the permeability is decreased, the distance CSF can travel within the tissue in a short time is limited and thus the extra volume during the infusion test has to be accommodated via strongly increased volume dilation close to the boundaries. The same is true for the volume dilation amplitude, as the absorption rate oscillates with the CSF pressure. With an open aqueduct of Sylvius, we could hardly observe any changes in either pressure or volume dilation with changes in the permeability model parameter M_0 for values between 0 and 8, since the volume dilation stays small (plots not shown). When

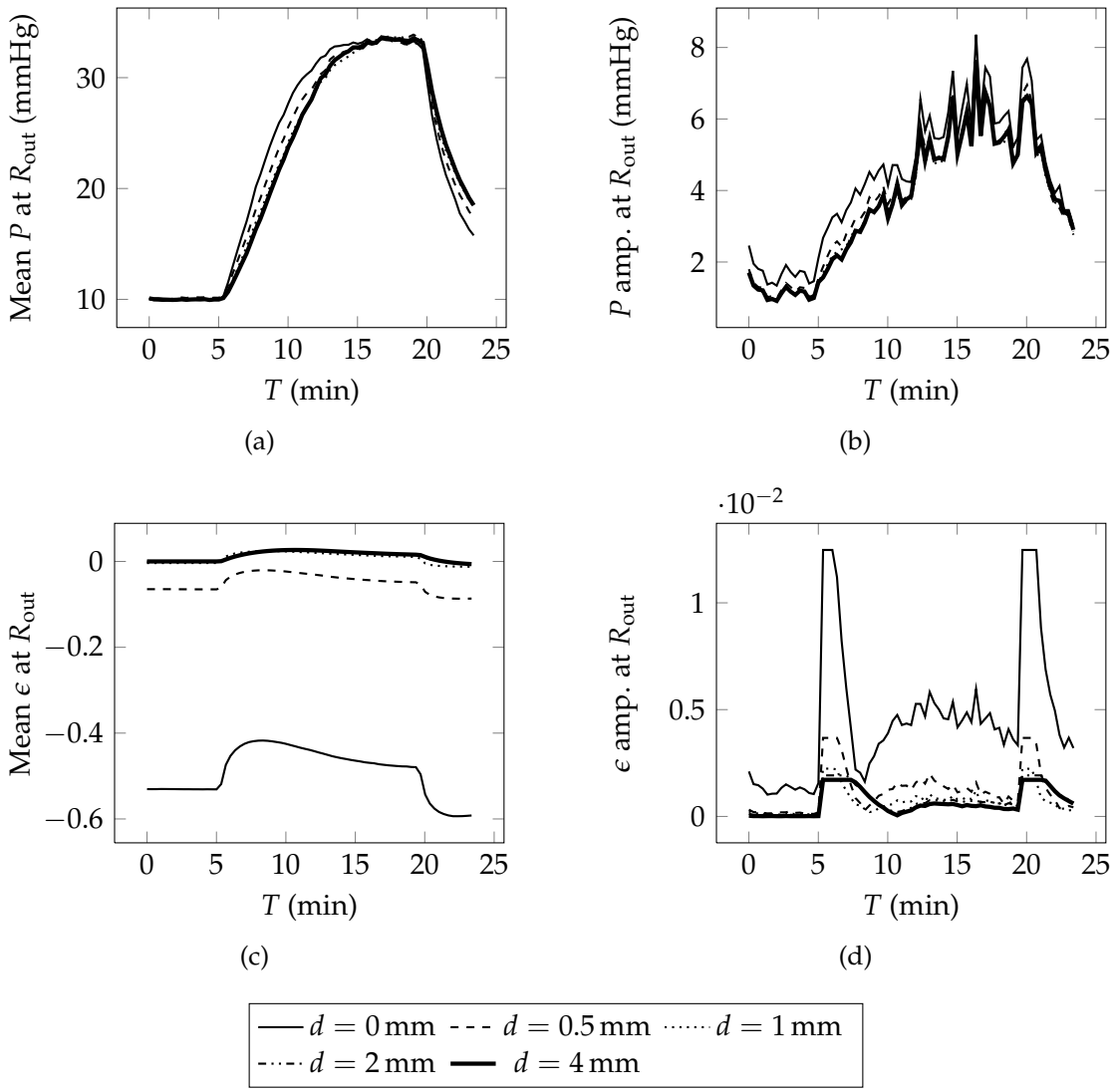

Figure 5.15: Variation of diameter, d, of aqueduct of Sylvius, connecting the ventricle and the subarachnoid space: (a) mean pressure at the skull, averaged over 20s window; (b) pulse pressure at the skull, difference of maximum and minimum value over 20s windows; (c) mean volume dilation at the skull, averaged over 20s windows; (d) pulse volume dilation, difference of maximum and minimum value over 20s windows. Spikes beyond twice the average in amplitude were capped.

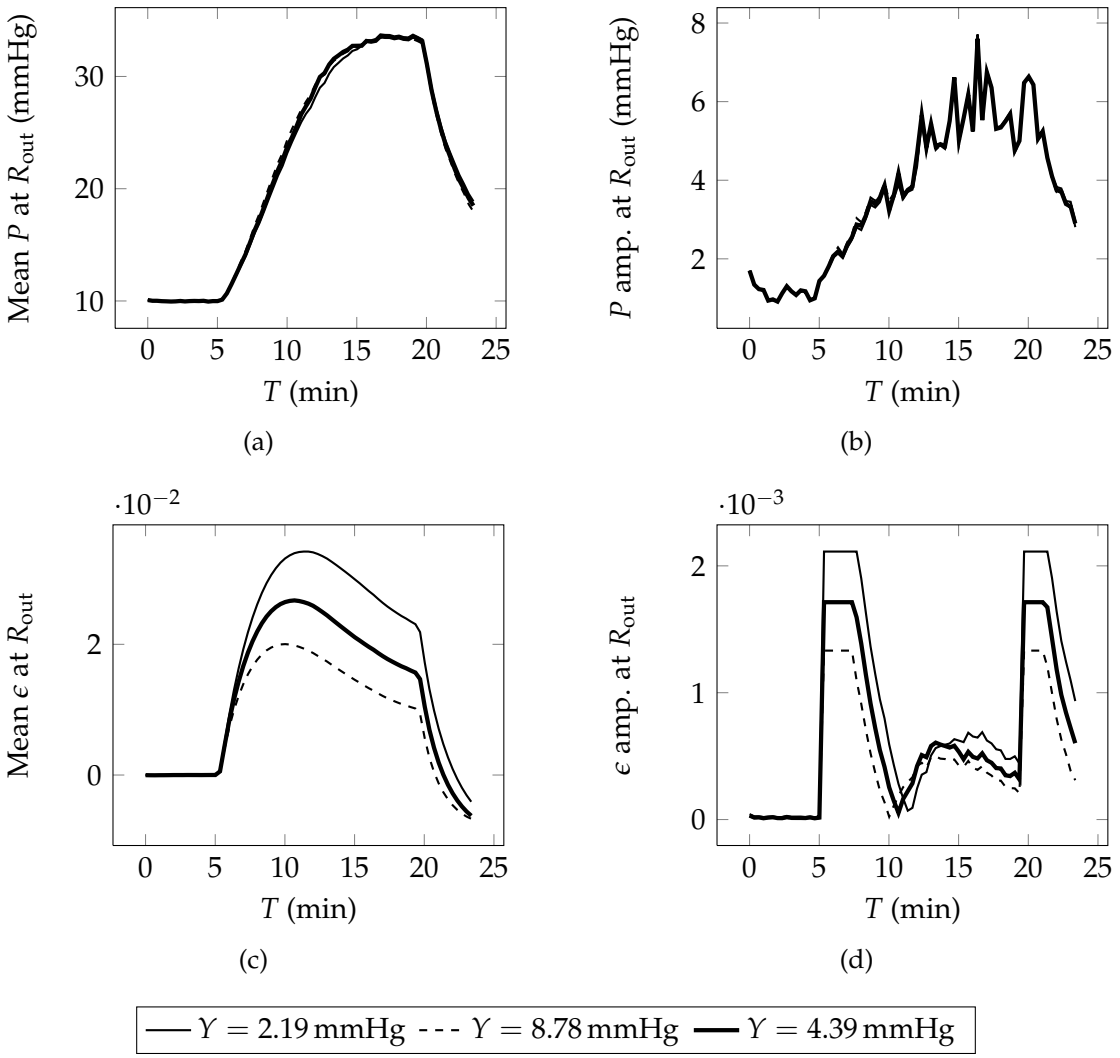

Figure 5.16: Variation of Young's modulus, Y, in mmHg: (a) mean pressure at the skull, averaged over 20s window; (b) pulse pressure at the skull, difference of maximum and minimum value over 20s windows; (c) mean volume dilation at the skull, averaged over 20s windows; (d) pulse volume dilation, difference of maximum and minimum value over 20s windows. Spikes beyond twice the average in amplitude were capped.

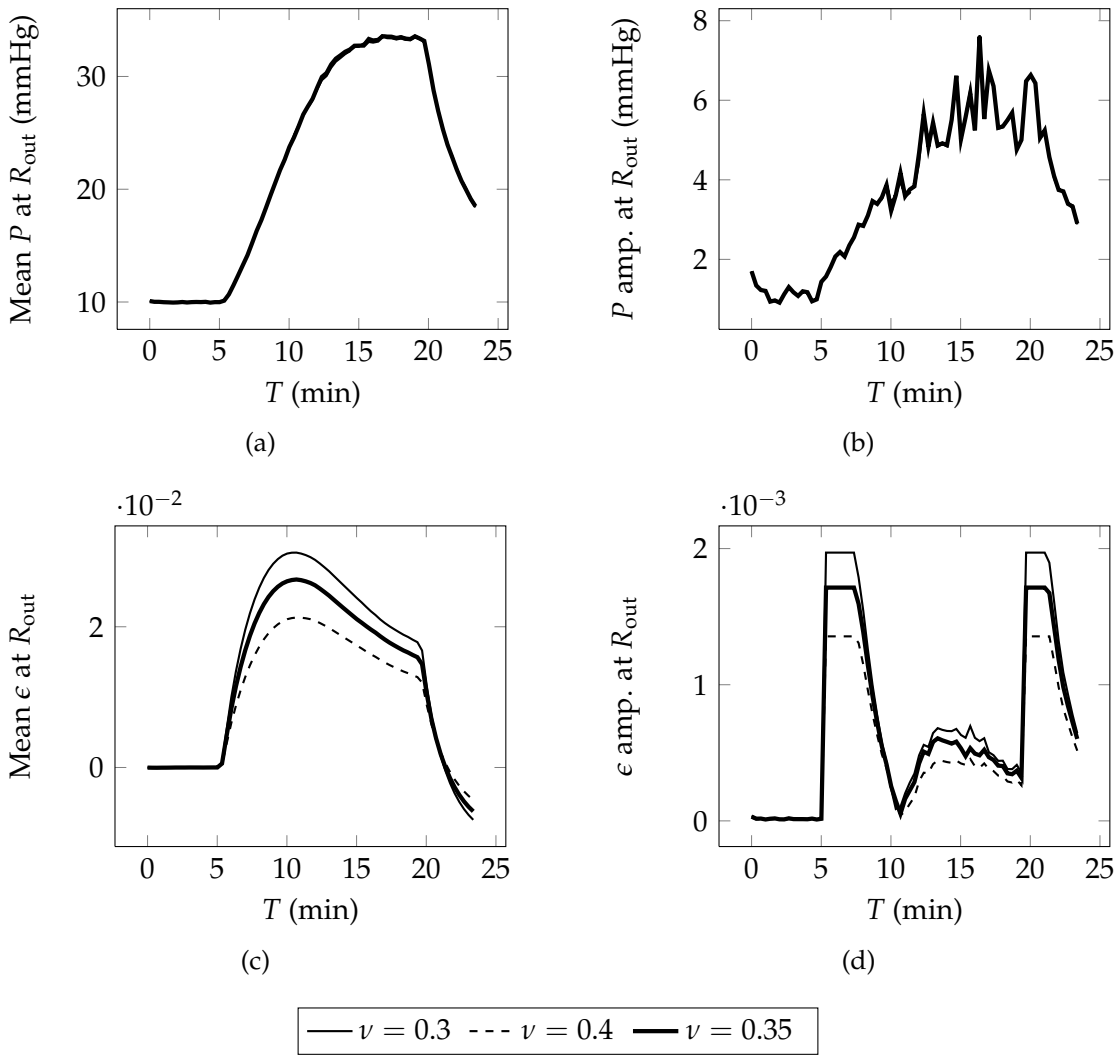

Figure 5.17: Variation of Poisson's ratio, ν: (a) mean pressure at the skull, averaged over 20s window; (b) pulse pressure at the skull, difference of maximum and minimum value over 20s windows; (c) mean volume dilation at the skull, averaged over 20s windows; (d) pulse volume dilation, difference of maximum and minimum value over 20s windows. Spikes beyond twice the average in amplitude were capped.

considering a hydrocephalic patient with large displacements then this parameter may play a role, but here, we can neglect it.

Unsurprisingly, changing the arterial blood storage coefficient γ_a mostly influences the amplitudes of pressure and volume dilation, while leaving the mean values practically unchanged (Figure 5.19). This parameter is the most likely candidate to change when the pressure amplitude of the simulation does not fit the clinical data, but increasing this parameter increases the pressure amplitude over the whole test proportionally, whereas the ratio between pressure amplitude at different mean pressures is instead determined by the compliance ratio at those pressure levels.

There is uncertainty about the value of the Biot–Willis parameter, α. Wirth and Sobey (2009) estimated the value to be between 0.9992 and 0.9999, based on relating the Biot–Willis parameter via the CSF storage coefficient to the CSF compliance. This change from their earlier estimate of 0.83, based on the volume fractions of blood and CSF (Wirth and Sobey, 2006), is much bigger than it seems, since it reduces the quantity $(1 - \alpha)$ by several orders of magnitude. The strong dependence of the infusion test result on the value of $(1 - \alpha)$ can be observed in the parameter variation in Figure 5.20.

Hardly any change in the pressure or volume dilation can be observed when the value of α is decreased from 1 to 0.9995, but as the value $(1 - \alpha)$ is increased beyond the range estimated by Wirth and Sobey (2009), a much larger fraction of the load from the pressure inside the ventricle has to be balanced by elastic stresses at the ventricle wall according to the boundary condition (3.121). Hence, the tissue is more and more compressed towards the skull and the storage of additional CSF volume happens more and more in the ventricle rather than within the porous

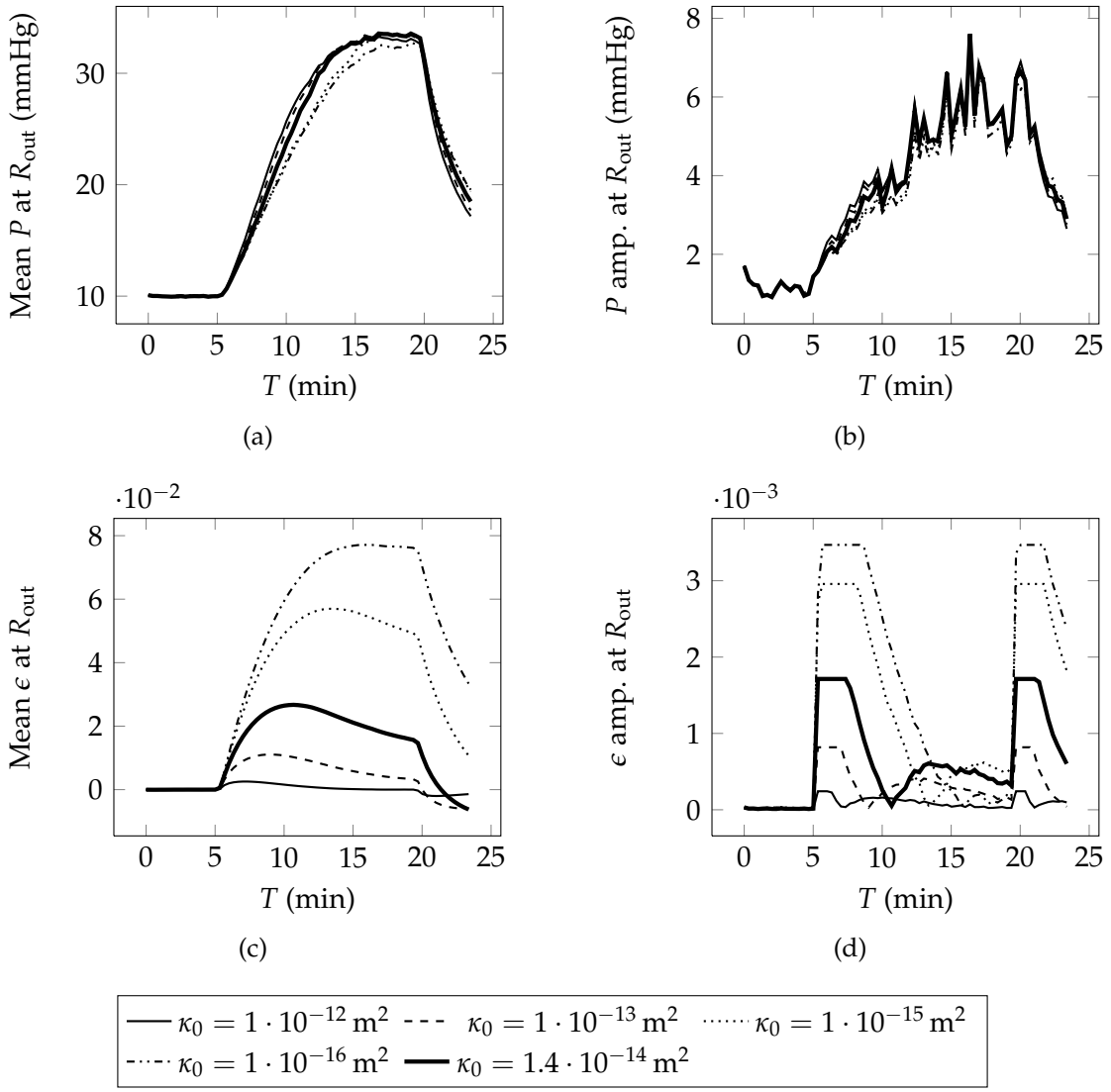

Figure 5.18: Variation of the permeability constant, κ_0: (a) mean pressure at the skull, averaged over 20s window; (b) pulse pressure at the skull, difference of maximum and minimum value over 20s windows; (c) mean volume dilation at the skull, averaged over 20s windows; (d) pulse volume dilation, difference of maximum and minimum value over 20s windows. Spikes beyond twice the average in amplitude were capped.

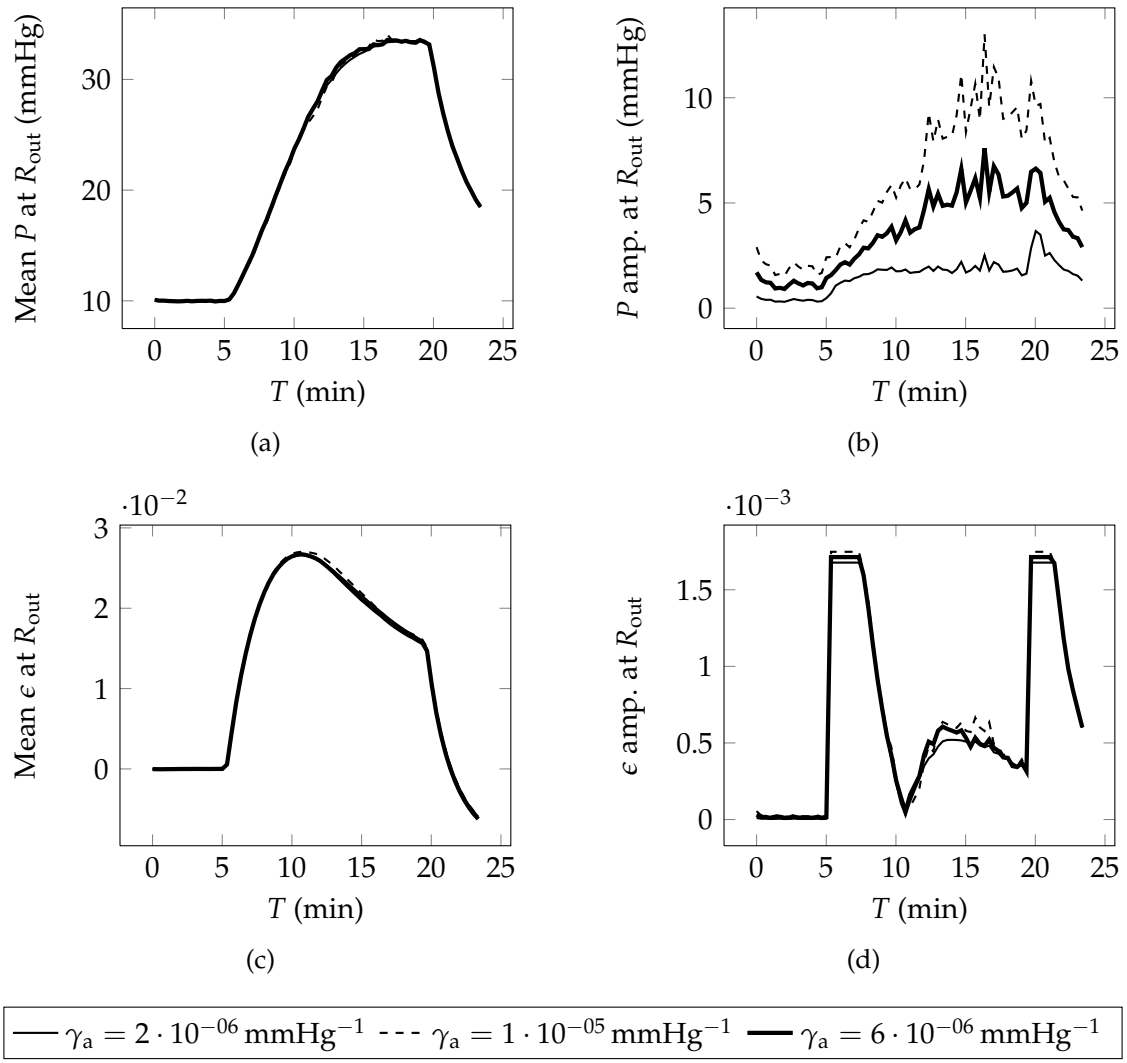

Figure 5.19: Variation of arterial blood storage coefficient, γ_{a}, in mmHg^{-1}: (a) mean pressure at the skull, averaged over 20s window; (b) pulse pressure at the skull, difference of maximum and minimum value over 20s windows; (c) mean volume dilation at the skull, averaged over 20s windows; (d) pulse volume dilation, difference of maximum and minimum value over 20s windows. Spikes beyond twice the average in amplitude were capped.

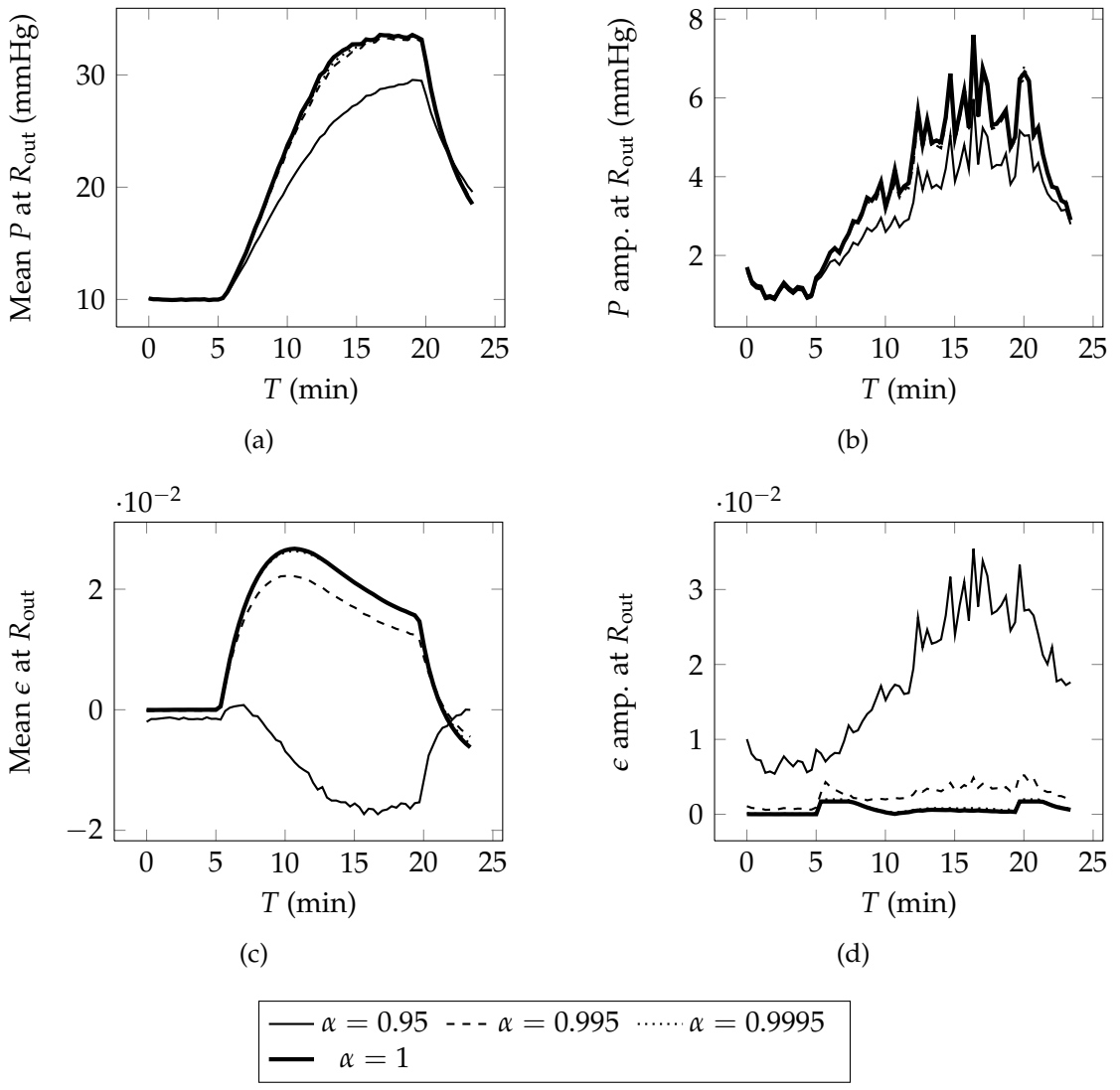

Figure 5.20: Variation of CSF Biot–Willis parameter α: (a) mean pressure at the skull, averaged over 20s window; (b) pulse pressure at the skull, difference of maximum and minimum value over 20s windows; (c) mean volume dilation at the skull, averaged over 20s windows; (d) pulse volume dilation, difference of maximum and minimum value over 20s windows. Spikes beyond twice the average in amplitude were capped.

tissue. Thus, the relationship we made between the multi-fluid poroelastic model and the compartment model in 3.5.4 breaks down. Due to this apparently more efficient storage of fluid, the pressure appears to plateau at a much lower value. Nevertheless, this cannot be a steady state yet, since at this pressure, the infusion rate is not balanced by the absorption rate. In this case, the resistance to CSF outflow would routinely be underestimated by constant infusion tests.

While we will use the values for the Biot–Willis parameter proposed by Wirth and Sobey (2009) in the remainder of this chapter, it is important to note for future poroelastic modelling of CSF flow in the brain how sensitive the results are to this parameter and that better ways of measuring its value should be found soon. One potential indirect experiment would be to compare the fractions of ventricular and porous CSF storage during an infusion test with suitable imaging techniques.

Assuming the value $\alpha = 0.9995$ from Wirth and Sobey (2009), we can explore the range 0 to 0.0005 for the arterial blood Biot–Willis parameter α_a (Figure 5.21). There is no change in pressure and changes in mean or amplitude of volume dilation are only visible once the value of α_a reaches the maximum possible order of magnitude. At and below the order of magnitude of 10^{-5} proposed by Wirth and Sobey (2009), the change in volume dilation is negligible.

As long as the values of $(1 - \alpha)$ and α_a are kept within the order of the values estimated by Wirth and Sobey (2009), the changes in CSF pressure and tissue volume dilation are very small. Taking these orders of magnitude for granted, we introduce little error by setting the values to $\alpha = 1$ and $\alpha_a = 0$, respectively. Nevertheless, the values of these parameters and potential biomechanical derivations for their values should be examined further.

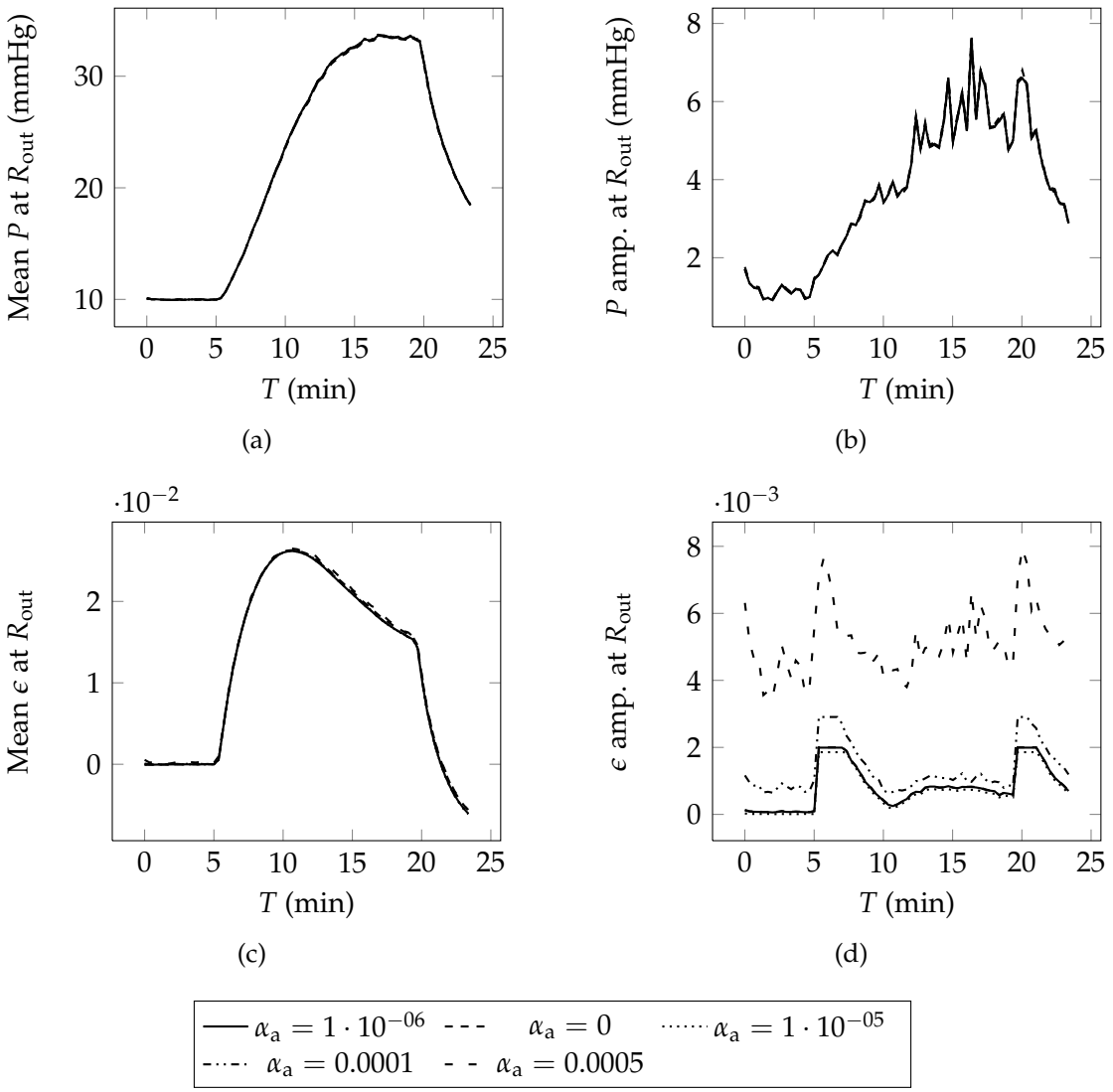

Figure 5.21: Variation of arterial blood Biot–Willis parameter, α_a, with the CSF Biot–Willis parameter set to $\alpha = 0.9995$: (a) mean pressure at the skull, averaged over 20s window; (b) pulse pressure at the skull, difference of maximum and minimum value over 20s windows; (c) mean volume dilation at the skull, averaged over 20s windows; (d) pulse volume dilation, difference of maximum and minimum value over 20s windows. Spikes beyond twice the average in amplitude were capped.

Given the parameter variations, we can see which parameters we do not need to consider when trying to fit a simulation better to clinical pressure measurements. There is no gain in changing parameters that have no or only very little influence on the pressure. These include most of the poroelastic parameters: Young's modulus, Poisson's ratio, the two parameters describing the strain-dependent permeability and the Biot–Willis parameter for the CSF and arterial blood networks. In addition, we will keep the three geometry parameters at their default values. The influence of the ventricle and outer brain radii on the pressure amplitude is only indirect via scaling of the storage coefficient with the parenchyma volume. If data about the patient's ventricle or head size were available, then this could be taken into account to estimate the radii. A blockage of the aqueduct does not significantly change the pressure response at the outer boundary and would instead be diagnosed by other means than a lumbar infusion test.

Since the parameters relating to the compartment model have already been fitted to the mean pressure behaviour during the infusion, these should be changed only very carefully. In particular, it should not be necessary to change the resistance to CSF absorption. Furthermore, the sagittal sinus pressure and CSF production rate should, if at all, only be changed together to keep the baseline pressure unchanged. The parameter that most likely will need to be adapted is the arterial blood storage coefficient, which increases or reduces the pressure amplitude overall. If the pressure oscillations need to change differently at different pressure levels, then the compliance may need to be adapted via the reference pressure. It may then be necessary to change the elasticity as well to correct the mean pressure response.

5.4 Analysis of infusion tests

We now consider for a group of data sets how well the simulations fit the measured pressure if the compliance parameters estimated for the single compartment model in chapter 2 and default values for the other poroelastic parameters and the geometry are used. Furthermore, we try to improve these fits by changing some of the parameters manually. In 5.3, we noted which parameters should best be considered for changes in the pressure response. The clinical data sets contain waves and irregularities on time scales of a few minutes, for example due to biological processes or movements of the patient. These are not captured by the multi-fluid poroelastic model. They also imply that the minimum and maximum pressure within a longer time interval may be much further apart than the peak-to-peak amplitude associated with the arterial blood pressure oscillations. To reduce this effect, time windows for averaging and estimation of the amplitude have been reduced to 5 seconds for the following plots.

The first set considered, is in our notation data set 00. This is the same data that was used previously for the parameter variations in section 5.3. Figure 5.22 shows the measured pressure average response and amplitude, as well as the results from the multi-fluid poroelastic model for the default set of parameters given in Table 5.1. Since the parameters of the compartment model, which describe the average pressure behaviour, were fitted to the pressure measurements in chapter 2, Table 2.6, it is not surprising that we obtain a good fit of the average pressure with the simulation.

The pressure amplitude, on the other hand, can clearly still be improved. It is obvious that the simulated amplitude is overall too low. This can be explained

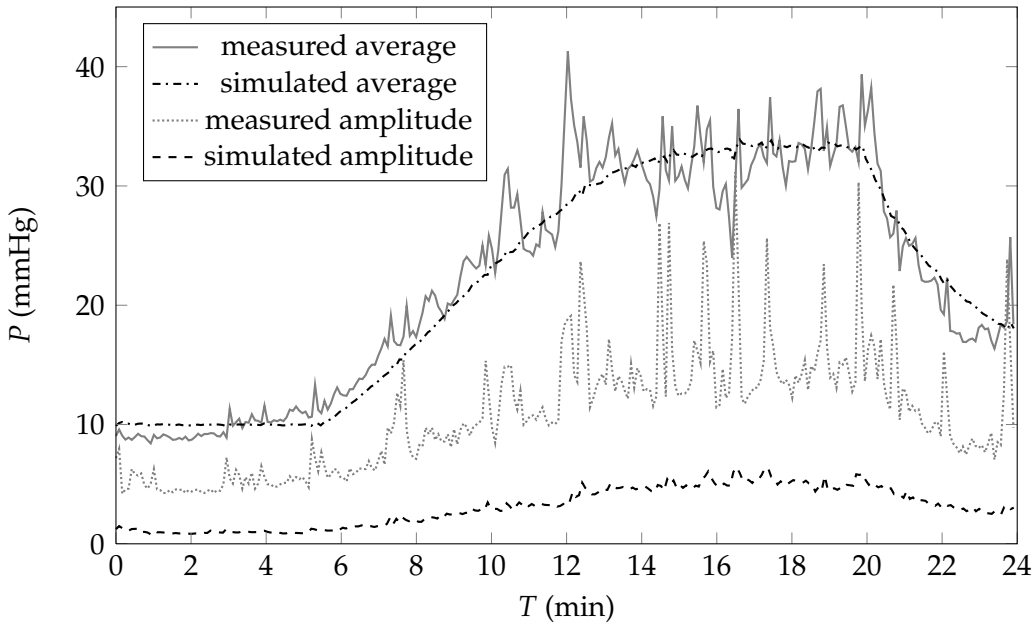

Figure 5.22: Comparison of measured and simulated intracranial pressure for data set 00, where the simulation uses the default parameters from Table 5.1.

by the fact that we have used the value for the arterial blood storage coefficient, γ_a, from Wirth and Sobey (2009), who fitted their value to clinical data, but in our case, the parenchyma volume is lower due to the decreased outer brain radius. As seen in 5.3, Figure 5.14, this reduces the pressure amplitude due to scaling of the CSF storage compliance, $\gamma(P)$.

However, an increase in the value for γ_a would not be enough to obtain a good fit of the pressure amplitude. The reason is that a change in this value only scales the simulated amplitude over the whole test, but the ratios of the amplitude before the infusion and at the plateau pressure are different. For the measured data, the amplitude at the plateau pressure is about three times that before the infusion. In the simulation result, the factor is 5.33. Thus a change in the CSF compliance is necessary as well.

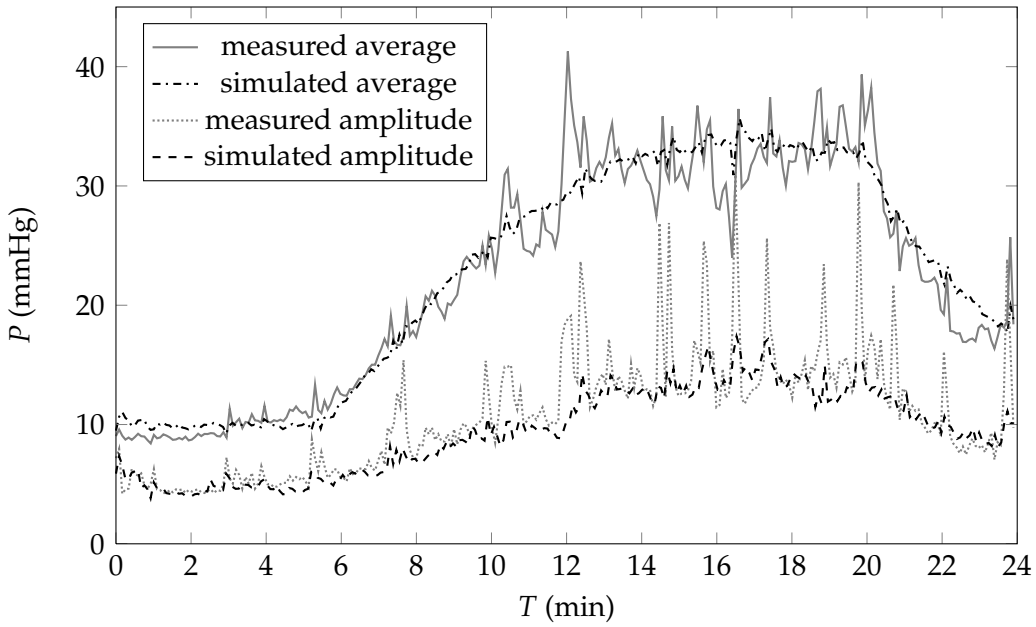

Figure 5.23: Comparison of measured and simulated intracranial pressure for data set 00, with the parameters from Table 5.1, except for $E = 0.15\,\mathrm{ml}^{-1}$, $P_\mathrm{r} = -10\,\mathrm{mmHg}$, $\gamma_\mathrm{a} = 1.8 \cdot 10^{-5}\,\mathrm{mmHg}^{-1}$.

At first, we decrease the reference pressure, P_r, to improve this ratio. The new value we choose is $P_\mathrm{r} = -10\,\mathrm{mmHg}$. This of course also affects the average pressure response, as it overall decreases the compliance, thus the pressure rises quicker at the beginning of the infusion. To remedy this, in the second step, the elasticity, E, is modified. In the final step, we increase the arterial blood storage coefficient, γ_a, to fit the pressure amplitude. The result of the simulation with these new parameter values can be found in Figure 5.23. Except for wave-like behaviour, the pressure amplitude now fits the measured data almost perfectly. In addition, the average pressure behaviour seems to have improved compared to the simulation with default parameter values seen in Figure 5.22.

In the measurements of data set 02, the pressure amplitude is practically constant for the whole duration of the test (Figure 5.24a). This requires a reference pressure

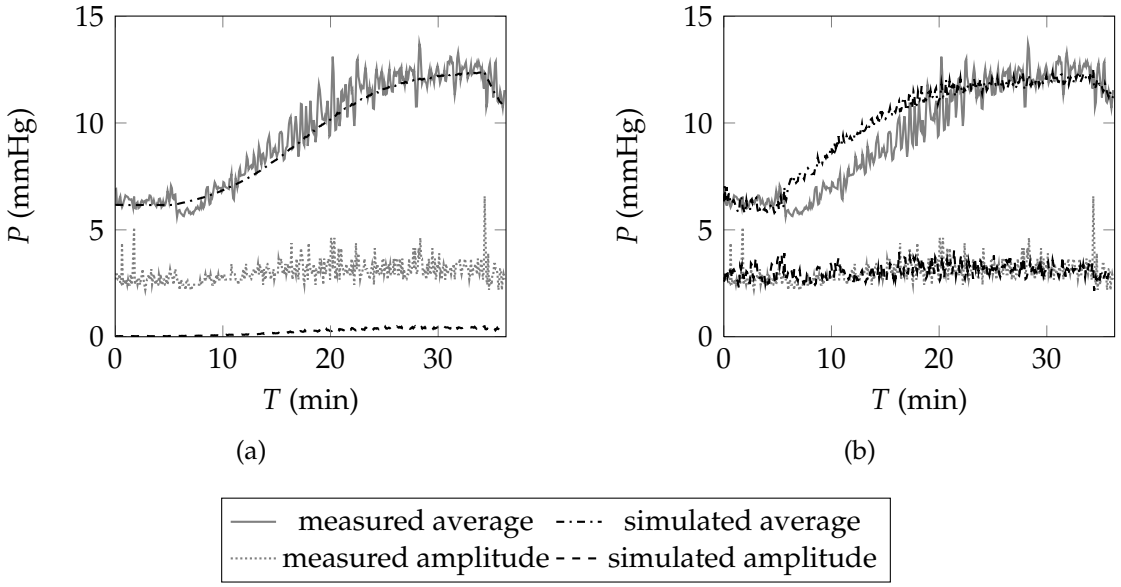

Figure 5.24: Comparison of measured and simulated intracranial pressure for data set 02 (a) with default parameter values from Table 5.1 for the geometry and poroelastic parameters and Table 2.6 (row 02 A) for the compliance parameters, (b) with constant compliance $C = 1.84\,\mathrm{ml/mmHg}$, $\gamma_a = 8.4 \cdot 10^{-5}\,\mathrm{mmHg}^{-1}$ and other parameters from Tables 5.1 and 2.6 (row 02 A).

with a large negative value, or a power index n close to zero in the generalised compliance model. Instead the automatic optimisation in chapter 2 estimated the value to be very close to the baseline pressure, forcing the pressure to stay almost constant at the beginning of the infusion. This is caused by the drop in average pressure at the beginning of the infusion, which is of unknown origin and not included in the simulation. To get a better fit of the pressure amplitude, we set the compliance to a constant. Its value is determined by manually fitting the slope of the average pressure of the simulation to that in the measurements. Again, the final step is an increase in the arterial blood storage coefficient, γ_a, to fit the pressure amplitude (Figure 5.24b).

The parameters for data set 06 can be fitted to the measurements in the same way as for set 00. For panel a of Figure 5.25, we have used the default values for that

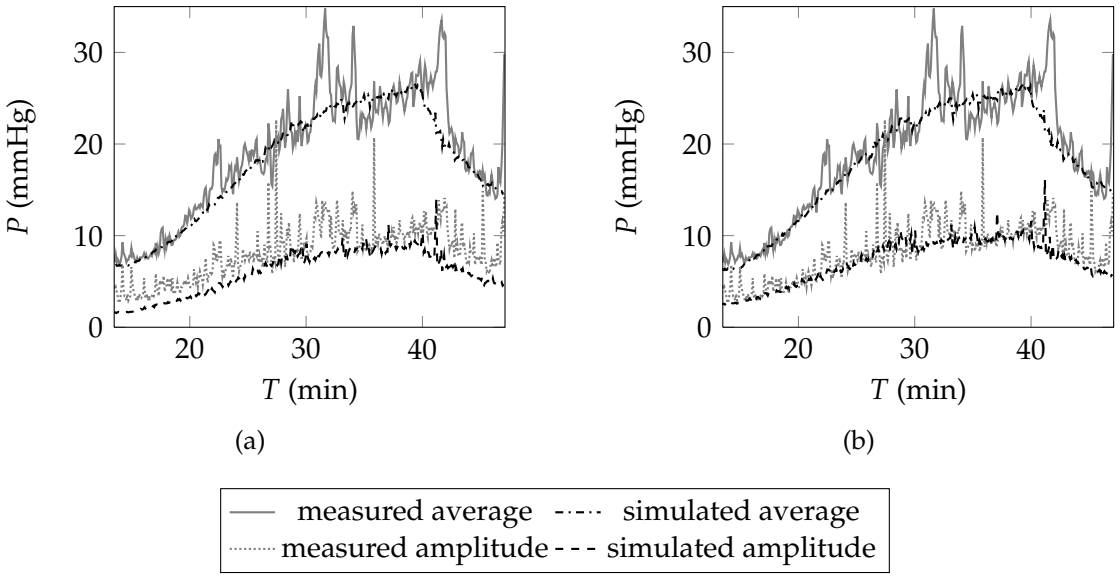

Figure 5.25: Comparison of measured and simulated intracranial pressure for data set 06 (a) with default parameter values from Table 5.1 for the geometry and poroelastic parameters and Table 2.6 (row 06 A) for the compliance parameters, except for $\gamma_a = 24 \cdot 10^{-6}\,\mathrm{mmHg}^{-1}$, (b) with $E = 0.12\,\mathrm{ml}^{-1}$, $\gamma_a = 2.4 \cdot 10^{-5}\,\mathrm{mmHg}^{-1}$. and other parameters from Tables 5.1 and 2.6 (row 06 A).

set, but have already increased the arterial blood storage coefficient, γ_a, to be able to better see the amplitude ratio. Decreasing the reference pressure to zero yields a good fit of the amplitude with this value of γ_a. Thus scaling the elasticity, E, to improve the average pressure behaviour and scaling the arterial blood storage coefficient, γ_a, with the inverse factor leads to the pressure amplitude staying approximately unchanged.

For the other sets, that is sets 03, 04, 07 and 08, we have not attempted to fit the pressure oscillation of the simulations to the measured data, but only give, in Figure 5.26, the plots comparing the simulations with their respective default parameter values according to Table 5.1 for the geometry and poroelastic parameters and Table 2.6 for the compliance parameters with the measurements. Again, we

observe the discrepancy between the average pressure behaviour and the ratio of the pressure amplitude from before the infusion to the plateau pressure. For the data sets 03, 04 and 07 (Figure 5.26a–c), the amplitude ratio of the simulated pressure is larger than that of the measured pressure, most notably so for set 07 (Figure 5.26c). For these cases, the procedure would be the same as above. For data set 08 (Figure 5.26d), the simulated pressure has not reached a plateau yet, whereas this seems to be the case for the pressure measurements. The reasons for this are most likely the large waves in the pressure, which lead to errors in the optimisation procedure in chapter 2. For this data set, the resistance to outflow and the CSF production rate or the sagittal sinus pressure need to be revised in addition to the compliance parameters.

For the two data sets 00 and 06, we can compare the compliance function estimated by the optimisation procedure in chapter 2 with that estimated by taking the pressure oscillations into account (Figure 5.27). For data set 00, the two compliance functions are of similar size, but their pressure dependence is quite different, due to a large change in reference pressure (Figure 5.27a). For data set 06, on the other hand, the two compliance functions almost agree over about half the pressure range of the infusion test and only diverge for lower pressures (Figure 5.27b). These differences and similarities are also reflected in the average pressure response. The difference in mean pressure for data set 00 (Figures 5.22, 5.23) is more evident than that for data set 06 (Figure 5.25).

By design, in both cases, the second compliance function leads to a better fit of the pressure amplitude, which was disregarded in chapter 2. In addition, at least visually, the second compliance function for data set 00 fits the mean pressure measurements better than the first. Thus, we see again the challenge for automatic

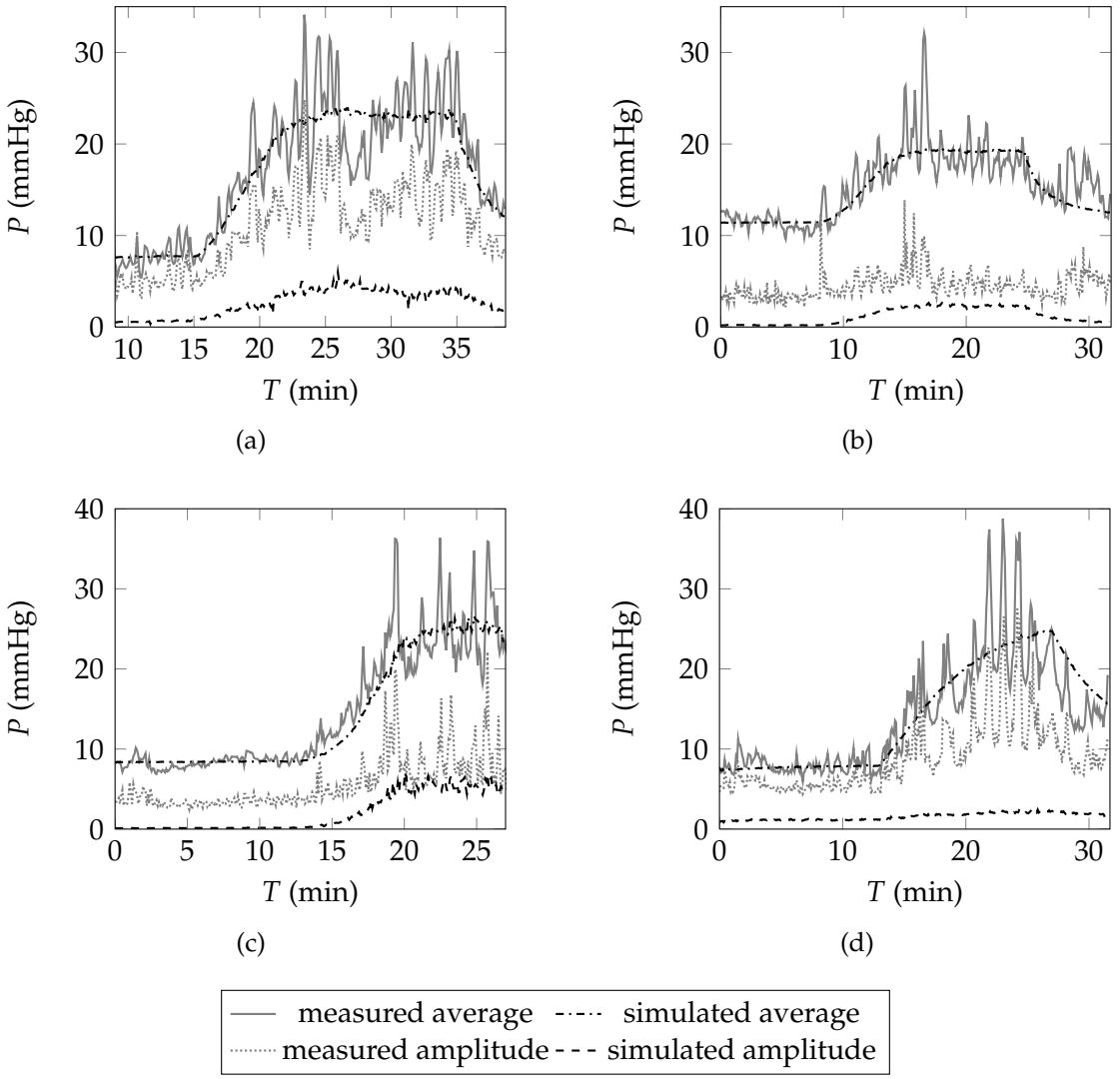

Figure 5.26: Comparison of measured and simulated intracranial pressure for data sets (a) 03, (b) 04, (c) 07 and (d) 08 with their respective default parameter values according to Table 5.1 for the geometry and poroelastic parameters and Table 2.6 for the respective compliance parameters.

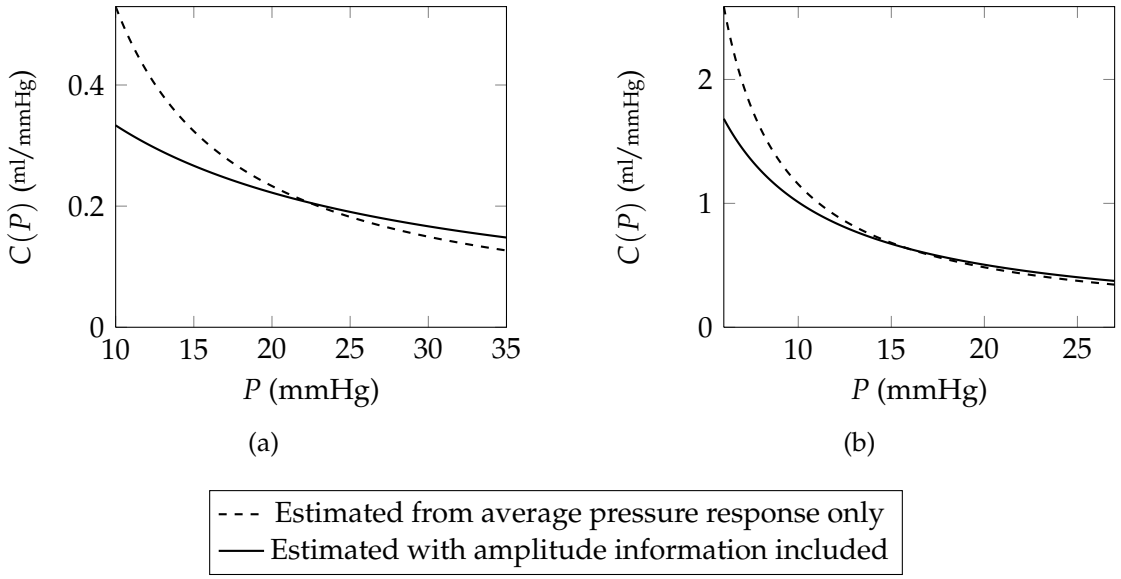

Figure 5.27: Comparison of compartment functions estimated from the average pressure response only or with amplitude information included for (a) data set 00 and (b) data set 06.

estimation of parameter variations from the mean pressure response alone. Taking into account the pressure amplitude during the test may make estimation of the compliance from infusion test data more reliable. In this context, the constant pressure infusion test (Eklund et al., 2007) may be preferable to the constant rate infusion test, because the different pressure levels are easier to distinguish and thus the dependency between mean pressure and pressure amplitude is more clearly visible. However, this requires our assumption of a pressure-independent arterial blood storage coefficient, γ_a, to be at least approximately valid. Again, we stress that the actual values of the elasticity and reference pressure, or any other set of parameters used to describe the compliance, are not anywhere near as important as the functional form of the compliance that they encode together.

5.5 Distribution of fluid volume for continued infusion

The plots of the simulation with default parameter values in 5.2 indicate that no steady state has been reached yet when the infusion is stopped (Figures 5.3–5.7). Instead, CSF still flows from both boundaries into the porous tissue and further distributes within the tissue. Thus, to investigate the long term behaviour of an infusion test, we consider one simulation with the default parameters with a continuous infusion over 48 hours. Since there is no arterial blood pressure data for such a long time and to keep the computation times short, the arterial blood pressure was set constant to the average value over the full infusion test of data set 00.

The first observation we make is that the "plateau" pressure which would be observed during an infusion test of less than half an hour is not the final steady state pressure, but only a transient maximum. The pressure drops thereafter by about 0.4 mmHg over the following hours of continued infusion (Figure 5.28). At the same time, the parenchyma displacement slowly relaxes and the volume dilation returns to its pre-infusion state (Figure 5.29). After 20 hours, the difference between the current volume dilation and that in the initial condition is below the relative tolerance of 10^{-6}, which we have used in our simulations, and is decreasing further over the remaining 28 hours of simulated infusion. This means that an infusion test of up to about half an hour duration will slightly overestimate the plateau pressure and thus the resistance to CSF absorption.

In Figure 5.30, we can see where the additional CSF volume is stored. Initially, on the time scale of the infusion test, most of the volume is stored inside the ventricle

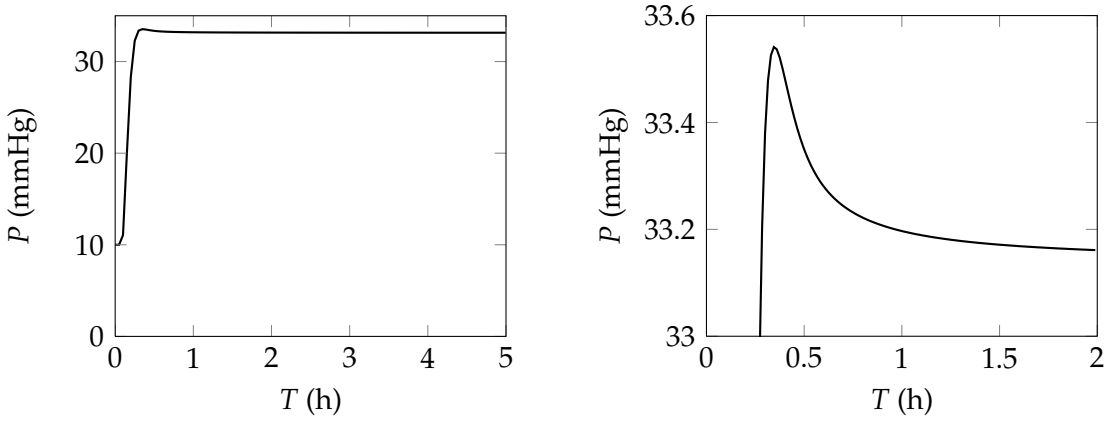

Figure 5.28: Pressure versus time for continuous infusion: (a) pressure during the first 5 hours, (b) close up of the increased pressure during the first two hours.

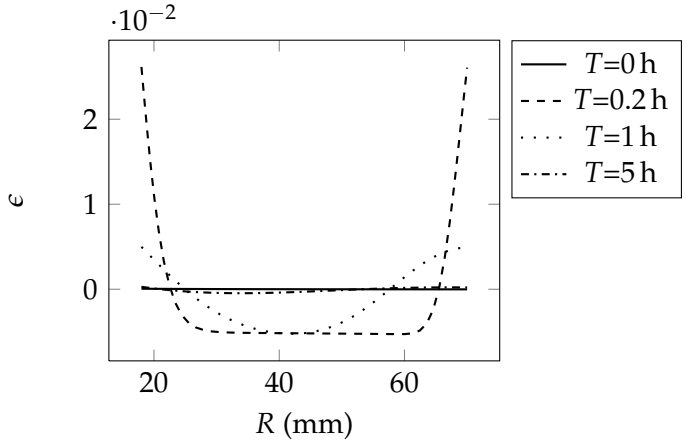

Figure 5.29: Volume dilation across the parenchyma radius for different times during continuous infusion started at 5 min of the test.

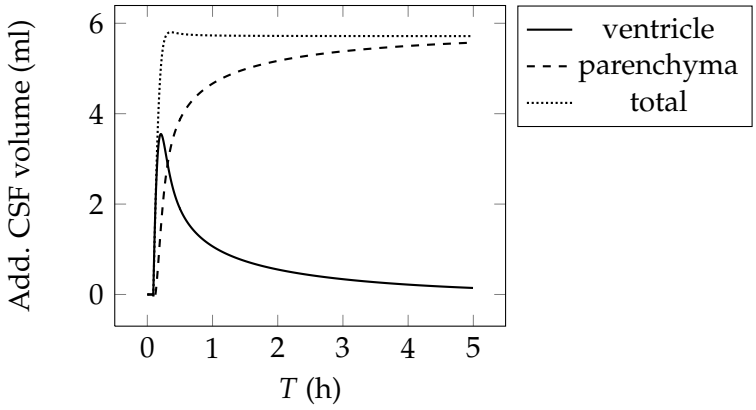

Figure 5.30: Additional CSF volume storage in the ventricle, in the parenchyma and in total during the first five hours of continuous infusion, started at 5 min.

by compression of the bulk of the brain tissue. This compression is possible due to localised displacement of blood from the tissue. As time progresses, all of the additional fluid volume that is not absorbed flows slowly into the brain tissue where it is accommodated by a rather constant displacement of blood throughout the parenchyma due to the increased CSF pressure. For values of the Biot–Willis parameter below one, the results are not significantly different. The majority of the additional fluid is stored in the tissue due to the increased pressure and the ventricles are only dilated slightly in the long term, possibly through a small overall compression of the tissue. As mentioned earlier in 5.2, the subarachnoid space is not explicitly included in our model. Particularly the spinal subarachnoid space would accommodate a considerable portion of this additional fluid, however the distribution of the remaining fluid between the ventricle and the parenchyma would likely be the same.

Chapter 6

Conclusions and outlook

Contents

6.1 Conclusions

6.1.1 Compartment models

In this thesis, we have considered two types of models for the CSF dynamics during a constant rate infusion test: single-compartment models and spherically symmetric poroelastic models. In 3.5.4, we have shown how these two models can be related to each other by spatial integration of the poroelastic model over the parenchyma.

In chapter 2, we compared two single-compartment models with different functional descriptions of the compliance. These models describe the average pressure response to a given infusion rate as a single ODE, neglecting oscillations at heart

rate and slower pressure waves, as well as any spatial dependence. In clinical practice, the compliance is usually modelled via an inverse pressure relation, following the observation of an exponential pressure-volume curve by Marmarou et al. (1975). We termed this the "standard compliance model". Wirth and Sobey (2008) derived a generalisation of this compliance model with an inverse pressure power law from considerations on the collapsibility of the bridging veins in the brain. We have estimated the parameters for both models by fitting the simulated pressure to artificial data sets and clinical measurements during constant rate infusion tests. The result of these parameter estimations depends strongly on the quality of the data. Infusion tests that had to be aborted before a steady plateau pressure was reached were found to not contain sufficient information for reliable estimates. Even if the test was successful, oscillations at the cardiac cycle and slower pressure waves of unknown origin act as noise in the data and make the extraction of the average pressure response and hence the parameter values a difficult problem. If a plateau pressure was clearly reached, then the resistance to CSF absorption can be recovered reliably with either model. This parameter is often used in shunting decisions, in conjunction with other clinical tests.

With respect to the compliance, we conclude that both proposed models essentially describe the same compliance-pressure curve over the limited pressure range observed during an infusion test and hence predict the same pressure response. The biomechanical considerations by Wirth and Sobey (2008) offer a good explanation for this functional form of the compliance, which has been observed and repeatedly confirmed over the last three decades. Our work also demonstrates the interdependence between the parameters encoding this compliance-pressure curve. Different sets of parameter values lead to almost indistinguishable average pressure responses. This implies that neither of these parameters can be estimated

reliably with the data we have. Instead, we propose to consider the compliance-pressure curve directly when analysing a patient's compliance reserve. We stress that this curve was only estimated over the pressure range observed during the infusion test and extrapolations to other pressures should be considered with caution. While different sets of parameter values may lead to almost the same compliance curve over this limited pressure range, they can predict vastly different compliances for lower or higher pressures.

Finally, from the parameter estimations on the multi-fluid poroelastic model in chapter 5, we observe that the CSF pressure oscillations at heart rate also carry a lot of information about the compliance function. Thus, when considering only the average pressure response, as is generally done in single-compartment models, this additional information is neglected. Including the pressure amplitude in the analysis of the infusion test may provide more accurate and reliable estimates of the compliance function. Such reliable estimates are necessary for investigating the potential role and importance of the compliance in diagnosis and treatment planning of CSF related diseases.

6.1.2 Poroelastic models

Biomechanical models allow us to examine in more detail what influence the infusion has on the CSF dynamics. We have considered in particular a two-fluid poroelastic model proposed by Wirth and Sobey (2009). This is a generalisation of the linear single-fluid poroelastic theory by Biot (1941), where different fluid compartments interact via their pressures and volumes only indirectly through the tissue. Spherical symmetry reduces the number of spatial dimensions to one and allows us to integrate some of the PDEs in the resulting system analytically.

Nevertheless, the spherical description is fully three-dimensional and allows us to apply fluid volume conservation boundary conditions in the ventricle and at the skull, which are necessary to simulate the pressure response to an infusion.

As opposed to Wirth and Sobey (2009), we allow for two sources of non-linearity in the description. The first one is a strain dependency in the permeability, as used by Sobey and Wirth (2006) for a single-fluid poroelastic model of the brain. This limits the flow rate through the parenchyma and leads to ill-posed steady-state problems with possibly multiple solutions or no solution depending on the boundary conditions. However, in the case of an open aqueduct connecting the ventricle with the subarachnoid space, which we are mostly considering here, the strain remains small and its influence on the permeability turns out to be negligible.

The second non-linearity we consider is a pressure dependency in the CSF storage coefficient. This coefficient is a measure of the CSF volume change with changes in pressure and is the local counterpart of the CSF compliance in compartment models. By integrating the local fluid volume balance over the parenchyma and combining it with the boundary conditions and some small extra assumptions, we can relate the CSF storage coefficient directly to the compliance and thus obtain information about its value and functional form from the parameter estimations on the single compartment model. As noted before, for those estimations, the information carried by the oscillations was neglected and the compliance parameters need to be adjusted to fit both the average pressure response and the amplitude.

We have considered the simulation of one infusion test with a default set of parameter values in detail. When the infusion is started, the pressure and thus the absorption rate are still low and hence additional fluid needs to be stored at

a high rate. Due to the low permeability, CSF cannot flow deep into the tissue in a short time, so the volume dilation and tissue fluid content initially increase only locally, in thin layers at the boundaries. At short time scales, most of the additional fluid is instead stored in the ventricle, which enlarges at the expense of compression of the bulk of the parenchyma. As the infusion continues, the pressure increases and with it the rate of CSF absorption. As we can see from the simulation with continued infusion, the pressure and absorption rate actually temporarily exceed their steady-state values for the given infusion rate. As time progresses, CSF flows deeper into the tissue, where it is stored by displacement of blood due to the increased pressure. At the same time, the volume dilation of the tissue and with it the ventricle size slowly return to normal. In a real infusion test, the infusion is stopped long before this steady state is reached. As this happens, the absorption rate highly exceeds the CSF inflow rate and the effects are reversed. The ventricle shrinks below its initial value, fluid is extracted from the boundary layers of the tissue and the pressure decreases again. The increase in CSF pressure beyond its new steady state value is an interesting observation not modelled by single compartment models and could mean that the resistance to CSF outflow is routinely slightly overestimated.

With an extensive parameter variation, we examined the influence of each parameter on the pressure and volume dilation during an infusion test. We confirmed the influence of the parameters which appear in both the single compartment model and the poroelastic model on the average pressure response, but could also observe their effect on the pressure amplitude and the volume dilation. Surprisingly, several of the poroelastic parameters without counterpart in the compartment model have little to no effect on the pressure response, despite large

influences on the volume dilation. This means that crude estimates of these parameters are sufficient if we are only interested in the pressure response, but conversely implies that the pressure response carries very little information about these parameters. Thus, to be able to predict the tissue displacements and ventricle enlargement, these parameter values need to be obtained through other means.

The least well understood parameters of poroelastic models of biological tissue are probably the Biot–Willis parameter α and its equivalent α_a for arterial blood in the two-fluid model. As long as the values of $(1 - \alpha)$ and α_a are kept within the orders of magnitude proposed by Wirth and Sobey (2009), their exact value does not seem to have much influence and we can as well set both to zero. However, the value for α previously given in the literature of 0.83 (Wirth and Sobey, 2006) leads to a very different mechanical response of the brain tissue to an infusion test. Thus, the effect of this parameter needs to be examined further.

6.1.3 Numerics

Due to the spherical symmetry in our poroelastic model, only one spatial dimension needs to be considered. This allows us to analytically integrate two of the three coupled PDEs and express both the displacements and the pressure in terms of the volume dilation and further reduces the number of degrees of freedom in the discretised system. We discretise the volume dilation as a piecewise linear function on a non-uniform grid to be able to capture the strong boundary effects during the infusion test. From the weak form of the remaining PDE, we thus derive a system of non-linear ODEs for the values of the volume dilation at the nodes, using a method of lines and finite element approach.

Since some of the boundary conditions do not contain time derivatives, they lead to algebraic equations, making the spatially discretised system a system of differential-algebraic equations (DAEs). To have a larger choice in time-stepping methods, we have formulated these algebraic equations as differential equations in such a way that errors in satisfying the algebraic equations decay in time. To our knowledge, this is a new approach and its applicability in the current setting was tested numerically for different spatial meshes.

The discretised, non-linear steady-state system is solved iteratively with partial Newton steps and the time-dependent system solved via ODE solvers available in Matlab, both with straightforward preconditioning strategies. Spatial convergence in both cases could be confirmed on different types of meshes, but inaccuracies due to numerical rounding errors could be observed for very small step sizes. Comparisons of time-dependent solutions of the oscillatory multi-fluid poroelastic model with different time-stepping algorithms demonstrate stability problems of the solver ode23t, which could have been used to solve the DAE system directly, and thus support our approach of dealing with the algebraic boundary conditions.

6.2 Limitations of the models

6.2.1 Single compartment model

As is true of any mathematical model, the two models of CSF dynamics that we have considered have their limitations. The single-compartment model is only designed to predict the temporal pressure and volume changes of CSF. Its simplicity means that only few parameters need to be considered, but estimating

these from clinical data sets is still a difficult problem. Since this model only predicts the average pressure response to an infusion, all pressure changes on shorter time scales are considered noise, including oscillations at heart rate and other pressure waves of unknown origin. The Euclidean norm we have used in the least squares fit is particularly sensitive to large variations in the data. The estimation results could possibly be slightly improved by reducing the large pressure amplitudes through averaging in a preprocessing step, similar to the plots in chapter 5, or the use of a different norm.

Another problem is the strong interdependence of the parameters describing the functional form of the compliance. This has a negative effect on the objective function of the minimisation problem. A different parametrisation with independent parameters, for example the compliance value at different fixed pressures, could improve the reliability of the estimations. In addition, we have noted that the average pressure response neglects the extra information about the compliance available through the change in pressure amplitude. By scaling the amplitude with its pre-infusion value, the need for an additional parameter value in the two-compartment model, derived from the two-fluid poroelastic model, could be eliminated. In this case, two functions need to be fitted simultaneously to estimate the compliance function. Thus a good parametrisation of the compliance becomes even more important.

6.2.2 Poroelastic models

The poroelastic models are already more detailed than the compartment model. Yet, they only model the mechanical response of the brain and do not include

any biochemical processes. Such processes are strongly indicated by the pressure waves observed in clinical measurements, but as long as their origin is not understood, these effects cannot be modelled accurately. While the use of small strain theory can be defended in the particular case of an open aqueduct, considered here, assumptions such as the spherical geometry, isotropy and homogeneity of the brain tissue are clearly strong simplifications, which imply that predictions of spatial variations in our simulations are only qualitative.

In addition, we have used the phenomenological compliance model of the single compartment model to derive the pressure dependence of the CSF storage coefficient, in a way which also limits our choice of the value for the Biot–Willis parameter. It would be preferable to derive the storage coefficient from mechanical considerations on the brain tissue instead. Furthermore, we should note that in the description by Wirth and Sobey (2009), the Biot–Willis parameter and the CSF storage coefficient are related. Thus pressure dependence in one of them also implies pressure dependence in the other.

While the boundary conditions are clearly important for the simulation of an infusion test, we have also made simplifications there. Firstly, we have used steady Poiseuille flow through a straight tube to model flow through the aqueduct, whereas the real geometry is more complicated and the flow unsteady. Secondly, it is believed that at least part of the CSF is produced within the parenchyma Fishman (1992); Nolte (2009) and also absorption sites other than the arachnoid villi have been proposed (Levine, 1999; Johnston et al., 2004). But since the extent of these effects is unclear, we have fully neglected them and instead assumed production of CSF only in the ventricles and absorption only at the skull. Thirdly, the linearisation (3.69) of the change in ventricle volume leads to a small error with

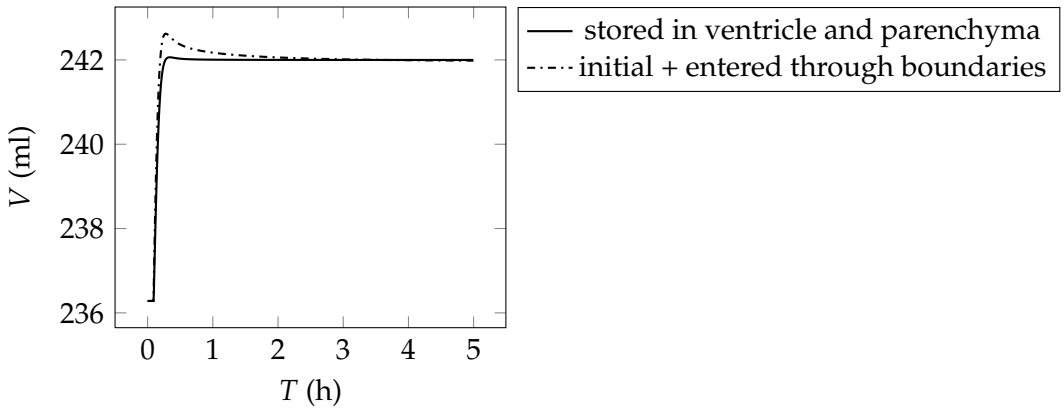

Figure 6.1: Comparison of total ventricular and parenchymal CSF volume stored in the system and total CSF volume in the system according to the boundary conditions.

the effect that some of the infused fluid gets lost and is neither stored nor absorbed (Figure 6.1). By far the biggest limitation with respect to the boundary conditions is the lack of a subarachnoid space and in particular a spinal compartment. With each cardiac cycle, some CSF flows between the ventricles and the spinal subarachnoid space. Without a spinal compartment, this flow is inhibited. This explains why, in our simulations, there are hardly any oscillations in the volume dilation or the displacements. In addition, as Levine (2000) noted, changes in the volume of the cranial subarachnoid space may explain how the ventricles can be decreased despite increased pressure, for example in idiopathic intracranial hypertension.

In chapter 5, we have only considered the average pressure response and its amplitude at heart rate as simulated by the two-fluid poroelastic model. Closer inspection of the wave form of the CSF pressure reveals differences between the simulation, which closely follows the arterial pressure pulse, and clinical measurements (Figure 6.2). One possible explanation is that pressure and volume pulses in different parts of the blood network, with phase shifts compared to the large arteries, all contribute to the CSF pressure wave form. So a more detailed

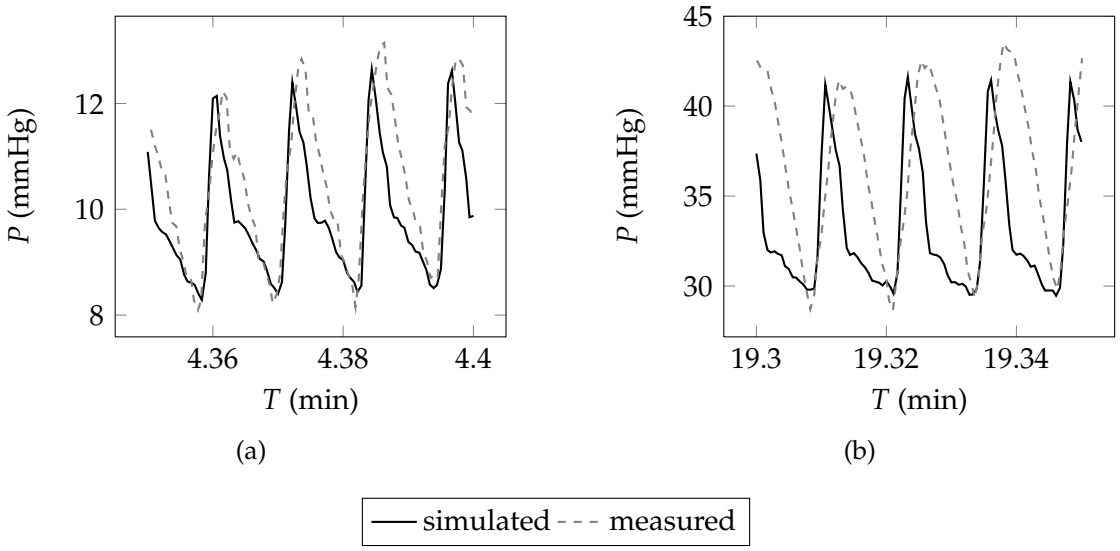

Figure 6.2: Comparison of simulated and measured pressure waveforms for data set 00, with optimised parameters (a) before the infusion, (b) at plateau pressure. The time intervals were chosen due to the good agreement of the average pressure and the amplitude. The peak of the measured CSF pressure is delayed compared to the simulated pressure, which closely follows the arterial pressure waveform.

model of blood flow in the brain may be necessary to model the wave form of the CSF pressure, for example a three-fluid model which treats arterial and venous blood separately. Another possible contribution may be viscoelasticity inherent in the solid phase in addition to porous effects, as for example shown by Franceschini et al. (2006).

6.3 Potential research directions

The long term goals of future research into and mathematical modelling of CSF dynamics in the human brain are improved understanding of the involved mechanical and biological processes and realistic, detailed models of the brain with

patient-specific geometry and parameter values, which can help in the diagnosis and treatment planning of CSF related diseases. In particular, the causes of non-obstructive hydrocephalus and symptoms such as normal pressure hydrocephalus or idiopathic intracranial hypertension are subjects of active research. With better mathematical models and improved imaging techniques, it may further be possible to reduce the need for invasive procedures such as intracranial pressure measurements or infusion tests.

On the way towards these long term goals, the existing mathematical models need to be refined step by step and each assumption and hypothesis thoroughly tested. While non-linear, large deformation models of the brain are clearly necessary for the simulation of the large deformations occurring during the development of hydrocephalus, they require knowledge of the underlying constitutive equations that describe the mechanical response of brain tissue in vivo and mechanical tests on living brain tissue are inherently complicated and highly invasive. In this context, we also stress again the importance of the geometric non-linearities in large deformation theory and the need for careful distinction between the Lagrangian and Eulerian frameworks.

In addition, there is still uncertainty about the values of several mechanical parameters of brain tissue, particularly with respect to their variability between patients, with age or disease and spatially throughout the brain. Improvements in imaging techniques have allowed, for example, promising advances in magnetic resonance elastography and poroelastography. For the Biot–Willis parameter, a possible, indirect way of measuring its value may be a comparison of the increase in ventricular volume and the amount of CSF stored within the tissue at constant increased pressure, neglecting oscillations due to the cardiac cycle, once the transi-

ent effects of the infusion have died down. However, accurate measurements of the ventricular size and the fluid content in the tissue during an infusion is at the very least technically challenging. Furthermore the continued infusion necessary to obtain such a steady state may be too invasive and may trigger compensatory biological processes which could distort the results.

To understand the constitutive equations, the focus may need to shift to smaller length scales temporarily. One example is the CSF storage coefficient. In our analysis, we have related it to the phenomenological compliance of the single compartment model, but as our comparison with the model by Wirth and Sobey (2008) has shown, the functional form of the compliance-pressure curve can essentially be derived from mechanical considerations of single veins. In addition, the exact meaning of the Biot–Willis parameter in poroelastic models of biological tissues is still unclear. While we have assumed this value to be constant, the description by Wirth and Sobey (2009) indicates a relationship between the Biot–Willis parameter and the CSF storage coefficient. Thus it would be very interesting to see if these two parameters, as well as others, can be traced back to local tissue and vessel properties. Homogenisation techniques could then be employed to derive large scale models of the whole brain and would lead to a better understanding of the meaning of the CSF compliance and its potential importance in clinical practice.

We have noted that the two-fluid poroelastic model cannot successfully reproduce the CSF pressure waveform and that including additional blood compartments or viscoelastic effects of the solid may improve this prediction. An alternative multi-fluid poroelastic description of the brain was proposed by Tully and Ventikos (2011), which includes fluid transport between compartments, but not the pressure volume coupling between them as modelled by Wirth and Sobey (2009). These

models are different special cases of a more general multi-fluid poroelastic model including both effects. In addition, flow-independent viscoelastic effects inherent in the solid can be included in a poroelastic framework, see for example Ehlers and Markert (2000). In the future, the influences of each of these effects on the simulated brain tissue response, more detailed geometries and boundary conditions including the subarachnoid space and a spinal compliance, such as the one-dimensional model proposed by Kim and Cirovic (2011), as well as biological processes, as far as these can be modelled mathematically, need to be considered.

Finally, studies such as that by Iliff et al. (2012) raise questions about assumptions regarding the permeability. They observed that tracer molecules flowed with CSF from the subarachnoid space into the parenchyma along paravascular channels, but entered the brain much less from the ventricles. In normal circumstances, the flow direction in the paravascular spaces followed that inside the blood vessels they surrounded, that is, CSF entered the brain along arteries and arterioles and left it alongside veins. Water and other small molecules are able to freely diffuse between the paravascular channels and the interstitial fluid, but larger molecules are confined to the paravascular channels. These observations indicate that the permeability to CSF flow is higher than indicated by earlier estimations with larger molecules, highly anisotropic and may in addition have preferred directions following the blood flow direction.

Modelling all the different effects relating to CSF dynamics mathematically to evaluate their relative importance in simulations and in diagnosis will be challenging. To meet these challenges in the future, continued communication between clinicians, engineers and mathematicians is essential.

Bibliography

ANSI/AAMI BP22-1994 blood pressure transducers: Comparison of BD DTX plus transducers & AAMI performance standard, Aug. 1994. Replaced by ANSI/AAMI BP22:1994/(R2011). 163

R. Aaslid, K.-F. Lindegaard, W. Sorteberg and H. Nornes. Cerebral autoregulation dynamics in humans. *Journal of the American Heart Association*, 20:45–52, 1989. doi: 10.1161/01.STR.20.1.45. 112

M. Abramowitz and I. A. Stegun, editors. *Handbook of Mathematical Functions with Formulas, Graphs, and Mathematical Tables*. Dover Publications, June 1965. 141, 142

G. C. Agarwal, B. M. Berman and L. Stark. A lumped parameter model of the cerebrospinal fluid system. *IEEE Transactions on Biomedical Engineering*, BME-16 (1):45–53, Jan. 1969. doi: 10.1109/TBME.1969.4502602. 36, 37

K. Andersson, I. R. Manchester, N. Andersson, A. Shiriaev, J. Malm and A. Eklund. Assessment of cerebrospinal fluid outflow conductance using an adaptive observer–experimental and clinical evaluation. *IOP Physiological Measurement*, 28:1355–1368, Oct. 2007. doi: 10.1088/0967-3334/28/11/003. 39

K. Andersson, I. R. Manchester, J. Malm and A. Eklund. Real-time estimation of cerebrospinal fluid system parameters via oscillating pressure infusion. *Medical and Biological Engineering and Computing*, 48:1123–1131, 2010. doi: 10.1007/s11517-010-0670-6. 35, 39

N. Andersson, J. Malm and A. Eklund. Dependency of cerebrospinal fluid outflow resistance on intracranial pressure. *Journal of Neurosurgery*, 109:918–922, Nov. 2008. doi: 10.3171/JNS/2008/109/11/0918. 38, 53

G. K. Batchelor. *An introduction to fluid dynamics*. Cambridge University Press, 1967. 98

A. Behrens, N. Lenfeldt, S. Qvarlander, L.-O. Koskinen, J. Malm and A. Eklund. Are

intracranial pressure wave amplitudes measurable through lumbar puncture? *Acta Neurologica Scandinavica*, 2012. doi: 10.1111/j.1600-0404.2012.01701.x. 166

J. G. Berryman and H. F. Wang. The elastic coefficients of double-porosity models for fluid transport in jointed rock. *Journal of Geophysical Research*, 100(B12): 24611–24627, 1995. doi: 10.1029/95JB02161. 120

L. E. Bilston. The effect of perfusion on soft tissue mechanical properties: A computational model. *Computer Methods in Biomechanics and Biomedical Engineering*, 5(4):283–290, 2002. doi: 10.1080/10255840290032658. 41

M. A. Biot. General theory of three-dimensional consolidation. *Journal of Applied Physics*, 12(2):155–164, Feb. 1941. doi: 10.1063/1.1712886. 37, 42, 79, 80, 82, 83, 84, 85, 110, 111, 209

G. Birkhoff and G.-C. Rota. *Ordinary differential equations*. Wiley, 3rd edition, 1978. 147

A. J. W. Boon, J. T. J. Tans, E. J. Delwel, S. M. Egeler-Peerdeman, P. W. Hanlo, H. A. L. Wurzer, C. J. J. Avezaat, D. A. De Jong, R. H. J. M. Gooskens and J. Hermans. Dutch normal-pressure hydrocephalus study: prediction of outcome after shunting by resistance to outflow of cerebrospinal fluid. *Journal of Neurosurgery*, 87:687–693, 1997. doi: 10.3171/jns.1997.87.5.0687. 35, 39

R. M. Bowen. Incompressible porous media models by use of the theory of mixtures. *International Journal of Engineering Science*, 18(9):1129–1148, 1980. doi: 10.1016/0020-7225(80)90114-7. 79

R. M. Bowen. Compressible porous media models by use of the theory of mixtures. *International Journal of Engineering Science*, 20(6):697–735, 1982. doi: 10.1016/0020-7225(82)90082-9. 79

M. W. B. Bradbury. Hydrocephalus. In P. H. Schurr and C. E. Polkey, editors, *Hydrocephalus*, chapter Anatomy and Physiology of CSF, pages 19–47. Oxford University Press, 1993. 30, 31

D. Braess. *Finite Elements*. Cambridge University Press, 2007. 124

K. E. Brenan, S. L. Campbell and L. R. Petzold. *Numerical Solution of Initial-Value Problems in Differential-Algebraic Equations*. North-Holland, 1989. 124, 125, 137

S. Cheng and L. E. Bilston. Unconfined compression of white matter. *Journal of Biomechanics*, 40:117–124, 2007. doi: 10.1016/j.jbiomech.2005.11.004. 45

S. Cheng, E. C. Clarke and L. E. Bilston. Rheological properties of the tissue of the central nervous system: A review. *Medical Engineering & Physics*, 30:1318–1337, 2008. doi: 10.1016/j.medengphy.2008.06.003. 41, 185

K. Cieślicki. Mathematical modelling of the infusion test. *Polish Journal of Medical Physics And Engineering*, 13(1):33–54, 2007. doi: 10.2478/v10013-007-0004-7. 39, 119

S. Cirovic. A coaxial tube model of the cerebrospinal fluid pulse propagation in the spinal column. *Journal of Biomechanical Engineering*, 131(2):021008, Feb. 2009. doi: 10.1115/1.3005159. 97

S. Cirovic and M. Kim. One-dimensional model for cerebrospinal fluid pulse in the spinal column. In C. Lim and J. Goh, editors, *6th World Congress of Biomechanics (WCB 2010)*, number 31 in IFMBE Proceedings, pages 366–369. Springer, 2010. doi: 10.1007/978-3-642-14515-5˙94. 97

S. Cirovic and M. Kim. A one-dimensional model of the spinal cerebrospinal-fluid compartment. *J. Biomech. Eng.*, Feb. 2012. doi: 10.1115/1.4005853. 97

S. Cirovic, C. Walsh and W. D. Fraser. Mathematical study of the role of non-linear venous compliance in the cranial volume-pressure test. *Medical & Biological Engineering & Computing*, 41:579–588, 2003. doi: 10.1007/BF02345321. 40, 50, 112, 113, 175

O. Coussy. *Poromechanics*. John Wiley & Sons, Ltd, Chichester, 2004. 79, 81, 83, 84, 98, 120

CureResearch. Statistics about hydrocephalus, May 2003. URL `http://www.cureresearch.com/h/hydrocephalus/stats.htm`. Accessed 2012-09-10. 34

M. Czosnyka and J. D. Pickard. Monitoring and interpretation of intracranial pressure. *Journal of Neurology, Neurosurgery, and Psychiatry*, 75:813–821, 2004. doi: 10.1136/jnnp.2003.033126. 35

M. Czosnyka, Z. Czosnyka, S. Momjian and J. D. Pickard. Cerebrospinal fluid dynamics. *Physiological Measurement*, 25:R51–R76, 2004. doi: 10.1088/0967-3334/25/5/R01. 38, 54, 97

Z. Czosnyka, B. Owler, N. Keong, T. Santarius, O. Baledent, J. D. Pickard and M. Czosnyka. Impact of duration of symptoms on CSF dynamics in idiopathic normal pressure hydrocephalus. *Acta Neurologica Scandinavica*, 123:414–418, 2011. doi: 10.1111/j.1600-0404.2010.01420.x. 39

H. Davson, G. Hollingsworth and M. B. Segal. The mechanism of drainage of the cerebrospinal fluid. *Brain*, 93(4):665–678, 1970. doi: 10.1093/brain/93.4.665. 38, 53

J. R. Dormand and P. J. Prince. A family of embedded Runge–Kutta formulae. *Journal of Computational and Applied Mathematics*, 6(1):19–26, 1980. doi: 10.1016/0771-050X(80)90013-3. 57

C. S. Drapaca, S. Sivaloganathan and G. Tenti. Nonlinear constitutive laws in viscoelasticity. *Mathematics and Mechanics of Solids*, 12:475–501, 2007. doi: 10.1177/1081286506062450. 41

P. Drysdale, J. Huber, P. Robinson and K. Aquino. Spatiotemporal bold dynamics from a poroelastic hemodynamic model. *Journal of Theoretical Biology*, 265(4):524 – 534, 2010. ISSN 0022-5193. doi: 10.1016/j.jtbi.2010.05.026. 44

T. Dutta-Roy, A. Wittek and K. Miller. Biomechanical modelling of normal pressure hydrocephalus. *Journal of Biomechanics*, 41(10):2263–2271, July 2008. doi: 10.1016/j.jbiomech.2008.04.014. 40, 41, 42

M. Egnor, A. Rosiello and L. Zheng. A model of intracranial pulsations. *Pediatric Neurosurgery*, 35:284–298, 2001. doi: 10.1159/000050440. 39

M. Egnor, L. Zheng, A. Rosiello, F. Gutman and R. Davis. A model of pulsations in communicating hydrocephalus. *Pediatric Neurosurgery*, 36:281–303, 2002. doi: 10.1159/000063533. 39

W. Ehlers and B. Markert. On the viscoelastic behaviour of fluid-saturated porous materials. *Granular Matter*, 2:153–161, 2000. doi: 10.1007/s100359900037. 220

A. Eisenträger, I. Sobey and M. Czosnyka. Parameter estimations for the cerebrospinal fluid infusion test. *Mathematical Medicine and Biology Advance Access published February, 16, 2012*. doi: 10.1093/imammb/dqs001. 49

A. Eklund, P. Smielewski, I. Chambers, N. Alperin, J. Malm, M. Czosnyka and A. Marmarou. Assessment of cerebrospinal fluid outflow resistance. *Medical and Biological Engineering and Computing*, 45:719–735, 2007. doi: 10.1007/s11517-007-0199-5. 35, 39, 203

H. C. Elman, D. J. Silvester and A. J. Wathen. *Finite Elements and Fast Iterative Solvers: with Applications in Incompressible Fluid Dynamics*. Numerical Mathematics and Scientific Computation. Oxford University Press, 2008. 124

R. A. Fishman. *Cerebrospinal Fluid in Diseases of the Nervous System*. Saunders, Philadelphia, 2nd edition, 1992. 30, 31, 33, 34, 38, 53, 69, 168, 172, 215

G. Franceschini, D. Bigoni, P. Regitnig and G. A. Holzapfel. Brain tissue deforms similarly to filled elastomers and follows consolidation theory. *Journal of the Mechanics and Physics of Solids*, 54:2592–2620, 2006. doi: 10.1016/j.jmps.2006.05.004. 42, 45, 217

F. B. Freimann, K.-J. Streitberger, D. Klatt, K. Lin, J. McLaughlin, J. Braun, C. Sprung and I. Sack. Alteration of brain viscoelasticity after shunt treatment in normal pressure hydrocephalus. *Neuroradiology*, 54(3):189–196, 2012. doi: 10.1007/s00234-011-0871-1. 42

J. J. García and J. H. Smith. A biphasic hyperelastic model for the analysis of fluid and mass transport in brain tissue. *Annals of Biomedical Engineering*, 37(2): 375–386, Feb. 2009. doi: 10.1007/s10439-008-9610-0. 44, 122

C. A. Giller and R. Aaslid. Estimates of pulse wave velocity and measurement of pulse transit time in the human cerebral circulation. *Ultrasound in Medicine & Biology*, 20(2):101–105, 1994. doi: 10.1016/0301-5629(94)90074-4. 114

M. A. Green, L. E. Bilston and R. Sinkus. In vivo brain viscoelastic properties measured by magnetic resonance elastography. *NMR in Biomedicine*, 21:755–764, 2008. doi: 10.1002/nbm.1254. 42, 122

J. E. Guinane. An equivalent circuit analysis of cerebrospinal fluid hydrodynamics. *American Journal of Physiology*, 223(2):425–430, Aug. 1972. URL `http://ajplegacy.physiology.org/content/223/2/425`. 36, 37, 38

S. Hakim and C. Hakim. A biomechanical model of hydrocephalus and its relationship to treatment. In K. Shapiro, A. Marmarou and H. Portnoy, editors, *Hydrocephalus*, pages 143–160. Raven Press, New York, 1984. 69

S. Hakim, J.-G. Venegas and J. Burton. The physics of the cranial cavity, hydrocephalus, and normal pressure hydrocephalus: Mechanical interpretation and mathematical model. *Surgical Neurology*, 5:187–210, 1976. 36, 40, 42, 44

J. S. Hesthaven and T. Warburton. *Nodal Discontinuous Galerkin Methods: Algorithms, Analysis, and Applications*, volume 54 of *Texts in Applied Mathematics*. Springer Science+Business Media, LLC, 2008. 124

Hydrocephalus Association. Life-threatening complications of hydrocephalus. URL `https://www.hydroassoc.org/hydrocephalus-education-and-support/learning-about-hydrcephalus/life-threatening-complications-of-hydrocephalus/`. Accessed 2012-09-10. 33

J. J. Iliff, M. Wang, Y. Liao, B. A. Plogg, W. Peng, G. A. Gundersen, H. Benveniste, G. E. Vates, R. Deane, S. A. Goldman, E. A. Nagelhus and M. Nedergaard. A paravascular pathway facilitates CSF flow through the brain parenchyma and the clearance of interstitial solutes, including amyloid β. *Science Translational Medicine*, 4(147):147ra111, Aug. 2012. doi: 10.1126/scitranslmed.3003748. 30, 31, 220

M. Johnston, A. Zakharov, C. Papaiconomou, G. Salmasi and D. Armstrong. Evidence of connections between cerebrospinal fluid and nasal lymphatic vessels in humans, non-human primates and other mammalian species. *Cerebrospinal Fluid Research*, 1:2, Dec. 2004. doi: 10.1186/1743-8454-1-2. 53, 215

H. Juniewicz, M. Kasprowicz, M. Czosnyka, Z. Czosnyka, S. Gizewski, M. Dzik and J. D. Pickard. Analysis of intracranial pressure during and after the infusion test in patients with communicating hydrocephalus. *Physiological Measurement*, 26:1039–1048, 2005. doi: 10.1088/0967-3334/26/6/013. 35, 38, 39, 47, 50, 51, 52, 54, 57, 62

M. Kaczmarek, R. Subramaniam and S. Neff. The hydromechanics of hydrocephalus: Steady state solution for cylindrical geometry. *Bulletin of Mathematical Biology*, 59:295–323, 1997. doi: 10.1007/BF02462005. 43, 69

G. Kellie. An account of the appearances observed in the dissection of two of three individuals presumed to have perished in the storm of the 3d, and whose bodies were discovered in the vicinity of Leith on the morning of the 4th, November 1821; with some reflections on the pathology of the brain. *Transactions - Medicochirurgical Society of Edinburgh*, 1:84–169, 1824. 36

M. Kim and S. Cirovic. A computational model of the cerebrospinal fluid system incorporating lumped-parameter cranial compartment and one-dimensional distributed spinal compartment. *Journal of Biorheology*, pages 1–10, 2011. doi: 10.1007/s12573-011-0041-4. 220

D. Klatt, U. Hamhaber, P. Asbach, J. Braun and I. Sack. Noninvasive assessment of the rheological behavior of human organs using multifrequency MR elastography: a study of brain and liver viscoelasticity. *Physics in Medicine and Biology*, 52(24):7281–7294, 2007. doi: 10.1088/0031-9155/52/24/006. 42, 122

S. K. Kyriacou, A. Mohamed, K. Miller and S. Neff. Brain mechanics for neurosurgery: modeling issues. *Biomechanics and Modeling in Mechanobiology*, 1:151–164, 2002. doi: 10.1007/s10237-002-0013-0. 45

J. C. Lagarias, J. A. Reeds, M. H. Wright and P. E. Wright. Convergence properties

of the Nelder–Mead simplex method in low dimensions. *SIAM Journal on Optimization*, 9(1):112–147, 1998. doi: 10.1137/S1052623496303470. 64

W. M. Lai and V. C. Mow. Drag-induced compression of articular cartilage during a permeation experiment. *Biorheology*, 17:111–123, 1980. 83

D. N. Levine. The pathogenesis of normal pressure hydrocephalus: A theoretical analysis. *Bulletin of Mathematical Biology*, 61:875–916, 1999. doi: 10.1006/bulm.1999.0116. 33, 43, 53, 215

D. N. Levine. Ventricular size in pseudotumor cerebri and the theory of impaired CSF absorption. *Journal of the Neurological Sciences*, 177:85–94, 2000. doi: 10.1016/S0022-510X(00)00348-8. 33, 43, 84, 96, 101, 216

X. Li, H. von Holst and S. Kleiven. Influence of gravity for optimal head positions in the treatment of head injury patients. *Acta Neurochirurgica*, pages 1–8, 2011. doi: 10.1007/s00701-011-1078-2. 44

Life Science Databases (LSDB). Lateral ventricle. [CC-BY-SA-2.1-jp (`http://creativecommons.org/licenses/by-sa/2.1/jp/deed.en`)], via Wikimedia Commons. Version 16:34, 13 September 2009. URL `http://commons.wikimedia.org/wiki/File:Lateral_ventricle.gif`., 2009. Accessed at 2010-11-26. 32

A. A. Linninger, C. Tsakiris, D. C. Zhu, M. Xenos, P. Roycewicz, Z. Danziger and R. Penn. Pulsatile cerebrospinal fluid dynamics in the human brain. *IEEE Transactions on Biomedical Engineering*, 52(4):557–565, Apr. 2005. doi: 10.1109/TBME.2005.844021. 40

A. A. Linninger, B. Sweetman and R. Penn. Normal and hydrocephalic brain dynamics: The role of reduced cerebrospinal fluid reabsorbtion in ventricular enlargement. *Annals of Biomedical Engineering*, 37(7):1434–1447, June 2009a. doi: 10.1007/s10439-009-9691-4. 45

A. A. Linninger, M. Xenos, B. Sweetman, S. Ponkshe, X. Guo and R. Penn. A mathematical model of blood, cerebrospinal fluid and brain dynamics. *Journal of Mathematical Biology*, 59:729–759, 2009b. doi: 10.1007/s00285-009-0250-2. 40

J. Löfgren and N. N. Zwetnow. Cranial and spinal components of the cerebrospinal fluid pressure-volume curve. *Acta Neurologica Scandinavica*, 49:575–585, 1973. doi: 10.1111/j.1600-0404.1973.tb01331.x. 97

B. MacMahon, T. F. Pugh and T. H. Ingalls. Anencephalus, spina bifida, and hydrocephalus: Incidence related to sex, race, and season of birth, and incidence in siblings. *British Journal of Preventive and Social Medicine*, 7(4):211–219, Oct 1953. URL `http://www.jstor.org/stable/25565060`. 34

I. R. Manchester, K. S. Andersson, N. Andersson, A. S. Shiriaev and A. Eklund. A nonlinear observer for on-line estimation of the cerebrospinal fluid outflow resistance. *Automatica*, 44:1426–1430, 2008. doi: 10.1016/j.automatica.2007.09.025. 39

A. Marmarou, K. Shulman and J. LaMorgese. Compartmental analysis of compliance and outflow resistance of the cerebrospinal fluid system. *Journal of Neurosurgery*, 43(5):523–534, Nov. 1975. doi: 10.3171/jns.1975.43.5.0523. 35, 36, 38, 50, 208

A. Marmarou, K. Shulman and R. M. Rosende. A nonlinear analysis of the cerebrospinal fluid system and intracranial pressure dynamics. *Journal of Neurosurgery*, 48(3):332–344, Mar. 1978. doi: 10.3171/jns.1978.48.3.0332. 54

T. Matsumoto, H. Nagai, Y. Kasuga and K. Kamiya. Changes in intracranial pressure (ICP) pulse wave following hydrocephalus. *Acta Neurochirurgica*, 82 (1-2):50–56, 1986. doi: 10.1007/BF01456319. 97

U. Meier and P. Bartels. The importance of the intrathecal infusion test in the diagnosis of normal pressure hydrocephalus. *Journal of Clinical Neuroscience*, 9 (3):260–267, 2002. doi: 10.1054/jocn.2001.1004. 33, 35, 39

K. Miller. Modelling soft tissue using biphasic theory – a word of caution. *Computer Methods in Biomechanis and Biomedical Engineering*, 1(3):261–263, Jan. 1998. doi: 10.1080/01495739808936706. 42

K. Miller. Constitutive model of brain tissue for finite element analysis of surgical procedures. *Journal of Biomechanics*, 32:475–479, 1999. doi: 10.1016/S0021-9290(99)00010-X. 40, 41

A. Monro. *Observations on the structure and functions of the nervous system. : Illustrated with tables*. Edinburgh : Printed for, and sold by, William Creech; and Joseph Johnson, ... London., M DCC LXXXIII, 1783. 36

T. Nagashima, N. Tamaki, S. Matsumoto, B. Horwitz and Y. Seguchi. Biomechanics of hydrocephalus: A new theoretical model. *Neurosurgery*, 21:898–904, 1987. URL `http://journals.lww.com/neurosurgery/Fulltext/1987/12000/Biomechanics_of_Hydrocephalus__A_New_Theoretical.19.aspx`. 37, 42

National Institute of Neurological Disorders and Stroke. Hydrocephalus fact sheet, Dec. 2011. URL `http://www.ninds.nih.gov/disorders/hydrocephalus/detail_hydrocephalus.htm`. Accessed 2012-09-10. 34

NHS Choices. Hydrocephalus, June 2011a. URL `http://www.nhs.uk/conditions/Hydrocephalus/Pages/Introduction.aspx`. Accessed 2012-09-10. 34

NHS Choices. Symptoms of hydrocephalus, July 2011b. URL http://www.nhs.uk/Conditions/Hydrocephalus/Pages/Symptoms.aspx. Accessed 2012-09-10. 33

J. Nolte. *The Human Brain: An Introduction to its Functional Anatomy*. Mosby, 6th edition, 2009. 30, 31, 33, 38, 53, 69, 168, 215

Office for National Statistics. *2011 Census - Population and Household Estimates for England and Wales, March 2011*. July 2012. URL http://www.ons.gov.uk/ons/dcp171778_270487.pdf. 34

P. Perriñez, F. Kennedy, E. Van Houten, J. Weaver and K. Paulsen. Magnetic resonance poroelastography: An algorithm for estimating the mechanical properties of fluid-saturated soft tissues. *IEEE Transactions on Medical Imaging*, 29(3):746–755, Mar. 2010. ISSN 0278-0062. doi: 10.1109/TMI.2009.2035309. 44, 122

W. H. Press, S. A. Teukolsky, W. T. Vetterling and B. P. Flannery. *Numerical Recipes: The Art of Scientific Computing*. Cambridge University Press, 3rd edition, 2007. 141, 142, 143

S. Qvarlander, J. Malm and A. Eklund. The pulsatility curve: the relationship between mean intracranial pressure and pulsation amplitude. *IOP Physiological Measurement*, 31:1517–1528, 2010. doi: 10.1088/0967-3334/31/11/008. 39, 175

I. Sack, B. Beierbach, J. Wuerfel, D. Klatt, U. Hamhaber, S. Papazoglou, P. Martus and J. Braun. The impact of aging and gender on brain viscoelasticity. *NeuroImage*, 46(3):652 – 657, 2009. ISSN 1053-8119. doi: 10.1016/j.neuroimage.2009.02.040. 42

C. A. Sánchez, C. Drapaca, S. Sivaloganathan and E. Vrscay. Elastography of biological tissue: Direct inversion methods that allow for local shear modulus variations. In A. Campilho and M. Kamel, editors, *Image Analysis and Recognition*, volume 6112 of *Lecture Notes in Computer Science*, pages 195–206. Springer, 2010. ISBN 978-3-642-13774-7. doi: 10.1007/978-3-642-13775-4˙20. 42, 122

K. Shahim, J.-M. Drezet, J.-F. Molinari, R. Sinkus and S. Momjian. Finite element analysis of normal pressure hydrocephalus: influence of CSF content and anisotropy in permeability. *Applied Bionics and Biomechanics*, 7(3):187–197, 2010. doi: 10.1080/11762322.2010.490044. 44, 122

K. Shahim, J.-M. Drezet and B. A. Martin. Ventricle equilibrium position in healthy and normal pressure hydrocephalus brains using an analytical model. *Journal of Biomechanical Engineering*, 134(4):041007 (10 pages), 2012. doi: 10.1115/1.4006466. 43

L. Shampine, M. W. Reichelt and J. A. Kierzenka. Solving index-1 DAEs in MATLAB and Simulink. *SIAM Review*, 41(3):538–552, Sept. 1999. doi: 10.1137/S003614459933425X. 137

L. F. Shampine and M. W. Reichelt. The MATLAB ODE suite. *SIAM Journal on Scientific Computing*, 18:1–22, 1997. doi: 10.1137/S1064827594276424. 143, 159

S. Sivaloganathan, J. Drake and G. Tenti. Mathematical pressure volume models of the cerebrospinal fluid. *Applied Mathematics and Computation*, 94:243–266, 1998. doi: 10.1016/S0096-3003(97)10093-5. 38, 50, 53, 69

S. Sivaloganathan, M. Stastna, G. Tenti and J. Drake. A viscoelastic approach to the modelling of hydrocephalus. *Applied Mathematics and Computation*, 163: 1097–1107, 2005a. doi: 10.1016/j.amc.2004.06.037. 40, 41

S. Sivaloganathan, M. Stastna, G. Tenti and J. Drake. A viscoelastic model of the brain parenchyma with pulsatile ventricular pressure. *Applied Mathematics and Computation*, 165:687–698, 2005b. doi: 10.1016/j.amc.2004.04.086. 37, 40, 41

S. Sivaloganathan, M. Stastna, G. Tenti and J. M. Drake. Biomechanics of the brain: A theoretical and numerical study of Biot's equations of consolidation theory with deformation-dependent permeability. *International Journal of Non-Linear Mechanics*, 40:1149–1159, 2005c. doi: 10.1016/j.ijnonlinmec.2005.04.004. 43

F. H. Sklar and I. Elashvili. The pressure-volume function of brain elasticity. *Journal of Neurosurgery*, 47:670–679, Nov. 1977. doi: 10.3171/jns.1977.47.5.0670. 38

A. Smillie, I. Sobey and Z. Molnar. A hydroelastic model of hydrocephalus. *Journal of Fluid Mechanics*, 539:417–443, 2005. doi: 10.1017/S0022112005005707. 43, 44, 80, 96, 100, 106

I. Sobey and B. Wirth. Effect of non-linear permeability in a spherically symmetric model of hydrocephalus. *Mathematical Medicine and Biology*, 23:339–361, 2006. doi: 10.1093/imammb/dql015. 43, 80, 82, 93, 96, 116, 210

I. Sobey, A. Eisenträger, B. Wirth and M. Czosnyka. Multi-fluid poro-elastic modelling of the CSF infusion test. In C. T. Lim and J. C. H. Goh, editors, *6th World Congress of Biomechanics (WCB 2010)*, volume 31 of *IFMBE Proceedings*, pages 362–365. Springer, Oct. 2010. doi: 10.1007/978-3-642-14515-5˙93. 45, 69, 114

I. Sobey, A. Eisenträger, B. Wirth and M. Czosnyka. Simulation of cerebral infusion tests using a poroelastic model. *International Journal of Numerical Analysis and Modeling, Series B*, 3:52–64, 2012. URL `http://www.math.ualberta.ca/ijnamb/Volume-3-2012/No-1-12/2012-01-04.pdf`. 45, 114, 116

D. Soler, T. Cox, P. Bullock, D. M. Calver and R. O. Robinson. Diagnosis and management of benign intracranial hypertension. *Archives of Disease in Childhood*, 78:89–94, 1998. doi: 10.1136/adc.78.1.89. 33

R. B. Spertell. The response of brain to transient elevations in intraventricular pressure. *Journal of the Neurological Sciences*, 48(3):343–352, Dec. 1980. doi: 10.1016/0022-510X(80)90107-0. 37, 40, 41

K.-J. Streitberger, E. Wiener, J. Hoffmann, F. B. Freimann, D. Klatt, J. Braun, K. Lin, J. McLaughlin, C. Sprung, R. Klingebiel and I. Sack. In vivo viscoelastic properties of the brain in normal pressure hydrocephalus. *NMR in Biomedicine*, 24(4): 385–392, 2011. ISSN 1099-1492. doi: 10.1002/nbm.1602. 33, 42, 185

E. Süli and D. Mayers. *An Introduction to Numerical Analysis*. Cambridge University Press, 2006. 124, 141, 142

N. Sundström, K. Andersson, A. Marmarou, J. Malm and A. Eklund. Comparison between 3 infusion methods to measure cerebrospinal fluid outflow conductance. *Journal of Neurosurgery*, 113:1294–1303, 2010. doi: 10.3171/2010.8.JNS10157. 35, 39

Z. Taylor and K. Miller. Reassessment of brain elasticity for analysis of biomechanisms of hydrocephalus. *Journal of Biomechanics*, 37:1263–1269, 2004. doi: 10.1016/j.jbiomech.2003.11.027. 44, 121

G. Tenti, J. Drake and S. Sivaloganathan. Brain biomechanics: Mathematical modelling of hydrocephalus. *Neurological Research*, 22:19–24, 2000. 46

B. Tully and Y. Ventikos. Coupling poroelasticity and CFD for cerebrospinal fluid hydrodynamics. *IEEE Transactions on biomedical engineering*, 56(6):1644–1651, June 2009. doi: 10.1109/TBME.2009.2016427. 43, 97

B. Tully and Y. Ventikos. Cerebral water transport using multiple-network poroelastic theory: application to normal pressure hydrocephalus. *Journal of Fluid Mechanics*, 667:188–215, Jan. 2011. doi: 10.1017/S0022112010004428. 10, 33, 37, 81, 110, 120, 219

B. Tully, J. Byrne and Y. Ventikos. Is normal pressure hydrocephalus more than a mechanical disruption to CSF flow? In *Engineering in Medicine and Biology Society (EMBC), 2010 Annual International Conference of the IEEE*, pages 235–238, 2010. doi: 10.1109/IEMBS.2010.5627772. 45

H. F. Wang. *Theory of Linear Poroelasticity with Applications to Geomechanics and Hydrogeology*. Princeton University Press, 2000. ISBN 0-691-03746-9. 79, 81, 83, 84

R. A. Weerakkody, M. Czosnyka, M. U. Schuhmann, E. Schmidt, N. Keong, T. Santarius, J. D. Pickard and Z. Czosnyka. Clinical assessment of cerebrospinal fluid dynamics in hydrocephalus. Guide to interpretation based on observational study. *Acta Neurologica Scandinavica*, 124(2):85–98, Aug. 2011. doi: 10.1111/j.1600-0404.2010.01467.x. 39

K. P. Wilkie, C. S. Drapaca and S. Sivaloganathan. A theoretical study of the effect of intraventricular pulsations on the pathogenesis of hydrocephalus. *Applied Mathematics and Computation*, 215:3181–3191, 2010. doi: 10.1016/j.amc.2009.09.054. 37, 41

K. P. Wilkie, C. S. Drapaca and S. Sivaloganathan. A nonlinear viscoelastic fractional derivative model of infant hydrocephalus. *Applied Mathematics and Computation*, 217(21):8693–8704, July 2011. doi: 10.1016/j.amc.2011.03.115. 41, 69

K. P. Wilkie, C. S. Drapaca and S. Sivaloganathan. A mathematical investigation of the role of intracranial pressure pulsations and small gradients in the pathogenesis of hydrocephalus. *International Journal of Numerical Analysis and Modeling, Series B*, 3(1):36–51, 2012a. URL `http://www.math.ualberta.ca/ijnamb/Volume-3-2012/No-1-12/2012-01-03.pdf`. 41, 43

K. P. Wilkie, C. S. Drapaca and S. Sivaloganathan. Aging impact on brain biomechanics with applications to hydrocephalus. *Mathematical Medicine and Biology*, 29 (2):145–161, June 2012b. doi: 10.1093/imammb/dqr001. 33, 41

B. Wirth. A mathematical model for hydrocephalus. Master's thesis, Oxford University, 2005. URL `http://ora.ox.ac.uk/objects/uuid:dcdae88a-9f3d-4531-8861-778464b5c154`. 93

B. Wirth and I. Sobey. An axisymmetric and fully 3d poroelastic model for the evolution of hydrocephalus. *Mathematical Medicine and Biology*, 23:363–388, 2006. doi: 10.1093/imammb/dql014. 44, 84, 85, 113, 168, 185, 189, 212

B. Wirth and I. Sobey. A model for an inverse power constitutive law for cerebral compliance. *Mathematical Medicine and Biology*, 25:113–131, 2008. doi: 10.1093/imammb/dqn006. 3, 39, 40, 47, 50, 51, 54, 56, 63, 71, 84, 113, 118, 208, 219

B. Wirth and I. Sobey. Analytic solution during an infusion test of the linear unsteady poroelastic equations in a spherically symmetric model of the brain. *Mathematical Medicine and Biology*, 26(1):25–61, 2009. doi: 10.1093/imammb/dqn021. 37, 45, 47, 80, 82, 84, 86, 96, 110, 111, 113, 114, 116, 120, 168, 189, 193, 197, 209, 210, 212, 215, 219

B. Wirth, I. Sobey and A. Eisenträger. Conditions for choking in a poroelastic flow model. *IMA Journal of Applied Mathematics*, Sept. 2012. doi: 10.1093/imamat/hxs062. 80, 84, 87, 121